Pulse Detonation Exhaust and Methods for Damping its Transient Characteristic

vorgelegt von

M. Sc.

Mohammad REZAY HAGHDOOST

an der Fakultät V – Verkehrs- und Maschinensysteme der

TECHNISCHEN UNIVERSITÄT BERLIN

zur Erlangung des akademischen Grades

Doktor der Ingenieurwissenschaften

– Dr.-Ing. –

genehmigte Dissertation

Promotionsausschuss

Vorsitzender:	Prof. Dr.-Ing. Dieter PEITSCH
Gutachter:	Prof. Dr.-Ing. Kilian OBERLEITHNER
	Prof. PhD DSc. Ephraim GUTMARK
	Prof. Dr. sc. Panagiotis STATHOPOULOS
	Dr. Daniel EDGINGTON-MITCHELL

Tag der wissenschaftlichen Aussprache: 16. Juli 2021

Berlin 2022

Vorwort

Diese Dissertation entstand im Rahmen meiner wissenschaftlichen Tätigkeit an der Technischen Universität Berlin im Rahmen des von der Deutschen Forschungsgemeinschaft geförderten Sonderforschungsbereiches SFB1029. An dieser Stelle möchte ich mich bei allen bedanken, die durch ihre Unterstützung zum Gelingen dieser Arbeit beigetragen haben.

Zu allererst gilt mein Dank meiner Frau Christina, die mich großartig unterstützte und mir immer den Rücken freigehalten hat. Ohne Deine Unterstützung wäre diese Arbeit sicherlich nicht zustande gekommen.

Weiterhin gilt mein Dank meinem Doktorvater, Prof. Dr.-Ing. Kilian Oberleithner, für die exzellente Betreuung und Zusammenarbeit, nicht nur auf der wissenschaftlichen, sondern auch persönlichen Ebene. Ich bedanke mich für das Vertrauen und die Geduld, die Du mir entgegengebracht hast und insbesondere für den gewährten wissenschaftlichen Freiraum. Deine freundliche Art und uneingeschränkte Unterstützung während der gesamten Bearbeitungsphase dieser Arbeit werden mir in sehr guter Erinnerung bleiben. Außerdem möchte ich mich bei Herrn Prof. Dr.-Ing. Oliver Paschereit für die immerwährende Unterstützung sowie das Etablieren eines harmonischen Arbeitsumfeldes am HFI bedanken.

I wish to extend special thanks to Dr. Daniel Edgington-Mitchell for offering excellent advice and support during the entire work. This thesis could only be completed because of your valuable suggestions. Your enthusiasm has been a never-ending source of inspiration during the long journey of this work. Furthermore, I express my gratitude to Prof. Dr. sc. Panagiotis Stathopoulos, Prof. Dr.-Ing. Dieter Peitsch and Prof. Ph.D. D.Sc. Ephraim Gutmark for serving on my dissertation committee.

Bei den vielen Kolleginnen und Kollegen am HFI sowie SFB1029 möchte ich mich für die Unterstützung bedanken, insbesondere Dr.-Ing. Moritz Sieber, Bhavraj Thethy, Niclas Garan, Maikel Nadolski, Prof. Dr.-Ing. Rupert Klein, Johann Vinkeloe, Finn Lückoff, Tim Rähse, Joseph Saverin, Fabian Habicht, Fatma Yücel, Dr.-Ing. Thoralf Reichelt, Dr.-Ing. Joshua Gray, Eric Bach, Phoebe Kuhn, Jens Müller, Jan Beuth, Dr.-Ing. Thomas Kaiser, Sirko Bartholomay, Jakob von Saldern, Dr.-Ing. Sebastian Schimeck, Dr.-Ing. Navid Nayeri, Andy Göhrs, Joachim Kraatz, Martin Franke, Maria Lück und Sandy Meinecke. Weiterhin möchte ich mich bei meinen vielen studentischen Hilfskräften für ihren wertvollen Einsatz bedanken. Hierbei gilt mein Dank insbesondere Jonas Förster, Bonggyun Seo, Farkhondeh Rouholahnejad und Malte Mütter.

Ein besonderer Dank gilt meinem Mathe- und Physiklehrer auf dem Carl-Zeiss-Gymnasium: Herr Reinhard, der Zuspruch und Mut, den Sie mir trotz meiner damaligen großen Defizite in der deutschen Sprache geschenkt haben, war maßgeblich für meine Entwicklung. Dafür bin ich Ihnen für immer dankbar.

Zu guter Letzt möchte ich mich bei meinen lieben Eltern sowie meinen Schwestern bedanken. Danke für Eure bedingungslose Unterstützung und dass ich mich jederzeit auf Euch verlassen kann.

Zusammenfassung

Die druckerhöhende Verbrennung (PGC) kann nicht zuletzt aufgrund ihres vielversprechenden Potentials für eine deutliche Effizienzerhöhung auf einen Zeitraum von mehr als einem Jahrhundert Forschung zurückblicken. Im Gegensatz zur konventionellen deflagrationsbasierten Verbrennung führt die PGC zu einer deutlichen Steigerung des gemittelten Druckes über die Brennkammer. Einer der in diesem Zusammenhang zumeist untersuchten Ansätze basiert auf dem Einsatz von Pulsdetonationsbrennkammern (PDC), welche im Rahmen der aktuellen Forschungskonzepte als eine Komponente in unterschiedlichen Maschinen zum Einsatz kommen. Hierzu zählen unter anderem Ramjets, Raketen sowie Gasturbinen. Bei diesen Pulsdetonationstriebwerken (PDE) wird üblicherweise der hohe Druck aus der Brennkammer entweder über eine Düse zur Schuberzeugung oder über eine Turbine zur Energie- und Schuberzeugung verwendet.

Obwohl das Potential der PDE bereits unter Beweis gestellt wurde, sind noch zahlreiche Herausforderungen zu überwinden, bevor ein flächendeckender Einsatz von PDE aus der Forschung heraus in der realen Welt realisiert werden kann. Eine zentrale Rolle hierbei ist der pulsierenden Charakteristik der PDC zuzurechnen. Die daraus resultierende höchst instationäre Ausströmung aus der PDC stellt eine große Herausforderung für die Auslegung von Komponenten dar, die eine effiziente Entspannung der PDC-Ausströmung ermöglichen sollen. Die Adressierung dieser Problematik entspricht dem Hauptziel dieser Arbeit. Hierzu wird zunächst die PDC-Ausströmung untersucht, bevor mit der Entwicklung von Lösungsansätzen fortgefahren wird, die eine effiziente Entspannung der Ausströmung herbeiführen sollen.

Diese Dissertation dient zum Teil einer Charakterisierung der PDC-Ausströmung. Hierzu werden zum einen Strömungsmerkmale identifiziert, die während der initialen Ausströmung auftreten. Zum anderen werden globale Merkmale untersucht, die die gesamte Ausströmungsphase charakterisieren lassen. Unter Einsatz unterschiedlicher optischer Messsysteme werden zeitaufgelöste Daten zur Charakterisierung des Fundamentalproblems des startenden unterexpandierten Strahls erhoben. Ein Modell wird entwickelt, das Rückschlüsse auf den zugrundeliegenden Mechanismus für die Entstehung des zweiten Dreifachpunktes des unterexpandierten Strahls erlaubt. Während viele Analogien zu einem Stoßrohr-Strahl aufgezeigt werden, werden die Hauptunterschiede zwischen dem PDC-Strahl und Stoßrohr-Strahl hervorgehoben. Weiterhin wird der komplette Zyklus der PDC-Ausströmung einschließlich des Einflusses der Brennstoff-Füllmenge quantitativ erfasst. Es zeigt sich, dass eine Vielzahl von Aus- und Einströmungsphasen für ein einziges Detonationsereignis auftreten. Während die Brennstoff-Füllmenge nur die erste Ausströmungsphase beeinflusst, wird die Düsengeometrie als ein entscheidender Parameter für die Modifikation der Anzahl sowie Stärke der Aus- und Einströmungsphasen identifiziert.

Zwei Konzepte werden untersucht, die auf eine Verbesserung der PDC-Ausströmung hinsichtlich einer effizienten Expansion abzielen. Die Eignung der beiden Konzepte, Stoß-Teiler sowie Plenum, werden unter Beweis gestellt. Es zeigt sich, dass die exzessive Energie einer führenden Stoßwelle durch den Einsatz von Stoß-Teilern umverteilt werden kann. Basierend auf numerischen Studien werden der Einfluss von Auslegungsparametern sowie konkrete Optimierungsansätze für die Auslegung der Stoß-Teiler diskutiert.

Es stellt sich heraus, dass die zeitliche Umverteilung der Energie mit dem Breitenverhältnis der Stoß-Teiler-Kanäle zunimmt, dies jedoch auf Kosten des Totaldruckes geschieht. Darüber hinaus werden die Messgenauigkeit sowie die dynamischen Beschaffenheiten unterschiedlicher konventioneller Drucksensoren untersucht. Diese Sensoren werden anschließend in einem Plenum verbaut, um die Entwicklung des höchst instationären Druckes innerhalb des stromab der PDC angebrachten Plenums zu erfassen. Durch den Einsatz des Plenums kann eine signifikante Schwächung der führenden Stoßwelle sowie räumliche und zeitliche Umverteilung der PDC-Ausströmungsenergie aufgezeigt werden. Die vorgestellten Ergebnisse unterstreichen das Potential des Plenums hinsichtlich der Verbesserung der PDC-Ausströmung für eine stromab anzubringende Turbine. Während sich sowohl das Plenum als auch der Stoß-Teiler hinsichtlich ihres vorgesehenen Grundkonzeptes bewährt haben, bietet ihr generisches Design eine Menge Anreize für potentielle Folgestudien.

Abstract

Pressure **g**ain **c**ombustion (PGC) has been the subject of research for over a century due to the potential for significant efficiency increase in combustion systems. Contrary to conventional deflagration-based combustors, PGC induces a significant rise in the averaged total pressure across the combustor. One of the most promising PGC applications is based on **p**ulse **d**etonation **c**ombustors (PDCs), which are components in many recent concepts such as ramjets, rocket and gas turbines. In these **p**ulse **d**etonation **e**ngines (PDEs), the high-pressure combustion products expand either through a nozzle for thrust generation or through a turbine for thrust and power generation.

Although the promising potential of PDEs has already been demonstrated, many challenges remain for its broad deployment in a real world environment. A key challenge of the PDEs arises from the intermittent nature of the PDC operation. The pulsating character and highly transient exhaust of the PDC makes the design of devices for efficient expansion very challenging. The main purpose of this work is to address these challenges and begins with a detailed examination of the exhaust of the PDC before proceeding with the development of methods toward an efficient expansion of the PDC exhaust.

The present thesis contributes to the characterization of the exhaust flow field of a PDC. Various flow features observed during the jets initial evolution as well as global features of the exhaust full cycle are identified. Using different optical measurement techniques, time-resolved data are obtained to characterize the fundamental flow dynamic problem of the highly underexpanded starting jet. A model is developed to identify the underlying mechanism leading to the formation of the second triple point of the jet. While many of the flow features are analogous to those observed in the exhaust of an open-end shock tube, the main differences between the initial evolution of a PDC and shock tube exhaust are highlighted. Furthermore, a quantitative characterization of the full cycle of the PDC exhaust is conducted, including the impact of fill fraction. Multiple exhaust and suction phases are determined for a single detonation event. While the fill fraction is found to only affect the first exhaust phase, the nozzle geometry is identified as a parameter for altering the strength and the amount of the exhaust and suction phases.

Two concepts, with the objective of enhancing the PDC exhaust for efficient expansion, are studied. The capability of both concepts, shock divider and plenum, for damping the PDC exhaust transient characteristics is demonstrated. The excessive energy of an incident shock wave is redistributed by using a shock divider. The impact of design parameters on the divider flow evolution is discussed, including design improvement suggestions based on numerical studies. The temporal redistribution of the initial shock wave energy is found to increase with the divider width ratio, but at the expense of total pressure. Following this, an assessment of the accuracy and dynamic response of pressure transducers is conducted. The transducers are then used to measure the pressure evolution in a plenum, downstream of an array of PDCs. The impact of the plenum on the temporal and spatial redistribution of the PDC exhaust energy, as well as significant attenuation of the PDC transmitted leading shock waves, is demonstrated. While both the divider and the plenum show the capability to enhance the PDC exhaust for a downstream turbine, their generic design provides a wide range of incentives for follow-up studies.

Contents

List of Figures

Nomenclature

Latin letters

$\dot{m}$	Mass flow rate
Ma	Mach number
c	Speed of sound
e	Internal energy
h	Enthalpy
h_f	Enthalpy of formation
L	Length of the combustor
p	Pressure
q	Specific head addition
s	Entropy
T	Temperature
t	Time
u, v	Flow velocity components
v	Specific volume
x, y, z	Cartesian coordinates

Greek letters

γ	Adiabatic index
ρ	Density
X	Molar fraction

Subscripts

$()_1$	Reactants
$()_2$	Products

Abbreviations

AC	**A**lternating **C**urrent
BOS	**B**ackground **O**riented **S**chlieren
CEA	**C**hemical **E**quilibrium with **A**pplications
CFD	**C**omputational **F**luid **D**ynamics
CJ	**C**hapman **J**ouguet
CMOS	**C**omplementary **M**etal **O**xide **S**emiconductor

CRVR **C**ounter **R**otating **V**ortex **R**ings

CVC **C**onstant **V**olume **C**ombustion

DC **D**irect **C**urrent

DDT **D**eflagration to **D**etonation **T**ransition

GE **G**eneral **E**lectric

GSD **G**eometrical **S**hock **D**ynamics

HITRAN **Hi**gh resolution **Tran**smission molecular absorption database

ICP **I**ntegrated **C**ircuit **P**iezoelectric

IEA **I**nternational **E**nergy **A**gency

LAS **L**aser **A**bsorption **S**pectroscopy

LED **L**ight **E**mitting **D**iode

PDC **P**ulse **D**etonation **C**ombustor

PDE **P**ulse **D**etonation **E**ngine

PGC **P**ressure **G**ain **C**ombustion

PIV **P**article **I**mage **V**elocimetry

PM **P**randtl **M**eyer

RDC **R**otating **D**etonation **C**ombustor

RDE **R**otating **D**etonation **E**ngine

SFC **S**pecific **F**uel **C**onsumption

TDLAS **T**unable **D**iode **L**aser **A**bsorption **S**pectroscopy

vN **v**on **N**eumann

VRES **V**ortex **R**ing **E**mbedded **S**hock

ZND **Z**eldovic von **N**eumann **D**öring

To my parents,

Shahin and Hossein

Chapter 1

Introduction and Motivation

Five facts about climate change: It is *real*. *We* are the cause of it. It is *dangerous*. The experts are *unanimous*. We can *still* do something about it. Although these statements seem somewhat bold, they represent the key messages concerning climate change, according to a consortium of leading climate research institutes in Germany [1]. The main motivation of this work ties to the very last statement, in the hope of making a minor contribution to it.

Despite global concerns on climate change, today's global energy demand is still supplied mainly by fossil fuels, by more than 80% [2]. According to the **I**nternational **E**nergy **A**gency (IEA), the global carbon dioxide emissions from fuel combustion started rising again in 2017, having a significant impact on man-made climate change [3]. While the deployment of conventional environmentally sustainable renewable energy technologies is growing, their potential is limited and may well be much lower than current global energy usage [4, 5]. Considering the increase in global energy demand of nearly 1% per year [6], reducing the global energy consumption as well as utilizing alternative energy sources is crucial to avert a significant climate change.

While the two primary environmentally sustainable renewable energy sources, wind and solar power are inherently intermittent, efficient storage of energy from a fluctuating supply in a large scale is still very challenging at the current level of technology. Therefore, load balancing power generation technologies are assumed to play an important role during the transformation of the global energy system, if not even beyond. In contrast to conventional power plants such as nuclear or coal power plants, gas turbines are ideal for quick start and shut down. Start time in the order of minutes allows for load balancing, and thereby maintaining grid stability. Besides power generation, gas turbines are the primary propulsion technology for air transport due to their superiority over alternative methods. Considering that power generation and transport account for over two-thirds of the total global emissions [6], the potential of gas turbine technology to mitigate climate change is indisputable.

One way to enhance the impact of gas turbines on climate change is to obtain emission reduction by using alternative propellants. Renewable propellants such as hydrogen obtained from power-to-gas technology are part of comprehensive, long-term plans of stakeholders and regulatory agencies for a net-zero carbon emissions vision by 2050 [7–9]. However, many challenges need to be solved for a broad deployment of zero-carbon emission gas turbines in a real world environment [10, 11]. Another approach to enhance the impact of gas turbines on the environment is to improve the fuel-to-power efficiency,

usually referred to as **s**pecific **f**uel **c**onsumption (SFC). By increasing the SFC, the gas turbine technology can contribute to both emission reduction as well as cutting into the use of finite fossil energy sources.

Although the gas turbine engines are subject to continuous optimization, the technology trend has shown only an incremental gain in efficiency in the last few decades. The fact that modern gas turbine engines are approaching an asymptotic efficiency limit suggests the necessity of a paradigm shift in gas turbine optimization efforts [12]. Since entropy production is detrimental to gas turbine efficiency, substantial efficiency gains can be obtained by optimizing the process that causes the maximum entropy. The entropy generated by different processes in a gas turbine can be evaluated based on the temperature-entropy (T-s) diagram. Figure 1.1 shows the T-s diagram for the ideal Brayton cycle (blue line), which is also referred to as the Joule process, representing the thermodynamic cycle of conventional gas turbines. As shown in the diagram, the combustion process results in considerable entropy production. Hence, the selection of the combustion mode has the potential for a dramatic increase in efficiency.

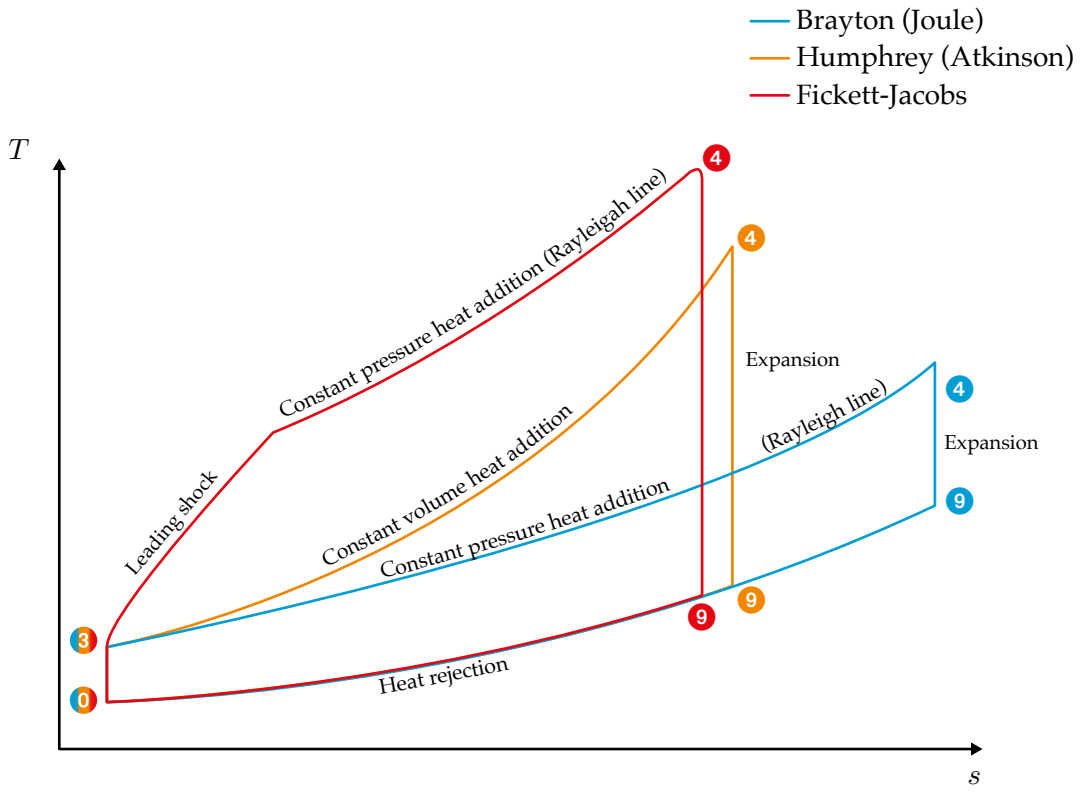

FIGURE 1.1: Temperature-Entropy diagram for ideal Brayton, Humphrey and Fickett-Jacobs cycle. Adapted from [13].

A promising alternative to the deflagration combustion of the conventional gas turbine is **p**ressure **g**ain **c**ombustion (PGC). The term PGC refers to all combustion concepts that exhibit an increase in the averaged total pressure across the combustor in addition to temperature. PGC is associated with higher thermodynamic efficiency than the respective ideal gas turbine cycle due to the physical boundary condition during the heat addition;

while the heat addition occurs at constant pressure for an ideal Brayton cycle, it occurs at constant volume for the ideal Humphrey cycle, as illustrated in Fig. 1.1. The latter, also known as the Atkinson cycle, is often used to represent the thermodynamic cycle of PGC engines. The Humphrey cycle shows a significant reduction in entropy generation during the combustion than the Brayton cycle (orange vs. blue line from state ③ to ④ in Fig. 1.1). In a study conducted by Jones & Paxson [14] the application of PGC in commercial propulsion systems was estimated to induce a reduction in fuel consumption in the order of 4-9%. Thus, the PGC is a promising technology due to its potential for higher SFC compared to conventional gas turbines.

Various PGC concepts have been proposed in the last few decades. The most commonly investigated types are those associated with wave rotors, pulsejets, **p**ulse **d**etonation **c**ombustors (PDCs) and **r**otating **d**etonation **c**ombustors (RDCs). Despite dissimilar fundamental design and operating modes, all of these devices provide a total pressure increase during the combustion process. In a propulsion application, the increase in pressure can be used to produce thrust by expanding directly into the ambient atmosphere. PGC can also be applied for power generation by using high pressure, high-temperature combustion products to drive a downstream turbine. The engines utilizing the former concept are referred to as *PDC-nozzle* engines and the latter *PDC-turbine* engines in the remainder of this thesis.

Although the constant-volume combustion and its corresponding Humphrey cycle are a reasonable approximation for PGC, the detonation-based combustors such as PDC and RDC have the potential for even higher efficiency. The thermodynamic cycle for the detonation based PGC is usually represented by the ideal Fickett-Jacobs cycle. As shown in Fig. 1.1, the Fickett-Jacobs cycle (red line) exhibits higher available energy with less entropy generation compared to the constant volume Humphrey and constant pressure Brayton cycle. However, despite the superior thermodynamic efficiency of the Fickett-Jacobs cycle, there has been no commercial application of PGC reported to date. The PGC gas turbines have not yet overcome a demonstration phase, as there are various serious technical challenges to be solved. If these challenges are not addressed appropriately, the thermodynamic benefit of the entire cycle may be insufficient to make the technology competitive.

One of the key challenges of the PGC devices is caused by the intermittent nature of their operating cycle, a feature all proposed PGC concepts have in common. The resulting transient flow affects both thermodynamic and gasdynamic analysis of the PGC. As discussed before, the classical Humphrey cycle is commonly used in the literature to describe the potential performance of PGC engines, although it does not account for the transient nature of the PGC. However, as pointed out by Paxson & Kaemming [15], the classical Humphrey (or Fickett-Jacobs) cycle is unsuitable and may lead to misinterpretation and errors when analyzing the potential performance of PGC devices, as done by many researchers [13, 16, 17]. At the heart of the problem is that although all reactants in the combustor reach state ④ (shown in Fig. 1.1), only an infinitesimal mass of the fluid leaves the combustor in this state. This fact has considerable consequences for the thermodynamic and gasdynamic analysis of PGC devices. As a first point, the temperature in state ④ is only momentary, as it represents the maximum temperature

throughout the cycle. In fact, the total temperature decreases during the exhaust phase. Hence, the available energy shown in Fig. 1.1, which corresponds to the integral of the curve, misrepresents the actual average energy throughout the cycle. Therefore, the direct comparison between the steady Brayton cycle of conventional gas turbines and the transient Humphrey cycle of PGC devices based on Fig. 1.1 is not feasible. However, by accounting for the transient exhaust, the thermodynamic process can be modeled, which again demonstrates the PGCs potential for efficiency gain compared to conventional gas turbines [15, 18, 19].

A further consequence of the transient exhaust concerns the expansion of the combustion products. When applying the ideal Humphrey cycle to the PGC, it is presumed that the transient combustor exhaust expands isentropically from state ④ to ⑨, as illustrated in Fig. 1.1. The expansion can occur either through a nozzle to provide thrust (PDC-nozzle engine) or via a turbine to convert the heat addition to work (PDC-turbine engine). However, even a moderate-loss expansion of the highly transient combustor exhaust flow remains a technically significant challenge for both nozzle and turbine designers, not to mention an isentropic expansion. The challenges for an efficient expansion are exacerbated by the fact that the stronger waves provide a higher level of pressure gain, but also result in a more intense transient flow. Hence, an efficient expansion of the transient combustor exhaust is one of the crucial, if not the most, remaining challenges to promote the PGC technology to a serious competitor for isobaric combustion in conventional gas turbines.

Among various PGC concepts, the PDC poses one of the most significant challenges for an efficient expansion. This challenge is mainly caused by the PDCs inherent severe pulsating exhaust. Although much progress has been made towards understanding the PDC exhaust, there are still no sophisticated approaches for an efficient expansion. As the efficient expansion of the PDC exhaust is the main motivation of this work, a brief literature overview is given in the following. First, the PDC-nozzle application will be discussed before considering the PDC-turbine concept.

The performance of a PDC-nozzle engine can be modified by utilizing different devices at the exit of the combustor. Various studies on the impact of nozzle shapes on PDC-nozzle engines have been conducted in the last few decades. The most studied nozzle shapes are convergent, divergent and convergent-divergent nozzles. It was shown that in contrast to a steady flow, a converging section is not needed to obtain a choked nozzle [20, 21]. Furthermore, the diverging nozzles usually result in higher impulses than other nozzle shapes, as optimum performance is achieved only if the combustion products are expanded efficiently through the nozzle [22]. A comprehensive review on the various PDC nozzles can be found in the work of Kailasanath [23] and a brief but recent overview in [22]. For a steady flow, there is a nozzle geometry to obtain an isentropic expansion. However, for the highly transient PDC exhaust, any fixed geometry will result in entropy generation. Assuming a fixed nozzle geometry, any infinitesimal mass of the fluid leaving the combustor will expand to a different state than the state ⑨ shown in Fig. 1.1. Consequently, by using a fixed nozzle geometry, the available energy may well be far less than the one obtained from the ideal Humphrey cycle. Moreover, the design of an efficient nozzle becomes even more complicated when considering that real engines run under different operating conditions.

Another device for modifying the exhaust of PDC-nozzle engines that has been studied by several research groups is the so-called ejector [24–29]. An ejector is typically a coaxial duct placed around the exit of the PDC, allowing for direct entrainment of the surrounding flow into the PDC exhaust. It was shown that besides a significant decrease in noise [30], a thrust augmentation over 2 can be achieved by coupling an ejector with a PDE [29, 31]. The performance of the ejector for pulsed flow exhibits a considerable performance benefit than a steady-flow ejector. Furthermore, it was found that the optimum ejector diameter roughly coincides with the size of the primary vortex ring, which forms during the initial exhaust phase of the combustor [27, 32]. Hence, the enhanced performance, obtained with the transient starting jets over comparable ejectors driven by steady jets, was mainly attributed to the structure of the starting vortex-type flow associated with the transient flow evolution [27]. Opalski et al. [27] concluded that further characterization of the starting jet, including the structure of the vortex ring, is required to optimize the coupling between PDEs and ejectors.

An alternative approach to PDCs in combination with nozzles and ejectors for thrust generation (PDC-nozzle engine) is implementing PDCs into a gas turbine to provide work through a turbine (PDC-turbine engine). However, the transient pulsed PDC exhaust is detrimental for conventional turbines, resulting in low turbine efficiency. The most studied turbine types for pulsating inflow conditions are turbochargers facing pulsating flow in reciprocating engines. Previous studies on turbocharges show that turbine efficiency decreases due to different phenomena such as variable blade loading, incident angle variation, and passage vortex formation [33–37]. Similar phenomena accompanied by strong shock wave reflections are observed in the few available numerical studies for axial turbines driven by pulsating flow [38–41]. Generally, two types of inflow conditions are used to investigate the response of turbines to the PDC exhaust. In some studies the PDC exhaust is simulated using pulsed air, while others use the exhaust of one or multiple PDCs to drive a turbine. An overview regarding these studies is given in the following.

Various studies were conducted at the University of Cincinnati to investigate the interaction of PDCs with a downstream turbine. Glaser et al. [42] compared the performance of an axial turbine driven by conventional deflagration combustors with the turbine driven by an array of PDCs. By measuring the power generated by the turbine, it was shown that the efficiency of the turbine was comparable for both PDC-driven and conventional deflagration combustors. However, a minimum of 79% secondary air was mixed with the exhaust of the PDCs to drive the turbine, which is attributed to be the primary mechanism for the enhanced performance of the PDC-driven turbine [39]. The same axial single stage turbine was used by George et al. [43] to investigate the turbine response to cold pulsating air flow. It was shown that the turbine efficiency decreases by about 10% from steady to pulsating flow. In a recent study conducted by Anand et al. [44] the same test rig was used, but the turbine was driven by detonative flow from an array of six PDCs. In contrast to the study by Glaser et al. [42], no secondary air was used while the PDCs were directly attached to the turbine. Consequently, the efficiency of the PDC-driven turbine was four times less than the turbine rated efficiency for steady flow. While these studies provide abundant invaluable information, they emphasize the unresolved challenge of efficient coupling of PDCs to a turbine.

A series of experiments were conducted at GE Global Research Center by Rasheed et al. [45, 46] using eight PDCs to drive a single-stage axial turbine. The PDC-turbine system shows a 4% increase in overall efficiency compared to the steady-state operation. The efficiency increase is attributed to some extent to the pressure gain provided by the detonation wave, which overcomes the efficiency loss of the turbine. It is notable that an increase in overall efficiency was achieved, although no attempts were made to optimize the performance of the PDC-turbine system. However, also in these studies, the PDC exhaust was mixed with secondary air prior to entering the turbine, which is believed to considerably contribute to the measured performance gain by increasing the mass flow rate and damping the combustor exhaust fluctuations.

Both Glaser et al. [42] and Rasheed et al. [46] used a relatively small plenum between the PDC exhaust and turbine inlet. However, as the primary purpose of the plenum was the mixing of bypass air with the PDC exhaust, the plenum design was not optimized for minimizing the pressure pulses. In fact, Glaser et al. [42] used a converging nozzle at the plenum inlet, which intensifies the incident shock strength and thereby increases the amplitude of the pressure peak entering the turbine. Moreover, the PDC exit was directly attached to the turbine inlet to maximize the fluctuations in turbine inlet quantities in the studies conducted by George et al. [43] and Anand et al. [44]. Although strong fluctuations may well be beneficial for studying the impact of the pulsating flow on the turbine, they are deteriorative for its performance. In a recent study conducted by Fernelius & Gorrell [47], it was demonstrated that it is the amplitude of the pressure fluctuations that are primarily responsible for decreasing the turbine efficiency. Accordingly, the PDC-turbine engines performance is presumably highly sensitive to the coupling of the PDCs and the turbine.

The discussion above underlines the necessity of suitable devices between the PDCs and the turbine that allow for mitigation of the pulsation as well as efficient harvesting of the combustor's exhaust gas kinetic energy. Although mixing the PDC exhaust with secondary air was shown to increase the turbine efficiency, it comes at a price as any secondary air needs to be provided by a compressor. Alternative approaches for efficient enhancement of turbine inflow conditions are of great interest, as the operation of PDCs directly attached to a conventional turbine without secondary airflow can easily result in a less efficient system than a conventional gas turbine. This hypothesis leads to the main objectives of this thesis, which starts with the experimental acquisition of high-resolution and high-fidelity data for a characterization of the PDC exhaust. Based on the collected data, different approaches are presented to mitigate the severity of the PDC exhaust pulsation. Furthermore, by analyzing the PDC exhaust, the fundamental flow dynamic problem of supersonic starting jets is investigated in detail.

The present cumulative thesis includes four publications with various experimental and numerical investigations. In chapter 2, the fundamentals of the conducted research are presented. Chapter 3 provides details on experimental methods extending the information given in each publication. The four publications are presented subsequently in chapter 4. The thesis is concluded in chapter 5 by a comprehensive discussion based on the main results of each publication. The thesis closes with some suggestions for follow-up studies.

Chapter 2

Pulse Detonation Fundamentals

In this chapter, a brief overview is given regarding the fundamentals of the detonation phenomenon. Furthermore, the operating cycle of the pulse detonation combustor is introduced. The chapter closes with a brief discussion concerning the fundamental gasdynamic features and wave dynamics inside the combustor.

2.1 Detonation

As the application of detonation waves in gas turbines is the subject of this thesis, the fundamentals of detonation waves are presented first. This section begins by introducing the characteristics of self-propagating combustion waves, including detonation waves. Then, the mechanism for the transition across detonation waves is presented based on a one-dimensional model. This section ends with a brief discussion of the complex three-dimensional structure of detonations.

Upon ignition a combustion wave propagates inside a combustible mixture, resulting in a large change in the thermodynamic state across the wave. The change in the thermodynamic state occurs by the conversion of the potential energy stored in the chemical bonds of the reactants into the internal and kinetic energy of the products. For a combustible mixture, the thermodynamic state of the products is predominately governed by the type of the combustion wave. Generally, there are two different types of self-propagating combustion waves: deflagration and detonation. The two combustion waves differ mainly in wave velocity and propagation mechanism, resulting in different thermodynamic states downstream of the combustion wave [48].

A *deflagration* wave propagates at relatively low subsonic velocity with respect to the reactants. Consequently, disturbances downstream of the wave can propagate upstream and impact the initial state of the reactants. While a deflagration is an expansion wave, resulting in a pressure attenuation across the wave, a *detonation* wave induces a significant increase in pressure. The detonation propagates at supersonic speed with respect to the reactants ahead. Accordingly, the disturbances and information downstream of the wave (e.g., the rear boundary condition for a detonation propagating inside a tube) cannot reach the detonation wave. Therefore, the reactants remain unchanged prior to the arrival of the detonation. Hence, the propagation velocity of the detonation wave does not depend on the rear boundary condition but only on the initial state of the reactants.

Whether a deflagration or detonation occurs in a combustible mixture mainly depends on the initial mixture, ignition source, and boundary conditions. Different types of

deflagration and detonation waves and aspects to consider for finding a unique solution are presented in the following.

2.1.1 Chapman-Jouguet Theory

Possible types of combustion waves for given boundary conditions and initial mixture can be determined based on the steady one-dimensional conservation equations. For this purpose, a combustion wave is considered that propagates inside a tube from left to right in the laboratory reference frame at the velocity u_1. By fixing the coordinate system to the combustion wave, the wave becomes stationary as illustrated in Figure 2.1. The reactants enter the combustion wave at the velocity u_1, and the products exits the wave at the velocity u_2. The conservation equation of mass, momentum, and energy are given by

$$\rho_1 u_1 = \rho_2 u_2, \tag{2.1}$$

$$p_1 + \rho_1 u_1^2 = p_2 + \rho_2 u_2^2, \tag{2.2}$$

$$h_1 + q + \frac{u_1^2}{2} = h_2 + q + \frac{u_2^2}{2}, \tag{2.3}$$

where u is the gas velocity, p is the pressure, ρ is the density, h is the enthalpy and q is the difference between the enthalpies of formation h_f of the reactants and products:

$$q = \sum_{i}^{\text{Reactants}} X_i h_{f,i} - \sum_{j}^{\text{Products}} X_j h_{f,j}, \tag{2.4}$$

where X is the mole fraction of the species in the reactants i and products j.

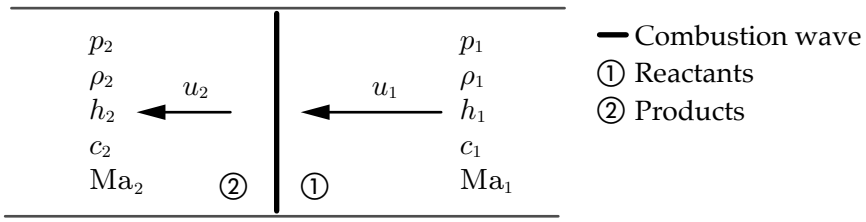

FIGURE 2.1: Schematic illustration of an one-dimensional propagating combustion wave inside a tube. The coordinate system is fixed to the wave.

The following relation can be obtained by utilizing the conservation of mass and momentum (equations 2.1 and 2.2) and the relation for the specific volume $v = 1/\rho$:

$$\frac{p_2 - p_1}{v_2 - v_1} = \rho_1^2 u_1^2 = \rho_2^2 u_2^2 = \dot{m}^2, \tag{2.5}$$

where $\dot{m}$ is the mass flux per unit area. Using equation 2.5 to plot p versus v results in the so-called *Rayleigh line* (Fig. 2.2(a)). This line represents the thermodynamic path in which the transition from reactants to combustion products occurs. This expression is used in

the subsequent discussion to identify physically accessible regions of deflagration and detonation waves.

Requiring the energy equation to be satisfied in addition to the conservation of mass and momentum leads to the *Hugoniot* relation. The velocities in the energy equation (equation 2.3) can be eliminated by using equation 2.5 to obtain:

$$h_2 - h_1 = q + \frac{1}{2}(v_1 - v_2)(p_2 - p_1). \tag{2.6}$$

The equation above can be expressed in terms of p and v simply by using the definition of internal energy $h = e + pv$ and the ideal gas assumption:

$$q = \frac{\gamma}{\gamma - 1}(p_2 v_2 - p_1 v_1) - \frac{1}{2}(p_2 - p_1)(v_1 + v_2), \tag{2.7}$$

where γ is the heat capacity ratio. The reactive Hugoniot relation, given in equation 2.7, represents the locus of possible thermodynamic equilibrium states behind a combustion wave. For $q = 0$, i.e., no heat releases across the wave, the expression above becomes the well-known Rankine-Hugoniot equation for a nonreactive normal shock wave.

Both Rayleigh line and the Hugoniot relation (equations 2.5 and 2.7) can be represented in a p-v diagram, as shown in Fig. 2.2(a). The point (1,1) highlights the initial state of the reactants. As a real combustion process must satisfy both Hugoniot and Rayleigh relations simultaneously, possible solutions for the reactants can only occur at the intersections of the Rayleigh line with the Hugoniot curve. The various intersection points of the two curves are highlighted in Fig. 2.2(a), representing different types of combustion waves.

Before discussing the different combustion waves, we first consider the region between the points D and E, highlighted as a dashed line in Fig. 2.2(a). This region represents physically unrealizable solutions, as it requires a nonphysical complex mass flux according to equation 2.5. Therefore, no valid Rayleigh line exists between the reactants' initial state at point (1,1) and the dashed segment of the Hugoniot curve. Accordingly, the points D and E in Fig. 2.2(a) represent the limits of the physically possible solutions corresponding to **c**onstant-**v**olume **c**ombustion (CVC) and constant-pressure combustion, respectively. The remaining physical solutions lie between the upper and lower branch of the Hugoniot curve, separating the detonation from the deflagration region. These regions are color-coded in Fig. 2.2(a) in which the green box includes all possible deflagration and the pink box the detonation solutions.

First, the physical possibility of the deflagration solutions is discussed before proceeding with the detonation solutions. The first considered solution in the lower branch of the Hugoniot curve (green box in Fig. 2.2(a)) is the constant pressure combustion (point E), which marks the intersection of the horizontal Rayleigh line originating from (1,1) with the Hugoniot curve. However, at point E the mass flux becomes zero based on equation 2.5 for the constant pressure combustion, as $p_1 = p_2$. Since a zero mass flux is not physical, point E belongs to the physically unrealizable solutions that are spanned between the points D and E. The solutions below point E are known as weak deflagration (point F). For weak deflagrations, the combustion wave propagates at subsonic speed with respect to the reactants. The flow Mach number downstream of the wave is also subsonic. Weak

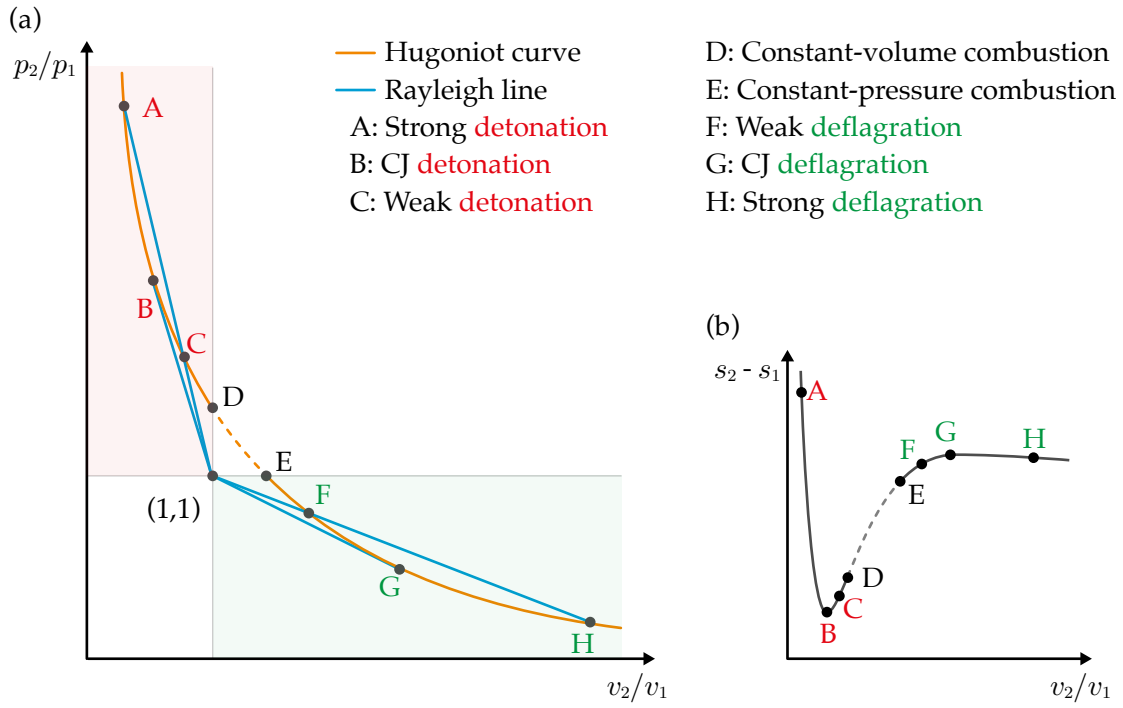

FIGURE 2.2: (a) Reactive Hugoniot curve and Rayleigh line. Intersections of these curves represent possible combustion waves with different characteristics. (b) Entropy variation along Hugoniot curve for a perfect gas. Adapted from [49].

deflagrations are commonly encountered in experiments. Following the Hugoniot curve further down from point F, the flow Mach number increases continuously until it reaches the sonic condition at point G, which marks the limiting Rayleigh line that is tangent to the lower branch of the Hugoniot curve. The tangency solution corresponds to the so-called **C**hapman-**J**ouguet (CJ) deflagration. Following the Hugoniot curve further down, the CJ solution is followed by the strong deflagration (point H). The strong deflagration is characterized by a supersonic flow downstream of the wave. Such a wave does not exist in reality, as the subsonic reactants would have to accelerate to a supersonic velocity during their transition to combustion products. The supersonic velocity would require a physically unfeasible rarefaction shock wave. Accordingly, among the theoretically possible solutions on the lower branch of the Hugoniot curve (green box in Fig. 2.2(a)), only weak deflagrations commonly occur in reality.

Similar to the lower branch of the Hugoniot curve, there are weak, strong, and tangency solutions for detonation waves on the upper branch of the curve (pink box in Fig. 2.2(a)). The intersection points of the Rayleigh line with the Hugoniot curve correspond to the strong and weak detonation solutions, points A and C in Fig. 2.2(a), respectively. The strong detonation is sometimes referred to as overdriven detonation, while the weak detonation is also known as pathological detonation. The weak detonation (point C) occurs under rare and special condition. As demonstrated by von Neumann [50] theoretically and experimentally, such a detonation wave can exist in explosive mixtures with partially reacted Hugoniot curves that intersect each other. While the combustion product velocity

for the weak detonation is supersonic, it is subsonic for the strong detonation. Accordingly, the subsonic condition downstream of the strong detonation enables expansion waves to penetrate and thereby attenuate the detonation wave. Therefore, strong detonations are unstable and attenuate toward the stable CJ detonation solution (from A to B in Fig. 2.2(a)). The CJ detonation (point B) represents the solution in which the Rayleigh line is tangent to the upper branch of the Hugoniot curve.

Different solutions have been discussed so far, however, to find a unique solution, an additional criterion is necessary, as the three conservation equations and the equation of state provide only four equations for the five unknown quantities. These quantities represent the thermodynamic state of the products (p_2, ρ_2, u_2, h_2) and the velocity of the reactants u_1. The latter is directly related to the wave propagation velocity in the laboratory reference frame.

Around the beginning of the 20th century, David Chapman and Émilie Jouguet independently provided the missing criterion for determining the wave propagation velocity for a detonation. Chapman postulated to choose the minimum wave velocity, as only a unique detonation velocity had been observed experimentally for a mixture with a given initial and boundary condition [51]. As shown in Fig. 2.2(a), both strong and weak solutions converge to one solution when the Rayleigh line is tangent to the Hugoniot curve. Chapman determined that this point represents the solution with a minimum velocity, which must be the correct detonation solution. In contrast, Jouguet postulated to choose the minimum entropy solution, which corresponds to the sonic condition behind the detonation wave. It was shown that both postulations, namely the minimum-entropy and minimum-velocity solutions, are equivalent, representing the tangency solution (point B in Fig. 2.2(a)). The provided criterion by Chapman and Jouguet is known as the Chapman-Jouguet or CJ-theory.

Besides providing a criterion for determining the detonation solution, the CJ-theory can be further utilized to underline the potential of pulse detonation combustion for high-efficiency propulsion devices. For optimizing the overall propulsion system efficiency, a minimum entropy combustion process is desirable. Figure 2.2(b) shows the entropy rise during the combustion process as a function of specific volume for transient propulsion devices, such as pulse detonation engines [49]. Considering that the strong detonation (point A) can be neglected as it is unstable, the maximum entropy is generated by the CJ *deflagration* (point G). The CJ *detonation* (point B) on the other hand induces the minimum entropy rise. Hence, following the discussion regarding the combustion modes in chapter 1, the CJ detonation is the favorable combustion mode to maximize the thermal efficiency.

While the CJ theory represents one of the most fundamental theories for detonation waves, it is associated with limitations. Although the wave speed based on the CJ criterion agrees very well with experimental observations, the theory remains a heuristic postulation, as no rigorous physical or mathematical argument has yet demonstrated the validity of CJ criterion. Furthermore, the CJ theory is based only on the equilibrium states of reactants and products; thus, the theory does not account for detailed transition across the detonation wave. Hence, the CJ theory is unable to provide a mechanism by which a detonation wave propagates through a combustible mixture. Such a mechanism can be derived based on a one-dimensional model, which is introduced in the next section.

2.1.2 ZND Model

A comprehensive model for the structure of detonation waves was first proposed during the Second World War independently by **Z**eldovich in Russia, von **N**eumann in the United States and **D**öring in Germany. This model is commonly referred to as ZND model [50, 52, 53].

The ZND model considers the detonation wave as a one-dimensional structure, consisting of a precursor shock followed by an induction and reaction zone. Figure 2.3 presents a schematic illustration of the model. The leading shock wave results in an adiabatic compression of the reactants, as illustrated with the red lines in Fig 2.3. The shock wave is considered as a discontinuous jump in the thermodynamic quantities since the shock wave is in the order of a few molecular mean-free-paths. Thus, the shock wave is much thinner than the chemical reaction zone [48], as illustrated in Fig. 2.3. The post-shock state is commonly referred to as the **v**on **N**eumann (vN) state. The gas temperature in the vN state corresponds to the ignition temperature of the mixture. Accordingly, in the so-called induction zone (blue region in Fig. 2.3), reactants dissociate into radical species with small variations in thermodynamic quantities. Once the concentration of radical species is sufficient, rapid chain-branching exothermic reactions occur in the subsequent reaction zone (orange region in Fig. 2.3). The chemical reactions persist across the reaction zone until thermodynamic equilibrium is established. This thermodynamic equilibrium state corresponds to the CJ state, as indicated in Fig. 2.3.

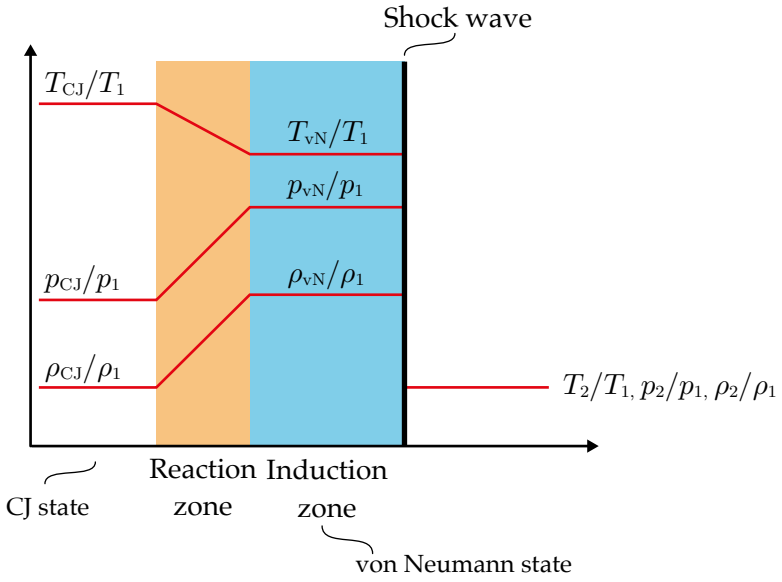

FIGURE 2.3: Schematic illustration of the ZND model. Adapted from [54].

A possible mechanism for the self-propagation of detonation waves through combustible mixtures can be provided based on the ZND model. The adiabatic compression of the reactants by the leading shock wave induces an auto-ignition. Accordingly, the shock wave initiates the chemical reactions, which occur once the induction time is elapsed. On the other hand, the propagation of the shock wave is supported by the subsequent

expansion of the reacting gas. These two mechanisms together lead to the self-sustained propagation of detonation waves.

Besides the introduced mechanism, the ZND model provides the thermodynamic transition path of the reactants to the combustion products. Figure 2.4 presents the transition path across the detonation wave based on the p-v diagram. The adiabatic compression by the shock wave occurs along the non-reactive Hugoniot curve, starting from (1,1) and moving up to the vN state at point A (Fig. 2.4). The thermodynamic transition across the induction and reaction zone occurs from the vN state (point A) along the Rayleigh line toward the CJ tangency point on the reactive Hugoniot curve (point B). Accordingly, the species thermodynamic properties across the detonation wave can be determined based on ZND, complemented with chemical kinetics models. Although ZND serves as an essential model, its underlying assumption of one-dimensional planar steady detonation is a radical simplification of the intrinsically unstable multidimensional detonation waves occurring in reality.

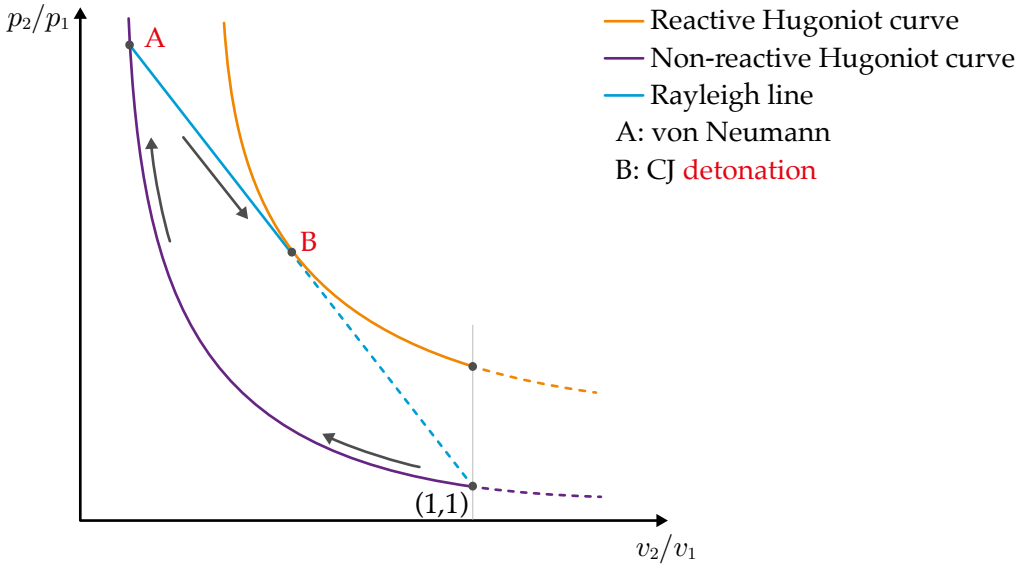

FIGURE 2.4: The thermodynamic path of a detonation along the non-reactive shock Hugoniot, the von Neumann state, the Rayleigh line, and the CJ state based on the ZND model. Adapted from [54].

2.1.3 Experimental Observations

The experimental observations leave no doubt that self-propagating detonations are transient, unstable, and multidimensional. Hence, the observed structure of unstable detonation waves deviates from the one-dimensional steady laminar structure provided by the ZND model. Consequently, the one dimensional CJ and ZND model are unsuitable for determining both dynamic detonation parameters and propagation mechanisms of unstable detonations. As discussed in chapter 2.1.2, the underlying propagation mechanism for detonation waves can be described based on the ZND model; the compression by the leading shock wave initiates the chemical reactions while the propagation of the shock wave is supported by the subsequent expansion of the reacting gas. However, the

provided mechanism applies only for *stable* detonations, whereas for the propagation of *unstable* detonations the role of turbulence, shock interactions, and hot spots is significant [54]. Accordingly, the determination of non-equilibrium dynamic detonation parameters, such as detonation sensitivity, critical tube diameter, and critical initiation energy based on the ZND model, can result in a large deviation compared to the experimental observations [55].

The most common quantity to describe the dynamic characteristic of the detonation is the cell size. The cell size mainly depends on the mixture composition and its initial thermodynamic state. As the cell size correlates with the detonation sensitivity, it is commonly used to measure the reactivity of a combustible mixture. It is also related to the critical tube diameter for unstable detonations. The smallest tube diameter for an unstable detonation that transmits successfully into an unconfined space is about 13 times the detonation cell width [56]. Figure 2.5(a) shows an image of a sooted foil after the passage of a detonation wave. The sooted foil was placed in the PDC filled with an H_2-air mixture. The resulting cellular structure indicates the multi-dimensional characteristic of the detonation wave. Figure 2.5(b) shows a schematic illustration of the cellular structure including the cell width. The cellular structure is directly related to the structure of the wave. In its simplest form, the shock wave of a detonation wave consists of an incident shock, a Mach stem, and a reflected shock (Fig. 2.5(c)). The latter is commonly referred to as transverse wave, as it propagates perpendicular to the detonation front. A mismatch in temperature, entropy, and velocity occurs between the boundaries of the regions downstream of the Mach disk, the incident, and the reflected shock. The shear layer produced by the slipstream between the low-speed and high-speed flow is attributed to the mechanism that traces the triple point trajectories onto the soot-foil, resulting in the cellular structure (Fig. 2.5(a)) [57].

Figure 2.5(b) illustrates schematically the structure of a two-dimensional detonation wave, with the transverse waves being reflected from each other as well as from the walls of the confinement. However, in a round tube, the transverse waves propagate both in the circumferential and radial directions, resulting in a more complex three-dimensional cellular structure. Following the collision of two transverse waves, the incident shock wave and the Mach stem interchange. The Mach stem propagates at a higher velocity than the incident shock, up to 1.6 times the CJ speed, as the reaction rate behind the Mach stem is significantly larger due to the elevated post-shock temperature and pressure. However, the Mach stem decelerates rapidly to the CJ speed due to the subsonic post-shock flow, allowing expansion waves trailing behind it. The leading shock wave can decay to propagation velocities as low as 0.5 times the CJ speed at the end of the cell. Nevertheless, the average propagation velocity of the leading shock agrees very well with the one obtained based on the one-dimensional CJ theory.

As a fundamental parameter, the detonation cell size directly impacts different aspects of PDCs. A minimum combustor tube diameter can be determined based on the detonation cell size since the detonation wave becomes unstable if the tube diameter is close to the detonation cell size [54]. Furthermore, it is desirable for safety reasons to prevent the transition of detonation to the downstream components of the engine. Hence, the critical tube diameter, and thus the cell size play an important role in the combustor design.

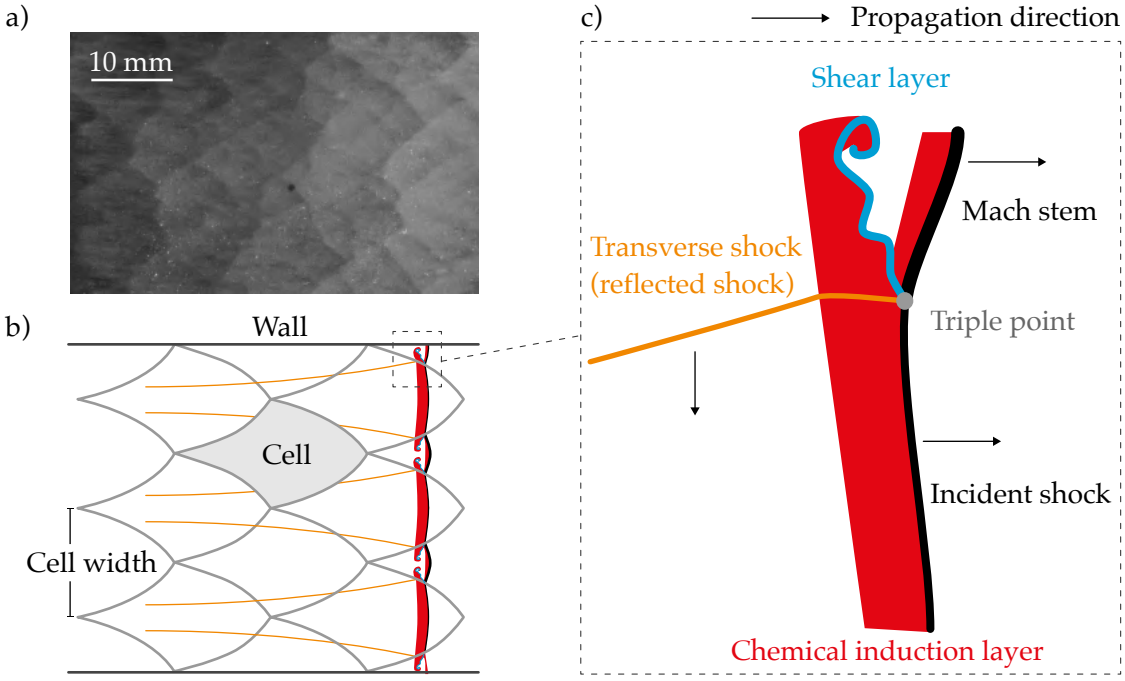

FIGURE 2.5: a) Soot-foil image of the cellular structure for a H_2-air mixture. The irregular cell structure indicates the unstable characteristic of the detonation. b) Schematic of cellular structure of a detonation wave, propagating from left to right. c) Schematic of the detonation front and its triple point structure. Adapted from [55].

2.2 Pulse Detonation Combustors

This section provides some insight into the PDC operation cycle. The main aspects of the waves propagation and associated gas dynamic features of the PDC are presented to facilitate the comprehension of the discussions provided in chapters 4 and 5.

2.2.1 PDC Operation Cycle

In its simplest form, a PDC consists of a straight tube with a constant cross-section, which is closed at one end and open at the other. The PDC operation cycle can be broken down into five phases, as illustrated schematically in Fig. 2.6. The cycle starts by filling the tube with a combustible mixture via injection ports, usually at the head-end of the tube (Fig. 2.6(a)). An ignition system, e.g., a spark plug, is used to initiate a deflagration wave (Fig. 2.6(b)). The transition from deflagration to detonation (DDT) is typically obtained by utilizing a Shchelkin spiral, a shock focusing nozzle, or an array of orifices. Following a successful DDT, a detonation wave propagates along the PDC toward its open-end (Fig. 2.6(c)). Subsequently, the high-pressure combustion products exit the tube, as depicted in Fig. 2.6(d). The characterization of the exhaust process is one of the main objectives of the present thesis and is discussed in detail in chapter 4. During the final phase (Fig. 2.6(e)), the remaining combustion products are purged by using a non-combustible gas, e.g., air. The purging allows for filling the PDC with fresh propellant to begin a new cycle.

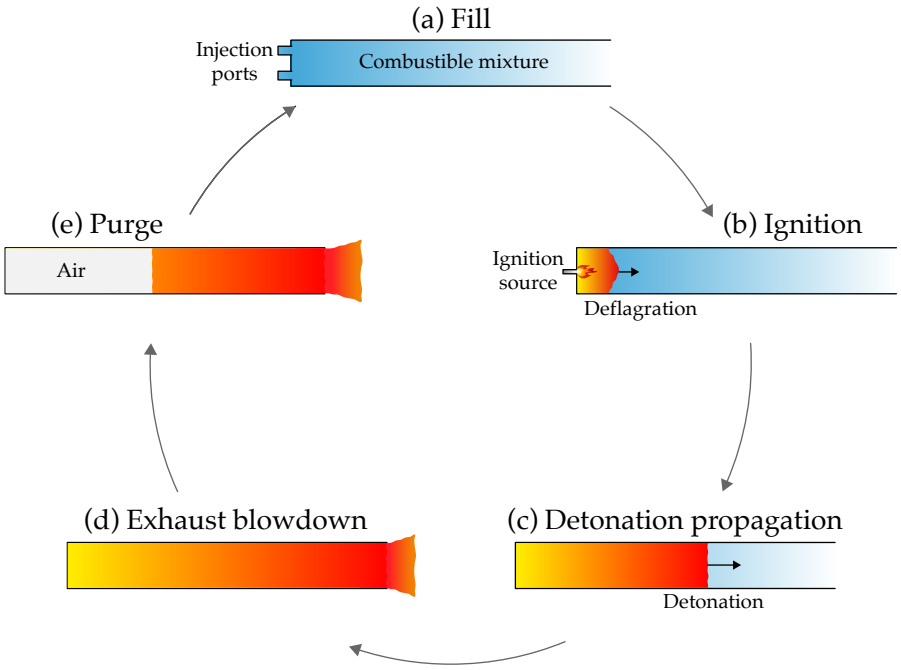

FIGURE 2.6: Phases of the PDC operation cycle.

2.2.2 Wave Dynamics of Fully and Partially Filled PDC

This section provides the primary gas dynamic features and their interactions inside the PDC. The phenomenological discussion given below is based on the literature as well as simulation results conducted for the specific PDC design used for the experiments. The simulations are performed using the one-dimensional reactive Euler equations solver developed by Berndt [58].

Figure 2.7(a) shows schematically the PDC fully filled with a combustible mixture. The corresponding wave space-time diagram is presented in Fig. 2.7(b). For the sake of simplicity, the DDT process is not considered here; the detonation is initiated at the head-end of the combustor. Once the detonation wave is initiated, it propagates toward the open-end of the PDC. At the time t_1 the detonation wave is close to the open-end, as indicated in Fig. 2.7(b). The compositions inside the PDC for t_1 are presented schematically in Fig. 2.7(c). The detonation wave separates the combustion products from the combustible mixture. The corresponding pressure profile inside the PDC is shown in Fig. 2.7(d). After the passage of the detonation wave, the pressure increases abruptly to the von Neumann pressure p_{vN}. However, the peak pressure behind the detonation wave decreases quickly to the CJ pressure p_{CJ}. It is worth to note that the width of induction and reaction zone, i.e., distance between p_{CJ} and p_{vN}, is enlarged in Fig. 2.7(d) for the sake of visualization. The CJ pressure is followed by a region with a negative pressure gradient. The elevated pressure downstream of the detonation wave is decreased by an expansion wave, known as the Taylor wave. As shown in Fig. 2.7(a), the Taylor wave is centered at the head-end of the PDC, and thus processes the combustion products. The Taylor wave decelerates the combustion products, which are initially set into motion toward the open-end of the PDC by the detonation wave. By decelerating the combustion products, the Taylor wave

ensures the gas to rest at the closed head-end to satisfy the closed wall boundary condition. As shown in Fig. 2.7(c), the Taylor wave terminates prior to the head-end for t_1, resulting in a uniform region with constant pressure close to the head-end (Fig. 2.7(d)). While the highly transient flow develops further inside the combustor, the thermodynamic state at the open-end changes only after the arrival of the detonation wave. The PDC exhaust process begins when the detonation wave exits the combustor. Once the detonation wave exits the PDC, an expansion wave reflects from the ambient, moving toward the head-end of the PDC [59], as illustrated by the green dashed line in Fig. 2.7(b). Accordingly, the reflected expansion wave accelerates the exhaust of detonation products while interacting with the Taylor wave. The discussion above provides the primary gas dynamic features of the fully filled PDC, which determine the PDC exhaust. Further information regarding the exhaust process is given in the publications presented in chapter 4.

One of the main control parameters of PDEs is the fill fraction, which is the percentage of the combustor volume filled with the combustible mixture. Changing the fill fraction is an effective method of throttling the PDE without changing its firing frequency [60–62]. For a partially filled PDC, a portion of the combustor is filled with a non-combustible gas. The purged air from the previous cycle (Fig. 2.6(e)) is commonly used by simply filling the combustor for a shorter time with the combustible mixture compared to the fully filled case. The resulting PDC composition for a partially filled PDC prior to detonation onset is shown schematically in Fig. 2.7(e). The corresponding wave space-time diagram is depicted in Fig. 2.7(f). At the time t_0 a contact surface separates the combustible mixture from the air (Fig. 2.7(f)). Subsequent to the detonation initiation, the detonation wave propagates toward the combustible mixture until it reaches the contact surface at t_1 (Fig. 2.7(f)). As discussed in chapter 2.1.2, the detonation wave consists of a precoursing shock wave and a combustion front according to the ZND model. As no combustion takes place in air, the combustion wave terminates at the contact surface, while the shock wave (blue line in Fig. 2.7(f)) propagates further toward the open-end of the PDC. Depending on the context, this shock wave is referred to as the transmitted shock as well as the incident or leading shock in the remainder of this thesis.

As discussed in section 2.1.1, the CJ detonation wave propagates inside the PDC at a constant velocity (straight red line in Fig. 2.7(f)) since disturbances are unable to reach the detonation wave due to the sonic CJ condition. However, this is not the case for the transmitted shock due to the absence of the sonic condition behind the shock wave. As shown in Fig. 2.7(f), the Taylor wave continuously overtakes the shock wave. Hence, the transmitted shock wave decelerates while it propagates toward the tube's open-end. The continuous deceleration is indicated by the increasing slope of the blue line in Fig. 2.7(f). Assuming the post-shock flow at the PDC exit is subsonic, an expansion wave (green dashed line) enters the combustor and propagates toward to its head-end as the shock wave exits the PDC [63]. It is worth to note that there will be no expansion wave propagating toward the tube's head-end directly after the exit of the incident shock, if the post-shock flow at the combustors exit is supersonic. The impact of the subsonic or supersonic post-shock flow on the PDC exhaust is discussed in chapters 4 and 5.

The collision of the detonation wave with the contact surface leads to both transmission as well as reflection of waves. While the transmitted wave is a shock wave propagating

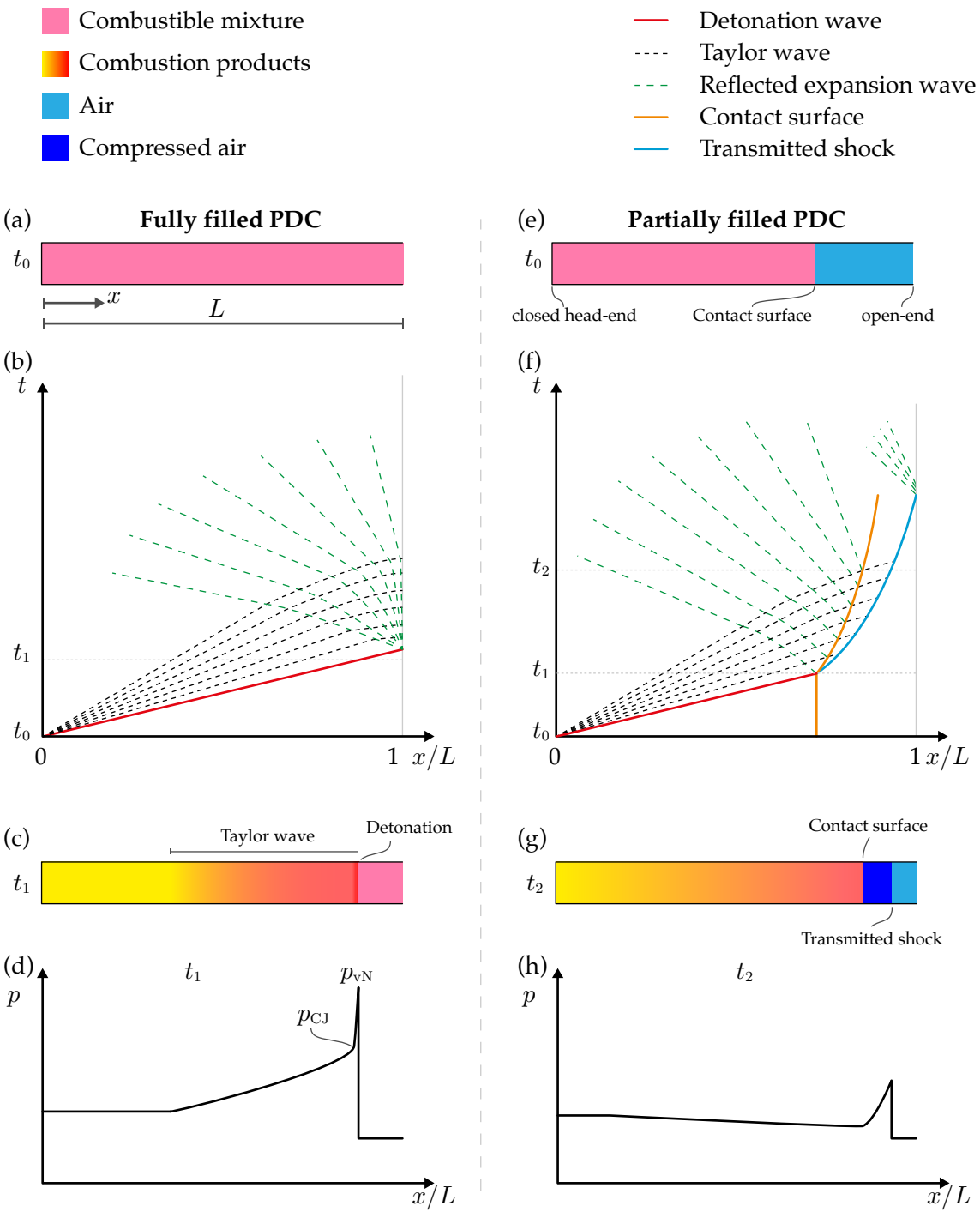

FIGURE 2.7: (a,e) Schematic of the PDC composition prior to the detonation initiation. On the left side the fully filled PDC and on the right side the partially filled PDC are shown. (b,f) The wave space-time diagram of the PDC. (c,g) Schematic of the PDC composition at t_1 for the fully filled and at t_2 for the partially filled case. (d,h) Pressure profile inside the PDC at t_1 for the fully filled and at t_2 for the partially filled case.

toward the open-end, the reflected wave propagates back to the head-end of the combustor. Depending on the acoustic impedance ratio of the mixture and air, the reflected wave can be either a shock wave, a Mach wave, or an expansion wave [64]. However, in the cases considered in this study, only expansion waves reflect from the contact surface. Accordingly, the reflected expansion wave from the contact surface is illustrated as dashed green lines in Fig. 2.7(f).

The pressure profiles inside the tube for the fully and partially filled cases are illustrated schematically in Fig. 2.7(d) and (h), respectively. Both illustrations depict the instant as the leading waves (detonation wave or transmitted shock wave) are close to the open-end of the PDC. The pressure profiles highlight the fundamental differences between these cases, which highly affects the PDC exhaust. The peak pressure behind the detonation wave in the fully filled case (Fig. 2.7(d)) is substantially higher compared to the peak pressure behind the transmitted shock wave in the partially filled case (Fig. 2.7(h)). In addition, the pressure distributions left to the leading waves differ considerably for these cases.

While the pressure distribution shown in Fig. 2.7(d) is representative for the fully filled case, the pressure distribution in the partially filled case is sensitive to the actual fill fraction and the combustor length. For instance, when the reflected expansion wave (green dashed line in Fig. 2.7(f)) reaches the closed-end wall, the expansion wave reflects again from the wall (not shown in Fig. 2.7(f) for the sake of simplicity). The second reflection results in an expansion wave moving toward the open-end, which leads to a further decrease of pressure. Whether a reflection occurs and how far the reflected wave propagates toward the open-end prior to the exit of the leading shock, depends mainly on the fill fraction and the length of the combustor for a given mixture. Thus, the fill fraction and the length of the combustor affect the pressure distribution inside the combustor prior to the exit of the leading shock, which set the initial condition for the PDC blowdown.

The flow inside the combustor downstream of the detonation wave and the transmitted shock differ significantly. While for the studied cases in this work the flow downstream of the CJ detonation is subsonic in the laboratory reference frame, there is initially a supersonic region behind the transmitted shock for a CJ detonation. However, the flow Mach number downstream of the leading shock decreases as the shock wave weakens while it propagates toward the open-end. Accordingly, the post-shock flow can be either subsonic or supersonic depending on the fill fraction.

Although for the sake of simplicity the provided discussion relies on various simplifications and assumptions (e.g., no DDT section, one-dimensional, inviscid flow), it provides some insight into the fundamental gas dynamic features for both fully and partially filled configurations. The provided discussion on the PDC wave propagation is essential for the comprehension of the publications and the subsequent discussion presented in chapters 4 and 5, respectively. Before proceeding with the publications, a brief overview of primary experimental methods applied in this work is given in the next chapter.

Chapter 3

Experimental Methods

The present chapter outlines the applied PDC instrumentation as well as experimental methods for the characterization of the PDC exhaust. First, the applied techniques are presented, including a discussion regarding their advantages and disadvantages. The overview is then extended by providing some alternative measurement techniques applied to the PDC exhaust reported in the literature.

3.1 Ionization Probes

Various instrumentations are frequently used to determine the operating conditions of PDCs. The most common approaches are based on measurements of the detonation wave propagation velocity using the time-of-flight method. For this purpose, the arrival time of the detonation wave is determined either by detecting the shock wave or the combustion front of the detonation wave, utilizing pressure transducers and ionization probes, respectively.

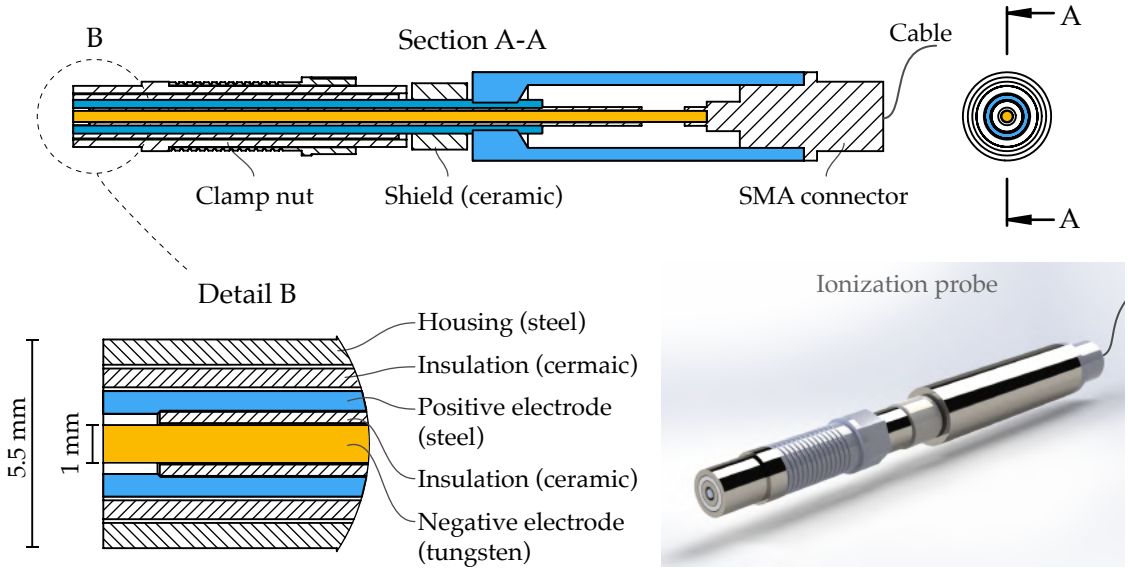

FIGURE 3.1: Illustration of the in-house made ionization probes.

Ionization probes are frequently used for the detection of flame and detonation waves in PGC combustors. As the name suggests, the probe detects the ionized species generated during combustion. Figure 3.1 shows the design of the ionization probes developed

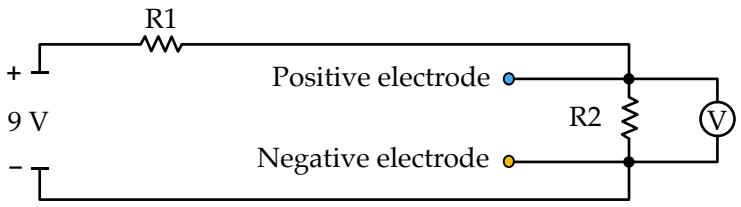

FIGURE 3.2: Circuit diagram of the ionization probes.

in the scope of this work. The probes are designed to fit in the same port as the PCB pressure transducers, which will be introduced in the next section. This allows for easy interchanging of pressure and ionization probes using the same flush-mounted PDC ports. The ionization probes consist essentially of two electrodes, which are color-coded in yellow and blue in Fig 3.1. The electrodes are electrically insulated using aluminum oxide ceramics. As illustrated in Fig 3.2, an electric potential difference is applied to the electrodes, allowing for an electric current to flow if ionized species are present at the head of the probe. By measuring the voltage between the electrodes, the presence of ionized species can be determined.

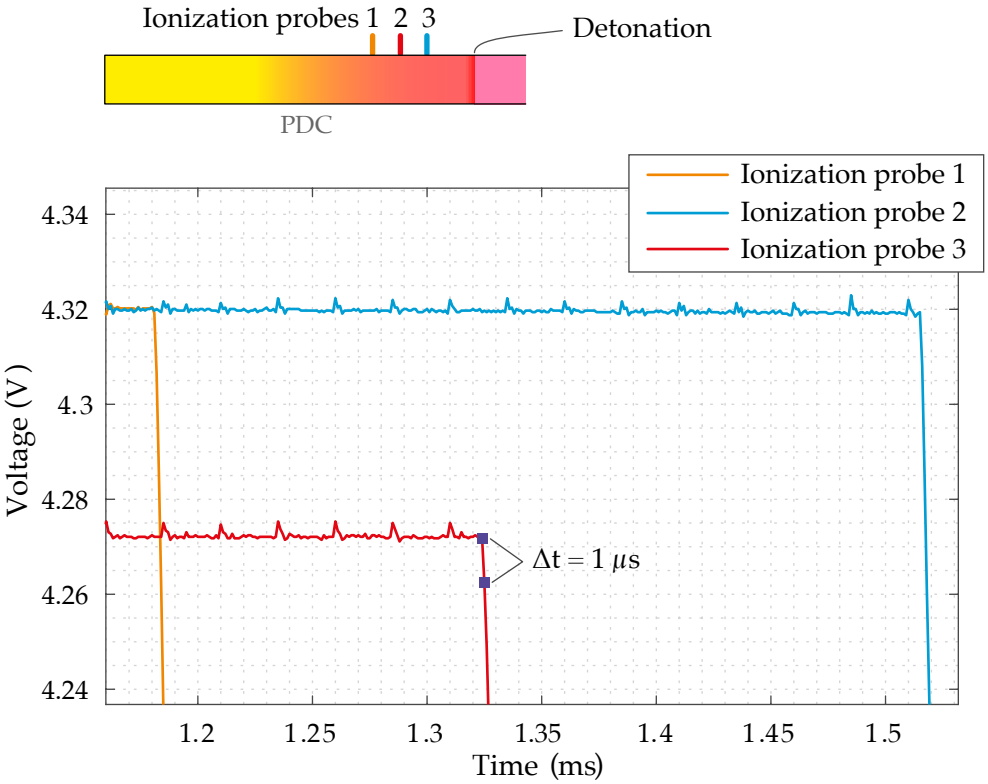

FIGURE 3.3: Measured signal of the ionization probes exposed to a passing detonation.

The ionization probes have many advantages compared to pressure transducers. Figure 3.3 shows typical signals of three ionization probes. These axially in the PDC distributed probes are exposed to a passing detonation wave. Once the detonation wave

reaches the probes, their voltage signal drops rapidly. The sharp edge of the signal allows for temporally accurate detection of the detonation wave arrival time. The signal quality is essential for detonation speed detection, considering that the uncertainty of only 1 μs corresponds to a velocity error of nearly 50 m/s in the present test rig. The low-noise signal of the current design was mainly achieved by galvanic isolation of the entire measurement system. For this purpose, the electrodes are electrically insulated from the test rig by utilizing ceramic tubes while using a battery as the power supply source to suppress any potential noise from both the test rig and power supply. In addition to the excellent signal-to-noise ratio, the ionization probes are inexpensive and highly robust. Furthermore, these probes can operate at high temperatures for a long period of time, which is crucial during the multi-cycle operation of the combustor. Accordingly, the ionization probes are very well suited for detonation detection.

3.2 Pressure Transducers

Accurate measurement of static and total pressure is of great importance in PDCs. Commonly, two types of pressure transducers utilizing piezoresistive or piezoelectric sensing elements are used for pressure measurements in PGC devices. A brief overview regarding these techniques is given in the following, including their primary advantages and disadvantages in the context of PGC applications.

3.2.1 Piezoelectric Transducers

Piezoelectric pressure transducers are frequently used for pressure measurements inside PDCs. The prefix "piezo-" means "to press" or "to squeeze". When a piezoelectric material undergoes mechanical stress, negative and positive ions accumulate on the opposed surfaces of the piezoelectric material, inducing an electric charge. As the electric charge is directly proportional to the applied force, the piezoelectric material is well suited for pressure measurements. Commonly, crystals are used as a piezoelectric material, which are also built inside the PCB transducers that are used for the measurements conducted in this work.

Many advantages are associated with piezoelectric transducers such as high resonant frequency, fast rise time, and robustness with respect to high-temperature environments. However, multiple negative effects are known when these transducers are applied in PGC devices. One of the major issues limiting the accuracy of piezoelectric transducers is the phenomenon known as thermal shock. The thermal shock refers to the transducer's response to an extensive heat flux, e.g., after the passage of a detonation, which can considerably affect the transducer's signal and accuracy. The excessive heat flux and the resulting increased temperature of the transducer alter the properties of the piezoelectric and composite substrate materials while affecting the moments in its structure [65]. Consequently, after the arrival of the detonation wave, the transducer's output voltage signal drops significantly, resulting in non-physical negative pressure. This effect can be mitigated by using high-temperature silicone coatings. However, this approach is impracticable, in particular in the multi-cycle operation mode, as the coating lasts only for a few detonation cycles. Furthermore, increased heat load in a multi-cycle operation

mode result in a negative drift of the signal without adequate cooling of the transducer. The negative drift can easily lead to signals out of the DAQ measurement range [66].

Another disadvantage of the piezoelectric transducers, which received less attention in the literature to date, is associated with the signal conditioning of the transducers. Depending on the operational temperature range, the signal conditioning electronics are either packed inside the transducer (usually as a miniature circuit inside the transducer head) or connected with a cable outside of the transducer. The piezoelectric transducers used in this work are manufactured by the company PCB. Two types of pressure transducers suitable for PGC devices are provided by PCB: the ICP and the charge mode type. While the charge mode sensors only contain a piezoelectric sensing element, the ICP transducers include built-in electronics for signal conditioning purposes. The main advantage of the charge mode transducers is their ability to operate in high temperature environments. Accordingly, to allow for measurements at high temperatures inside the detonation tube, the transducers used here are the charge mode models 112A05 and 113B03. However, the output of the charge mode transducer is a high impedance signal, which is converted to a low impedance signal prior to the data acquisition system by using a charge amplifier. The high impedance signal between the transducer and charge amplifier is highly sensitive to noise from environmental factors mainly due to electromagnetic interference. As will be discussed in section 4.4, the measured pressure signal in the PDC test rig is partially very poor, which is attributed to the vulnerability of the high impedance signal to noise sources.

3.2.2 Piezoresistive Transducers

The piezoresistive transducers operate on the principle of the piezoresistive effect. Following an applied mechanical strain, the electrical resistance of the piezoresistive material changes. Usually, silicon is used as a piezoresistive material due to its high sensitivity to mechanical strain, which is approximately two orders of magnitude larger than metals [67]. The silicon of the pressure transducer is usually attached to a pressure-sensitive diaphragm. A change in pressure results in a deflection of the diaphragm, followed by a change in resistance. A Wheatstone bridge converts the resistance change to a voltage signal proportional to the applied pressure [68].

One of the main advantages of piezoresistive compared to piezoelectric transducers is that the piezoresistive sensors have no limitation with respect to the total measurement time. The piezoelectric transducers are effectively AC coupled devices, and therefore only sense the alternating force. In contrast, the piezoresistive transducers are capable of measuring a DC signal. While piezoelectric transducers are suitable for measurements in harsh environments, piezoresistive transducers are rarely mounted directly in PGC combustors for long time operations. Due to the limitation in the operation temperature, the piezoresistive transducers are usually recessed [69, 70] or placed further downstream of the combustor, where the transducer is opposed to lower temperatures due to mixing of the combustor exhaust with secondary air [44, 71]. However, there are piezoresistive sensors with embedded cooling and temperature compensation methods available[68, 72].

Different piezoelectric and piezoresistive transducers are used in this work to measure the pressure inside and downstream of the PDC, including a prototype Kulite DTL sensor

for measurements in such harsh environments. The accuracy and the dynamic response of these transducers are investigated by using a shock tube as a dynamic pressure generator. The results of this study are presented in the publication provided in chapter 4.4.

3.3 Schlieren

The German word *Schliere* denotes an inhomogeneity in a transparent medium, commonly referring to disturbances in a glass plate or a window. The German scientist August Toepler was the first who implemented the schlieren method for visualization of density inhomogeneities in a flow field [73]. Today, the schlieren technique is one of the most applied measurement diagnostics for supersonic flows.

A classical schlieren image represents the path integral of the first spatial derivative of the fluid's refractive index, which is directly related to its density. Although some progress is made to gain quantitative data from schlieren measurements [74, 75], the schlieren technique has been used to date primarily for qualitative visualization of flow features. Different researchers used the schlieren and the similar shadowgraphy technique for visualization of flow features in the PDC exhaust [76–83]. Although tremendous progress has been made in the development of the schlieren technique, high-resolution, high-speed images of the PDC exhaust are rarely available. This is mainly attributed to the recent improvements of light sources using high-power **l**ight-**e**mitting **d**iodes (LEDs) [84] as well as high speed cameras utilizing advanced **c**omplementary **m**etal–**o**xide–**s**emiconductor (CMOS) chips.

High-resolution, high-speed schlieren images are used throughout different studies of this thesis. For this purpose, a regular z-type [73] schlieren technique is utilized, as illustrated in Fig. 3.4. An overdriven high-power LED [84] is used as light source, while two parabolic mirrors of 8-inch diameter allow for parallelizing and focusing of the light beam. High-resolution images are captured up to 80 kHz, using a Photron SA-Z camera.

The main advantage of the schlieren technique may be its simplicity and easily adjustable sensitivity [85]. However, there are some drawbacks associated with this technique. As mentioned before, the classical schlieren technique does not directly provide a thermodynamic quantity of the flow. Furthermore, the line-of-sight effect requires some precautions; although in contrast to shadowgraphy, the schlieren images are focused optical images, they do not represent a single measurement domain plane. As the light travels from the LED to the camera, all density gradients throughout the entire light beam affect the schlieren image. This is particularly essential for three-dimensional flow fields, as not only the density gradient of the focused plane but the entire flow field, being passed by the light beam, affect the final captured image. This has direct implications for applying schlieren measurements to the PDC exhaust. The combustion products occuring at the PDC exhaust outside of the focused plane can easily "distort" the schlieren image by overlaying the jet structures including shock waves and vorticies. This issue is further discussed in the publication presented in chapter 4.2. Nevertheless, the schlieren technique remains one of the primary diagnostic tools for PGC devices due to its capability for providing instructive flow visualization.

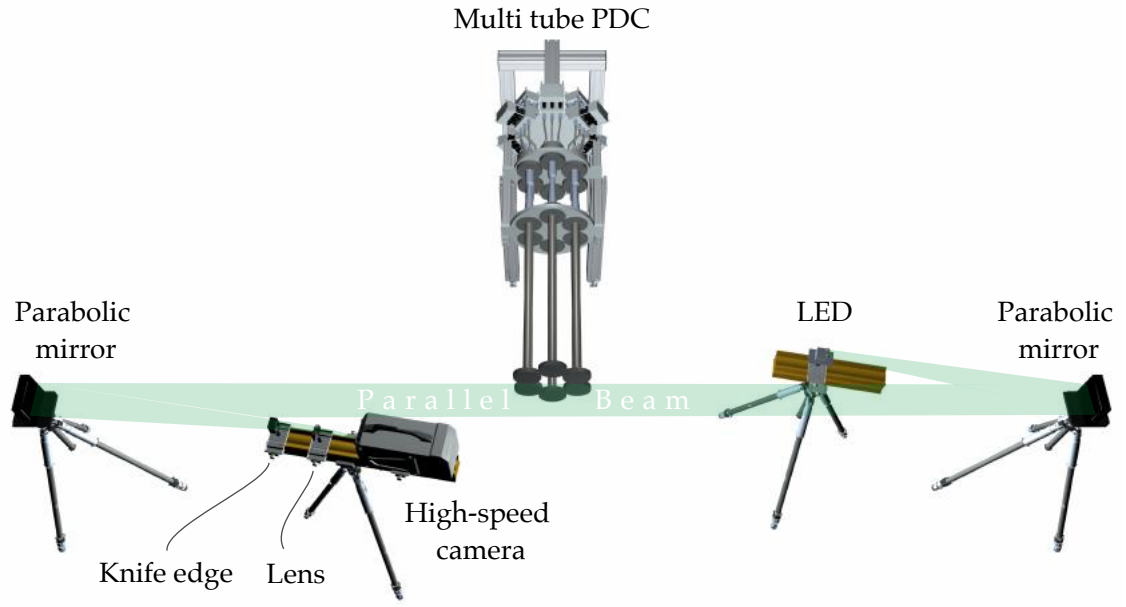

FIGURE 3.4: Illustration of the z-type schlieren setup applied at the multi-tube PDC test-rig.

3.4 Particle Image Velocimetry

Among the particle-based measurement techniques, which rely on tracer particles following the flow, the **p**article **i**mage **v**elocimetry (PIV) is one of the most advanced diagnostic techniques due to its ability to provide detailed, accurate and complete flow-field velocity information [86]. While a variety of different PIV applications exists, they are all based on determination of fluid velocity by measuring the displacement of the tracer particles during a short time.

Figure 3.5 represents the experimental setup for the planar PIV measurements of the PDC exhaust jet. The tracer particles are illuminated by means of a light sheet, originating from a pulsed high-speed laser. The thin light sheet is formed by a light guide using optical lenses. While the PDC prior to the onset of detonation is seeded with tracer particles, two fluidic oscillators mounted at the PDC exit (Fig. 3.5) provide ambient seeding. The exemplary particle image shown in Fig. 3.5 visualizes the vortex ring as well as shock structures of the starting jet.

Besides the visualization of the flow structures, the PIV technique allows for quantitative characterization of the flow field. Although PIV is widely popular throughout scientific fields involving fluid mechanics and combustion diagnostics, it has been rarely applied to characterize the PDC exhaust. To the best knowledge of the author, only one report by Opalski et al. [27] studied the exhaust flow of an overfilled PDC based on ensemble-averaged PIV velocity fields. While time-resolved PIV results are well suited for the characterization of the PDC exhaust over a wide range of operating conditions, no such data is reported in the literature. The absence of any time-resolved data is attributed to the substantial challenges associated with the application of PIV in harsh environments such as the PDC exhaust.

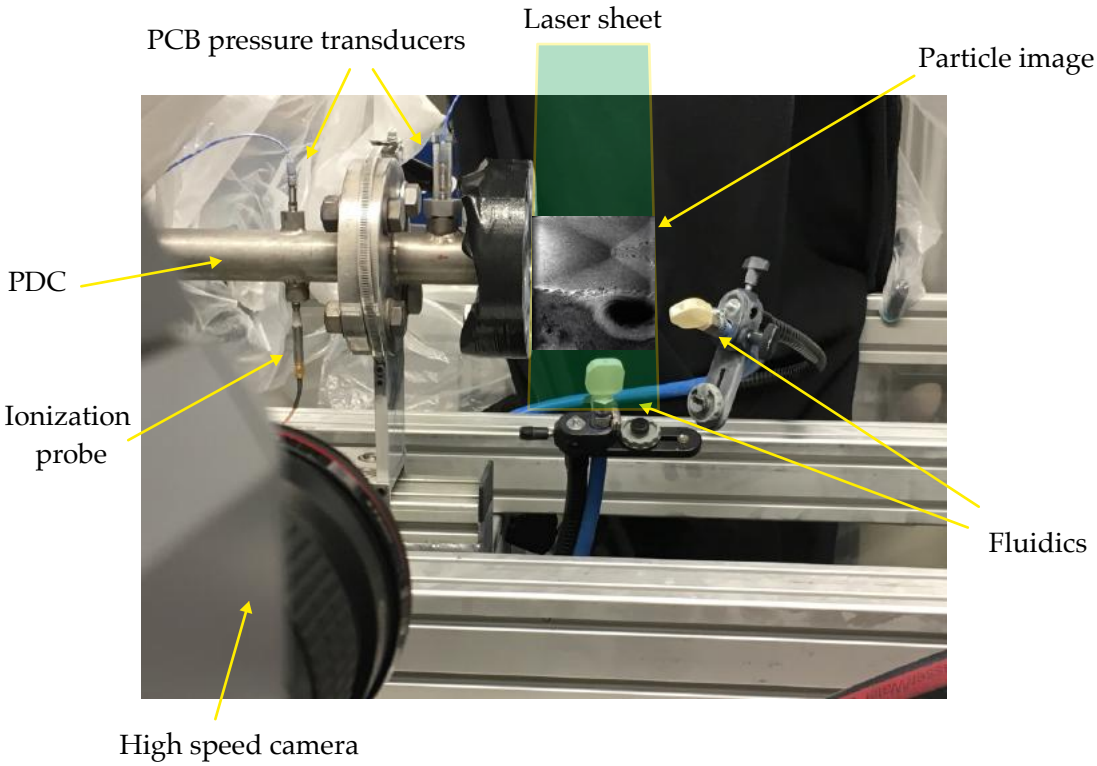

FIGURE 3.5: A photo showing the instrumentation of the PDC exit section and the PIV setup for velocity measurements of the PDC exhaust.

Before discussing the practical challenges, a brief overview of the main hardware requirements with respect to the light source and the camera is given in the following. The high-speed exhaust flow requires two laser pulses with sufficient energy of very short pulse width in the order of hundredths of nanoseconds, with a short pulse distance of the order of micro- to milliseconds. Sufficient energy is needed to illuminate the small tracing particles. The short pulse width is necessary to avoid streaks of high-velocity tracer particles. The flow velocity also requires a short pulse distance to avoid large particle displacement. Furthermore, a high-speed camera with a small interframing time and reasonable resolution at the corresponding frequency is required. The requirements stated above are fulfilled in the scope of this work by using a Photron SA-Z camera in combination with a Quantronix Darwin Duo laser, allowing for high speed planar PIV measurements of the PDC exhaust at 10 kHz.

One of the main assumptions of the PIV technique is the tracer particle flow-tracking fidelity. Solid particles such as oxidized metals are practically the only available option as seeding materials, as the high-temperature PDC exhaust precludes the use of any liquid tracer particles. However, the solid particles can easily have a higher mass density than the surrounding fluid, resulting in measurement bias. This is particularly important in regions of high velocity gradients occurring in supersonic flow, e.g., when crossing shock waves. Another source for measurement error is the particle size [87]. Solid particles at the micro- and nanoscale can agglomerate, resulting in a much larger particle size

than the grain size. On the other hand, strong shear forces in supersonic flow can break agglomerations, resulting in a large range of particle scales. Smaller particles may be too small to be resolved by the optical system, whereas large particles may well result in poor flow-tracking. Hence, a well-suited tracer particle is crucial for PIV measurements of the PDC exhaust. For this purpose, an effort is undertaken in the scope of this work to assess the suitability of different materials, reported in the publications presented in chapter 4.2 and [88].

While the tracer particle size is crucial for accurate PIV measurements, providing a uniform particle distribution throughout the entire PDC exhaust phase represents a serious challenge. Not only the tracer material itself, but also how it is injected into the flow is found to affect the homogeneity of the particle distribution significantly. An air-driven fluidized bed PIVsolid 8 is used in this work for seeding generation. The most uniform seeding distribution is achieved when the fluidized bed is operated with a constant mass flow rate to ensure steady-state operation of the seeder. However, the seeding air needs to be injected into the PDC only for a few milliseconds prior to ignition to avoid overseeding and overexposure. For this purpose, a 2/3 port solenoid valve is used to bypass the seeded air to the laboratory exhaust system after finishing the seeding of the PDC. Further details regarding the experimental setup can be found in chapter 4.2.

A simplified evaluation of the uncertainty in the velocity magnitude obtained from the PIV measurements is conducted based on the approach introduced in [89]. Accordingly, the velocity V can be expressed as $V = M_\mathrm{f}\frac{\Delta D_\mathrm{p}}{\Delta t}$, where M_f denotes the magnification factor in m/pixels , ΔD_p the particle displacement in pixels, and Δt the pulse distance between the two laser pulses in seconds.

The uncertainty in the velocity magnitude determined from the PIV data is estimated using the method introduced by Kline & McClintock [90]. The uncertainty of the velocity is expressed as

$$\frac{\delta(V)}{V} = \pm\sqrt{\left(\frac{\delta(M_\mathrm{f})}{M_\mathrm{f}}\right)^2 + \left(\frac{\delta(\Delta D_\mathrm{p})}{\Delta D_\mathrm{p}}\right)^2 + \left(\frac{\delta(\Delta t)}{\Delta t}\right)^2},$$

where $\delta(\cdot)$ is the error of the associated variable.

For the conducted PIV measurements the magnification factor is fixed which is determined carefully during the calibration process. Accordingly, the term $\frac{\delta M_\mathrm{f}}{M_\mathrm{f}}$ is neglected as it is assumed to be much smaller compared to the error in the particle displacement. Furthermore, the time accuracy of the laser pulse is assumed to be in the order of $\delta(\Delta t)$ =1 ns [89]. For the PIV measurements conducted in this work a pulse distance of $\Delta t = 4\mu$s was used, resulting in a relatively small error $\frac{\delta(\Delta t)}{\Delta t}$. Moreover, the nominal particle image displacement $\delta(\Delta D_\mathrm{p})$ is in the order of 0.1 pixels according to the study of Westerweel [91]. Hence, $\frac{\delta(\Delta D_\mathrm{p})}{\Delta D_\mathrm{p}} \gg \frac{\delta(\Delta t)}{\Delta t} \gg \frac{\delta(M_\mathrm{f})}{M_\mathrm{f}}$ and the uncertainty on the veloctiy can be simplified

to

$$\begin{aligned}\delta(V) &\approx V \cdot \frac{\delta(\Delta D_\mathrm{p})}{\Delta D_\mathrm{p}} \\ &= \frac{M_\mathrm{f}\Delta D_\mathrm{p}}{\Delta t} \cdot \frac{\delta(\Delta D_\mathrm{p})}{\Delta D_\mathrm{p}} \\ &= M_\mathrm{f} \cdot \frac{\delta(\Delta D_\mathrm{p})}{\Delta t}.\end{aligned}$$

Using the expression above the uncertainty for the velocity for the conducted PIV measurements is 1.8 m/s. This uncertainty corresponds to a maximum error of 0.01 to 6% with respect to the maximum measured velocity during the entire PDC exhaust phase. However, the given uncertainty based on the simplified approach introduced above should be treated with caution as it does not take into account all the error sources such as particle flow-tracking fidelity. The impact of the particle flow-tracking fidelity is discussed further in chapter 4.2.

3.5 Other Experimental Methods

Despite the above discussed techniques that are used in this work, some other experimental diagnostics for measuring flow quantities are applied in PDCs by other researchers. A brief overview of these techniques with the focus on publications regarding measurement of the exhaust flow is given below. The diagnostic techniques are categorized in the following based on the subjected measurand. As the most relevant pressure measurement techniques were already discussed in the last section, the remaining quantities to be considered are flow density, velocity, and temperature.

3.5.1 Density

In addition to the above discussed schlieren and shadowgraphy techniques, the **B**ackground **o**riented **s**chlieren (BOS) also allows for visualization of flow density gradients. In contrast to conventional schlieren and shadowgraphy, BOS provides a quantitative characterization of density gradients. Similar to the aforementioned techniques, BOS relies on the relation between the refractive index of a fluid and its density, given in a simplified form by the Gladstone-Dale equation [92]. The density gradients of the flow under investigation are commonly captured by the image displacement of a dotted background. Using a reference image of the background pattern, the local displacement of the pattern caused by the density gradient can be determined by applying image correlation methods.

The main advantage of this technique is its simplicity, as it only requires a camera and a dotted background. Another advantage of the BOS technique is the robustness of the correlation-based methods, as it utilizes the same post-processing methods, being extensively developed in recent years primarily for PIV and other speckle photography techniques. On the other hand, one of the main disadvantages of this technique is its limited resolution due to the statistical displacement computation. However, the limited resolution is counteracted by the ongoing progress in digital imaging and image processing techniques [92].

The exhaust of a PDC was investigated using BOS by Rouser et al. [93]. An overdriven pulsed LED illuminated the background in a transmission mode as a black light, which provided sufficient illumination during a short pulse width ($\sim 1 \mu s$) for high-frequency measurements at rates in excess of 24 kHz. Although the reported PDC exhaust density fields are limited in terms of resolution, the results show the applicability of this technique for PDCs. There are also multiple reports on using high-speed BOS for open-air explosions [94–98].

Although BOS theoretically has the capability of quantitative density measurement, it is frequently used for qualitative visualization of the flow due to challenges for quantitative determination of density and density gradient fields. Despite the limitations for capturing high-resolution density gradient images, one of the main challenges may occur in the process when determining the density from the measured density gradient. If the density is known in the captured data field at one point, the density of the entire field can be inferred from the known gradient. However, since the BOS technique is a line-of-sight integrating technique, any non-two-dimensionality needs to be considered during the post-processing of the data. Nevertheless, there are proposed correction methods utilizing Abel or Fourier transform inversion algorithm for axisymmetric flows, which may well be suitable for investigation of the PDC exhaust [99–101]. A comprehensive discussion regarding the BOS technique, including its limitations and challenges, can be found in [92].

3.5.2 Velocity

There is only a limited number of publications, reporting velocity measurements inside or of the exhaust of a PDC. This is mainly attributed to the harsh environment in the detonation tube as well as highly transient flow evolution, making the application of conventional techniques such as hot-wire anemometry or pressure-based methods practically infeasible. Hence, only optical diagnostics methods are left as suitable techniques, which can operate at high sampling frequencies while not being constrained by the limitations of intrusive methods.

Except for the above mentioned PIV measurements by Opalski et al. [27] there is no other report on velocity measurements of the PDC exhaust available to the best knowledge of the author. However, there have been some efforts to measure the particle velocity inside the PDC using different methods. Rouser et al. [93] applied particle streak velocimetry by capturing soot particles time histories inside the PDC with a high-speed camera. With an exposure time of a few microseconds, the soot particle positions were traced. The particle velocity was then determined by dividing the streak length by the exposure time. Although the measurement technique benefits from its simplicity, it has some substantial disadvantages. The accuracy of the technique can highly suffer from the soot particle size and mass, resulting in poor flow following fidelity. While PIV relies on the correlation of multiple particles inside interrogation windows, the particle streak velocimetry usually relies on a single particle, limiting the accuracy of the method substantially. Furthermore, the spatial resolution of the velocity field strongly depends on the amount of available soot particles. In the study conducted by Rouser et al. [93] the spatial resolution is significantly lower than typical PIV data mainly due to the adjustable particle amount

when using external seeding devices. Although particle streak velocimetry using soot particles may be suitable for limited velocity measurements inside the PDC, it is not feasible for measurements of the entire PDC exhaust velocity due to the absence of soot particles later in the exhaust phase.

Flow velocity measurements inside the PDC have been conducted by Caswell et al. [102] using tunable diode laser absorption spectroscopy. They used two counter-propagating laser beams to enable Doppler-based gas velocimetry. Considering only point measurements are delivered, the measurement setup for the diagnostic technique may be too complicated compared to PIV measurements. Furthermore, it is restricted to limitations in non-uniform flow along the beam path due to the line-of-sight integration, as discussed before. Hence, although challenging, PIV remains one of the most suitable methods for multidimensional velocity measurements in PGC devices. Accordingly, high-speed PIV has been recently used by a number of different research groups for RDE measurements [103–107].

3.5.3 Temperature

Although measuring the gas exhaust temperature is not considered in the scope of this thesis, for the sake of completeness, a brief review is given in the following regarding conducted gas temperature measurements in PDCs by other researchers.

Thin-Filament Pyrometry

While no temperature measurement of the PDC exhaust has been reported in the literature to date, some reports regarding temperature measurements within the detonation tube are available. Silicon carbide-based thin-filament pyrometry is one of these techniques, which was introduced initially by Vilimpoc et al. for temperature measurements in reacting flows [108, 109]. The technique is based on the measurement of the radiative emission of filaments. Assuming the filament temperature represents the gas temperature, the latter is determined from the radiative emissions using the Planck's law for the gray body. A discussion regarding the recent developments, factors affecting the accuracy, temporal response and spatial resolution can be found in [108, 110].

Rouser et al. [93] measured the combustion products temperature, directly behind the detonation wave inside a PDC at a frame rate of 11 kHz by using a PCO Dimax high-speed color camera. The spectral responsivity of the red, green, and blue channels of the camera was measured first by using a tungsten lamp and spectrometer. Rouser et al. [93] used silicon carbide particles instead of filaments to overcome the limitations of the fragile, small filaments. The particle temperature was determined by substituting the spectral responses and subsequent integration with a gray body function over the appropriate wavelengths. Although no discussion regarding validation and measurement error was provided, the simplicity of the method is presumably a strong argument for future temperature measurements inside a PDC. However, this technique is applicable only if sufficient radiation is emitted. This is only the case for high-temperature filaments occurring directly behind the detonation wave, as reported in [93]. Hence, the technique

is considered as unsuitable for the measurement of the gas temperature of the entire PDC exhaust.

Laser Absorption Spectroscopy

Laser **a**bsorption **s**pectroscopy (LAS) is one of the most common laser-based absorption techniques for quantitative measurement of species in the gas phase, which can be used for the assessment of different quantities, including species concentration, velocity, pressure, and temperature [102, 111]. LAS is a point measurement technique, which has recently become the method of choice by different researchers for species concentration and temperature measurements in PGC devices. The main advantage of LAS is its ability to provide high-bandwidth data as a non-intrusive technique for a wide range of species. Furthermore, it is a cost-effective technique compared to other routinely applied laser-based methods such as high-speed PIV or laser-induced fluorescence.

LAS relies on transmitting light through an absorbing gas and correlating the fractional transmission to the gas properties. Water vapor is usually selected as absorbing gas in PGC LAS applications, since H_2O is present in most combustion products and has a rich absorption spectrum in mid-infrared. Accordingly, an infrared laser is frequently used as a radiation source to emit collimated light at the desired frequency. Subsequent to emission, a part of the radiation is absorbed by the water molecules. The resulting total loss of light intensity is typically measured using photodetectors. According to the Beer-Lambert Law, the transmitted light intensity is a function of the spectral absorption, which is related to the thermodynamic properties of the gas.

Generally, LAS techniques can be divided into two categories. Direct absorption and Wavelength-modulation spectroscopy. Furthermore, the LAS techniques can be categorized into two subcategories: fixed wavelength and scanned wavelength methods. In the fixed wavelength direct absorption method, the laser operates at a fixed wavelength, at which a peak in the absorption of the investigated gas appears. Appropriate molecule absorbance spectra are usually determined using the HITRAN database. Fixed wavelength measurement has been applied successfully to PDCs for measurements of temperature and other combustion parameters [112]. However, fixed-wavelength LAS methods suffer from limited spectral information and are therefore less robust. Hence, most of the currently applied LAS measurements are based on scanned-wavelength techniques [111].

As for scanned-wavelength techniques, the laser beam is tuned over a range of wavelengths, typically utilizing a tunable diode laser. This technique is known as **T**unable **d**iode **l**aser **a**bsorption **s**pectroscopy (TDLAS). The tunable laser enables tuning the wavelength across one or a few absorption transitions to resolve the absorption spectrum of interest. While tuning is possible by varying the laser temperature, the laser driving current is commonly varied, which allows for tuning in MHz rates. The gas temperature is typically inferred from the integrated absorbance. However, in harsh environments, the scanned-wavelength direct absorption suffers from low signal-to-noise ratios. Therefore, advanced techniques such as scanned wavelength wave modulation have been developed by various researchers, mainly at Stanford University. The modulation of the signal is particularly of interest for harsh environments as in the PDC, which can extensively increase

the signal to noise ratio. A comprehensive review of different techniques, including their advantages and disadvantages is given in [111].

As discussed before, TDLAS is restricted to limitations imposed by the line-of-sight integration. However, this can be countered by using multiple absorption lines, which would however increase the cost and complexity of the technique. By using a sensor with four laser diodes, excellent temperature sensitivity in the range of 300-2500 K in the PDC has been demonstrated [113]. Furthermore, a number of different solutions for non-uniform flows have been developed by different research groups. A comprehensive overview including LAS challenges and solutions can be found in [111]. Although the application of LAS is challenging, and it merely provides point measurements, it is a reliable technique for accurate measurement of different quantities, including temperature for PGC devices, and thus worth considering for future PDC studies.

Chapter 4

Publications

- Publication I: **M. Rezay Haghdoost**, D. Edgington-Mitchell, M. Nadolski, R. Klein and K. Oberleithner. *Dynamic Evolution of a Transient Supersonic Trailing Jet Induced by a Strong Incident Shock Wave*. Physical Review Fluids. 2020. DOI: https://doi.org/10.1103/PhysRevFluids.5.073401

- Publication II: **M. Rezay Haghdoost**, D. Edgington-Mitchell, C. Paschereit and K. Oberleithner. *High-Speed Schlieren and Particle Image Velocimetry of the Exhaust Flow of a Pulse Detonation Combustor*. AIAA Journal. 2020. DOI: https://doi.org/10.2514/1.J058540

- Publication III: **M. Rezay Haghdoost,** B. Thethy, M. Nadolski, B. Seo, C.O. Paschereit, R. Klein, D. Edgington-Mitchell and K. Oberleithner; *Numerical and experimental evaluation of shock dividers*. Shock Waves, 2022. DOI: https://doi.org/10.1007/s00193-021-01062-2

- Publication IV: **M. Rezay Haghdoost,** B. Thethy, D. Edgington-Mitchell, F. Habicht, J. Vinkeloe, N. Djordjevic, C. Paschereit and K. Oberleithner. *Mitigation of Pressure Fluctuations from an Array of Pulse Detonation Combustors*. ASME Journal of Engineering for Gas Turbines and Power. 2021. DOI: https://doi.org/10.1115/1.4049857

4.1 Publication I

PHYSICAL REVIEW FLUIDS **5**, 073401 (2020)

Dynamic evolution of a transient supersonic trailing jet induced by a strong incident shock wave

Mohammad Rezay Haghdoost *
Laboratory for Flow Instabilities and Dynamics, Technische Universität Berlin, Germany

Daniel Edgington-Mitchell
Department of Mechanical and Aerospace Engineering, Monash University, Melbourne, Australia

Maikel Nadolski and Rupert Klein
Institut für Mathematik, FB Mathematik und Informatik, Freie Universität Berlin, Germany

Kilian Oberleithner
Laboratory for Flow Instabilities and Dynamics, Technische Universität Berlin, Germany

(Received 6 November 2019; accepted 13 May 2020; published 7 July 2020)

The dynamic evolution of a highly underexpanded transient supersonic jet at the exit of a pulse detonation engine is investigated via high-resolution time-resolved schlieren and numerical simulations. Experimental evidence is provided for the presence of a second triple shock configuration along with a shocklet between the reflected shock and the slipstream, which has no analog in a steady-state underexpanded jet. A pseudo-steady model is developed, which allows for the determination of the postshock flow condition for a transient propagating oblique shock. This model is applied to the numerical simulations to reveal the mechanism leading to the formation of the second triple point. Accordingly, the formation of the triple point is initiated by the transient motion of the reflected shock, which is induced by the convection of the vortex ring. While the vortex ring embedded shock moves essentially as a translating strong oblique shock, the reflected shock is rotating towards its steady-state position. This results in a pressure discontinuity that must be resolved by the formation of a shocklet.

DOI: 10.1103/PhysRevFluids.5.073401

I. INTRODUCTION

Supersonic transient underexpanded compressible jets can be found in many applications such as rocket propulsion, shock tubes, pulse detonation engines, etc. The transient supersonic jet is also of interest in the field of safety and security management, e.g., in case of an accidental release of a gas from a high-pressure reservoir or volcanic blasts. The characterization of such a flow field has been the subject of research in some detail for many years. The first stage of the jet evolution is the well known shock-diffraction phenomenon, which has been investigated numerically, experimentally and analytically by many researchers [1–4]. The next stage is the dynamic evolution of a highly transient supersonic trailing jet behind the leading shock, which has also received significant attention [5–11]. However, both the numerical and experimental study of the flow at this stage is inherently challenging [12,13] due to the short timescales and large dynamic ranges involved. The last stage

*rezayhaghdoost@tu-berlin.de

of the transient supersonic jet evolution is simply the steady underexpanded jet, which has been extensively investigated in the last few decades [14].

While the structures in a transient underexpanded jet evolve in time, many of the salient flow features are analogous to those observed in the more classical steady underexpanded jet. An expansion fan originating from the nozzle exit accounts for the mismatch in pressure between the jet and the surroundings. The expansion fan reflects as compression waves from the sonic lines. These compression waves converge to an oblique shock wave, which reflects as a shock wave at the jet centerline. This reflected shock again reflects at the sonic line and results in new expansion waves. A series of reflected shock and expansion waves result in the characteristic shock cell structure or "shock diamonds" of underexpanded jets. Highly underexpanded jets are characterized by a strong Mach disk as a result of a Mach reflection at the jet centerline. As the pressure ratio decreases, the Mach disk becomes smaller. It was originally thought that for weak underexpanded jets there are no Mach reflections but only regular reflections. However, it was shown that a regular reflection of a shock from an axis of symmetry is impossible, and therefore all reflections at the centerline of an axisymmetric jet must be Mach reflections [15]. The flow downstream of the Mach disk becomes subsonic, while the flow downstream of the oblique shocks remains supersonic. A mismatch in temperature, entropy, and velocity occurs between the boundary of these two regions. A shear layer produced by the slipstream between the low-speed core and high-speed annulus results in vortical structures, which persist across multiple shock cells [16]. In the steady-state jet these aforementioned structures are well understood; however, during the initial development of a transient jet their temporal evolution is far more complex yet has received less attention.

To introduce the flow structures relevant to the discussion to follow, a time series of schlieren images capturing key points in the early-stage evolution of a transient supersonic jet are presented in Fig. 1, for a shock wave with a Mach number of $\mathrm{Ms} = 1.76$ exiting from a circular tube. These images are separated by a uniform time interval of 50 μs; the time τ given above the images is nondimensionalized $\tau = (t\,Ms\,a_0)/D$, where t is the time after the shock wave leaves the tube exit, D is the tube exit diameter, and a_0 is the speed of sound ahead of the leading shock. The corresponding experimental setup is discussed in Sec. II.

The first stage of the jet evolution, the shock diffraction, is shown in Fig. 1(a). This image captures the moment immediately after the shock wave exits the tube. Towards the radial edge the shock wave has already undergone a three-dimensional diffraction as indicated by the partially curved shock; both diffracted and undisturbed leading shocks are clearly visible. The exhaust flow of the tube expands through a pseudo-steady Prandtl-Meyer expansion fan (PM) centered at the tube exit's sharp corner. The leading characteristic (LC) of these waves marks the separation point (SP) between the undisturbed leading shock and the diffracted shock. The same flow features have been observed first by Skews [1] at a plane-walled convex corner for a diffracting shock wave. The information about the area expansion travels along the LC toward the jet centerline leading to a fully curved leading shock wave [Fig. 1(b)]. Since the pressure at the tail of the PM expansion waves is lower than the pressure transmitted back by the leading shock wave, a second shock arises to match the two phases. Friedman [17] has shown that this second shock occurs due to the over-expansion caused by the increase of the volume, which does not arise in one-dimensional studies. Figure 1(b) captures the moment as this second shock is just being formed at the outer region of the jet next to the barrel shock. The upper and lower second shock waves, highlighted in Fig. 1(b) propagate toward the jet centerline to form a single shock wave. As these shocks coalesce, a single curved shock wave is formed [Fig. 1(c)]. The curved shock wave transforms to a disk-shaped shock wave shortly after, as can be seen in Fig. 1(d). This is the origin of the well-known Mach disk of a steady underexpanded jet.

Besides the Mach disk, several other features are visible in Fig. 1 that have been reported in the literature. The leading shock sets the gas inside the tube in motion by compressing the flow while propagating through the tube. Following the leading shock, a highly transient jet establishes itself at the outlet of the tube. Elder and De Haas [18] initiated the studies of transient supersonic jets of an open-end shock tube using spark schlieren measurements. They reveal the presence of a

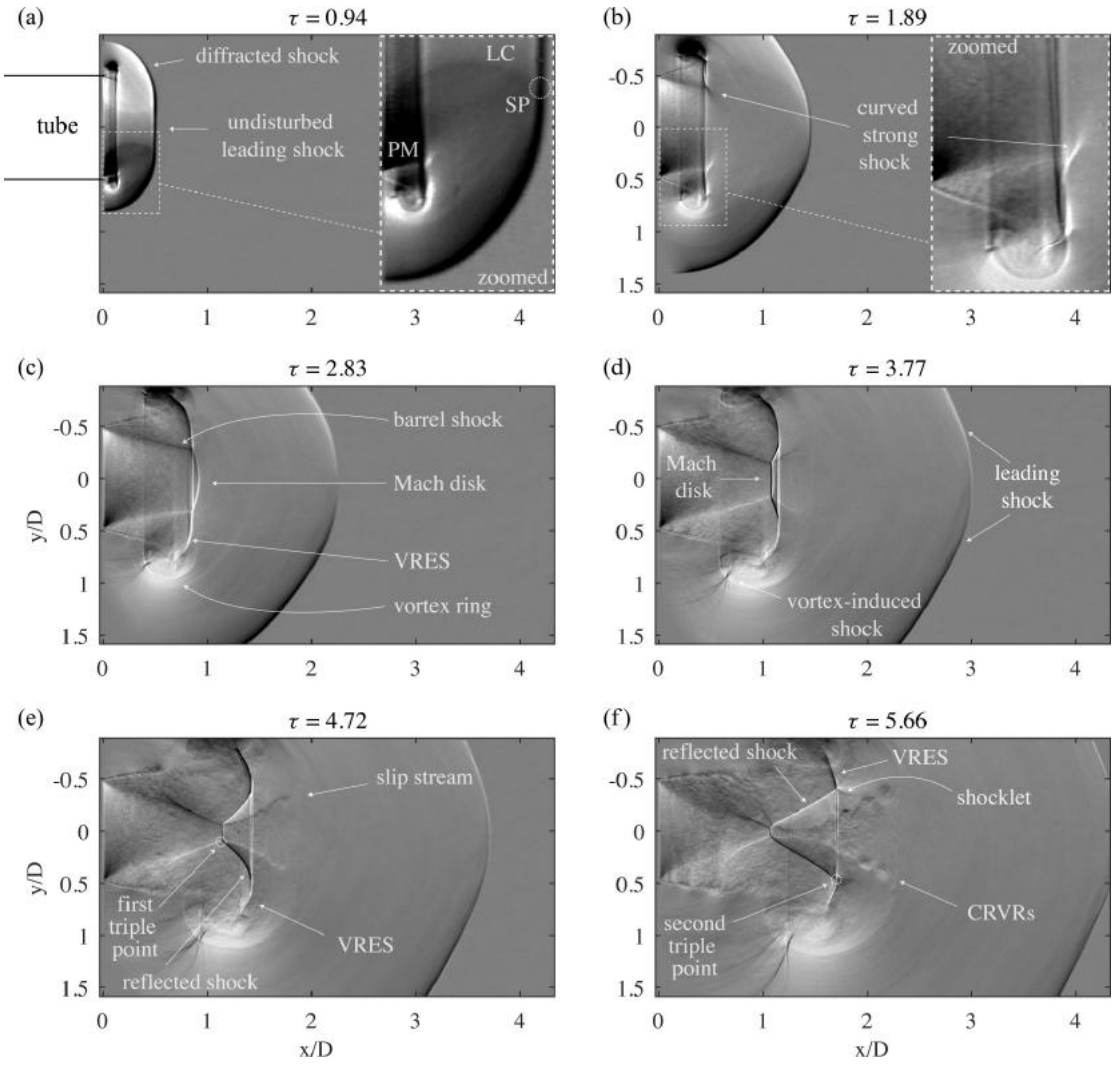

FIG. 1. Dominant features of a starting transient underexpanded jet. A time series of six $\overline{\frac{\partial \rho}{\partial y}}$ schlieren images shows the early stage of the exhaust flow for Ms = 1.76. The x and y coordinates are normalized by the tube diameter, D. The origin of the axis corresponds to the point on the tube centerline at the tube exit.

vortex ring in the trailing jet for Mach numbers Ms = 1.12 and 1.32, which grows nonlinearly with time and distance. In a systematic study Brouillette and Hebert [19] found three different types of flow fields of the trailing jet depending on the leading shock Mach number. Accordingly, there is a shock-free vortex ring characterized by a very thin core for Ms < 1.43. For higher Mach numbers the vortex ring contains an embedded shock, the so-called vortex-ring-embedded shock (VRES) [also visible in Fig. 1(c)]. Brouillette and Hebert [19] found the occurrence of counter-rotating vortex rings (CRVRs) for Ms > 1.6 [Fig. 1(f)]. The primary vortex ring can also contain an additional shock wave, the so-called vortex-induced shock as indicated in Fig. 1(d). These flow features can be seen more clearly in Fig. 2, where an overview of the dominant flow features at $\tau = 6.13$ is given.

Besides the shock waves associated with the vortex ring, the trailing jet can also contain a number of additional shock systems. Ishii *et al.* [7] exhibited the presence of a Mach disk and a triple shock configuration in the trailing jet for high-Mach-number leading shock flow. Figure 1(e) shows the corresponding shock system, which consists of the barrel shock, the reflected shock, and the Mach disk. The reflection of the barrel shock from the jet centerline as an axis of symmetry must be a Mach

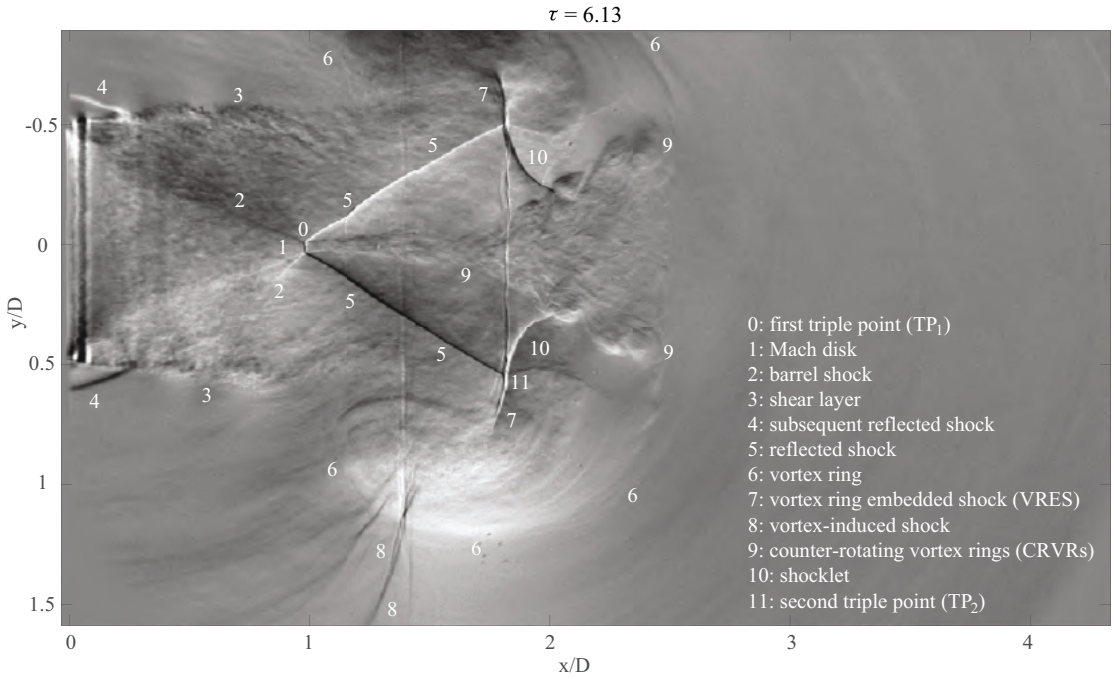

FIG. 2. Overview of the main flow features at $\tau = 6.13$.

reflection in the same manner as for a steady underexpanded jet [15]. The corresponding slipstream downstream of the triple point can be recognized in Fig. 1(e). Unlike the steady underexpanded jet the slipstream is inclined towards the jet boundary in radial direction. A number of CRVRs are apparent in Fig. 1(f). These vortices are generated by Kelvin-Helmholtz (KH) instabilities of the shear layers along the slipstream [7]. Dora *et al.* [8] showed that the evolution of CRVRs is driven by the same physical mechanism as for the Mach reflection. They claim that the shear layer along the slip stream grows spatially due to the eddy pairing. In accordance to that, the close-up views in Fig. 3 reveal a number of eddies along the slipstream growing in both size and strength. Moreover, the image sequence shows clear evidence for the pairing process confirming the observations of Dora *et al.* [8]. As shown by Kleine *et al.* [20], the CRVRs wraps around the vortex ring at a later time. In a recent study, Zhang *et al.* [21] demonstrated that the interaction of the CRVRs with the vortex ring increases the instability of the primary vortex ring.

The features observed in Figs. 1(a)–1(e) have been described in the previous studies of Dora *et al.* [8], Kleine *et al.* [20], and Zhang *et al.* [21]. There is, however, an additional feature in Fig. 1(f) that

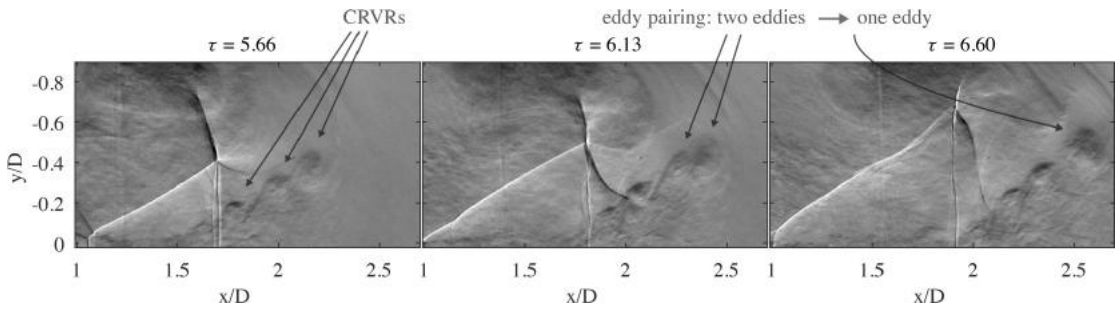

FIG. 3. $\overline{\frac{\partial \rho}{\partial y}}$ schlieren images showing the pairing of two eddies for Ms = 1.76.

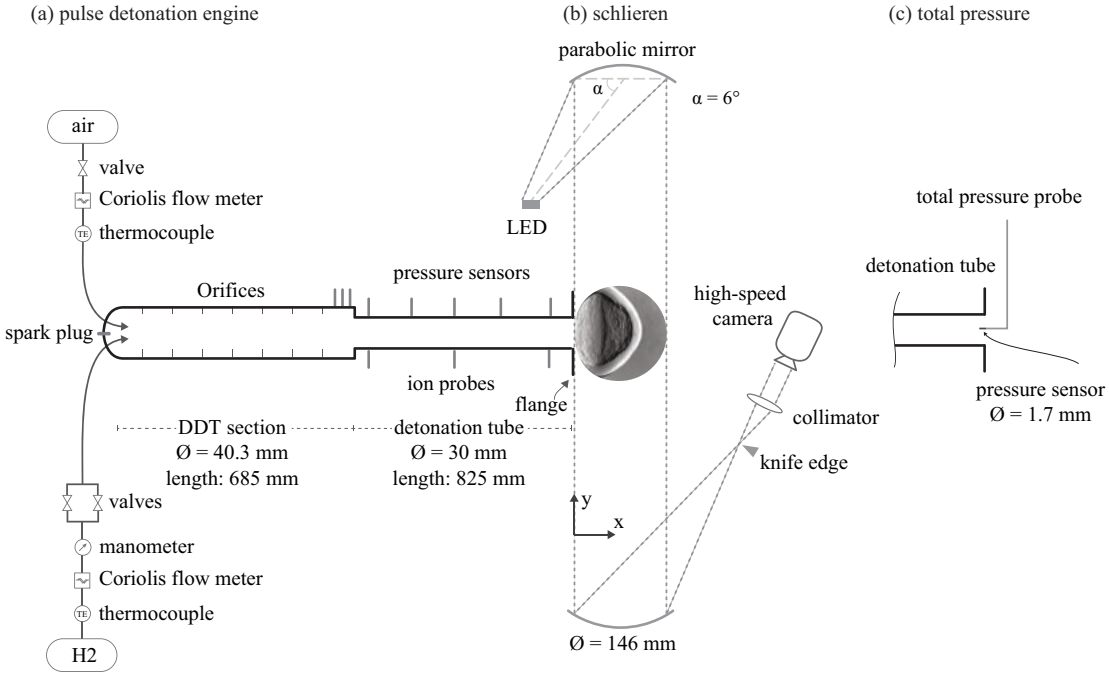

FIG. 4. Sketch of the experimental setup showing (a) the pulse detonation engine, pressure sensors, and ion probes, (b) the schlieren setup, and (c) the total pressure probe.

has received far less attention: a transient shocklet formed at the intersection of the reflected shock and the VRES resulting in a second triple point [see also Fig. 2 (10)]. This feature has no analog in steady-state jets yet has received little consideration in past research on transient jets. Thus, this paper presents an experimental and numerical investigation of the shock evolution in a highly underexpanded jet. The paper is laid out as follows. A general description of the facility, as well as the schlieren methodology is given in Secs. II A and II B, respectively. Section II D presents the numerical methodologies and the setup for the conducted simulations. Section III A considers the formation and evolution of the second triple point and its associated shock structure. Section III B provides a proposed mechanism for the formation of the second triple point by applying a developed model for determination of postshock flow condition.

II. METHODOLOGY

A. Experimental facility and instrumentation

In the current study a pulse detonation engine (PDE) is used to generate a shock wave. A PDE is, in its simplest form, a tube filled with a combustible mixture. Two different reactive waves can be generated using a PDE: a supersonically propagating combustion front, which is known as a detonation wave, and a subsonically propagating front, which is referred to as a deflagration wave. A schematic of the PDE and its instrumentation is presented in Fig. 4. The PDE consists of two sections, the deflagration-to-detonation transition (DDT) section and the detonation tube. Hydrogen is injected through eight circumferentially distributed fuel lines at the rear end of the tube. Air is injected directly upstream of the DDT section. Once the tube is filled with a combustible mixture a spark plug is used to initiate combustion. Orifices installed in the DDT section accelerate the flame. By varying the mixture volume and equivalence ratio the operation mode of the PDE can be adjusted. In the current study we are interested in the transient supersonic jet of a shock-induced flow, and, therefore, we want to minimize the impact of combustion on the exhaust flow. Hence,

the tube is only partially filled with a rich mixture prior to ignition to allow for the shock wave to decouple from the reaction front. The decoupling ensures a time gap between the arrival of the shock wave and combustion products at the tube exit.

The key governing parameter for the shock-induced flow is the Mach number of the shock wave propagating through the tube. To achieve comparability between the experimental and the numerical results we matched the respective Mach numbers of the leading shock waves at the tube exits, ensuring a similar flow field at the initial stage of the transient starting jet. The leading-shock Mach number for the schlieren and numerical results discussed in Sec. III A is Ms = 2.15.

Piezoelectric pressure sensors (PCB112A05) are used to measure the leading shock wave velocity using the time of flight model. Three pressure sensors are flush-mounted in the DDT section and five in the detonation tube. The last pressure sensor is mounted 4D upstream the tube end. The combustion front is tracked inside the tube by using ion probes flush-mounted in the opposite side to the pressure probes within the detonation tube. These sensors are used to ensure the decoupling of the leading shock wave from the combustion front. For measurements of total pressure at the tube exit a piezoresistive Kulite XCE-062 transducer is placed at $x/D = -0.3$ on the jet centerline, as shown in Fig. 4(c). A frequency response correction of the signal is applied by using a Kulite KSC-2 signal conditioner [22]. Two type-K thermocouples measure the temperature of air and hydrogen. The pressure in both the hydrogen and air supply lines is measured using Festo pressure transducers (SPTW-P10R). The mass flows of air and hydrogen are measured using Coriolis mass flow meters and are controlled using proportional valves. The data from ionization and pressure probes are collected on 11 channels using a National Instruments MXI-Express DAQ system at 1 MHz sampling rate.

B. Schlieren diagnostic

The flow at the open end of the PDE is investigated using time-resolved high-resolution schlieren measurements. Figure 4(b) presents a schematic illustration of the schlieren setup. A standard z-type configuration is used with two 6-inch parabolic f/8 mirrors for collimating and refocusing of light. A pulsed LED is used as a light source as suggested by Willert *et al.* [23]. A very high-intensity light pulse at a very short time span is generated using an overdriven-operated LED. An exposure time of 1 μs has shown to be the best trade off between smearing of high-speed flow features and image contrast. The schlieren images are captured at 20, 40, and 80 kHz with a Photron SA-Z camera. The spatial resolution of 0.15 pixel per millimeter results in approximately 200 pixels per tube diameter. The higher frame rates produce a smaller field of view, but the same spatial resolution. In the Cartesian coordinate system the x coordinate corresponds to the jet axis and the y and z coordinates to the radial directions. A razor blade aligned perpendicular and parallel to either the x or y coordinate is used. The resultant images correspond to path-integrated density gradients in the x direction $\overline{\frac{\partial \rho}{\partial x}}$ and y direction $\overline{\frac{\partial \rho}{\partial y}}$, respectively.

C. Experimental repeatability

The repeatability of the experiments is investigated based on both schlieren and pressure measurements. For this purpose a set of three measurement runs are conducted for the same configuration. As a measure for the repeatability the axial distance of the Mach disk to the tube exit on the jet center line is determined based on the schlieren images. The procedure is repeated for five configurations with different fill fractions. The maximum difference between the location of the maximum axial distance of the Mach disk is found to be 1.6%.

The repeatability of the experiments is also evaluated based on the total pressure measurements. Figure 5 shows the total pressure at the combustor exit averaged over for four test runs and the standard deviation, to evaluate the total pressure between the test runs. Moreover, the Mach number of the shock wave at the combustor exit is determined for the same test runs using the time-of-flight method. The values are given in the caption of Fig. 5 showing variations of less than

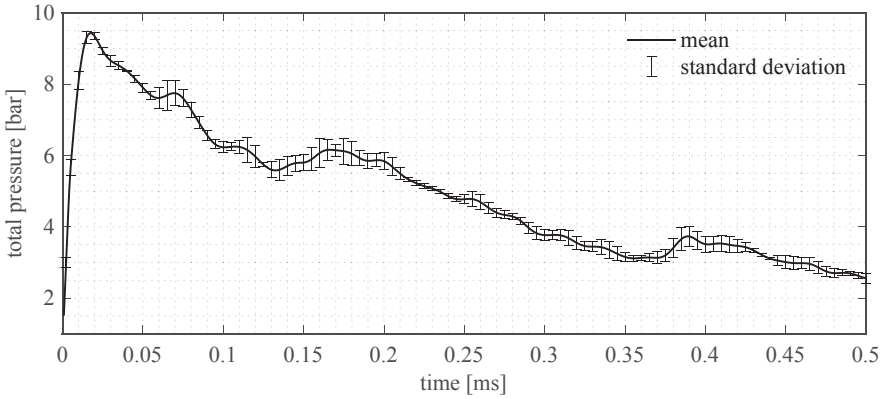

FIG. 5. Mean and standard deviation of total pressure for four test runs with Ms = 1.968, 1.977, 1.983, and 1.983 at $x/D = -0.3$.

1%. The remaining variations in the measured quantities between the experiments is mainly due to the stochastic aspects of turbulent detonation to combustion process in the detonation tube (DDT section).

D. Numerical simulations

1. Finite volume discretizations

The present numerical simulations are based on the three-dimensional Euler equations for an ideal gas, and the one-dimensional reactive Euler equations for an ideal gas mixture. In describing the respective numerical discretizations used, we will employ the following notation below: ρ is the density, $\mathbf{v}$ the flow velocity vector, p the pressure, $\mathbf{Y}$ the species vector, E the total energy, $\mathbf{I}$ the identity matrix, and γ the isentropic exponent of the mixture.

The three-dimensional Euler equations read

$$\begin{aligned} \frac{\partial}{\partial t}\rho + \nabla\cdot(\rho\mathbf{v}) &= 0, \\ \frac{\partial}{\partial t}(\rho\mathbf{v}) + \nabla\cdot[\rho\mathbf{v}\otimes\mathbf{v} + p\mathbf{I}] &= 0, \\ \frac{\partial}{\partial t}(\rho E) + \nabla\cdot[(\rho E + p)\mathbf{v}] &= 0, \end{aligned} \tag{1}$$

and we assume the equation of states for perfect gases

$$\rho E = \frac{p}{\gamma - 1} + \frac{1}{2}\rho\mathbf{v}\cdot\mathbf{v} \tag{2}$$

with $\gamma = 1.4$. To compute the numerical solution to (1) we use an explicit Godunov-type second-order finite volume scheme with an exact Riemann solver. The intercell fluxes are computed by a MUSCL reconstruction step on the conservative variables (ρ, $\rho\mathbf{v}$, ρE) and the slopes used in this step are limited by the van Leer limiter to control artificial oscillations at discontinuities (see, e.g., Ref. [24] for a textbook reference). Multidimensionality is handled using Strang splitting for the spatial derivatives in (1), and this leads in total to a second-order accurate scheme in regions of smooth solution behavior and to first-order nonoscillatory approximations near discontinuities and extrema. This scheme is augmented by the cut-cell approach for the representation of solid wall boundary conditions introduced by Klein *et al.* [25] and Gokhale *et al.* [26] which is compatible with directional operator splitting. The cylindrical boundary of the combustion tube is represented as a level set and is embedded in a regular Cartesian grid. We also make use of block-structured

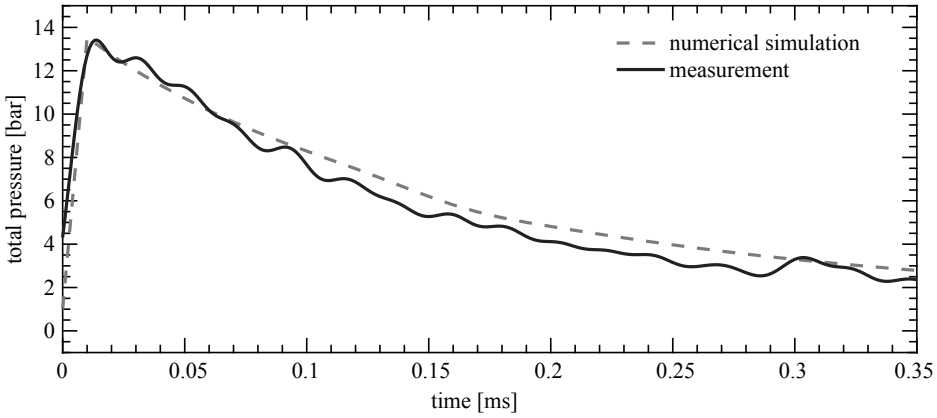

FIG. 6. Total pressure over time for $Ms = 2.15$ at $x/D = -0.3$.

adaptive mesh refinement techniques [27] to locally refine the grid in regions of interest, such as shock waves or cut-cells.

The one-dimensional reactive gas flow simulations in the detonation tube are based on the one-dimensional form of (1) with chemical reactions described by balance laws for the chemical species,

$$\frac{\partial}{\partial t}(\rho \mathbf{Y}) + \nabla \cdot (\rho u \mathbf{Y}) = -\rho \dot{\mathbf{Y}}. \tag{3}$$

Furthermore, the energy equation of state is modified to account for a mixture of gases,

$$\rho E = \rho \int_{T_0}^{T} c_v(\tau, \mathbf{Y})\, d\tau + \rho Q_0(\mathbf{Y}) + \frac{1}{2}\rho u^2, \tag{4}$$

where $c_v(\tau, \mathbf{Y})$ is the specific heat capacity at constant value and the formation enthalpy at $T = T_0$ is $Q_0(\mathbf{Y})$. In this study these functions, just as the reaction rate functions $\dot{\mathbf{Y}}(T, p, \mathbf{Y})$ are provided by an H_2-O_2 reaction mechanism for high pressure combustion following Burke *et al.* [28].

The numerical scheme used here is described in Ref. [29]. It differs from the inert gas 3D solver explained above by (1) the use of Strang splitting for the implementation of the chemical reaction terms, and (2) the use of the HLLE approximate Riemann solver as a numerical flux function. The HLLE solver is the version of the general HLL scheme of Harten *et al.* [30] with the numerical signal speeds determined according to Einfeldt [31]. This flux function provides added robustness and efficiency relative to the exact Riemann solver. Its advantages for detonation wave applications have been discussed by Berndt [32].

2. Initial data and boundary conditions for the approximate representation of the experiment

The combustion tube in the experiment is only partially filled with the combustible mixture, but its fill fraction and equivalence ratio along the tube is not known. Although we are given measured pressure data over time at the tube outlet in addition to the Mach number for the leading shock wave, a complete description of the thermodynamic quantities is not experimentally available. To approximate inflow boundary conditions into the three-dimensional simulation domain at the outlet of the combustion tube, we perform a series of one-dimensional simulations of H_2-O_2 detonations and compared the results with the measurements. Varying the equivalence ratio of the combustible mixture and the fill fraction of the tube we found a one-dimensional solution within the tube that matches the Mach number of the leading shock as well as the total pressure over time (Fig. 6) rather accurately.

Even if the flow states in the combustion tube can be well approximated by cross-sectional averages of the conserved quantities, thereby allowing for a one-dimensional approximation, the

flow states next to the tube exit are always affected nontrivially by multidimensional effects. To properly capture these, the three-dimensional simulations cover the entire length of the PDE in addition to a large flow domain beyond the tube exit. Initial conditions within the tube are given by the solution from the one-dimensional computation at a point in time right after the combustible mixture is entirely consumed, but before the leading shock wave has reached the tube exit. Outside the combustion tube we initially assume air at rest at atmospheric conditions.

III. THE EARLY-STAGE EVOLUTION OF THE TRANSIENT SUPERSONIC JET

In the following the formation and evolution of the second triple point and its associated shock structure are discussed based on both experimental and numerical results. Finally a proposed mechanism for the second triple point is presented.

A. Formation and evolution of the shocklet

In Fig. 2 we noted the presence of a second triple point at the intersection of the reflected shock and the vortex ring. Unlike the first triple point and its associated system of shocks, this second triple point is not observed in a steady underexpanded jet. While the shocks associated with this second triple point are visible in some published work, as of yet there has been no discussion of the mechanism by which it forms. The triple point is formed at the intersection of the reflected shock, the VRES, and a new transient shock structure which, due to its transient nature, we will refer to as a shocklet. The shocklet and its associated triple point are only present for a short time during the early evolution of the transient jet.

Figure 7 presents a series of numerical and experimental snapshots spanning this early evolution period. Experimental schlieren images are compared with numerical schlieren images produced by path integration through the three-dimensional simulation data. The numerical schlieren images display grayscales of the quantity

$$S(x, y) = \int_{z_0}^{z_1} \frac{\partial \rho}{\partial x}(x, y, z)\, dz.$$

In addition, a planar representation of the early evolution of the underexpanded jet is given in Fig. 7 by contour plots of the Mach number at $z = 0$. Subsonic and supersonic region of the jet cross section are color-coded with blue and red, respectively. There is very good agreement between the numerical and experimental schlieren results regarding the position and size of the large-scale flow features such as the vortex ring, the Mach disk, and the reflected shock. As a quantitative measure for the agreement of the numerical and experimental results, the Mach disk location on the jet centerline as well as the position of the triple point are compared frame by frame. The averaged discrepancy is found to be 4.2 and 3.0 % for the Mach disk and the first triple point locations, respectively. Figures 7(a)–7(c) show the leading shock wave and a triple point configuration consisting of the barrel shock, the Mach disk, and the reflected shock. Up to this time ($\tau \leqslant 4.08$) the reflected shock and the VRES are simply the same shock wave, and the size and position of this shock wave is primarily dictated by the strong vortex in which it is embedded. As the vortex propagates farther downstream, the upstream boundary condition for the shock is instead dictated by the Mach reflection arising from the incident shocks generated at the lip. At larger radial positions however, the shock is still very much a function of the velocity field induced by the vortex ring. At $\tau = 5.43$, while the shock still forms a contiguous surface, the angle set by the triple point is significantly different to that required in the vortex ring. This disparity increases as the vortex ring propagates farther from the nozzle, and while the shock surface remains contiguous, by $\tau = 6.79$ a sharp kink forms on this surface, separating the the VRES from the reflected shock [Figs. 7(g)–7(i)]. As the vortex ring moves farther downstream at $\tau = 8.15$, the kink becomes a triple point, and a second

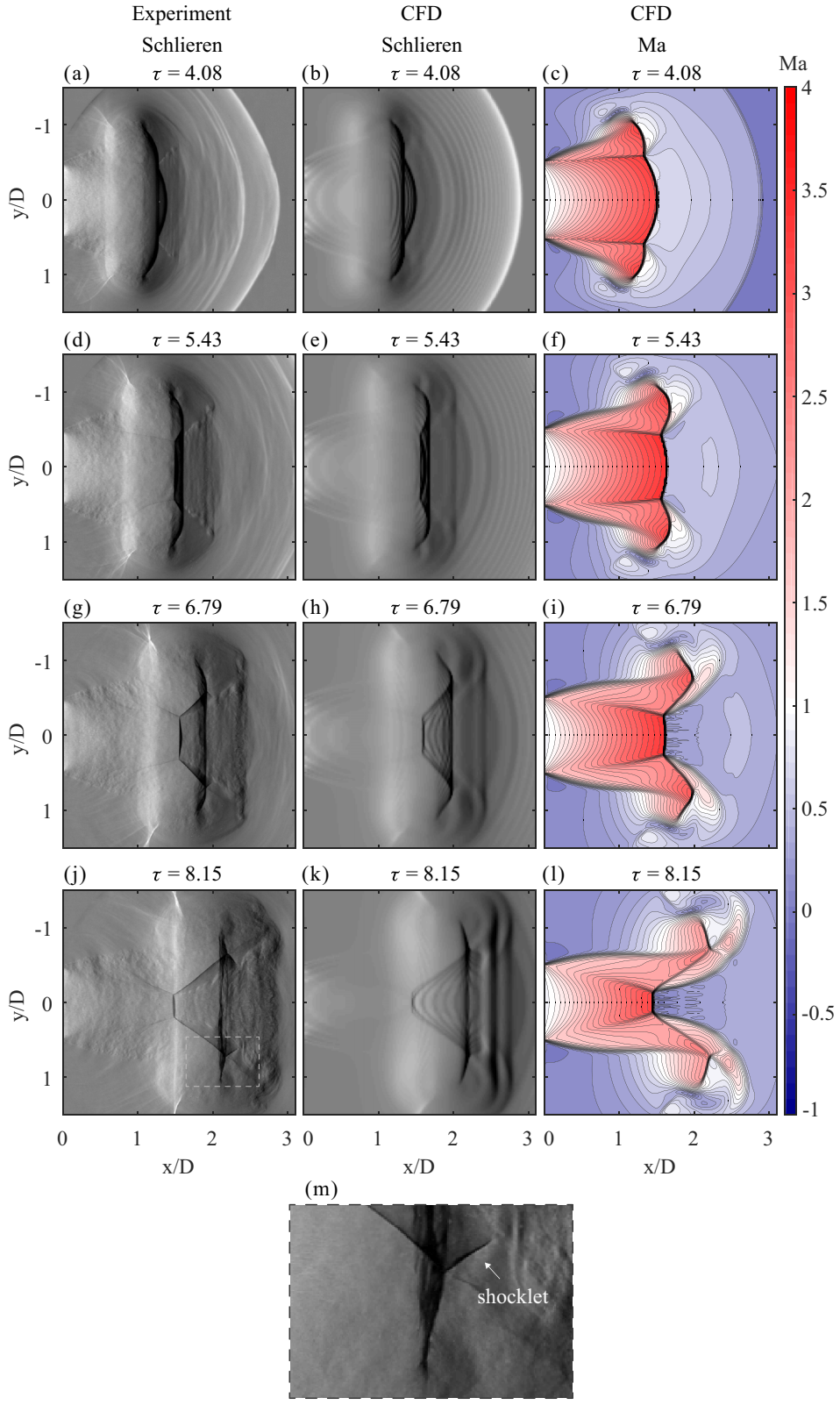

FIG. 7. Formation of the shocklet based on experimental $\overline{\frac{\partial \rho}{\partial x}}$ schlieren images for Ms = 2.15 (left column) numerical $\overline{\frac{\partial \rho}{\partial x}}$ schlieren images (center), and Mach number contour plots at $z = 0$ (right column).

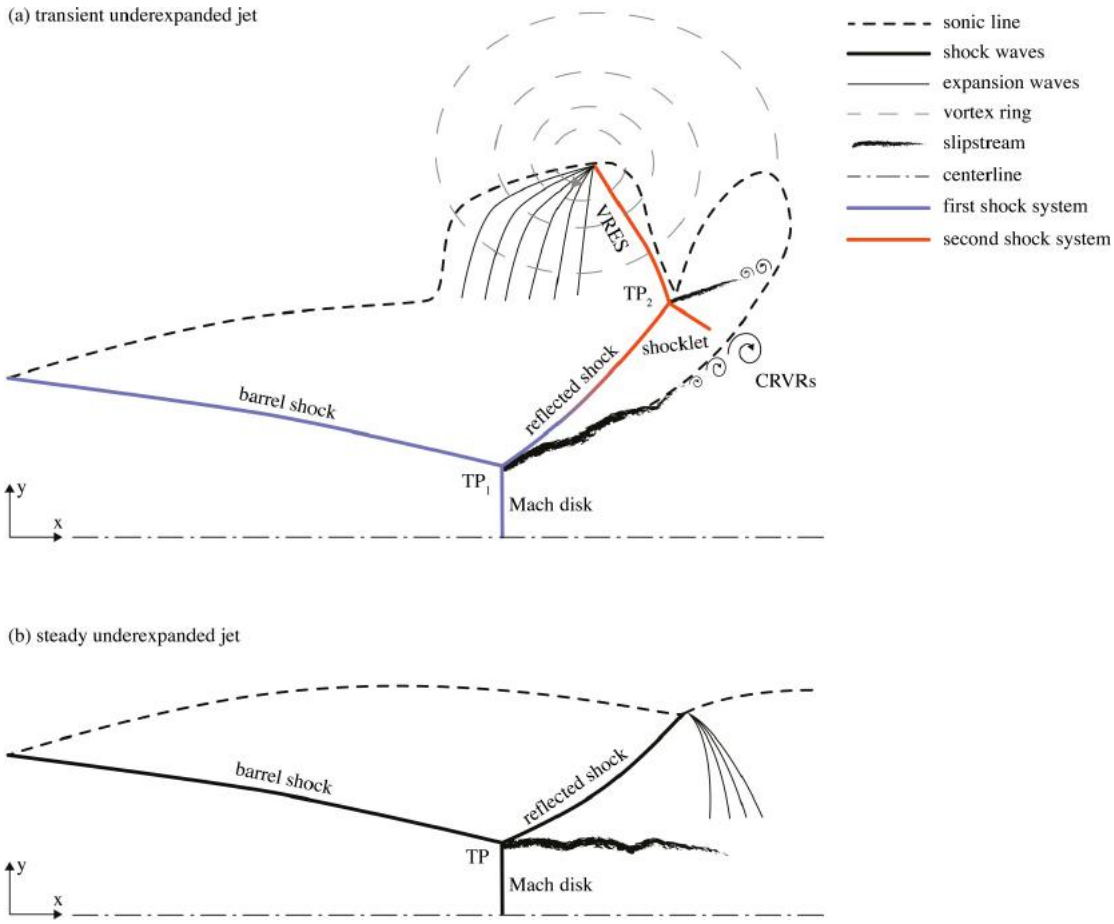

FIG. 8. Schematic illustration of the jet structure for the transient and steady underexpanded jet.

triple shock configuration occurs [Figs. 7(j)–7(m)]. The shocklet is clearly visible between the reflected shock and the CRVRs in both experimental and numerical data as shown in Figs. 7(j)–7(m).

To facilitate a clearer description of the formation of the shocklet, Fig. 8 presents a schematic comparison between the structures in the transient jet and those in its steady-state counterpart. The illustration in Fig. 8(a) corresponds approximately to the flow state shown in Figs. 7(j)–7(m). A triple point configuration as a result of a Mach reflection can be observed for both steady and transient jet. This shock system consists of the barrel shock, the Mach disk, the reflected shock, and the triple point (TP_1). In case of the steady underexpanded jet, the reflected shock of the primary shock system reflects as expansion waves from the sonic line [Fig. 8(b)]. However, for the transient jet the sonic line is significantly distorted by the presence of the vortex ring, and a simple reflection does not occur. Instead, a second triple shock configuration occurs, as illustrated in Fig. 8(a). This shock system consists of the reflected shock, the VRES and the shocklet, intersecting at a second triple point TP_2.

The subsequent evolution of the second shock system is shown in Fig. 9 based on a time series of five schlieren images. No further tilting of the reflected shock toward the jet center line can be observed; the initial angle of the reflected shock has reached an approximate steady state. In contrast, the vortex ring and its embedded shock (VRES) move farther downstream, with the VRES decreasing continuously in size. Therefore, the triple point TP_2 translates downstream and radially outwards [Figs. 9(a)–9(d)]. As the vortex ring convects further, the sonic line shifts inwards, and

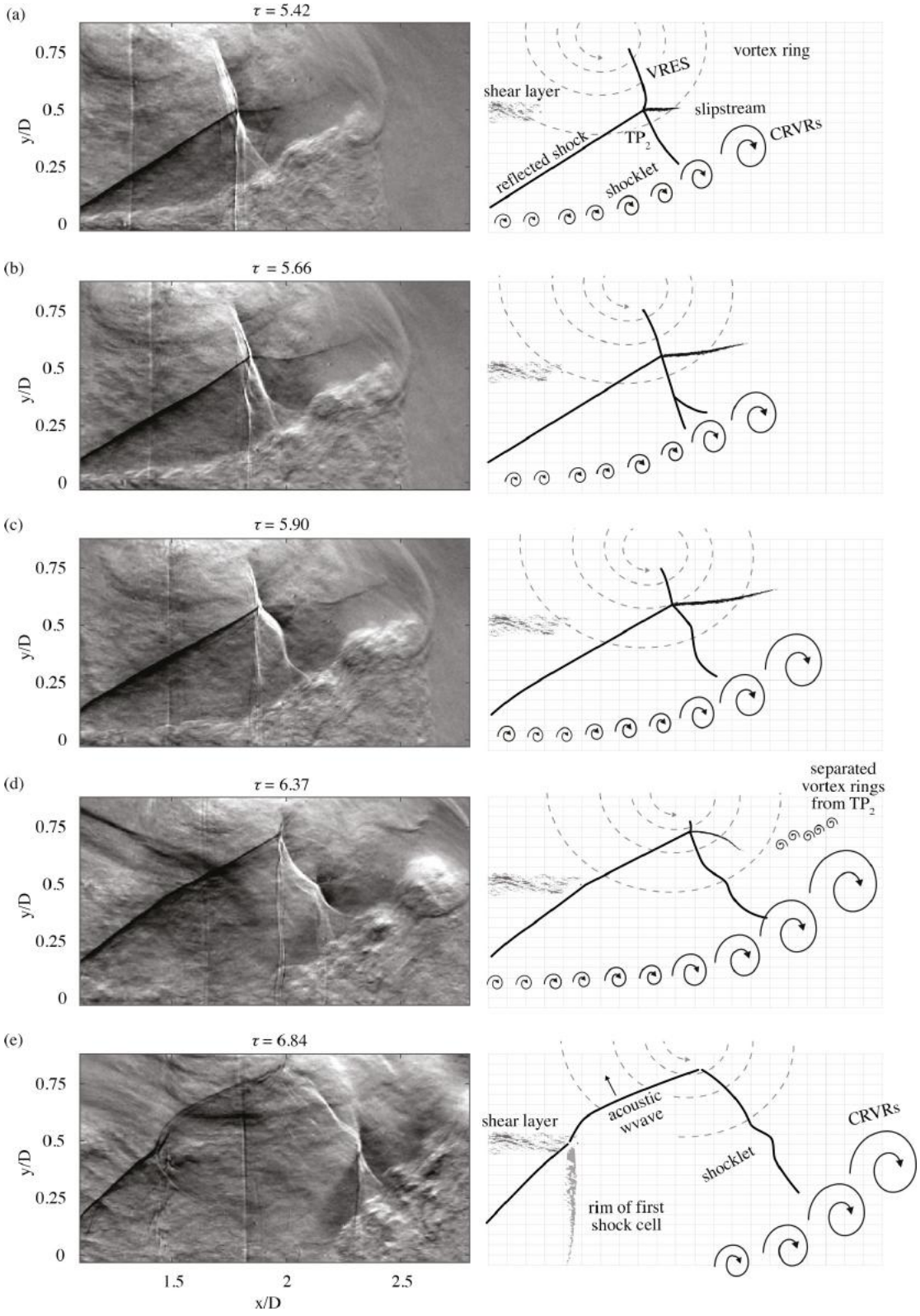

FIG. 9. $\overline{\frac{\partial \rho}{\partial y}}$ schlieren images for Ms = 1.76 showing the evolution of the second triple point configuration.

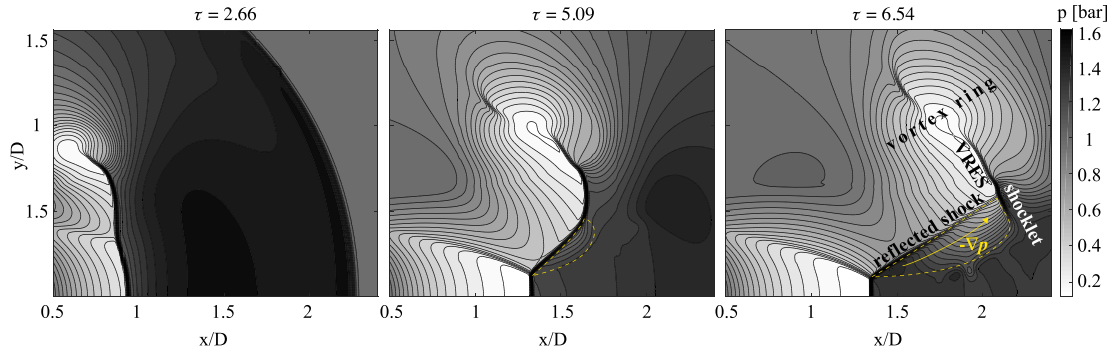

FIG. 10. Sequence of pressure contours determined from numerical simulations for a Riemann problem with Ms = 1.71. The yellow dashed line indicates the formation of a pressure gradient that potentially leads to the formation of the shocklet.

a portion of the reflected shock must become propagative; this upstream-propagating wave rapidly decays into an acoustic wave, in a manner analogous to the shock leakage process of jet screech [33]. The conversion of this part of the reflected shock into an upstream-propagating wave effectively terminates the second triple point [Fig. 9(e)]. While the second triple shock configuration and its corresponding slipline terminate, small vortex rings along the slipline separate from the triple point (TP_2), as shown in Fig. 9(d). Finally, the impingement point of the reflected shock upon the jet shear layer appears as a wavy line in the schlieren image, representing the rim of the first shock cell. Also evident in Fig. 9 is an interaction between the primary and second triple point configuration. The upper bound of the shocklet is the triple point, its lower bound is the sonic line associated with the internal shear layer generated by the first triple point. The shocklet undergoes deformation via interaction with the CRVRs generated along the primary slipline [Figs. 9(b)–9(d)] and the interaction produces lambda shocks close to the CRVRs [Fig. 9(b)]. Both the experimental and numerical data show a second triple point configuration.

B. A proposed mechanism for the formation of the second triple point

The formation of the second triple point in the transient jet has no equivalent in the steady jet, as visualized in Fig. 8. Thus, the explanation for its formation must lie inherently in the dynamics of a transient jet. The convection of the vortex ring and its associated shock structure is one such process, and the temporal variation in upstream flow conditions within the tube is another. In order to separate these processes, the numerical simulations were repeated with a constant inflow condition at the tube exit. Also, a different shock Mach number of Ms = 1.71 is chosen, to rule out the impact of the shock strength. The inflow conditions for the numerical simulations corresponds to the solution of the Riemann problem for a planar shock wave propagating at a constant speed corresponding to Ms = 1.71. The results are shown in Fig. 10, where the formation of the second triple point is clearly visible. Hence, this suggests that the transient interaction between the first triple point and the vortex ring are the likely explanation for the formation of the second triple point.

The consideration of the time series of pressure distributions shown in Fig. 10 demonstrates that unlike the steady jet counterpart, the reflected shock is nonstationary for a time before the formation of the second triple point. The reflected shock elongates and rotates, as the vortex ring and its embedded shock move farther downstream. As the reflected shock tilts toward the jet centerline, a strong pressure gradient parallel to the shock develops along its downstream face. This region of negative pressure gradient, from the jet core to the jet shear layer, is marked as $-\nabla p$ in Fig. 10. Unlike for a steady jet, this region of negative pressure gradient grows in size and strength with time for a transient jet. We suggest that it is the motion of the reflected shock, which results in a pressure

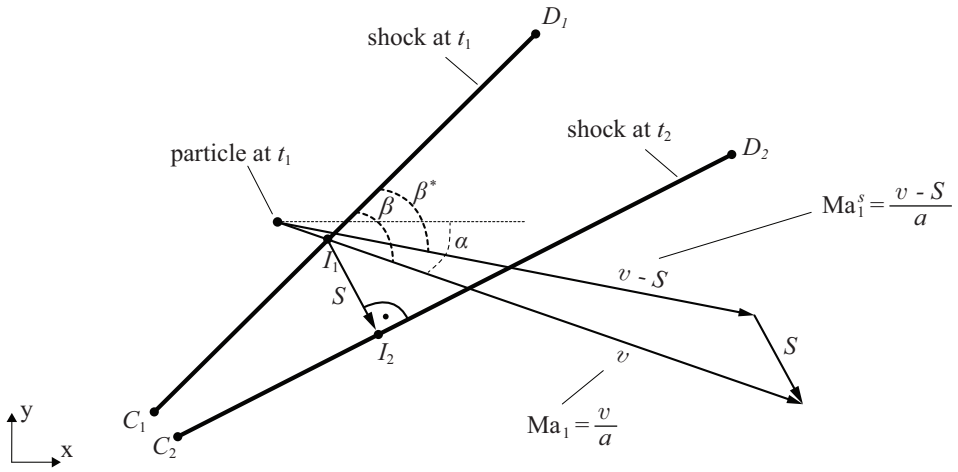

FIG. 11. Schematic illustration of the transient oblique shock (TOS) model. Shown are a transient shock wave at two time instances and the quantities used for the calculation of the postshock flow conditions of the particle at t_2.

gradient downstream of the reflected shock, that in turn leads to the formation of the shocklet and the second triple point. In the following we develop a model to evaluate this hypothesis.

1. Transient oblique shock model (TOS)

To test the hypothesis that it is the unsteady motion of the reflected shock that gives rise to the formation of the triple point, we develop a model for the effect of this motion. The model delivers the postshock flow conditions for a transient, rotating oblique shock wave based on the preshock flow conditions and the shock motion. The underlying assumption of the approach is that the moving shock wave can be treated as a quasisteady problem by converting the flow velocity into a reference frame that moves with the shock.

A schematic illustration of the problem is presented in Fig. 11. In a time period of $\Delta t = t_2 - t_1$ a shock wave moves from $\overline{C_1D_1}$ to $\overline{C_2D_2}$. The objective of the model is to determine the postshock condition for a particle upstream of the shock wave, which will be processed by the shock wave after a certain time. The particle at t_1 has already passed the shock wave at t_2, since the flow velocity v is higher than the corresponding shock velocity S.

A simple approach is used to estimate the shock velocity S. The intersection of v with $\overline{C_1D_1}$ is marked as a point I_1 in Fig. 11. A perpendicular line from I_1 to $\overline{C_2D_2}$ intersect with $\overline{C_2D_2}$ at a point I_2. The shock velocity S is approximated simply by the displacement of the shock $\overline{I_1I_2}$ over the time interval by $S = \frac{\overline{I_1I_2}}{\Delta t}$.

The determination of postshock properties for an oblique shock is an elementary gas-dynamics problem, solved by the simple application of the Rankine-Hugoniot equations. The problem here, however, involves a shock that is both translating and rotating. The proposed model is thus essentially an attempt to produce an appropriate coordinate transformation to allow the application of quasisteady one-dimensional conservation equations to a rotating shock. Therefore, the Mach number in the absolute reference $\mathrm{Ma}_1 = \frac{v}{a}$ must be converted into a reference frame that moves with the shock. Taking the shock velocity into account, the Mach number in the shock reference frame is simply $\mathrm{Ma}_1^s = \frac{v-S}{a}$. To apply the Rankine-Hugoniot equations for an oblique shock, the normal component of Ma_1^s is determined by considering the shock angle in the shock reference frame β^s. As shown in Fig. 11, β^* is the cross angle between $\overline{C_1D_1}$ and Ma_1^s. Assuming an infinitesimal $|\overline{I_1I_2}|$, the mean value of β and β^* is taken as the shock angle β^s. Hence, the normal Mach number in shock reference Ma_{n1}^s can be determined as $\mathrm{Ma}_{n1}^s = \mathrm{Ma}_1^s \sin\beta^s$. Finally, the postshock conditions

TABLE I. TOS results for $\tau = 2.66$ shown in Fig. 12(a).

	Input			Output				
	Ma_1	p_1	α	Ma^s_{n1}	Ma^s_1	β^s	S [m/s]	p_2 [bar]
x_1	2.22	0.43	9.7	1.60	1.62	79.9	188	1.2
x_2	2.24	0.43	10.8	1.60	1.64	78.5	188	1.2
x_3	2.28	0.4	12.5	1.63	1.68	76.2	188	1.2

are evaluated by applying the normal component of the Mach number in the Rankine-Hugoniot equations:

$$Ma_2^2 = \frac{1 + \frac{\gamma-1}{2}(Ma_1^s \sin\beta^s)^2}{\gamma(Ma_1^s \sin\beta^s)^2 - \frac{\gamma-1}{2}}, \tag{5}$$

$$\frac{p_2}{p_1} = 1 + \frac{2\gamma}{\gamma+1}\left[\left(Ma_1^s \sin\beta^s\right)^2 - 1\right], \tag{6}$$

$$\frac{\rho_2}{\rho_1} = \frac{(\gamma+1)\left(Ma_1^s \sin\beta^s\right)^2}{1 + (\gamma-1)\left(Ma_1^s \sin\beta^s\right)^2}, \tag{7}$$

$$\frac{T_2}{T_1} = \frac{p_2}{p_1}\frac{\rho_1}{\rho_2}. \tag{8}$$

Here p, ρ, and T are the pressure, density, and temperature, respectively. In the following section, this model is used to demonstrate the formation mechanism of the second triple point.

2. Formation mechanism of the triple point based on the TOS model

As previously stated, the formation of the secondary triple point must be linked to the transient evolution of the jet, as only the first triple point appears in steady-state underexpanded jets. The secondary triple point is made up of the reflected shock from the first triple point, the VRES, and the shocklet, as shown in Fig. 8(a). Of these, the first two have been discussed in the literature at some length; the shocklet is the component that has therefore gone undescribed. To establish why the shocklet forms, we apply the TOS model to the motion of the reflected shock, with a starting point well before the shocklet is observed. Initial observations suggest that the pressure gradient parallel to the downstream face of the reflected shock is likely linked to the shocklet's formation, thus we seek to test whether this pressure gradient is a result of the motion of the shock.

The application of the TOS model involves analysis of a series of discrete points parallel to the upstream face of the reflected shock (x_1 to x_n), as per Fig. 12. We use the early stages of evolution before the formation of the shocklet to test the validity of the model. Thus we start our analysis at $\tau = 2.66$, where the reflected shock and VRES are essentially a single contiguous shock wave [from TP_1 to O in Fig. 12(a)]. Three discrete points x_1 to x_3 are selected just upstream of the reflected shock for the TOS analysis. The changes in flow properties during passage through the shock wave are considered for particles originating at these points using the TOS model. To this end, the motion of the reflected shock is tracked for two snapshots ($\tau = 2.66$ and $\tau = 2.90$). A small time period of $\Delta\tau = 0.24$ is chosen for the TOS analysis, as an infinitesimal shock displacement is the underlying assumption of the model. The results of the TOS analysis are presented as several input and output parameters in Table I. Here the input parameters, Ma_1, p_1, α are the Mach number, the pressure, and the flow angle, respectively, extracted directly from the numerical results. The output parameters of the TOS analysis, Ma^s_{n1}, Ma^s_1, β^s, S, and p_2 are the normal Mach number in shock reference, the Mach number in shock reference, the shock angle, the shock velocity, and the pressure downstream of the reflected shock, respectively.

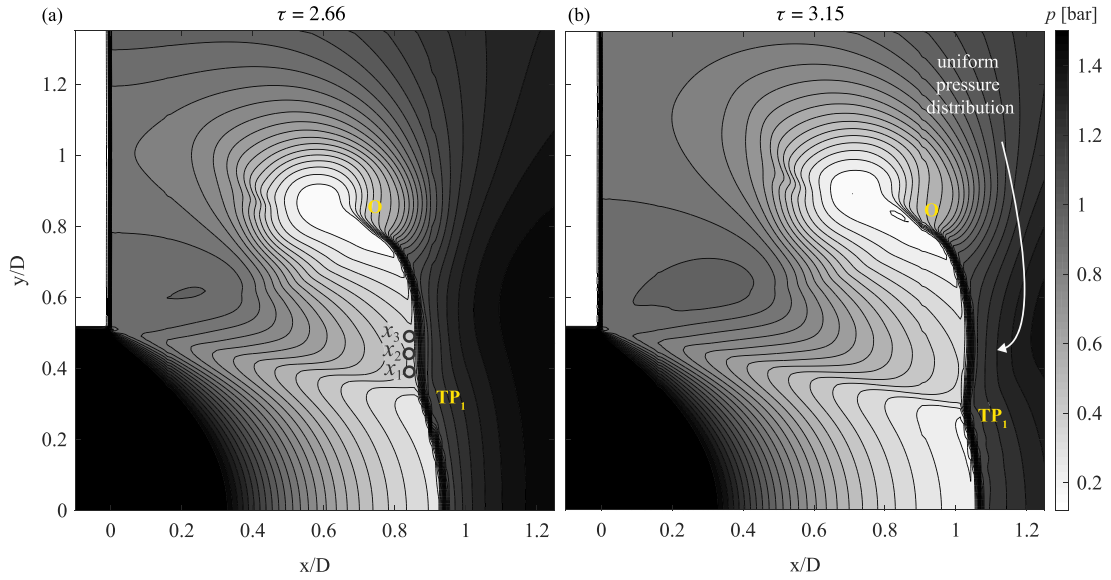

FIG. 12. (a) Pressure distribution at $\tau = 2.66$ as derived from the numerical simulations at constant inflow conditions with Ms $= 1.71$. TP_1 and O represent the first triple point and the tail of the VRES. The TOS model is applied for x_1, x_2, and x_3. The result of the TOS analysis is given in Table I. (b) Pressure distribution at $\tau = 3.15$ shows a uniform pressure distribution downstream of the reflected shock.

Figure 12(b) presents the pressure distribution based on the numerical simulation, shortly after the distribution in Fig. 12(a). This time interval $\Delta\tau = 0.48$ allows for the particle upstream of the reflected shock at $\tau = 2.66$ to be processed by the shock wave at $\tau = 3.15$. For the TOS analysis the calculated pressure downstream of the shock wave is given as p_2 in Table I. The results show a constant value of 1.2 bar for x_1, x_2, and x_3, i.e., a uniform pressure distribution. In accordance, the results from the numerical simulations confirm a uniform pressure distribution downstream of the reflected shock in Fig. 12(b). Hence, the predicted uniform pressure distribution downstream of the reflected shock based on the TOS analysis agrees qualitatively very well with the CFD results. This agreement sustains for the entire conducted analysis, as pointed out in the reminder of this section. Hence, the TOS model is considered as valid.

The pressure gradient is of course readily available from the numerical simulation; the purpose of the model is to determine the source of this gradient. According to Eq. (6), the pressure downstream of a moving shock, p_2, is a function of Ma^s_{n1} and p_1. While p_1 is fixed by the upstream flow conditions, Ma^s_{n1} can be highly affected by the displacement of the shock wave due to the shock propagation velocity S. Figure 13 illustrates the impact of the shock displacement on S. While an

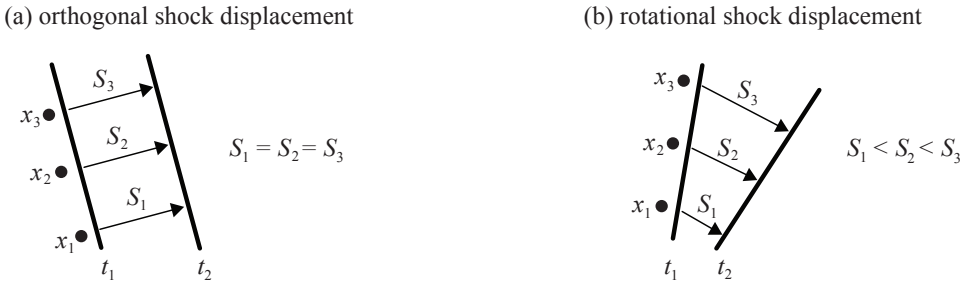

FIG. 13. Shock propagation velocity for (a) orthogonal and (b) rotational shock displacement.

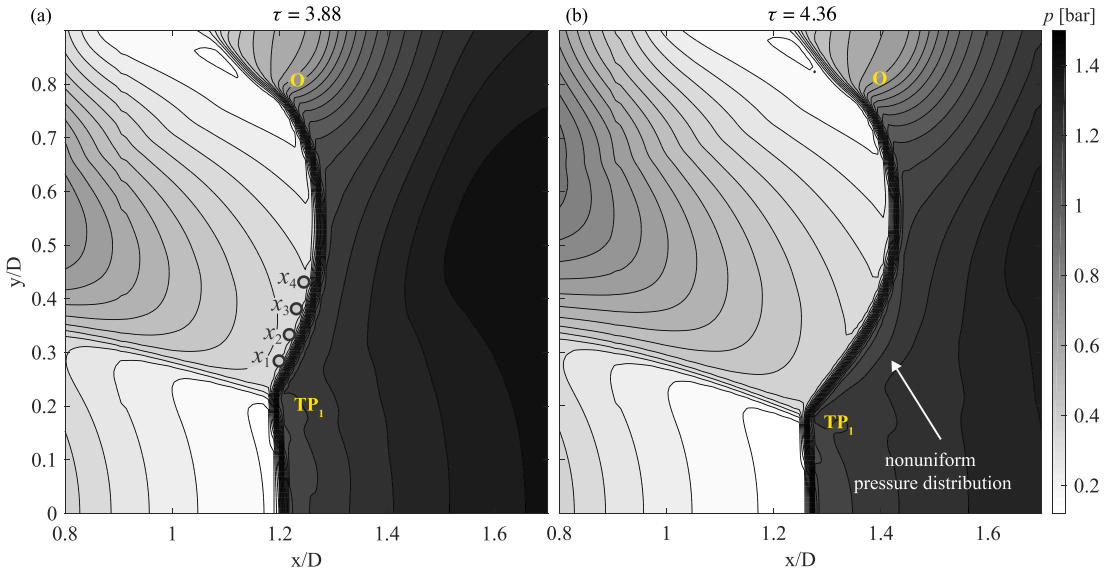

FIG. 14. (a) Pressure distribution at $\tau = 3.88$ as derived from the numerical simulations at constant inflow conditions with Ms = 1.71. TP_1 and O represent the first triple point and the tail of the VRES. The TOS model is applied for x_1 to x_4. The result of the TOS analysis is given in Table II. (b) Numerical pressure distribution at $\tau = 4.36$, showing a pressure gradient on the downstream face of the reflected shock.

orthogonal shock displacement results in an uniform S distribution [Fig. 13(a)], a rotational shock displacement leads into a gradient in S along the shock wave [Fig. 13(b)]. Here we seek to test whether the rotation of the shock is sufficient to explain the strength of the gradient observed in the pressure data.

3. Evolution of the pressure distribution downstream of the reflected shock

The pressure distribution downstream of the reflected shock is uniform up to $\tau = 3.15$ [Fig. 12(b)], since the motion of the reflected shock at this time point is primarily translation rather than rotation; this translational motion is indicated by the constant S distribution in Table I. However, as the vortex ring and its embedded shock translate farther downstream ($t > 2.66$), and pass the Mach disk [Fig. 14(a)], the inner part of the reflected shock begins to tilt. The TOS model is applied to four discrete points upstream of the tilted part of the reflected shock, as shown in Fig. 14(a). The results of the TOS analysis for x_1 to x_4 are shown in Table II. The model suggests a decreasing downstream pressure p_2 from $x_1 \rightarrow x_4$. Figure 14(b) exhibits the pressure field obtained from the numerical simulation a short time later, at $\tau = 4.36$. In accordance with the results of the TOS analysis, a nonuniform pressure distribution can be observed downstream of the reflected shock.

TABLE II. TOS results for $\tau = 3.88$, shown in Fig. 14(a).

	Input			Output					
	Ma_1	p_1 [bar]	α	Ma^s_{n1}	Ma^s_1	β^s	S [m/s]	$\frac{p_2}{p_1}$	p_2 [bar]
x_1	2.33	0.37	−1.3	1.81	1.97	66.6	123	3.65	1.35
x_2	2.36	0.36	0.2	1.77	1.97	64.3	134	3.51	1.27
x_3	2.40	0.35	2.4	1.73	1.97	61	149	3.33	1.16
x_4	2.44	0.33	4.2	1.69	1.99	58.3	161	3.18	1.06

The aforementioned results indicate that the pressure gradient observed in the simulation data can be caused purely by the rotation of the oblique shock. The next step is to determine a more exact mechanism. Therefore, we consider next the spatial distribution of the flow between the jet core and the jet shear layer [$x_1 \rightarrow x_4$ in Fig. 14(a)]. According to Table II there is a declining pressure ratio $\frac{p_2}{p_1}$ from $x_1 \rightarrow x_4$, as $\frac{p_2}{p_1}(x_1) > \frac{p_2}{p_1}(x_2) > \frac{p_2}{p_1}(x_3) > \frac{p_2}{p_1}(x_4)$, which results in a pressure gradient downstream of the shock wave. According to Eq. (6), the pressure ratio $\frac{p_2}{p_1}$ is a function of Ma_1^s and $\sin\beta^s$. The term $\sin\beta^s$ can be linearized to β^s under the small-angle approximation. Therefore, in the context of the model, the negative pressure ratio from $x_1 \rightarrow x_4$ can be ascribed to either decreasing Ma_1^s, decreasing β^s, or both. While Ma_1^s remains almost uniform from $x_1 \rightarrow x_4$, a significant decrease for β^s is evident, as shown in Table II. Consequently, if the mechanism leading to the distribution of Ma_1^s and β^s is known, the formation of the nonuniform pressure region downstream of the reflected shock can likewise be determined.

To elucidate the mechanism responsible for the distribution of Ma_1^s and β^s, we consider the displacement of the reflected shock; the corresponding shock propagation velocity S is given in Table II. The significant increase of the shock velocity from $x_1 \rightarrow x_4$ indicates a strong tilting motion of the shock wave. The increase in the shock velocity S leads inherently to a decrease in the relative Mach number in shock reference Ma_1^s, as $\mathrm{Ma}_1^s = \mathrm{Ma}_1 - \frac{S}{a}$. This correlation can also be recognized visually from Fig. 11, which illustrates a tilting shock wave. As shown in Table II, the approaching Mach number Ma_1 increases from $x_1 \rightarrow x_4$, which has the opposite effect on Ma_1^s, as can be seen from the equation above. However, the uniform distribution of Ma_1^s over $x_1 \rightarrow x_4$ indicates, that the increase of S compensates for the increase of Ma_1. Consequently, the uniform distribution of Ma_1^s is caused by the pronounced increase of S, i.e., due to the strong tilting of the reflected shock. Moreover, the tilting motion of the reflected shock also affects the shock angle β. The rotation of the shock results in an inherent reduction of the shock angle ($\beta^s < \beta$) as can be seen in Fig. 11. As shown in Table II, β^s decreases from $x_1 \rightarrow x_4$. Consequently, the tilting shock wave results in a negative pressure gradient by reducing Ma_1^s and β^s from $x_1 \rightarrow x_4$. Additionally, a small decrease in upstream pressure p_1 and an increase in α supports the formation of the pressure gradient by simply decreasing β and therefore β^s (Fig. 11). Hence, these results suggest that the tilting motion of the reflected shock and the alteration of the flow angle upstream of this shock are the primary mechanisms responsible for the reduction of Ma_1^s and β^s, and thereby for the formation of the pressure gradient downstream of the reflected shock.

At later times, the vortex ring propagates farther downstream (see Figs. 15 and 16). Thus the disparity in the angle dictated by the first triple point and that required by the VRES increases. Hence, a kink forms gradually within the shock wave (marked as K in Figs. 15 and 16), separating the reflected shock and the VRES. A dotted line in Figs. 15 and 16, originating from K separates two regions A and B, downstream of the reflected shock and the VRES, respectively. The TOS model is applied to three points for each region (Figs. 15 and 16). The corresponding results are presented in Tables III and IV. We first evaluate the results for region A, before proceeding further with region B. The comparison of the CFD pressure distribution at $\tau = 3.88$ to $\tau = 6.30$, shown in Figs. 14–16, exhibits an increases of the gradient in $-\nabla p$ region with time. In conformity with the CFD pressure distribution, the TOS results predict an increase of the pressure gradient with time downstream of the reflected shock; the pressure gradient $p_2(x_1)/p_2(x_4)$ increases by approximately 8% between $\tau = 3.88$ and $\tau = 4.60$ and by 86% from $\tau = 4.60$ to $\tau = 5.81$ (Tables II to IV). A comparison of the shock velocity S indicates that the tilting motion of the reflected shock becomes significantly stronger as $S(x_4)/S(x_1)$ increases with time. The quantity $S(x_4)/S(x_1)$ increases by approximately 4% from $\tau = 3.88$ to $\tau = 4.60$ and 1800% from $\tau = 4.60$ to $\tau = 5.81$ (Tables II to IV). For the reasons indicated above, the strong tilting results in a stronger compression, as $\Pi_{\tau=5.81} > \Pi_{\tau=4.60} > \Pi_{\tau=3.88}$, where $\Pi = \frac{p_2}{p_1}(x_1)/\frac{p_2}{p_1}(x_4)$. Hence, the gradient of the $-\nabla p$ region increases with time. The tilting of the shock is not the only mechanism by which the $-\nabla p$ changes as a function of time: there is also a small increase in the pressure gradient from $x_1 \rightarrow x_4$ upstream of the reflected shock, as $p_1(x_1)/p_1(x_4)$ increases 11%, 17%, and 30% between $\tau = 3.88$, $\tau = 4.60$

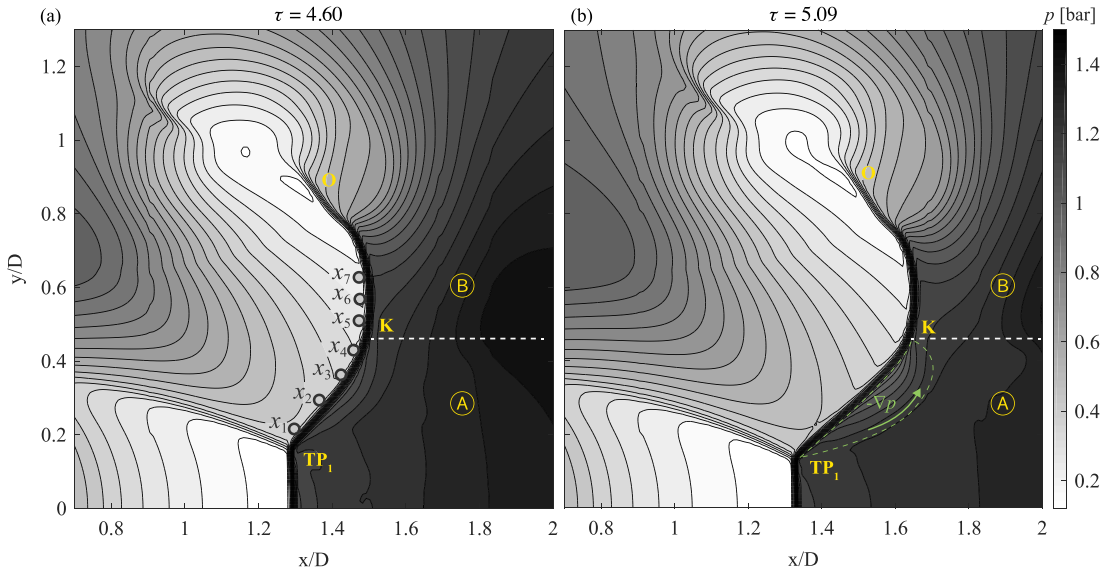

FIG. 15. (a) Pressure distribution at $\tau = 4.60$ as derived from the numerical simulations at constant inflow conditions with Ms = 1.71. TP_1 and O represent the first triple point and the tail of the VRES. The TOS model is applied for x_1 to x_7. The result of the TOS analysis is given in Table III. (b) Pressure distribution at $\tau = 5.09$.

and $\tau = 5.81$. Similarly, there is an increase in the flow angle α of 5.5°, 8.3°, and 16.6°, respectively. Nevertheless, the contribution of these mechanisms is relatively small compared to the gradients induced by the motion of the shock; the tilting of the reflected shock is the main reason for a pronounced pressure gradient downstream of the reflected shock wave.

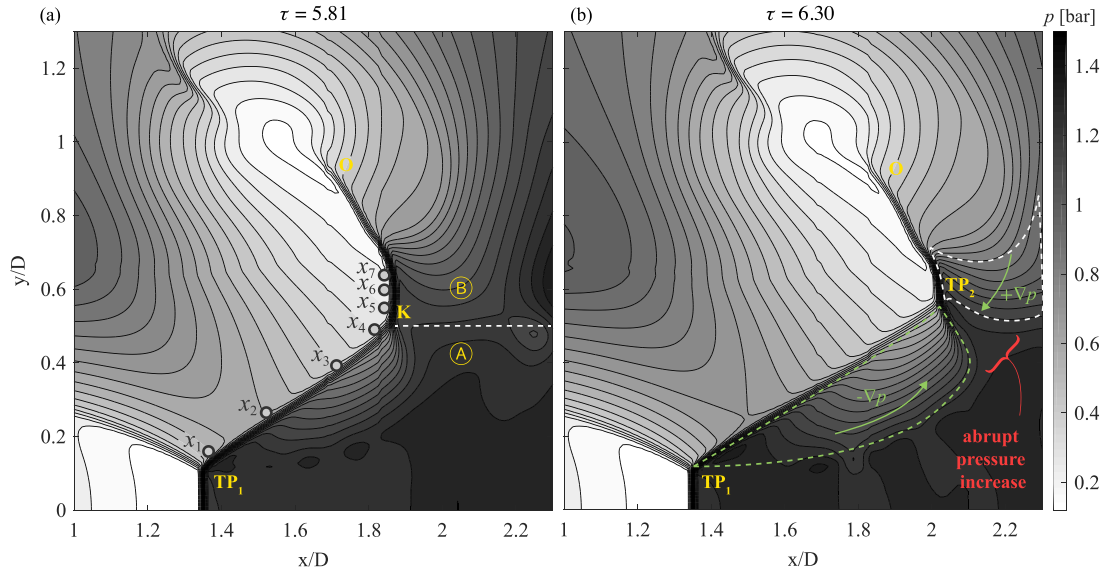

FIG. 16. (a) Pressure distribution at $\tau = 5.81$ as derived from the numerical simulations at constant inflow conditions with Ms = 1.71. TP_1 and O represent the first triple point and the tail of the VRES. The TOS model is applied for x_1 to x_7. The result of the TOS analysis is given in Table IV. (b) Pressure distribution at $\tau = 6.30$.

TABLE III. TOS results for $\tau = 4.60$, shown in Fig. 15(a).

	Input			Output					
	Ma_1	p_1 [bar]	α	Ma^s_{n1}	Ma^s_1	β^s	S [m/s]	$\frac{p_2}{p_1}$	p_2 [bar]
x_1	2.23	0.42	−7.9	1.74	2.04	58.5	70	3.35	1.40
x_2	2.29	0.41	−4.3	1.68	2.07	54.1	81	3.13	1.27
x_3	2.37	0.37	−1.0	1.64	2.14	49.9	91	2.95	1.09
x_4	2.4	0.35	0.4	1.61	2.17	48.1	95	2.87	1.02
x_5	2.57	0.29	5.1	1.96	2.00	78.1	169	4.31	1.24
x_6	2.63	0.27	7.1	1.97	2.04	75.3	177	4.36	1.16
x_7	2.73	0.23	10.2	2.06	2.07	83.5	185	4.79	1.12

As seen by the TOS model and the numerical simulations both the size and strength of the $-\nabla p$ region grow with time. The flow evolution from $\tau = 4.60$ to $\tau = 5.09$ (Fig. 15) shows that the reflected shock (TP_1-K) elongates with time. Consequently, the $-\nabla p$ region covers a wider area downstream of the reflected shock, as shown in Fig. 15(b). However, the $-\nabla p$ region occurs only downstream of the reflected shock, from TP_1 to K, and ends at the A-B interface. These observations based on the CFD results agree again with the results from the TOS analysis, shown in Table III; the $-\nabla p$ region elongates from x_1 to x_4 [Fig. 15(b)], as the pressure p_2 decreases from $x_1 \rightarrow x_4$, but there is a positive pressure gradient from A to B at their interface, as $p_2(x_5) > p_2(x_4)$ shown in Table III. This positive pressure gradient is the origin of a new shock wave, the shocklet, as will be discussed in the following.

4. Evolution of the pressure distribution downstream of the VRES

The formation of a positive pressure gradient from A to B can be further examined by considering the TOS results for the region B given in Table III. As shown in Fig. 15 and also indicated by the shock velocity S for x_5 to x_7 in Table III, the VRES tilts barely but translates predominantly in the axial direction. This is also the case for the approaching flow in region B, indicated by small α for x_5 to x_7 in Table III. The combination of the vertical shock, moving in the axial direction and small α results in significantly large shock angles β, leading to high-pressure ratios $\frac{p_2}{p_1}$ in region B (x_5 to x_7 in Table III). Hence, the pressure in region B is higher than A in the vicinity of their interfaces; there is a positive pressure gradient from A to B.

Figure 16(a) shows the flow evolution at a later stage in time for $\tau = 5.81$ and $\tau = 6.30$. The corresponding TOS results for x_1 to x_7 at $\tau = 5.81$ are given in Table IV. The evolution of the $-\nabla p$ region can be evaluated for an extended period of time based on the pressure

TABLE IV. TOS results for $\tau = 5.81$, shown in Fig. 16(a).

	Input			Output					
	Ma_1	p_1 [bar]	α	Ma^s_{n1}	Ma^s_1	β^s	S [m/s]	$\frac{p_2}{p_1}$	p_2 [bar]
x_1	2.09	0.46	−14.3	1.61	2.09	50.6	2	2.87	1.33
x_2	2.05	0.59	−9.2	1.40	2.01	44.3	20	2.13	1.26
x_3	2.31	0.42	−2.1	1.31	2.24	35.9	39	1.84	0.78
x_4	2.52	0.32	2.3	1.24	2.43	30.6	51	1.62	0.52
x_5	2.65	0.27	4.7	2.06	2.08	82.6	168	4.81	1.28
x_6	2.73	0.24	6.6	2.09	2.12	80.0	178	4.91	1.18
x_7	2.79	0.22	8.3	2.10	2.15	77.7	186	4.98	1.09

distribution $\tau = 4.60$ to $\tau = 6.30$ shown in Figs. 15 and 16. It is evident that the $-\nabla p$ region enlarges further and its pressure gradient increases with time. Similar to the $-\nabla p$, the pressure gradient in region B also becomes more distinctive with time. The TOS results confirm again the CFD results, showing an increase in pressure gradient with time in both regions A and B, as $[p_2(x_1)/p_2(x_4)]_{\tau=5.81} > [p_2(x_1)/p_2(x_4)]_{\tau=4.60} > [p_2(x_1)/p_2(x_4)]_{\tau=3.88}$ and $[p_2(x_5)/p_2(x_7)]_{\tau=5.81} > [p_2(x_5)/p_2(x_7)]_{\tau=4.60}$. Both, the CFD and the TOS results show the pressure gradients in both regions A and B increase with time. The pressure gradient downstream of the reflected shock in region A, from TP_1 to K, is negative. In contrast, there is a positive pressure gradient in region B, from O to K, as marked in Fig. 16(b). Hence, the increase in the pressure gradient in A and B results in higher pressure ratio along the A-B interface. Based on the TOS results, shown in (Tables III and IV), the pressure ratio $p_2(x_5)/p_2(x_4)$ increases from $\tau = 4.60$ to $\tau = 5.81$ by 102%. The result of this evolution can be observed in Fig. 16(b). The negative pressure gradient from TP_1 to K and the positive pressure gradient from O to K lead to an increase of the pressure within a very small region, between the $-\nabla p$ and $+\nabla p$ regions (Fig. 16). As both pressure gradients intensify with time, an abrupt pressure change occurs at the intersection of these regions. Consequently, the abrupt pressure rise leads to the formation of a new shock wave.

Now the formation of the second triple point and the shocklet can be summarized. The abrupt pressure rise, which necessitates the formation of the shocklet, is induced by the evolution of the pressure distribution downstream of the reflected shock. The pressure downstream of the reflected shock is highly affected by the displacement of this shock wave over time. This is due to two main facts: first, the flow velocity upstream of the reflected shock is higher than the propagation velocity of the shock wave. Consequently, the flow downstream of the shock wave is driven by the prior motion of this shock wave. Second, the displacement of the reflected shock is nonuniform along the shock wave with the reflected shock tilting toward the jet center line, driven by the convection of the vortex ring. As the vortex ring moves farther away from the first triple point, the angle dictated by the first triple point and the one required from the part of the shock wave, which is embedded in the vortex ring (VRES), differ. Hence, a kink appears within the shock wave, which separates the reflected shock from the VRES. Due to the rotational motion of the reflected shock, a negative pressure gradient arises in the radial direction, from the jet core to the jet boundary. This pressure gradient increases with time, as the reflected shock extends and rotates further. Hence, the pressure becomes relatively low downstream of the reflected shock. Its minimum value occurs right below the kink. In contrast, the pressure downstream of the VRES is relatively high. This is mainly due to the nearly axial displacement of the shock wave, leading into large shock angles along the wave. Consequently, the pressure above the kink becomes much higher than below the kink, resulting in an abrupt pressure rise. As the abrupt pressure rise leads into the formation of a new shock wave (shocklet), the kink becomes a triple point. Finally, the shocklet, the reflected shock and the VRES forms the second triple point configuration of the transient supersonic starting jet.

IV. CONCLUSION

The dynamic evolution of a starting transient supersonic flow has been studied by utilizing numerical simulations and high-resolution high-speed schlieren measurements. It has been shown that for a sufficiently strong leading shock, the interaction of the secondary shock system with the VRES will result in the formation a second triple point. Experimental evidence is provided for the presence of a second triple shock configuration along with a shocklet between the reflected shock and the slipstream, which results in the formation of further KH vortices.

A simple model was developed based on one-dimensional shock relations, in an attempt to determine the source of pressure distributions in the flow which could give rise to the shocklet. A comparison of the output of this model to the results of the numerical simulations suggested that the shocklet forms due to a different mechanism than the classical Mach reflection responsible for the first triple point.

The formation of the second triple point is initiated by the transient motion of the reflected shock, which is induced by the convection of the vortex ring. As the vortex ring overtakes the Mach disk, the part of the reflected shock next to the core begins to tilt, while the outer part of the shock propagates almost uniformly farther downstream. Consequently, a kink appears in the reflected shock, separating the reflected shock from the vortex ring embedded shock. Downstream of the reflected shock a negative pressure gradient in radial direction occurs, which is caused by the rotational motion of the reflected shock wave. This pressure gradient region grows in size and strength, as the reflected shock elongates and rotates further. Hence, the pressure just below the kink decreases with time. In contrast, the pressure downstream of the vortex ring embedded shock, particularly in the vicinity of the kink, is relatively high. Therefore, an abrupt pressure rise along the kink takes place. The kink becomes a triple point, while the abrupt pressure rise results in the formation of a new shock wave.

ACKNOWLEDGMENTS

The authors gratefully acknowledge support by the Deutsche Forschungsgemeinschaft (DFG) as part of the Collaborative Research Center SFB 1029 "Substantial efficiency increase in gas turbines through direct use of coupled unsteady combustion and flow dynamics." The authors also thank Dr. N. Nikiforakis's team at the Laboratory for Scientific Computing, Cambridge University, for the generous access to LSC_AMR, their Cartesian grid–cut cell–compressible flow solver. The authors also gratefully acknowledge support by the ARC DP190102220.

[1] B. W. Skews, The shape of a diffracting shock wave, J. Fluid Mech. **29**, 297 (1967).
[2] K. Takayama and H. Sekiguchi, Formation and diffraction of spherical shock waves in a shock tube, Rep. Inst. High Speed Mech., Tohoku Univ., Sendai, Japan, Rept. **43**, 89 (1981).
[3] M. Sun and K. Takayama, Vorticity production in shock diffraction, J. Fluid Mech. **478**, 237 (2003).
[4] T. V. Bazhenova, L. G. Gvozdeva, and M. A. Nettleton, Unsteady interactions of shock waves, Prog. Aerospace Sci. **21**, 249 (1984).
[5] H. Kleine, C. V. Le, K. Takehara, and T. G. Etoh, Development of shock-vortex systems emitted from an open shock tube, in *Proceedings of the 29th International Congress on High-Speed Imaging and Photonics, Iwate Medical University, Morioka, Japan*, pp. C-06-1-C-06-6, presented at 29th Int. Congr. High Speed Imaging and Photonics, Morioka, Japan, 20–24 September 2010.
[6] J. J. P. Fernández and J. Sesterhenn, Compressible starting jet: Pinch-off and vortex ring–trailing jet interaction, J. Fluid Mech. **817**, 560 (2017).
[7] R. Ishii, H. Fujimoto, N. Hatta, and Y. Umeda, Experimental and numerical analysis of circular pulse jets, J. Fluid Mech. **392**, 129 (1999).
[8] C. L. Dora, T. Murugan, S. De, and D. Das, Role of slipstream instability in formation of counter-rotating vortex rings ahead of a compressible vortex ring, J. Fluid Mech. **753**, 29 (2014).
[9] J. H. Arakeri, D. Das, A. Krothapalli, and L. Lourenco, Vortex ring formation at the open end of a shock tube: A particle image velocimetry study, Phys. Fluids **16**, 1008 (2004).
[10] H. Zare-Behtash, K. Kontis, and N. Gongora-Orozco, Experimental investigations of compressible vortex loops, Phys. Fluids **20**, 126105 (2008).
[11] M. Rezay Haghdoost, D. Edgington-Mitchell, C. O. Paschereit, and K. Oberleithner, High-speed Schlieren and particle image velocimetry of the exhaust flow of a pulse detonation combustor, AIAA J. (2020), doi:10.2514/1.J058540.
[12] H. Zare-Behtash, K. Kontis, N. Gongora-Orozco, and K. Takayama, Shock wave-induced vortex loops emanating from nozzles with singular corners, Exp. Fluids **49**, 1005 (2010).
[13] T. Murugan, S. De, C. L. Dora, and D. Das, Numerical simulation and PIV study of compressible vortex ring evolution, Shock Waves **22**, 69 (2012).

[14] E. Franquet, V. Perrier, S. Gibout, and P. Bruel, Free underexpanded jets in a quiescent medium: A review, Prog. Aerospace Sci. **77**, 25 (2015).
[15] H. G. Hornung, Oblique shock reflection from an axis of symmetry, J. Fluid Mech. **409**, 1 (2000).
[16] D. Edgington-Mitchell, D. R. Honnery, and J. Soria, The underexpanded jet Mach disk and its associated shear layer, Phys. Fluids **26**, 096101 (2014).
[17] M. P. Friedman, A simplified analysis of spherical and cylindrical blast waves, J. Fluid Mech. **11**, 1 (1961).
[18] F. K. Elder Jr. and N. De Haas, Experimental study of the formation of a vortex ring at the open end of a cylindrical shock tube, J. Appl. Phys. **23**, 1065 (1952).
[19] M. Brouillette and C. Hebert, Propagation and interaction of shock-generated vortices, Fluid Dyn. Res. **21**, 159 (1997).
[20] H. Kleine, C. V. Le, K. Takehara, and T. G. Etoh, Time-resolved visualization of shock–vortex systems emitted from an open shock tube, J. Visualization **13**, 33 (2010).
[21] H.-H. Zhang, N. Aubry, Z.-H. Chen, W.-T. Wu, and S. Sha, The evolution of the initial flow structures of a highly under-expanded circular jet, J. Fluid Mech. **871**, 305 (2019).
[22] A. M. Hurst, S. Carter, D. Firth, A. Szary, and J. VanDeWeert, Real-time, advanced electrical filtering for pressure transducer frequency response correction, in *Proceedings of the ASME Turbo Expo 2015: Turbine Technical Conference and Exposition. Volume 6: Ceramics; Controls, Diagnostics and Instrumentation; Education; Manufacturing Materials and Metallurgy; Honors and Awards, Montreal, Quebec, Canada, 15–19 June 2015*, Paper No. V006T05A015 (ASME Digital Collection, 2015).
[23] C. E. Willert, D. M. Mitchell, and J. Soria, An assessment of high-power light-emitting diodes for high frame rate schlieren imaging, Exp. Fluids **53**, 413 (2012).
[24] E. F. Toro, *Riemann Solvers and Numerical Methods for Fluid Dynamics* (Springer, Berlin, 2009).
[25] R. Klein, K. R. Bates, and N. Nikiforakis, Well-balanced compressible cut-cell simulation of atmospheric flow, Philos. Trans. R. Soc. London A **367**, 4559 (2009).
[26] N. Gokhale, N. Nikiforakis, and R. Klein, A dimensionally split Cartesian cut cell method for hyperbolic conservation laws, J. Comput. Phys. **364**, 186 (2018).
[27] M. J. Berger and J. Oliger, Adaptive mesh refinement for hyperbolic partial differential equations, J. Comput. Phys. **53**, 484 (1984).
[28] M. P. Burke, M. Chaos, Y. Ju, F. L. Dryer, and S. J. Klippenstein, Comprehensive H_2/O_2 kinetic model for high-pressure combustion, Int. J. Chem. Kinet. **44**, 444 (2011).
[29] P. Berndt, R. Klein, and C. O. Paschereit, A kinetics model for the shockless explosion combustion, in *Proceedings of the ASME Turbo Expo 2016: Turbomachinery Technical Conference and Exposition. Volume 4B: Combustion, Fuels and Emissions, Seoul, South Korea, 13–17 June 2016*, Paper No. V04BT04A034 (ASME, 2016).
[30] A. Harten, P. D. Lax, and B. van Leer, On upstream differencing and Godunov-type schemes for hyperbolic conservation laws, SIAM Rev. **25**, 35 (1983).
[31] B. Einfeldt, On Godunov-type methods for gas dynamics, SIAM J. Numer. Anal. **25**, 294 (1988).
[32] P. Berndt, On the use of the HLL-scheme for the simulation of the multi-species Euler equations, in *Finite Volumes for Complex Applications VII—Elliptic, Parabolic and Hyperbolic Problems*, Springer Proceedings in Mathematics & Statistics, Vol. 78, edited by J. Fuhrmann, M. Ohlberger, and C. Rohde (Springer, Cham, 2014), pp. 809–816.
[33] D. Edgington-Mitchell, Aeroacoustic resonance and self-excitation in screeching and impinging supersonic jets—A review, Intl. J. Aeroacoustics **18**, 118 (2019).

4.2 Publication II

AIAA JOURNAL
Vol. 58, No. 8, August 2020

High-Speed Schlieren and Particle Image Velocimetry of the Exhaust Flow of a Pulse Detonation Combustor

Mohammad Rezay Haghdoost*
Technical University of Berlin, D-10623 Berlin, Germany
Daniel Edgington-Mitchell†
Monash University, Clayton, Victoria 3800, Australia
and
Christian Oliver Paschereit‡ and Kilian Oberleithner§
Technical University of Berlin, D-10623 Berlin, Germany

https://doi.org/10.2514/1.J058540

The exhaust flow of a pulse detonation combustor (PDC) is investigated for different operating conditions. The PDC consists of two units: the deflagration to detonation transition section, and the exhaust tube with a straight nozzle. High-speed high-resolution schlieren images visualize the shock dynamics downstream of the nozzle. The flow dynamics during one full PDC cycle is examined via high-speed particle image velocimetry. A well-suited solid tracer particle for supersonic reactive flow is determined in a preliminary study to minimize the PIV measurement error. The investigated operating conditions of the PDC differ in fill fraction, which is the percentage of the tube filled with a reactive mixture. With increasing fill fraction, the flow features grow in size and strength as the propagation velocity of the leading shock increases. The blowdown process of the PDC is characterized by several exhaust and suction phases. An increase in the fill fraction results in a stronger first exhaust phase, whereas the subsequent suction and exhaust phases remain almost unaffected.

Nomenclature

D	=	pulse detonation combustor exhaust tube diameter
D_N	=	Nozzle exit diameter
M	=	flow Mach number
Ms	=	shock Mach number
t	=	time
u	=	flow velocity
$u_{\min/\max}$	=	velocity minima or maxima
$\dot{V}(t)$	=	volume flux
x, y, z	=	laboratory Cartesian coordinate system
α	=	schlieren mirror offset angle
ρ	=	density
τ_p	=	particle relaxation time
Φ	=	equivalence ratio

I. Introduction

PRESSURE gain combustion (PGC) is a well-established concept with the potential to drastically increase the efficiency of gas turbines. Detonation-based approaches have received significant attention in recent years because even a small increase in total pressure across the combustor leads to a substantial increase in cycle efficiency. The thermodynamic benefit of the PGC technology is captured by the idealized Humphrey cycle, which replaces the isobaric Brayton cycle used to model conventional gas turbines.

There are several approaches to realize PGC: rotating detonation engine [1], resonant pulse combustor [2], and pulse detonation engine (PDE) [3,4], all of which have been the focus of research in recent decades. Among the various designs for PDE systems that have been proposed, the hybrid PDE is one of the more promising configurations [5]. Hybrid here refers to the integration of an annular array of pulse detonation combustor (PDC) tubes in a gas turbine engine, replacing the conventional combustion chambers.

The PDC cycle is composed of several phases. Initially, the detonation tube is filled with a detonatable mixture. The mixture is then ignited. A deflagration front propagates through the tube until it transitions to a detonation wave. Combustion products exit the tube after the detonation wave leaves the open end of the tube. Depending on the PDC design and operating condition, no or several suction phases may occur. In the final phase, the tube is purged, enabling the reinitialization of the next cycle.

One of the main challenges for implementing a PDC in a gas turbine is maintaining reliable operation of the turbine components. Excessively high temperatures, the presence of shocks, and high-pressure and -temperature fluctuations produced by the inherent unsteady combustion process are undesirable for both the compressor upstream and the turbine downstream of the PDC. In the work of Xisto et al. [6] a PDC–turbine system is investigated, revealing that the mismatch between the transient inlet flow conditions of the rotor and the constant blade speed results in a significant amount of losses. In their study, the PDC was directly attached to the turbine without any additional devices in between. If the PDC is not carefully integrated with the turbine components, these phenomena could easily eliminate any potential gain in cycle efficiency provided from the PGC [7]. One possible approach for the coupling of PDCs and a downstream turbine would be using shape-optimized devices. Modifying the turbine blades to account for supersonic inlet flow is one possible approach [8]. Also, using an additional device such as a plenum chamber between the PDCs and the turbine is currently the subject of research [9]. The main purpose of this device is to minimize the turbine inlet flow fluctuations. However, to design such a device, the detailed knowledge of the flow dynamics in the PDC exhaust is crucial.

The basic feasibility of connecting a PDC to a conventional axial turbine has been demonstrated by different research groups. In the study performed by Rasheed et al. [5] at the General Electric Company's facility, eight PDC tubes were operated up to 30 Hz to drive a

Presented as Paper 2019-1512 at the AIAA Scitech 2019 Forum, San Diego, CA, January 7–11, 2019; received 30 April 2019; revision received 26 September 2019; accepted for publication 30 October 2019; published online 12 June 2020.

*Ph.D. Student, Laboratory for Flow Instabilities and Dynamics, Institute of Fluid Dynamics and Technical Acoustics.

†Senior Lecturer, Laboratory of Turbulence in Aerospace and Combustion, Department of Mechanical and Aerospace Engineering.

‡Professor, Chair of Fluid Dynamics, Institute of Fluid Dynamics and Technical Acoustics.

§Professor, Laboratory for Flow Instabilities and Dynamics, Institute of Fluid Dynamics and Technical Acoustics.

single-stage turbine. Neither the coupling of the PDC with the turbine nor the turbine itself was optimized for the PDC application. Nevertheless, the PDC-fired operation showed a slight performance benefit when compared to the steady performance. In a study at the University of Cincinnati, the performance of an axial turbine with six PDC tubes was investigated. Glaser et al. [10] conducted performance measurements for both a constant-pressure combustor-driven turbine and for the PDC–turbine case. It was found that the performance of the PDC-driven turbine was comparable to that of a constant-pressure combustor-driven turbine across its operating map. They further showed that an increase in fill fraction, which is the percentage of the tube filled with a reactive mixture, causes a decrease in turbine efficiency. The mechanism responsible for this decrease in efficiency was not determined.

To develop an efficient hybrid PDE, the coupling of the PDC and the turbine needs to be understood in detail. For this purpose, the knowledge of the highly unsteady exhaust flow of the PDC tube is crucial. This has been the subject of a number of research efforts in the last decades [11–16]. Among these, Allgood et al. [13] investigated the blowdown process of an overfilled PDC tube using a shadowgraph technique. They visualized the dynamic evolution of the exhaust flow for straight and convergent nozzles. Glaser et al. [17] performed similar shadowgraph visualizations for different equivalence ratios and fill fractions. Despite limited image resolution, they were able to detect some of the flow features, such as small vortices and the corresponding slipstream within the primary vortex ring. Opalski et al. [16] studied the exhaust flow of an overfilled PDC quantitatively via particle image velocimetry (PIV). They characterized the transient flowfield based on ensemble-averaged velocity fields. Their data showed a short duration of a higher-velocity outlet flow of about 4 ms, where a peak axial velocity along the tube axis centerline of 1880 m/s was measured. Overall, these previously conducted experiments emphasized the highly unsteady nature of the flowfield exiting the PDC tubes, which poses significant challenges on experimental techniques to reveal the flow physics involved.

With the aim to manipulate the unsteadiness of the PDC exhaust flow and to improve the overall operability, different parameters and geometrical variations of the PDC have been investigated. By using an ejector downstream of the PDC, Opalski et al. [16] were able to reduce the unsteadiness of the exhaust flow successfully for an overfilled configuration. Allgood et al. [18] observed the performance of the ejector used in their study to be sensitive to the inlet geometry as well as its axial position relative to the exhaust plane of the PDC. Moreover, the impact of the fill fraction on the PDE performance has been the subject of research in some detail [13,19,20]. Thereby, an increase in fuel specific impulse with smaller fill fraction was shown numerically [19] and experimentally [20]. Although there are some performance measurements for different fill fractions and a limited number of studies on the exhaust flow of the PDC, a detailed experimental study on the impact of fill fraction on the exhaust flow is missing. Moreover, very little attention has been paid to the impact of the fill fraction on the evolution of the exhaust flow, which is important for the coupling with the turbine.

In the current study, a series of schlieren and PIV measurements are conducted at the outlet of a PDC for various operating conditions. The operating conditions differ primarily by the fill fraction, which is one of the main controlling parameters for the PDC cycle. The recorded high-resolution high-speed data allow for a detailed investigation of the exhaust flow. The shock dynamics at the initial stage of the PDC cycle are characterized in detail based on schlieren images, whereas the exhaust flow rate is quantified via PIV for the full PDC cycle. The combination of these two measurement techniques allows the important local and global features of the exhaust flow to be tracked for different fill fractions, which provides a sound empirical base for future numerical and analytic studies. For example, this study provides experimental proof for substantial flow reversal during the PDC cycle, which is of significant importance for coupling of the PDC with a downstream turbine.

II. Methodology

A. PDC Test Rig and Experimental Setup

Figure 1 presents a schematic of the pulse detonation combustor and the instrumentation of the experimental setup. The PDC used in this study consist of two sections: the section where the deflagration-to-detonation transition (DDT) takes place, and the exhaust tube. In this valveless design, the air supply is not being modulated but is attached directly to the upstream end of the PDC tube. Hydrogen is injected through eight circumferentially distributed fuel lines.

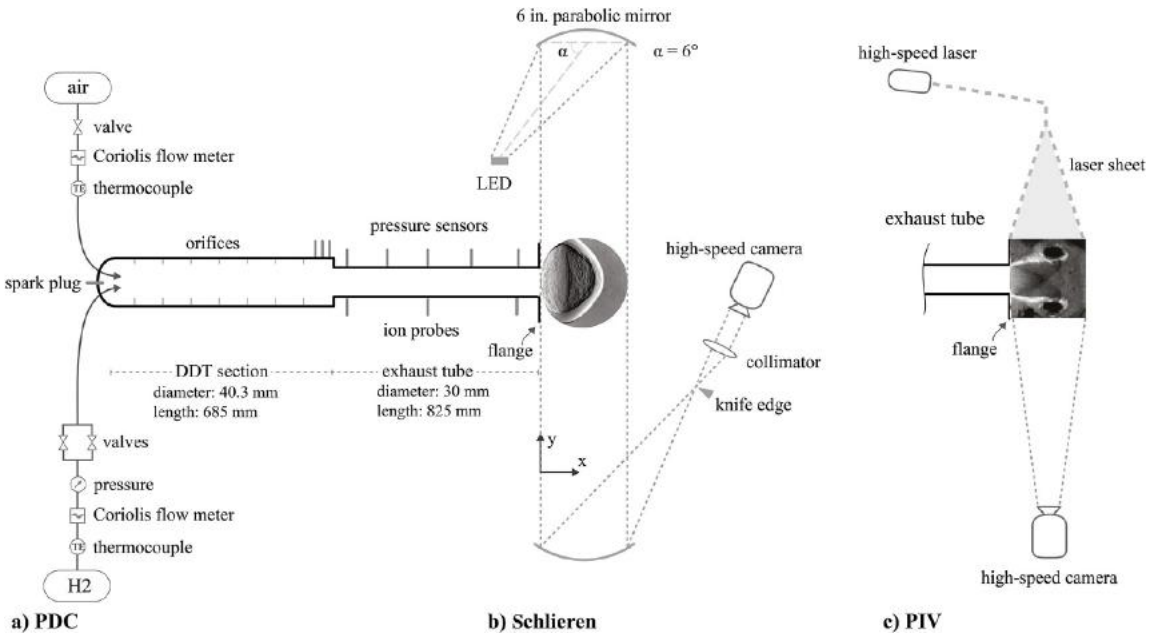

Fig. 1 Illustration of experimental setup showing a) the pulse detonation combustor, b) high-speed schlieren setup, and c) high-speed PIV setup at the tube exit. Images at tube exit indicate enlarged measurement domain.

The design of the air and hydrogen injection scheme was described by Gray et al. [21].

Combustion is initiated with a spark plug positioned at the upstream end of the DDT section. Orifices positioned in the DDT section accelerate the flame propagation. The speed of the incident shock is determined by five piezoelectric pressure probes (PCB112A05) flush mounted to the exhaust tube, as shown in Fig. 1a. To assess whether the detonation state has been reached before the wave front enters the exhaust tube, three additional closely spaced pressure probes are placed at the rear of the DDT section.

The combustion front is tracked by three flush-mounted ionization probes, which are mounted on the opposite side of the pressure probes. The ionization probes, which are fabricated in-house, consist of two electrodes separated by a ceramic coating. The ionized species in the combustion region allow an electric current to flow as a potential difference is applied to the electrodes. The resulting voltage drop indicates the arrival of the reaction front.

The data from pressure and ionization probes are acquired simultaneously on 11 channels using a National Instruments MXI-Express data-acquisition system at a 1 MHz sampling rate. The mass flow rate of air and hydrogen is measured with two different Endress+Hauser Coriolis mass flow meters. Two type-K thermocouples are used for measuring the temperature of air and hydrogen. A Festo pressure transmitter (SPTW-P10R) is used to measure the pressure of hydrogen upstream of the injection valves.

As shown in Fig. 1b, a standard z-type schlieren setup is used with two 6 in. parabolic $f/8$ mirrors for collimating and refocusing light. The schlieren images are captured with a 1 megapixel Photron SA-Z high-speed camera at frequencies up to 80 kHz. A pulsed light-emitting diode (LED) is used as a light source, as suggested by Willert et al. [22]. The overdriven-operated Luminus LED PT-120-TE at 10.3 V provides a high-intensity light pulse with an exposure time of 1 μs.

Particle images are acquired using the SA-Z camera with an array size of 1024×1024 pixels mounted orthogonally to the PDC outlet as illustrated in Fig. 1c. A Darwin-Duo diode-pumped Nd:YLF laser operated at its maximum frequency of 10 kHz supplies illumination. A series of lenses create a light sheet of approximately 1 mm in width at the center of the exhaust tube. An ILA 5150 synchronizer is used for timing of the laser and the camera. An air-driven fluidized bed PIVsolid 8 is used to seed both the tube and the ambient air close to the PDC outlet. Uniform distribution of the ambient seeding is aided by using two FDX fluidic oscillators [23]. The exhaust tube used for the PIV measurements is 45 mm longer than the one shown in Fig. 1a, which is used for the schlieren measurements.

The PIV parameters are presented in Table 1. A laser pulse separation of 4 μs is chosen as a compromise for small and large flow velocities during the entire cycle. The magnification of 13.75 pixels(px)/mm results in a particle displacement of 5.5 px for 100 m/s and 105 px for 1900 m/s. To account for the relatively large particle displacement at high velocities, an iterative multigrid approach including image deformation with an initial sampling window of 128×128 px is chosen [24,25]. Erroneous velocity vectors are identified by a dynamic mean value operator and replaced by interpolation with immediate neighbors. For the applied evaluation strategy, the subpixels error is in the range of 0.1 pixels based on the particle image diameter [26]. This corresponds to a measurement uncertainty of 1.8 m/s. The error is approximately between 0.01 and 6% of the maximum velocity during the entire exhaust phase.

Table 1 PDC PIV parameters

Parameter	Value
Interrogation window, px	32×24
Interrogation window, D	0.08×0.06
Overlap, %	50
Pulse distance, μs	4
Pulse width, ns	550–600
Pulse power, W	40–45
Field of view, D	2.3×2.5
Digital resolution, px/D	411
Particle relaxation time, μs	0.84
Exposure time, ns	159

B. Preliminary Investigation of PIV Seeding Materials

The flow-tracking fidelity of the tracer particle is a fundamental assumption for tracer particle-based measurement techniques such as PIV. This becomes critical for detonation applications due to the characteristics of reactive supersonic flows. On the one hand, the fluid velocity changes abruptly across strong shock waves. On the other hand, the high temperatures associated with reactive flows precludes the use of liquid seeding material, necessitating the use of oxidized metals with higher mass density than the surrounding fluid. Hence, high-inertia solid particles crossing shock waves may result in a significant slip velocity, and therefore biased measurement results. These errors may be further exacerbated by a nonuniform particle size distribution [27]. The fundamental particle size for solid particle seeding can be misleading; particles at the micro- and nano-scale will form larger agglomerates: both at rest and in flight [28]. Strong shear forces in a compressible flow can then break these agglomerates up in flight, resulting in a large range of particle scales: both too small to be well resolved by the optical system and too large to accurately track the flow velocity. Hence, a well-suited seeding material is required to minimize the measurement error. To this end, the particle response to a step change in fluid velocity and the raw image quality of six different seeding particles have been investigated in a preliminary study, which will be outlined in the following. Additional information can be found in Ref. [29].

To investigate the response time of different particles, PIV measurements with different seeding materials such as TiO_2, SiO_2, and ZrO_2 were conducted for the velocity step across a Mach disk of a highly underexpanded steady jet in a separate facility. In addition, schlieren measurements were conducted to obtain the actual location of the Mach disk. By comparing the PIV results with the schlieren images, the particle lag in the presence of shock waves is evaluated.

Figure 2 presents the schlieren and PIV results for two different seeding materials. In Figs. 2a and 2b, grayscale contours represent the schlieren image intensity, and color contours represent the axial velocity determined from PIV data. The intensity of the schlieren image is inverted and overlaid on the velocity contour plot gained from the PIV measurements. The velocity $\bar{u}$ corresponds to an average of 5000 snapshots and is normalized by the peak velocity $\bar{u}_{\max}$. The comparison of the schlieren and velocity fields for the TiO_2 particle (Fig. 2a) shows very good agreement between the locations of the Mach disk, the reflected shock, and the barrel shock. The same plot for the PIV data using the zirconium dioxide (ZrO_2CS01) as seeding is presented in Fig. 2b. The slow particle response leads to smearing of the velocity gradients, which is particularly notable in the vicinity of the Mach disk. A quantitative comparison between the two velocity fields is given in Fig. 2c. The largest deviations occur in areas where the velocity gradients are the largest. The TiO_2 particles move at a higher speed in regions of positive velocity gradients. This corresponds to the red region in $0 < x/D_N < 1.34$ in Fig. 2c, where an expansion fan forms at the nozzle lip. Downstream of the Mach disk, the velocity decreases abruptly. Hence, the largest discrepancy between the particle velocities appears in this region at $x/D_N \approx 1.43$. Further downstream, there is an additional red area $x/D_N > 1.55$ and $-0.25 < x/D_N < 0.25$. This indicates that both the vortices in the slipstream and the acceleration of the flow due to the reflection of the reflected shock at the jet boundary as an expansion fan are captured more accurately with the TiO_2 particles. These results clearly emphasize that, by using seeding with slow particle response, the strong velocity gradients in supersonic flows cannot be accurately measured with the PIV technique.

Figure 3 presents the axial mean velocity along the jet centerline normalized by the maximum velocity. A strong decay of the velocity after crossing the Mach disk is noticeable for all investigated seeding materials. The slope of the curves, however, indicates the different response of the seeding materials to the step change in the velocity

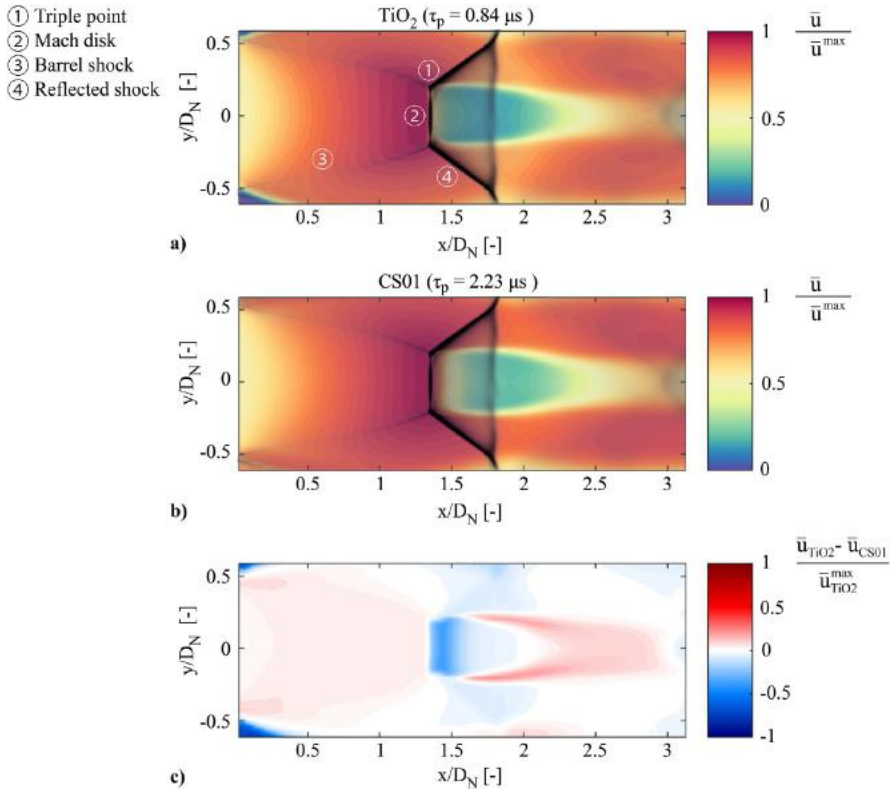

Fig. 2 Steady underexpanded jet with a nozzle pressure ratio of 5.2: a) PIV with TiO_2 seeding, b) PIV with ZrO_2CS01 seeding, and c) their normalized deviation. Spatial coordinates are normalized with respect to nozzle diameter D_N.

downstream of the Mach disk. The SiO_2R104 exhibits the best response among the investigated seeding materials, followed by SiO_2R202 and TiO_2. However, all three zirconium dioxide materials show a longer region of deceleration after passing the shock wave.

The particle response is typically quantified by the particle relaxation time τ_p. This is the time required for the velocity lag, downstream of a step change in velocity, to be reduced by the factor of $1/e$. The particle response time for each seeding material is evaluated by examining their motion through the Mach disk using the method developed by Melling [30] and Ragni et al. [31]. The determined values range from 0.32 to 2.29 μs, as shown in Table 2. The best particle response is achieved using SiO_2 particles followed by the TiO_2 particles.

The raw image quality of the PIV images has also been taken into account for choosing well-suited seeding particles. Inspection of the raw images shows that the TiO_2 powders exhibit more uniform seeding than the other materials. Figure 4 shows exemplary snapshots of the raw images for TiO_2 and SiO_2 R104. The silicon dioxides exhibit a much wider range of particle intensities in the images. Moreover, the TiO_2 raw images exhibit better contrast. Considering all these aspects, the TiO_2 shows an overall best performance. Therefore, the TiO_2 particles have been chosen as the seeding particles for the PIV measurement of the PDC.

C. PDC Operating Conditions

The present experimental investigations are conducted in a single-cycle manner; i.e., only a single combustion event (deflagration or detonation) is undertaken for each measurement. The tube is first filled with a combustible mixture for a certain amount of time and subsequently ignited. The corresponding exhaust flow is captured with schlieren and PIV techniques. All cases considered in this

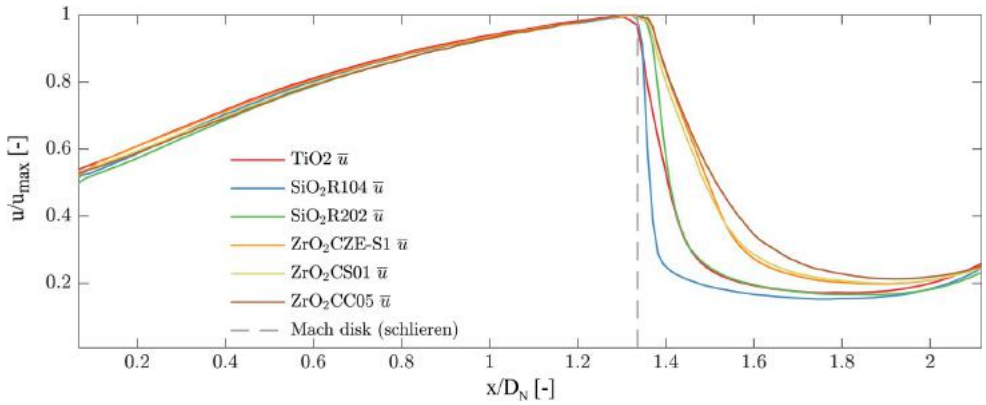

Fig. 3 Axial profiles of normalized mean velocity along jet centerline for six different tracer materials.

Table 2 Measured relaxation times for tracer materials

Name	τ_p, μs
SiO_2R104	0.32
SiO_2R202	0.61
TiO_2	0.84
ZrO_2CC05	2.22
ZrO_2CS01	2.23
ZrO_2CZE-S1	2.29

study differ only in the hydrogen filling time. This leads to a different fill fraction and equivalence ratio, as will be described in the following.

A schematic illustration of the valve timing during the fill process is shown in Fig. 5a. In this valveless design, the air flows through the test rig continuously at 100 kg/h. As indicated in Fig. 5a, the filling time refers to the time period during which hydrogen is injected into the PDC tube rig. The ignition is initiated at the same time that the hydrogen valves are closed.

Changing the filling time results in different operating conditions for the PDC, with a low filling time corresponding to a low fill fraction. In our setup, it also leads to a gradient in the equivalence ratio Φ along the tube. The dependence of the equivalence ratio on the filling time is due to the fact that the pressure in the H_2 supply line decreases exponentially once the valve is opened. This is illustrated in Fig. 5b. The pressure reaches a plateau value approximately 1 s after the valve is opened. This pressure level was set to achieve the desired mass flow rate corresponding to $\Phi > 1$. Hence, a decreasing supply pressure during the filling process resulted in a stratification of the mixture with a positive equivalence ratio gradient along the tube.

Three different cases with various filling times are presented in this paper, which are referred to as Det_{full}, Det_{part} and Def. A schematic representation of these cases is given in Fig. 5c at three different time stages of the PDC cycle. A rich mixture is chosen for all operating conditions, and the fill fraction (ff) is varied to investigate its impact

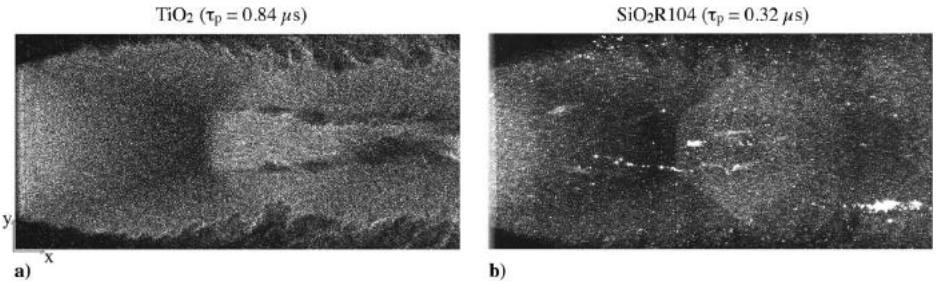

Fig. 4 Mie scattering images of SiO_2R104 and TiO_2 for a steady underexpanded jet.

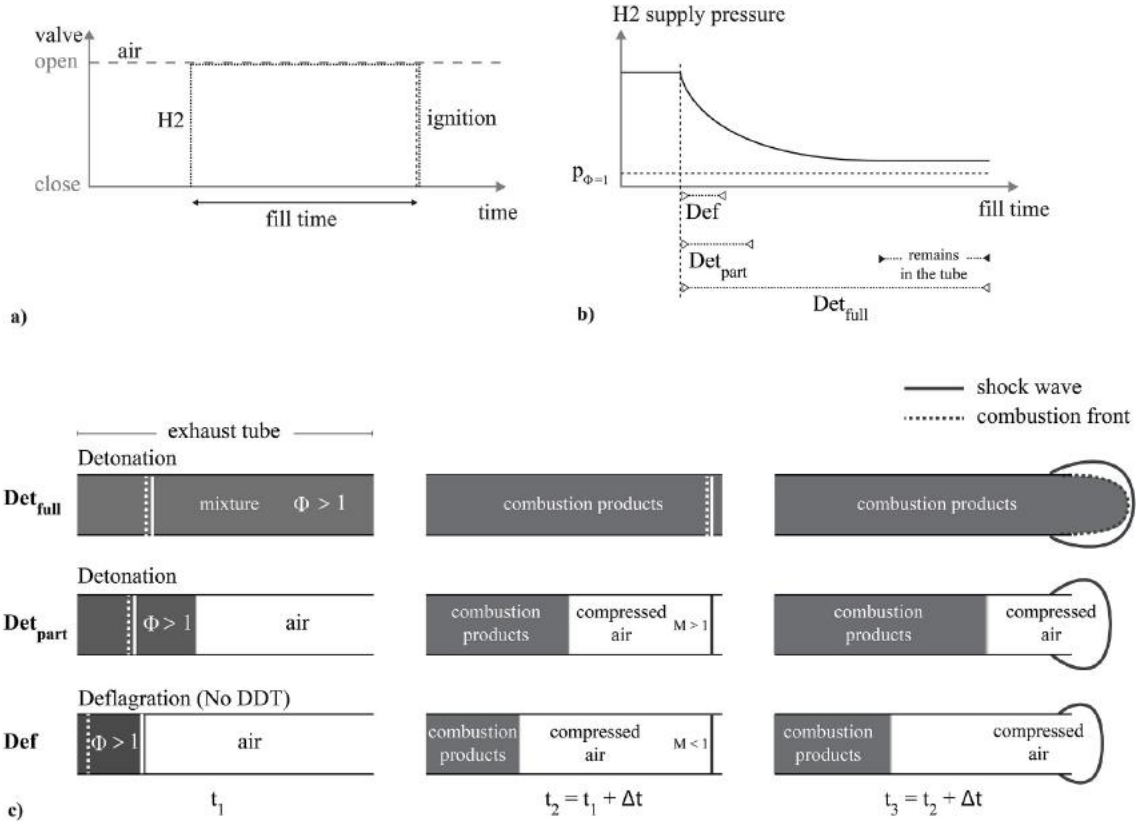

Fig. 5 Representations of a) valve switching timeline for injection of air and hydrogen into test rig, b) supply pressure of H_2 as function of filling time (shown schematically for different cases), and c) illustration of experimental cases considered in this study.

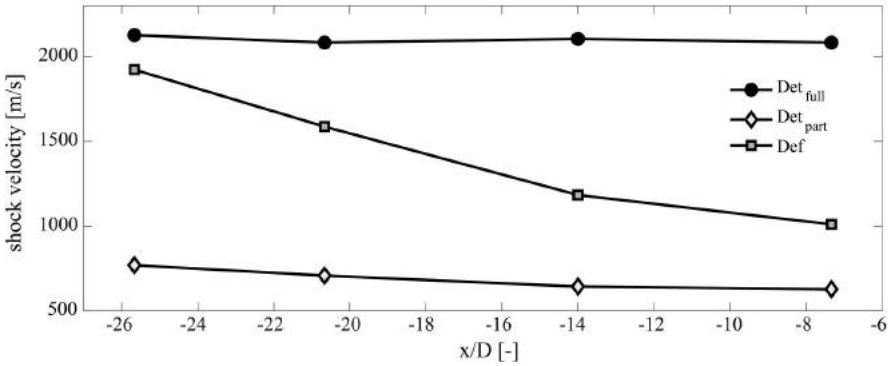

Fig. 6 Leading shock velocity in the laboratory reference frame based on time-of-flight method.

on the exhaust flow. Different fuel fractions and equivalence ratios Φ in the exhaust tube are shown as the hydrogen filling time changes: $\bar{\Phi}_{\mathrm{Def}} > \bar{\Phi}_{\mathrm{Det_{part}}} > \bar{\Phi}_{\mathrm{Det_{full}}}$, and $\mathrm{ff}_{\mathrm{Def}} < \mathrm{ff}_{\mathrm{Det_{part}}} < 1 < \mathrm{ff}_{\mathrm{Det_{full}}}$. Propagation of the shock and the reaction front within and outside of the exhaust tube is represented schematically for each case. In the case of $\mathrm{Det_{full}}$, the filling time is roughly 200 times longer than it needs to fill the whole tube. Thus, not only the exhaust tube is fully filled with the detonable mixture but the mixture also extends downstream of the tube exit (ff $>$ 1). In this case, the hydrogen mass flow needed for a rich mixture is adjusted by setting the pressure in the hydrogen supply line. A comparison of the Chapman–Jouguet (CJ) detonation velocity computed with the NASA CEA code [32] and the one determined with the ionization and pressure probes shows that the tube is filled with a rich mixture corresponding to $\Phi \approx 1.4$–2.

As illustrated by t2 in Fig. 5c, the detonation wave entering the exhaust tube also leaves the tube as a detonation wave. However, this is not the case for the two other investigated operating conditions. A shorter filling time is chosen for the $\mathrm{Det_{part}}$ case when compared to the $\mathrm{Det_{full}}$ case. Therefore, the exhaust tube of the PDC is filled only partially with a reactive mixture (ff $<$ 1). As illustrated in Fig. 5c at time t_2, the detonation wave is transmitted as a shock at the contact surface (mixture–air interface) and moves downstream through the air; the data from the pressure and the ionization probes confirm that the shock wave leaves the tube without a reaction zone directly behind it, as illustrated by t3 in Fig. 5. Following the collision of the detonation wave with the contact surface, a rarefaction wave is also generated at the contact surface, which propagates toward the upstream end of the PDC [33]. While the transmitted shock wave compresses and accelerates the air toward the tube exit, the detonation products are expanded and accelerated toward the tube exit by the rarefaction wave.

A CJ detonation wave is followed by a self-similar rarefaction wave (Taylor wave), which decelerate the burned gas to satisfy the closed wall boundary condition at the upstream end of the PDC [34]. Once the detonation wave is transmitted as a shock wave at the contact surface, the Taylor wave overtakes the transmitted shock wave. This results in a considerable attenuation of the shock wave as it propagates through the air [35]. Similar to a shock tube viscous effects also contribute to the deceleration of the leading shock wave [36,37].

These considerations are in line with the shock propagation velocity as shown in Fig. 6. The velocities were estimated from the experiments using the time-of-flight method. The arrival time of the shock wave at the location of the pressure probes was determined from the pressure signals, and the shock velocity between the probes was estimated by using the arrival time and the distance between the pressure probes. The pressure probes in the exhaust tube are located at $x/D = -27$, -24, -17, -11, and -4. According to Fig. 6, the detonation wave propagates at a nearly constant velocity along the entire exhaust tube in the $\mathrm{Det_{full}}$ case, whereas a significant deceleration of the shock propagation velocity is evident for the $\mathrm{Det_{part}}$ case.

For the Def case, an even shorter filling time is chosen (see illustrations in Fig. 5) and no transition to detonation takes place. In comparison to the $\mathrm{Det_{part}}$ case, the mixture is richer and fills even less volume of the exhaust tube. An accelerated deflagration wave propagates toward the tube exit until the combustion front quenches at the mixture–air interface. Due to the closed wall boundary condition at the upstream end of the PDC, the increase in the specific volume of the combustion products results in a displacement of the reactants ahead of the combustion front. Therefore, the reactants move toward the open end of the tube before the combustion. As a result of the displacement of the flow, precursor compression waves are formed in front of the reaction front [38]. The rapid increase of the flame surface is caused by the obstacles in the DDT section. Furthermore, the flame burning rate increases due to a number of instabilities, such as Kelvin–Helmholtz and Rayleigh–Taylor instabilities [39]. Further pressure waves are generated ahead of the flame front because the flame propagates along the DDT section, whereas its burning rate increases. These pressure waves eventually coalesce to a single shock wave leaving the PDC. However, due to the low fill fraction, the accelerated flame front does not catch up with the preceding shock wave to form a detonation wave. Also, for the Def case, the measured pressure next to the tube exit indicates an expansion wave attached to the leading shock wave. This may be caused by a highly accelerated flame, which results in an expansion wave to satisfy the closed wall boundary condition [39]. The expansion waves and viscous effects decelerate the leading shock wave while it propagates along the exhaust tube (Fig. 6).

The Mach number of the incident shock is the key quantity for the flowfield behind it. In particular, the initial flow evolution at the tube exit is governed by the shock strength at the tube exit. Therefore, the incident shock velocity at the tube exit is determined by extrapolating the estimated shock velocity along the tube. The shock velocities in the laboratory reference frame at the tube outlet for all the operating conditions are listed in Table 3. Also, the shock Mach number is given in Table 3. According to Rankine–Hugoniot equations, the flow behind a nonreactive one-dimensional shock wave is supersonic if the shock strength is beyond Ms $= 2.07$. Thus, at the tube exit ($x/D = 0$), the flow behind the incident shock wave is subsonic for the Def case and supersonic for the $\mathrm{Det_{part}}$ case. For the sake of completeness, the shock Mach number for the $\mathrm{Det_{full}}$ case in reference to the unburned gas is also given in Table 3. However, the flow behind the reactive CJ detonation is sonic relative to the wave but subsonic in the laboratory reference frame. PIV measurements were performed only for the $\mathrm{Det_{full}}$ and Def cases. As shown in Table 3, the shock wave velocity is somewhat reduced when PIV is conducted. This is due to the additional seeding air required for PIV, which dilutes the mixture.

Table 3 Velocities and Mach numbers of the incident shock at the tube exit

Operating condition	$u_{\mathrm{schlieren}}$, m/s	u_{PIV}, m/s	$\mathrm{Ms_{schlieren}}$	$\mathrm{Ms_{PIV}}$
$\mathrm{Det_{full}}$	2058	1930	4.88	4.78
$\mathrm{Det_{part}}$	909	— —	2.53	— —
Def	606	508	1.65	1.37

III. Influence of Fill Fraction on Initial Jet Evolution

The dynamic evolution of the PDC exhaust flow depends on its operating conditions. In the case of $\mathrm{Det_{full}}$, the incident shock exits the tube as a detonation wave, whereas for the $\mathrm{Det_{part}}$ cases, the detonation wave dies out before it exits the tube and the incident shock is separated from the reaction zone. This is analog to the Def case where a single shock exits the tube. In the following, the evolutions of the incident shock and other shock-dynamic characteristics of the exhaust flow at its initial stage are investigated in detail, based on the acquired high-speed schlieren images.

A. Small Fill Fraction Def

We start with the discussion of the Def case because the flow visualizations are the easiest to interpret and many of the features are common to all three cases. As the fill fraction is smallest for this case, the time span between the shock arrival and the contamination of the schlieren images by the combustion products is largest.

The corresponding schlieren images of the Def case are presented in Fig. 7. These 12 $\partial\rho/\partial y$ images depict the key moments of the flow evolution from the time the shock exits the PDC tube until the density gradients of the succeeding combustion products dominate the schlieren images. In all images, the primary exhaust flow moves from left to right. The x and y axes are normalized by the tube diameter of $D = 30$ mm, and the origin of the axis corresponds to the point on the tube centerline at the tube exit. The time shown above each image corresponds to the time after the shock passes the pressure sensor, which is mounted 4D upstream of the tube exit. The first seven images are uniformly separated by a time interval of 50 μs, whereas the remaining images are separated by longer intervals. From the time series of the schlieren images presented in Fig. 7, the flow evolution can be determined in detail. Figure 7a shows the moment right after the shock diffracts around the tube exit corner. At this time instant, a part of the shock has already undergone an axisymmetric diffraction as indicated by the partially curved shock. Both the undisturbed and the diffracted shock are clearly visible. An unsteady expansion wave moves toward the tube and accelerates the subsonic flow inside the tube. The exhaust flow expands further and forms a Prandtl–Meyer (PM) expansion fan centered at the tube exit corner [40]. The leading characteristic (LC) of the expansion wave marks the separation point (SP) between the undisturbed incident shock and the diffracted shock.

Figure 7b depicts the moment when a slightly curved strong shock is being formed at the outer region of the jet next to the barrel shock. Downstream of the expansion fan, the pressure is lower and the velocity is higher as compared to the flow being set into motion by the incident shock. Hence, a system of shocks consisting of a Mach disk and a barrel shock occurs. This shock system processes the exhaust flow to match the pressure and velocity of the overexpanded exhaust flow with the one being set into motion by the incident shock [41]. The upper and lower curved strong shocks, marked in Fig. 7b, propagate toward the jet centerline to form the Mach disk. When these shocks coalesce, a Mach disk is formed, which develops to its typical disk shape shortly after, as can be seen in Fig. 7c.

A characteristic feature of the PDC exhaust flow is the vortex ring, which arises as the shear layer at the trailing edge rolls up. There are two vortex-ring-associated shocks, the vortex-induced shock and the vortex-ring-embedded shock (VRES), which are marked in Figs. 7c and 7d. The VRES exists only within the vortex ring and not inside the jet core. However, a part of this shock appears in the schlieren image as a vertical line along the entire jet core. This is due to the fact that the schlieren image represents line-of-sight integrated values of the refractive-index gradient of the axisymmetric three-dimensional flow. Hence, the vertical line represents the occurrence of a vertical part of the VRES in the circumferential direction.

Figure 7e shows the moment when the Mach disk is located at its maximum axial position of about $x/D \approx 1.17$. Although the vortex ring propagates further downstream, a triple shock system becomes apparent. The shock system consists of the barrel shock, the Mach disk, and the reflected shock. The reflection of the barrel shock from the jet centerline (axis of symmetry) must be, by its nature, a Mach reflection [42]. The corresponding triple point and the slipstream are shown in Fig. 7e. The slipstream occurs because of the velocity mismatch between the region downstream of the reflected shock and downstream of the Mach disk. As seen in Figs. 7d–7j, a number of counter-rotating vortex rings (CRVRs) occur, resembling the classical slipstream flow features [43]. These vortex rings are generated by the Kelvin–Helmholtz (KH) instability of the shear layer along the slipstream [44].

A number of subsequent compression waves are visible at the time of $t = 0.498$ ms, as shown in Fig. 7g. They are most likely generated due to reflection of pressure waves on the boundaries in the PDC: both the orifices within the DDT section and the cross-section contraction between the DDT section and the exhaust tube.

Figures 7g–7j show the later development of the CRVRs during the blowdown phase and further relevant flow features. Their truncated conical shape (Fig. 7g) is due to the inclination of the of the shear layer and the trajectory of the triple point. As the Mach disk becomes smaller with time, the triple point moves futher toward the tube exit. The CRVRs remain downstream of the VRES for at least $4D$. They move continuously away from the jet centerline in the radial direction. Eventually, the CRVRs move around the vortex ring and reappear in the field of view, upstream of the vortex ring (Fig. 7j). The propagation of the CRVRs around the main vortex ring occurs shortly after the vortex ring separates from the trailing jet.

The vortex-ring separation, commonly referred to as pinch-off, takes place between $t = 0.498$ and 0.598 ms (Figs. 7g and 7h). Although the vortex ring is still attached to its trailing edge at $t = 0.498$ ms (Fig. 7g), the VRES is separated from the reflected shock at 0.598 ms (Fig. 7h). As the vortex ring moves further downstream, the first shock cells appear, resembling the flowfield of a steady underexpanded jet (Figs. 7i–7k) [45]. As more and more combustion products leave the tube, the shock cells become less visible and disappear behind the high-density gradients of the burned gas (Fig. 7l).

B. Medium Fill Fraction ($\mathrm{Det_{part}}$)

As described in Sec. II.C, the fill time for the $\mathrm{Det_{part}}$ case is longer than the Def case, resulting in most of the tube containing combustible mixture at time of ignition. Therefore, a successful transition to detonation takes place within the DDT section. The resulting detonation wave travels through the combustible mixture until it reaches the intersection of the reactive mixture with air. The detonation wave is then transmitted as a shock. This shock propagates further through the air-filled section of the tube, as indicated in Fig. 5c. A nonreactive shock exits the tube in the same manner as in the Def case. However, this shock is much stronger due to the detonation process. Consequently, the incident shock Mach number of $M = 2.53$ for the $\mathrm{Det_{part}}$ case is considerably greater than $M = 1.65$ of the Def case.

A series of $\partial\rho/\partial y$ schlieren images is presented for the $\mathrm{Det_{part}}$ case in Fig. 8. The given time above each image corresponds to the time elapsed after the shock passes the pressure probe next to the exhaust tube outlet. The time interval between the images is 0.025 ms. The first image at $t = 0.126$ ms depicts the moment just after the shock leaves the tube. Both the diffracted and the undisturbed incident shocks are visible. By the time of $t = 0.176$ ms (Fig. 8b), the incident shock is fully diffracted, which is indicated by its curved shape. The Prandtl–Meyer expansion waves located between the barrel shock and the jet centerline are clearly visible. The formation of the Mach disk can be observed from Figs. 8b and 8c.

The flow features observable in Figs. 8a–8d for the $\mathrm{Det_{part}}$ case are essentially the same as for the Def case (Figs. 7a–7d), and they were discussed in the previous section. However, with an increasing incident shock Mach number, the shocks produced in the jet are stronger, as is their influence on the jet evolution [44]; both the size and the axial distance of the Mach disk are larger when compared to the Def case (Figs. 7c and 8c). In addition, the shape of the barrel shock is less conical but more barrel-like, which is characteristic of highly underexpanded jets [45]. In Fig. 8d, a pronounced wavy line at the rear of the VRES appears. This line represents the impingement

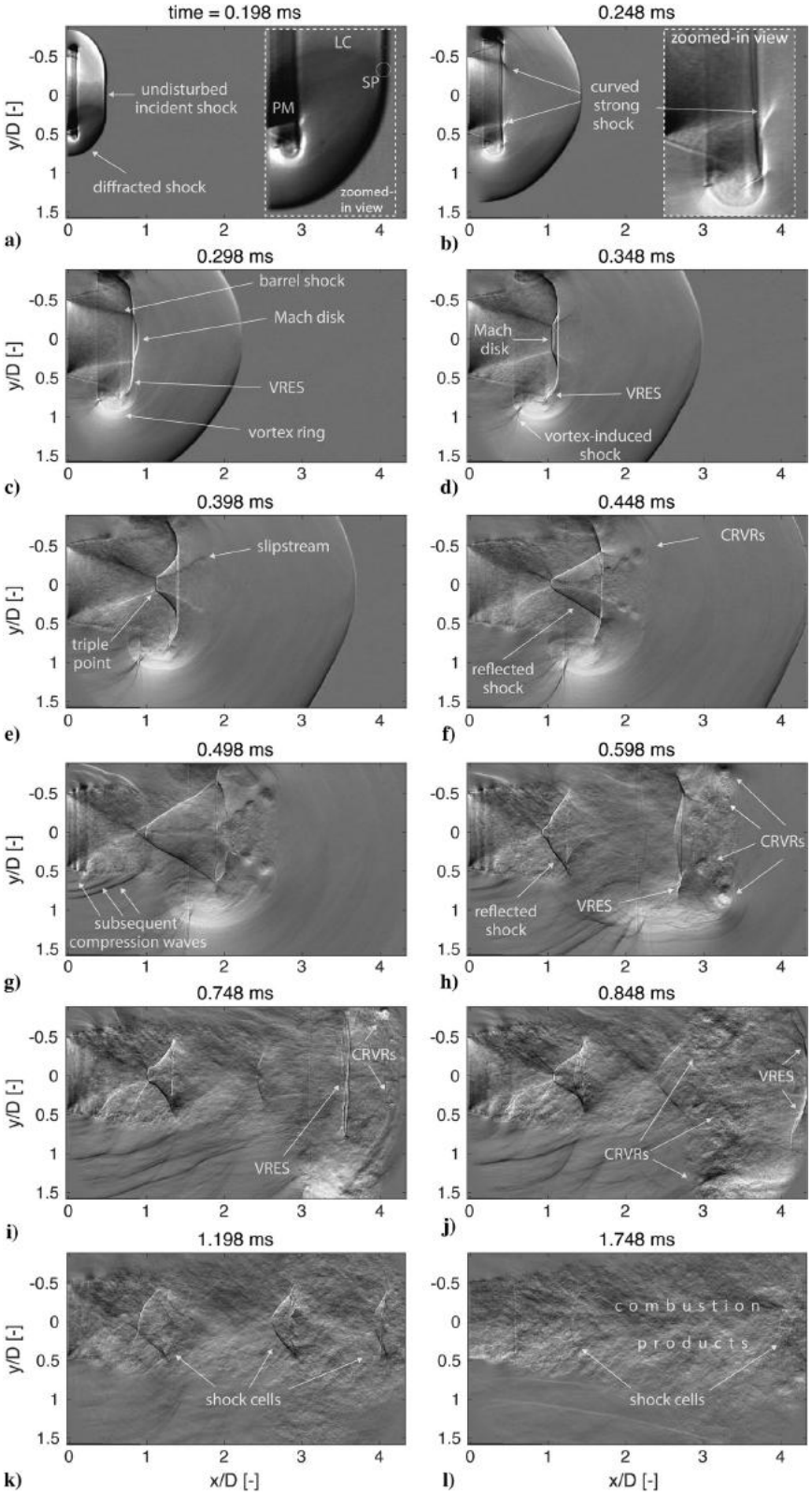

Fig. 7 Detailed evolution of exhaust flow at its early stage showing the appearance and further development of dominant flow features. (Case: Def.)

point of the shock on the jet boundary [46]. This wavy line is one of several flow features more pronounced as compared to the Def case.

The later stage of the jet evolution, shown in Figs. 8e–8i, is also consistent with the evolution of the flow for the Def case. The Mach disk becomes smaller, whereas its axial distance to the tube outlet

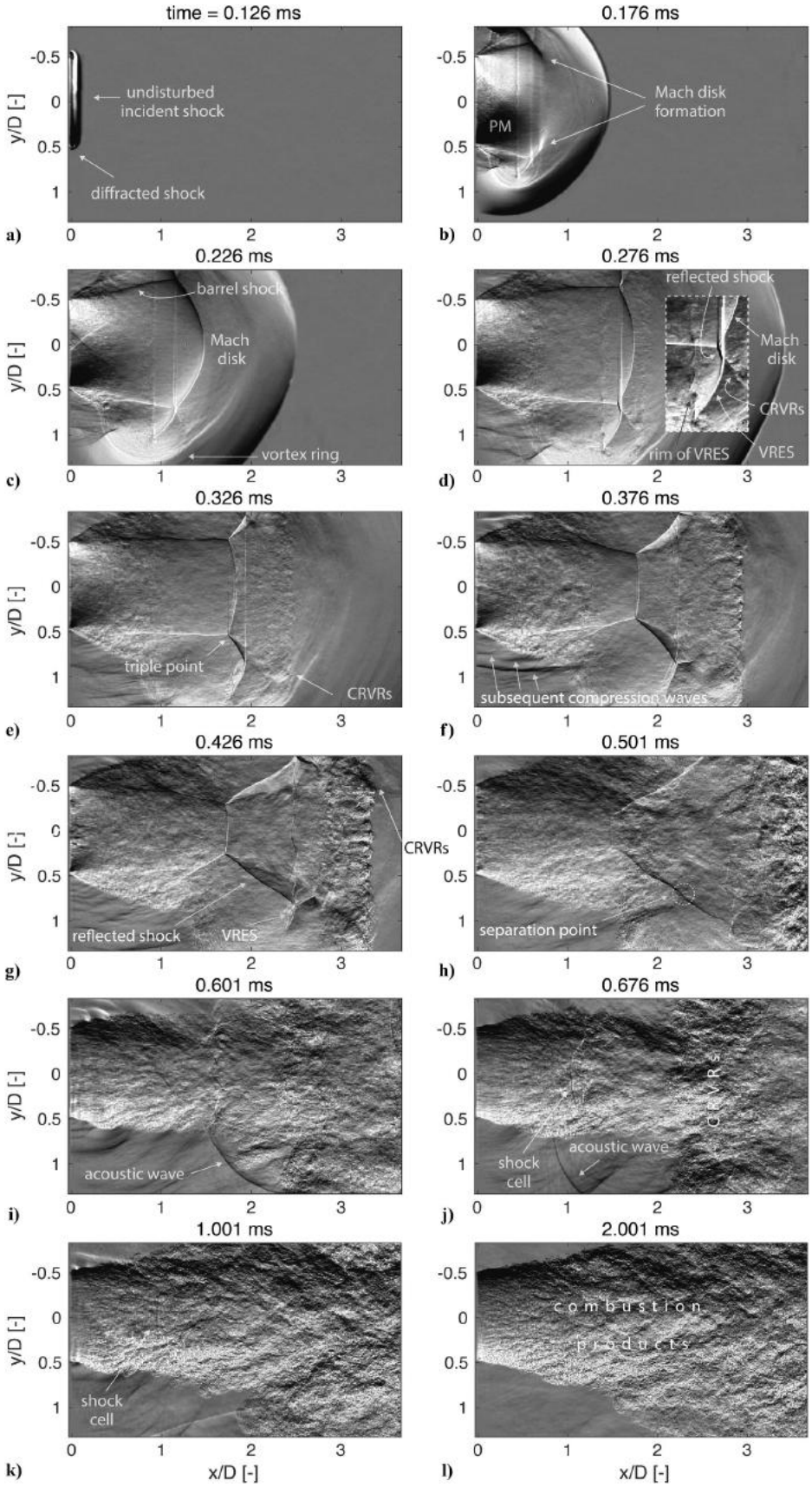

Fig. 8 Details of flow features for the Det_{part} case. Jet evolution is visible until combustion products dominate measurement area.

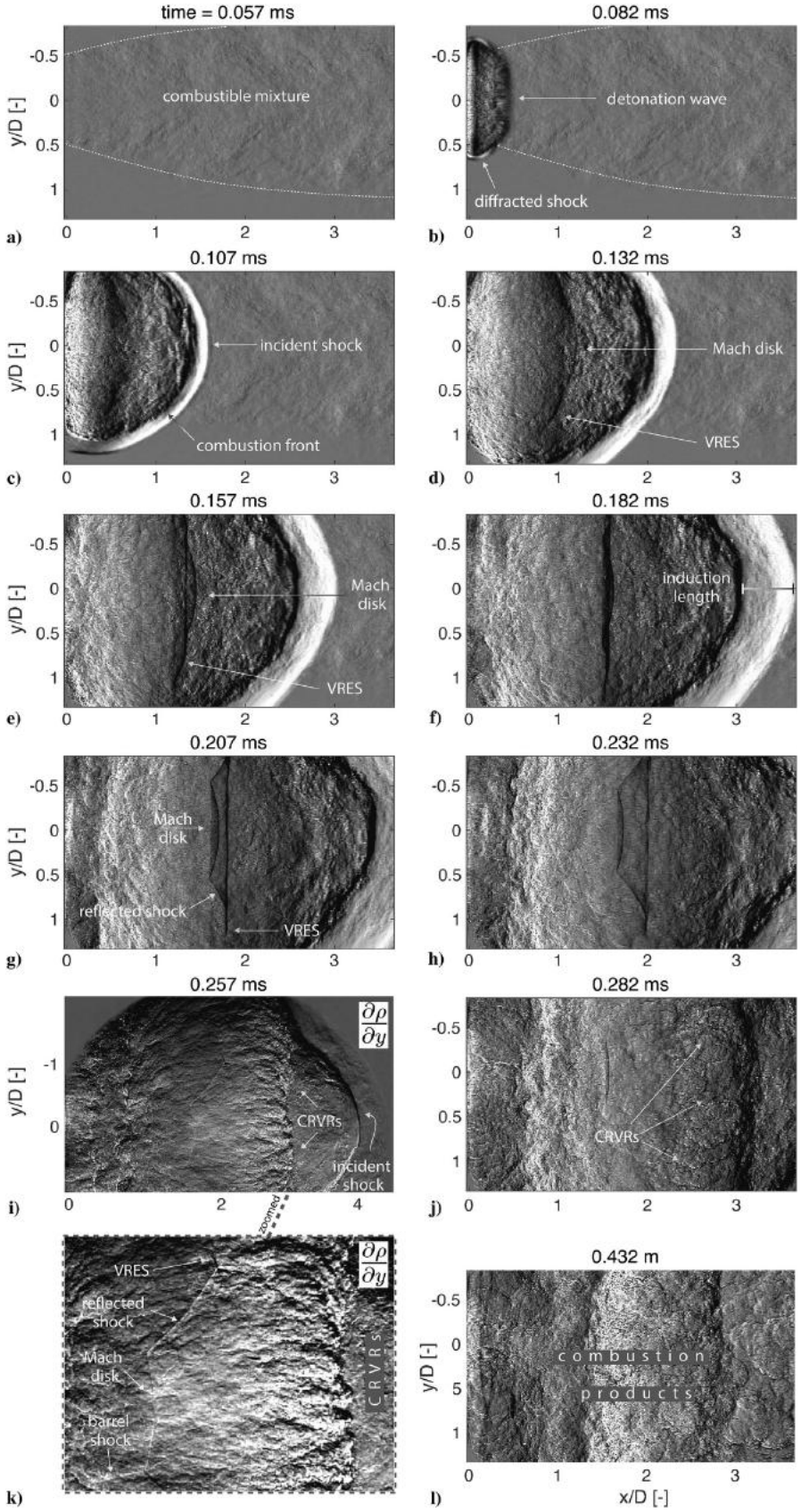

Fig. 9 Evolution of the flow features as a detonation wave exits an overfilled tube.

decreases with time. As the vortex ring propagates further downstream, it separates from the trailing jet. Figure 8g depicts the moment as the elongated reflected shock is about to detach from the VRES. The rear part of the reflected shock separates at its intersection with the shear layer and propagates as an acoustic wave toward the tube exit (Figs. 8h–8j). By the time of $t = 0.676$ ms, the vortex ring is separated from the trailing jet and the CRVRs upstream of the vortex ring appear.

In the same manner as for the Def case, the high-density gradient combustion products mask the shock cell structure at later times. Due to the large fill fraction, this occlusion occurs sooner in the schlieren images as compared to the Def case. Hence, in contrast to the Def case, the diamond-shaped shock structure is barely visible. However, the vertical part of the first shock cell is notable in Figs. 8j and 8k.

The appearance of combustion products is confirmed by the signal of the ion probe mounted close to the tube exit. It detects the passage of combustion wave at $x/D = -4$ at the latest from $t = 0.55$ ms on. This correlates very well with the observations from the schlieren images, and it confirms the assumption of the high-density gradient combustion products masking the underlying shocks. The image in Fig. 8l depicts the exhaust flow at $t = 2.001$ ms. At this time, the high-density gradient exhaust flow dominates the entire schlieren image.

As presented earlier in this paper, the dynamic flow features observed for the Def and $\mathrm{Det_{part}}$ operating conditions are qualitatively similar. However, for the $\mathrm{Det_{part}}$ case, the shocks are significantly stronger: as are the flow structures generated by or associated with these shocks. Moreover, the flow characteristics at both operating conditions correspond very well with those reported in the literature for the exhaust flow of a shock tube and for a compressible starting jet [44,46–50]. This is not surprising because the early phase of the exhaust flow for both the partially filled PDC and a shock tube is dominated by a transient incident shock wave propagating toward the tube exit. However, there is a significant distinction with regard to the evolution of the flow features. In contrast to the open-ended shock tube, the flow features in the PDC exhaust weaken at an early stage. This is, in particular, noticeable in the evolution of the Mach disk. In the classical open-ended shock tube flow, the Mach disk converges continuously to its steady size and position [44,51]. However, the Mach disk in the PDE exhaust shrinks and moves toward the tube exit soon after its formation is completed, regardless of the leading shock Mach number. This is believed to be due to the presence of the Taylor wave attached to the leading shock for both $\mathrm{Det_{part}}$ and Def cases, as discussed in Sec. II.C. Consequently, once the shock wave leaves the tube, the pressure declines at the PDC exit. Hence, the less underexpanded flow results in weaker flow features over time. Nevertheless, except for the strength of the flow features, the overall initial PDC exhaust flow dynamics remain qualitatively similar to the one of the open-ended shock tube.

C. Maximum Fill Fraction ($\mathrm{Det_{full}}$)

When the tube is overfilled with a combustible mixture, a detonation wave propagates the entire length of the exhaust tube. A time sequence of schlieren images at the outlet of the PDC is presented in Fig. 9. Figures 9a–9j correspond to a time sequence with time increments of 25 μs. Figure 9k is a close-up view of ig. 9i, which shows a larger section of the exhaust tube. All images in this figure represents $\partial\rho/\partial x$ schlieren images with the exception of Figs. 9i and 9k, which represents $\partial\rho/\partial y$ images.

The outflow of combustible mixture from the tube can be seen in the schlieren image (Fig. 9a) due to the strong density gradients between the ambient air and the fuel. At $t = 0.082$, the detonation has already passed the exit of the exhaust tube (Fig. 9b). The combustion region is characterized by a dark and noisy pattern. This pattern occurs as a result of density gradients in a very small length scale. In the vicinity of the jet core, the undisturbed part of the wave propagates as a detonation wave, whereas the outer part of the incident shock diffracts at the corner (Fig. 9b). The diffracted part of the wave is characterized by a small, bright region. This region corresponds to the zone between the incident shock and the combustion front. The jet boundary of the reactive mixture marks the intersection point between the detonation wave and diffracted shock with no combustion front right behind it. By the time of $t = 0.107$ ms, the incident shock is already fully separated from the combustion region along the entire wave front (Fig. 9c). Hence, the detonation wave fails shortly after it exits the tube.

The Mach disk and the VRES are initially entirely obscured by the combustion products, but they become apparent (Figs. 9d and 9e) as the jet expands further and the strength of the shocks increases. Although the vortex ring is not observable due to the combustion products, the presence of the VRES indicates the presence of a vortex ring. Similar to the exhaust flow of the $\mathrm{Det_{part}}$ and Def cases, the VRES overtakes the Mach disk (Figs. 9g and 9h).

The evolution of the flow features shown in Fig. 9 and its similarity to those of the other operating conditions lead to the conclusion that the exhaust flow of the PDC for $\mathrm{ff_{Def}} > 1$ undergoes qualitatively the same fluid dynamic development as it does for $\mathrm{ff_{Def}} < 1$. Therefore, we assume the presence of a Mach reflection for an overfilled PDC in the same manner as for the cases with a smaller fill fraction. The Mach reflection consists of the reflected shock, the Mach disk, and the

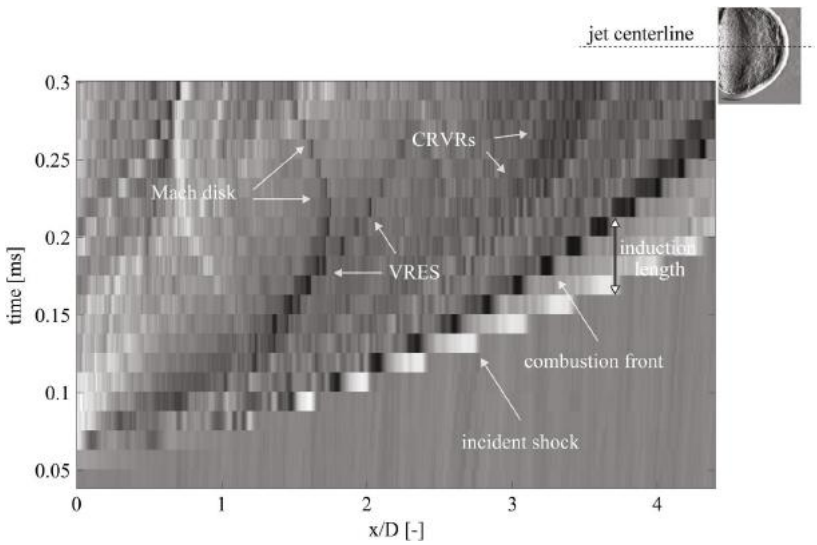

Fig. 10 *x-t* **diagram showing evolution of main flow features of diffracting detonation along jet centerline. The *x* axis is normalized by the tube diameter, whereas the *y* axis shows the time from 0 to 0.3 ms. (Case: $\mathrm{Det_{full}}$.)**

barrel shock. However, the latter is not visible in the $\partial\rho/\partial x$ images (Figs. 9g and 9h). This is again due to the combustion products masking the underlying barrel shock because its pressure gradients in the axial direction are relatively small. However, the barrel shock becomes visible in the $\partial\rho/\partial y$ image as shown in Fig. 9i and is marked in the corresponding close-up view in Fig. 9k.

As shown in Fig. 9i, CRVRs appear more distinctly in the $\partial\rho/\partial y$ schlieren image in the region of $x/D \approx 2.5$ to 3.5. The CRVRs are also notable in the $\partial\rho/\partial x$ image as a dark region elongated in vertical direction in Fig. 9j. With time, the combustion products dominate the image more and more (Fig. 9l). Therefore, further analysis of the flow development based on schlieren images becomes unfeasible.

The spatiotemporal evolution of the essential flow features can be evaluated based on an x-t diagram. Figure 10 shows an x-t diagram derived from the schlieren images recorded at 80 kHz along the jet centerline. To reduce the noise, the pixel intensity is averaged in the vertical direction for 30 pixels, which corresponds to $0.15D$. The combustion front decays at a faster rate than the incident shock,

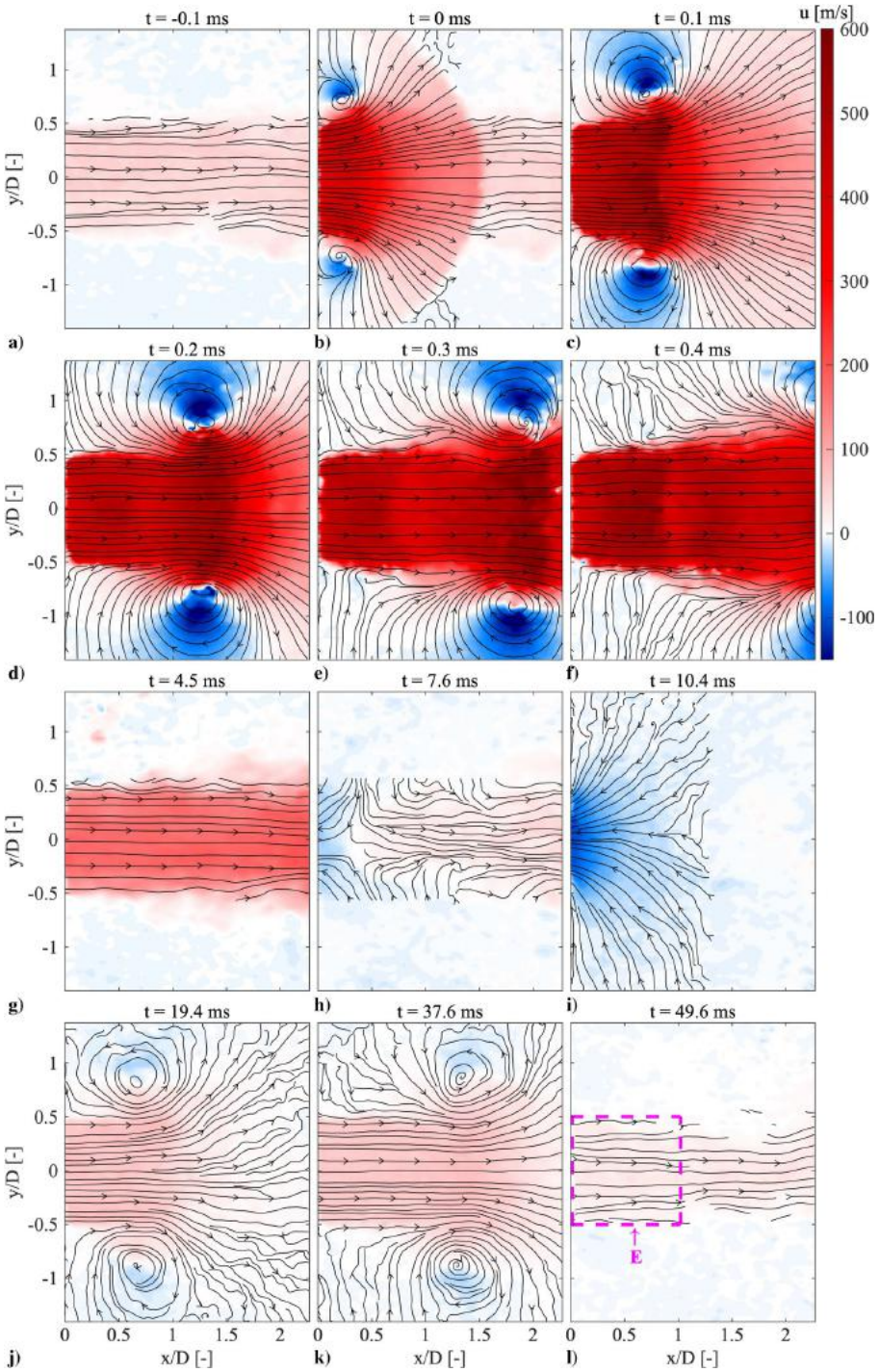

Fig. 11 Contours of axial velocity of the exhaust flow at 12 time steps showing evolution of flow for Def case. Streamlines calculated from instantaneous velocity fields are superimposed on contours to indicate flow direction.

which results in a continuous growth of the induction length. At $t \approx 0.2$ ms, the Mach disk reaches its maximum axial distance and recedes backward toward the tube exit. The vertical line of the VRES indicates the propagation path of the vortex ring. Also, the CRVRs upstream of the vortex ring are notable in the x-t diagram, indicating that these vortex rings move around the primary vortex ring. With the exception of the combustion front, the dynamic evolution of all flow features corresponds qualitatively very well with the underfilled operating conditions, as discussed in the previous sections.

To summarize, the preceding discussion emphasizes the similarity of the main flow features for all three operating conditions. This is not only true for the presence of these features but also for their dynamical evolution.

IV. Influence of Fill Fraction on the Full PDC Cycle

After the discussion of the initial development of the exhaust flow for different operating conditions, we now address the full cycle of

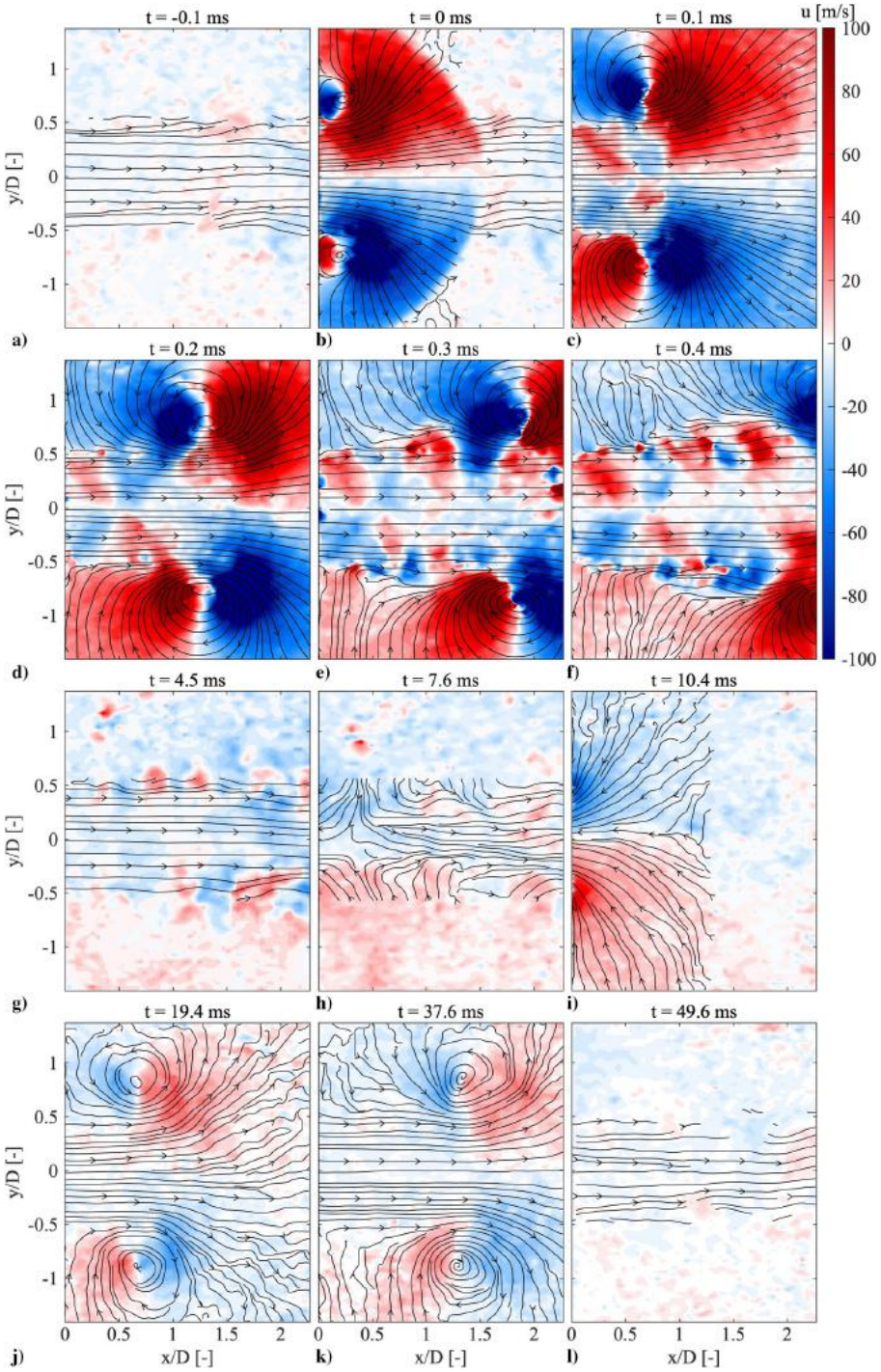

Fig. 12 Contours of radial velocity of exhaust flow at 12 time steps showing evolution of flow for Def case. Streamlines calculated from instantaneous velocity fields are superimposed on contours to indicate flow direction.

the PDC. For this purpose, the PIV results are used and the impact of the fill fraction on the full cycle of the exhaust flow is examined. Cases Def and $\mathrm{Det}_{\mathrm{full}}$, representing the minimum and maximum fill fractions, are investigated.

A. Flow Snapshots During Blowdown

Figures 11 and 12 show a series of contour plots of the instantaneous axial and radial velocities for the Def case. The first six consecutive plots in Figs. 11 and 12 (Figs. 11a–11f and Figs. 12a–12f) exhibit the initial stage of the flow evolution. As mentioned in Sec. II.A, the PDC is purged with air before the combustion takes place. Figure 11a shows the corresponding purge flow jet just before the incident shock arrives at the tube exit. Figure 11b depicts the moment when the incident shock is fully diffracted outside of the tube. The corresponding schlieren image is shown in Fig. 7b. The maximum velocity occurs where the flow expands through the PM-expansion fan. The negative axial velocity (dark blue region) indicates the presence of a vortex ring. For the subsequent discussion, we set the clock to time of $t = 0$ at the instance shown in Fig. 11b when the incident shock appears for the first time in the measurement domain. Figure 11c shows the exhaust flow 0.1 ms later, which corresponds to the schlieren image shown in Fig. 7d. Compared to Fig. 11b, the jet is now further expanded and the vortex ring is larger. As the vortex ring propagates further downstream (Figs. 11d–11f), the jet close to the tube exit begins to exhibit the shock structures characteristic of an underexpanded jet. The radial velocity presented in Figs. 12d–12f shows the typical velocity field for a shock cell structure within the supersonic jet ($-0.5 < y/D < 0.5$). The shock cell structure is characterized by regions of positive and negative radial velocities because the flow is redirected in the transverse direction by the oblique shocks.

The leading shock wave is followed by a rarefaction wave known as the Taylor wave. Furthermore, when the leading shock wave leaves the tube, a set of rarefaction waves is generated, which propagate back into the tube. Therefore, the pressure inside the tube decreases; consequently, the jet velocity at the tube exit decreases. Eventually, the pressure drops sufficiently low that the supersonic underexpanded jet becomes a subsonic jet. From Fig. 12g, it seems that, at $t = 4.5$ ms, the supersonic underexpanded jet has already transformed to a subsonic jet because no shock cell structure can be observed. Although the pressure inside the tube decays further, the jet velocity decreases accordingly until the flow direction reverses. Figure 11h shows the moment when the fluid close to the tube exit flows back toward the tube. Figure 11i, shows a high-momentum reverse flow with a minimum axial velocity of -109.2 m/s, which takes place at the outlet. The first suction phase lasts about 10 ms. Figures 11j and 11k show two vortex rings at $t = 19.4$ ms and $t = 37.6$ ms, which indicate two additional exhaust phases. Figure 11l shows the purge jet as the blowdown process is finished.

B. Global Flow Quantities During Blowdown

To get an impression of the overall flow fluctuations that occur during the PDC cycle, we extract centerline global flow quantities from the PIV data. The first quantity, termed $u_{\mathrm{min\,/\,max}}$, represents the local velocity minima or maxima, whereas the second quantity $\dot{V}$ represents the global (radially integrated) streamwise volume flux close to the tube exit. With these two quantities, the local extreme

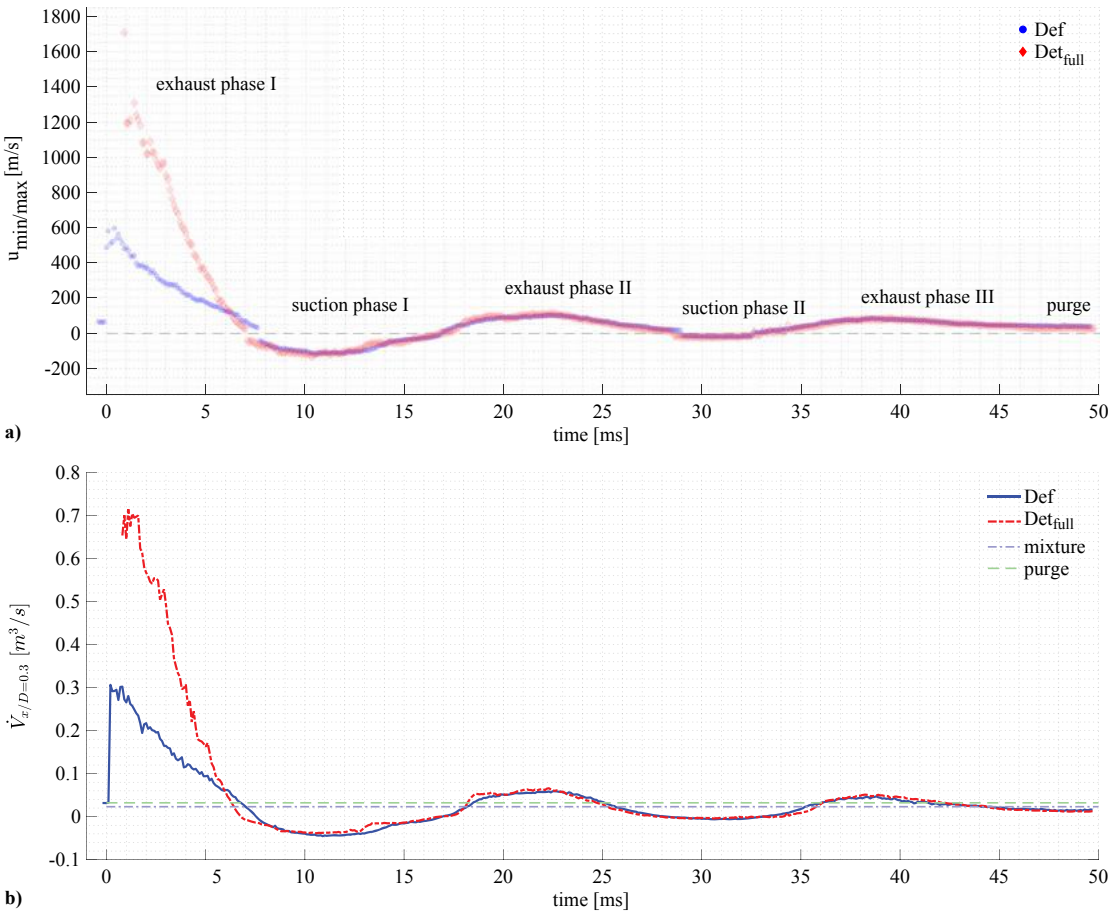

Fig. 13 Representations of a) axial velocity $u_{\mathrm{min\,/\,max}}$ and b) volume flux at $x/D = 0.3$ over time, showing the exhaust and suction phases of the PDC exhaust flow for $\mathrm{Det}_{\mathrm{full}}$ and Def cases.

events and the overall global dynamics of the flowfield at the exhaust can be quantified.

The volume flux at the tube exit is defined as

$$\dot{V}(t) = \oint_A u_x(t)\,\mathrm{d}A$$

where u_x is the instantaneous streamwise velocity component, and A is the tube cross-sectional area. Because the PIV data are only available in a plane perpendicular to the cross-sectional area, the integral is conducted only in radial direction assuming an axisymmetric flowfield. As seen from the snapshots shown in Fig. 11, this assumption is valid. Moreover, PIV is not available exactly at the tube outlet, and the volume flux is determined at the most reliable upstream measurement location of $x/D = 0.3$.

Regarding the local measure $u_{\min/\max}$ of the exhaust flow velocity, the definition is less straightforward. The purpose of this quantity is to reveal the highest absolute velocity occurring in the flowfield during the blowdown and suction phases. For this purpose, we define a region E near the tube exit, where this quantity is evaluated (see dashed rectangle in Fig. 11l). We then evaluate the average flow direction from spatially averaging the vectors within this area. Thereafter, we search for the highest velocity in this direction in area E and assign this value to the quantity $u_{\min/\max}$. In practice, instead of taking the highest velocity, we take an average of the five highest velocities to minimize the impact of outliers. In that sense, this quantity represents the local maximum axial velocity in the vicinity of the tube exit while accounting for the flow direction. It complements the global measure of the axial volume flux.

Figure 13a presents the quantity $u_{\min/\max}$ for both Def and $\mathrm{Det_{full}}$ cases for the first 50 ms of the PDC cycle. We start evaluating the Def case before proceeding further with the $\mathrm{Det_{full}}$ case. After the shock wave leaves the tube, the velocity increases up to 483 m/s at $t = 0$. The further expansion of the jet caused by the expansion waves (Fig. 11f) leads to a maximum velocity of 601 m/s at $t = 0.4$ ms. The oscillation of $u_{\min/\max}$ up to $t = 0.5$ ms is mainly due to the presence of shock cells (Figs. 12c–12f). From $t = 0.5$ to 7.6 ms, the velocity decreases gradually (Fig. 13a). At $t = 7.7$ ms, the axial velocity is negative, indicating the presence of a reverse flow. The maximum backflow velocity of −118 m/s occurs at $t = 10.5$ ms. The first suction phase lasts up to $t = 16.9$ ms. A secondary exhaust phase takes place from $t = 17$ to 28.9 ms (exhaust phase II) with a maximum velocity of 104.6 m/s. This is followed by a secondary suction phase from $t = 29$ to 32.5 ms. A third exhaust phase is notable from $t = 32.6$, which is again followed by a decreasing velocity phase. The several exhaust and suction phases are caused due to the compression and expansion waves propagating inside the PDC. These waves reflect at the interface between the combustible mixture and the air within the DDT section (Fig. 5c), the cross-section contraction, the closed end, and the open end of the tube.

The impact of the fill fraction on the evolution of the exhaust flow is estimated by comparing the axial velocity and the volume flux at the tube exit of the $\mathrm{Det_{full}}$ case to the Def case. As seen in Fig. 13a, the $\mathrm{Det_{full}}$ case also features three exhaust phases and two suction phases. In comparison to the Def case, the axial velocity in the first exhaust phase is significantly higher, which is caused by the detonation wave propagating through the entire exhaust tube. Due to difficulties with the seeding of the flow just upstream the detonation wave, the first accurate measurement point occurs at $t = 0.9$ ms. The velocity at this time is the maximum measured axial velocity of the exhaust flow ($u_{\min/\max} = 1708$ m/s). From Fig. 13, it is clear that, in the first exhaust phase, the flow decelerates at a higher rate when compared to the Def case. Figures 14a–14c show the corresponding axial velocity contour plots of the jet. The first suction phase begins at $t = 7.1$ ms, as shown in Fig. 13. From here on, the jet evolution is very similar to the Def case. The high-momentum reverse flow and the subsequent vortex rings of the second and third exhaust phases are presented in Figs. 14d–14f, respectively. These plots show the velocity field of the $\mathrm{Det_{full}}$ case for the same moments ($t = 10.4$, 19.4, and 37.6 ms) as Figs. 11i–11k for the Def case. The almost identical flowfields emphasize the similarity of the exhaust flow once the first suction phase begins.

Figure 13b shows the global volume flux $\dot{V}$ evaluated at $x/D = 0.3$ for both $\mathrm{Det_{full}}$ and Def cases. The horizontal lines in the figure

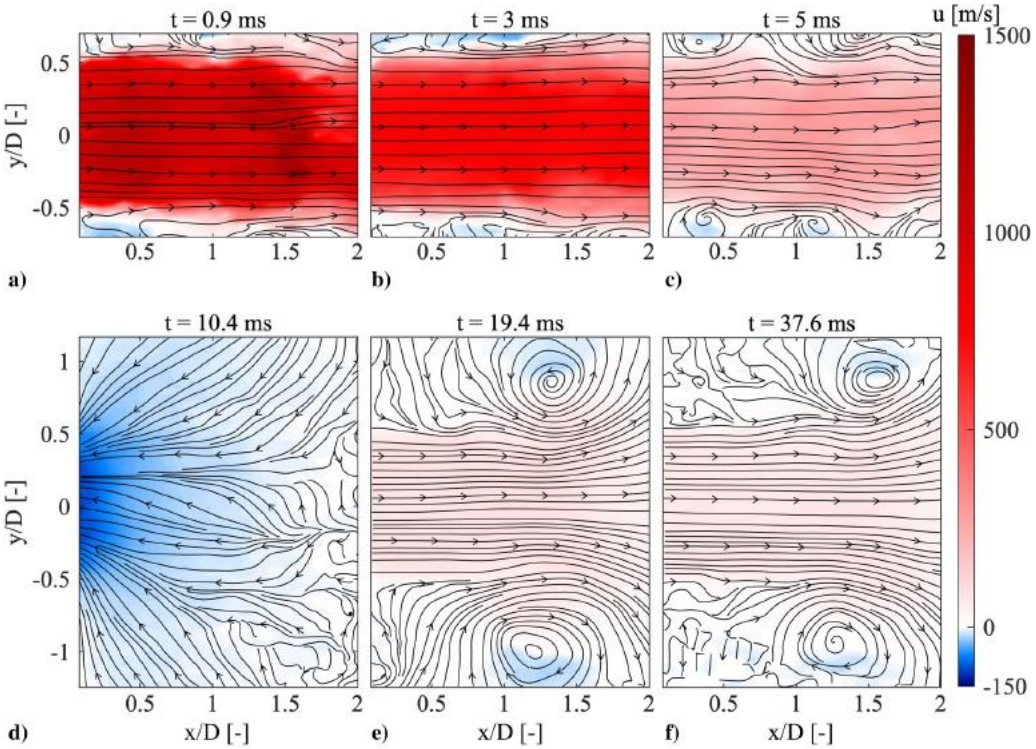

Fig. 14 Axial velocity fields of exhaust flow at six time steps showing evolution of flow for $\mathrm{Det_{full}}$ case. Streamlines calculated from instantaneous velocity fields are superimposed on contours to indicate flow direction.

further indicate the volume flux determined from the preset values of the air and hydrogen flow rates for the mixture and purge phases. As seen for the Def case, the preset value for the purge phase agree very well with the time of $t = 0$, which justifies the accuracy of the PIV results and the determination of $\dot{V}$. Once the shock wave exits the tube, the volume flux increases abruptly from 0.032 m^3/s at $t = 0$ to its maximum value of 0.31 m^3/s at $t = 0.2$ ms for the Def case, and it is more than twice this value for the Det_{full} case. The relative difference between the two is very similar to the one observed for the local streamwise velocities discussed before. Moreover, the global volume flux shows a very similar oscillatory behavior to the local velocity measure. It is further evident that the oscillations asymptotically converge to the preset volume flow (horizontal line).

These results suggests that, for the current PDC design, the fill fraction impacts only the first exhaust phase in regard to the exhaust velocity. The subsequent suction and exhaust phases are very similar in terms of timing, velocity magnitude, and the overall flow topology. The exhaust flow after the first exhaust phase is assumed to be mainly controlled by the rarefaction and compression waves travelling along the tube. Interestingly, the pressure measured close to the tube outlet shows a similar arriving time and amplitude for the subsequent expansion and compression waves for a number of different fill fractions. The mechanism responsible for this nearly identical wave dynamics, however, remains an open question.

V. Conclusions

In this study, the exhaust flow of a PDC was investigated using high-speed schlieren and PIV. To conduct reliable PIV measurements for theses strongly shock-driven flows, the relaxation times of different PIV seeding particles were evaluated in a preliminary study based on the PIV of a highly underexpanded steady jet. These studies suggest that TiO_2 particles are most suitable in terms of time lag and particle dispersion. These particles were then used to conduct PIV in the PDC exhaust flow for three different PDC fill fractions. To the authors' knowledge, this is the first time that high-speed PIV is used to resolve the full cycle of a PDC. The acquired flow data combine very well with the high-resolution schlieren images presented in this study.

The high-speed schlieren images reveal the initial evolution of the flow features in detail. For the partially filled tube, the exhaust flow corresponds to the flowfield of a classical open-ended shock tube. The incident shock diffracts as it exits the tube. The flow is characterized by a vortex ring and a secondary shock system. A number of counter-rotating vortex rings emerge from the shear layer of a slipstream, which originates from the triple point of a Mach reflection. These vortex rings propagate around the main vortex ring shortly after the main vortex ring separates from the trailing jet. After the pinchoff process, an underexpanded jet evolves, which is characterized by its typical shock diamond structure. As more and more combustion products leave the tube, the schlieren images become dominated by high-density gradient combustion products. Very similar flow features are also found for the cases with higher fill fractions where a detonation wave occurs. Based on the schlieren images, the same flow dynamics are observed but the strength and size of the flow features have increased as the velocity of the leading shock increases. In this situation, however, many details about the shock structures are blurred in the schlieren images due to the combustion products arriving shortly after the leading shock wave.

The full cycle of the exhaust flow is investigated based on the PIV data acquired at the tube exit. The high-speed PIV results show that the initial exhaust phase is followed by an even longer suction phase. A subsequent second exhaust–suction phase occurs, which is followed by a third exhaust phase. These exhaust and suction phases are caused by a number of compression and expansion waves propagating inside the PDC. Comparing the PIV results for the partially and overfilled operating conditions shows that the fill fraction only affects the first exhaust phase with respect to the local axial velocity and the global volume flux. The subsequent suction and exhaust phases are surprisingly similar in terms of timing and velocity. The fact that the local flow features determined from schlieren also remain similar leads to the conclusion that the exhaust flow of the PDC for the overfilled configuration undergoes the same fluid dynamic development as it does for a partially filled case. Although, with the increasing of the fill fraction, the combustion products occur earlier, the nature of the exhaust flow remains unchanged.

The characterization of the dynamic evolution of the PDC exhaust flow can be used for various purposes. The detailed description in this work concerning the evolution of the various flow features and their interactions with each other helps to gain a better understanding of the exhaust flow of a detonation or shock tube. Moreover, from the application point of view for the PDC, these results support the design and optimization process for the coupling of the PDC with a turbine. Furthermore, the results can be used as a benchmark for validation of computational simulations.

Acknowledgments

The authors gratefully acknowledge support by the Deutsche Forschungsgemeinschaft as part of collaborative research center SFB 1029 "Substantial Efficiency Increase in Gas Turbines Through Direct Use of Coupled Unsteady Combustion and Flow Dynamics" on project C01. The authors also acknowledge FDX Fluid Dynamix GmbH, for providing fluidic oscillators.

References

[1] Kailasanath, K., "Recent Developments in the Research on Rotating-Detonation-Wave Engines," *55th AIAA Aerospace Sciences Meeting*, AIAA Paper 2017-0784, 2017.

[2] Yungster, S., Paxson, D. E., and Perkins, H. D., "Numerical Investigation of Shrouded Ejector-Enhanced Pulse Combustor Performance at High Pressure," *Journal of Propulsion and Power*, Vol. 33, No. 1, 2016, pp. 29–42.

[3] Pandey, K., and Debnath, P., "Review on Recent Advances in Pulse Detonation Engines," *Journal of Combustion*, Vol. 2016, No. 5, 2016, pp. 1–16.
https://doi.org/10.1155/2016/4193034

[4] Wolański, P., "Detonative Propulsion," *Proceedings of the Combustion Institute*, Vol. 34, No. 1, 2013, pp. 125–158.
https://doi.org/10.1016/j.proci.2012.10.005

[5] Rasheed, A., Furman, A. H., and Dean, A. J., "Experimental Investigations of the Performance of a Multitube Pulse Detonation Turbine System," *Journal of Propulsion and Power*, Vol. 27, No. 3, 2011, pp. 586–596.
https://doi.org/10.2514/1.B34013

[6] Xisto, C., Petit, O., Grönstedt, T., Rolt, A., Lundbladh, A., and Paniagua, G., "The Efficiency of a Pulsed Detonation Combustor–Axial Turbine Integration," *Aerospace Science and Technology*, Vol. 82, Nov. 2018, pp. 80–91.
https://doi.org/10.1016/j.ast.2018.08.038

[7] Lisanti, J. C., and Roberts, W. L., "Pulse Combustor Driven Pressure Gain Combustion for High Efficiency Gas Turbine Engines," *Combustion for Power Generation and Transportation*, Springer, New York, 2017, pp. 127–152.

[8] Paniagua, G., Iorio, M., Vinha, N., and Sousa, J., "Design and Analysis of Pioneering High Supersonic Axial Turbines," *International Journal of Mechanical Sciences*, Vol. 89, Dec. 2014, pp. 65–77.
https://doi.org/10.1016/j.ijmecsci.2014.08.014

[9] Topalovic, D., Wolff, S., Heinrich, A., Peitsch, D., and King, R., "Minimization of Pressure Fluctuations in an Axial Turbine Stage Under Periodic Inflow Conditions," *AIAA Propulsion and Energy 2019 Forum*, AIAA Paper 2019-4213, 2019.

[10] Glaser, A., Caldwell, N., and Gutmark, E., "Performance of an Axial Flow Turbine Driven by Multiple Pulse Detonation Combustors," *45th AIAA Aerospace Sciences Meeting and Exhibit*, AIAA Paper 2007-1244, 2007.

[11] Arienti, M., and Shepherd, J., "A Numerical Study of Detonation Diffraction," *Journal of Fluid Mechanics*, Vol. 529, April 2005, pp. 117–146.
https://doi.org/10.1017/S0022112005003319

[12] Schultz, E., "Detonation Diffraction Through an Abrupt Area Expansion," Ph.D. Thesis, California Inst. of Technology, Pasadena, CA, 2000.

[13] Allgood, D., Gutmark, E., Meyer, T., Hoke, J., Katta, V., Schauer, F., and Gord, J., "Computational and Experimental Studies of Pulse Detonation Engines," *41st AIAA Aerospace Sciences Meeting and Exhibit*, AIAA Paper 2003-0889, 2003.

[14] Ma, F., Choi, J.-Y., and Yang, V., "Thrust Chamber Dynamics and Propulsive Performance of Single-Tube Pulse Detonation Engines," *Journal of Propulsion and Power*, Vol. 21, No. 3, 2005, pp. 512–526. https://doi.org/10.2514/1.7393

[15] Hoke, J., Naples, A., Goss, L., and Schauer, F., "Schlieren Imaging of a Single-Ejector, Multi-Tube Pulsed Detonation Engine," *47th AIAA Aerospace Sciences Meeting Including the New Horizons Forum and Aerospace Exposition*, AIAA Paper 2009-1065, 2009.

[16] Opalski, A., Paxson, D., and Wernet, M., "Detonation Driven Ejector Exhaust Flow Characterization Using Planar DPIV," *41st AIAA/ASME/SAE/ASEE Joint Propulsion Conference & Exhibit*, AIAA Paper 2005-4379, 2005.

[17] Glaser, A., Allgood, D., and Gutmark, E., "Experimental Investigation Into the Off-Design Performance of a Pulse Detonation Engine," *42nd AIAA Aerospace Sciences Meeting and Exhibit*, AIAA Paper 2004-1208, 2004. https://doi.org/10.2514/6.2004-1208

[18] Allgood, D. C., Gutmark, E., Rasheed, A., and Dean, A., "Experimental Investigation of a Pulse Detonation Engine with a Two-Dimensional Ejector," *AIAA Journal*, Vol. 43, No. 2, 2005, pp. 390–398. https://doi.org/10.2514/1.8125

[19] Li, C., Kailasanath, K., and Patnaik, G., "A Numerical Study of Flow Field Evolution in a Pulsed Detonation Engine," *38th Aerospace Sciences Meeting and Exhibit*, AIAA Paper 2000-0314, 2000.

[20] Schauer, F., Stutrud, J., and Bradley, R., "Detonation Initiation Studies and Performance Results for Pulsed Detonation Engine Applications," *39th Aerospace Sciences Meeting and Exhibit*, AIAA Paper 2001-1129, 2001.

[21] Gray, J., Lemke, M., Reiss, J., Paschereit, C., Sesterhenn, J., and Moeck, J., "A Compact Shock-Focusing Geometry for Detonation Initiation: Experiments and Adjoint-Based Variational Data Assimilation," *Combustion and Flame*, Vol. 183, Sept. 2017, pp. 144–156. https://doi.org/10.1016/j.combustflame.2017.03.014

[22] Willert, C. E., Mitchell, D. M., and Soria, J., "An Assessment of High-Power Light-Emitting Diodes for High Frame Rate Schlieren Imaging," *Experiments in Fluids*, Vol. 53, No. 2, 2012, pp. 413–421. https://doi.org/10.1007/s00348-012-1297-1

[23] Bobusch, B. C., Woszidlo, R., Krüger, O., and Paschereit, C. O., "Numerical Investigations on Geometric Parameters Affecting the Oscillation Properties of a Fluidic Oscillator," *21st AIAA Computational Fluid Dynamics Conference*, AIAA Paper 2013-2709, 2013.

[24] Willert, C. E., and Gharib, M., "Digital Particle Image Velocimetry," *Experiments in Fluids*, Vol. 10, No. 4, 1991, pp. 181–193. https://doi.org/10.1007/BF00190388

[25] Scarano, F., "Iterative Image Deformation Methods in PIV," *Measurement Science and Technology*, Vol. 13, No. 1, 2001, paper R1. https://doi.org/10.1088/0957-0233/13/1/201

[26] Raffel, M., Willert, C. E., Scarano, F., Kähler, C. J., Wereley, S. T., and Kompenhans, J., *Particle Image Velocimetry: A Practical Guide*, Springer, New York, 2018, pp. 166–169.

[27] Mitchell, D., Honnery, D., and Soria, J., "Particle Relaxation and its Influence on the Particle Image Velocimetry Cross-Correlation Function," *Experiments in Fluids*, Vol. 51, No. 4, 2011, pp. 933–947. https://doi.org/10.1007/s00348-011-1116-0

[28] Yao, W., Guangsheng, G., Fei, W., and Jun, W., "Fluidization and Agglomerate Structure of SiO2 Nanoparticles," *Powder Technology*, Vol. 124, Nos. 1–2, 2002, pp. 152–159.

[29] Rezay Haghdoost, M., Förster, J., Edgington-Mitchell, D., and Oberleithner, K, "Experimental Investigation of Solid Tracer Particle Response Across a Mach Disk by PIV and Schlieren," *Proceedings of the 19th International Symposium on Application of Laser and Imaging Techniques to Fluid Mechanics*, Lisbon, 2018, pp. 1922–1940.

[30] Melling, A., "Tracer Particles and Seeding for Particle Image Velocimetry," *Measurement Science and Technology*, Vol. 8, No. 12, 1997, pp. 1406–1416. https://doi.org/10.1088/0957-0233/8/12/005

[31] Ragni, D., Schrijer, F., Van Oudheusden, B., and Scarano, F., "Particle Tracer Response Across Shocks Measured by PIV," *Experiments in fluids*, Vol. 50, No. 1, 2011, pp. 53–64. https://doi.org/10.1007/s00348-010-0892-2

[32] Gordon, S., and McBride, B. J., "Computer Program for Calculation of Complex Chemical Equilibrium Compositions and Applications," NASA Reference Publication 1311, 1996.

[33] Li, C., and Kailasanath, K., "Partial Fuel Filling in Pulse Detonation Engines," *Journal of Propulsion and Power*, Vol. 19, No. 5, 2003, pp. 908–916. https://doi.org/10.2514/2.6183

[34] Taylor, G. I., "The Dynamics of the Combustion Products Behind Plane and Spherical Detonation Fronts in Explosives," *Proceedings of the Royal Society of London, Series A: Mathematical and Physical Sciences*, Vol. 200, No. 1061, 1950, pp. 235–247. https://doi.org/10.1098/rspa.1950.0014

[35] Peace, J., and Lu, F., "Detonation-to-Shock Wave Transmission at a Contact Discontinuity," *Shock Waves*, Vol. 28, No. 5, 2018, pp. 981–992. https://doi.org/10.1007/s00193-018-0804-6

[36] Mirels, H., "Attenuation in a Shock Tube Due to Unsteady-Boundary-Layer Action," NACA Rept 1333, supersedes NACA TN 3278, 1957.

[37] Glass, I., "A Theoretical and Experimental Study of Shock-Tube Flows," *Journal of the Aeronautical Sciences*, Vol. 22, No. 2, 1955, pp. 73–100. https://doi.org/10.2514/8.3282

[38] Lee, J. H., *The Detonation Phenomenon*, Vol. 10, Cambridge Univ. Press, Cambridge, 2008.

[39] Ciccarelli, G., and Dorofeev, S., "Flame Acceleration and Transition to Detonation in Ducts," *Progress in Energy and Combustion Science*, Vol. 34, No. 4, 2008, pp. 499–550. https://doi.org/10.1016/j.pecs.2007.11.002

[40] Sun, M., and Takayama, K., "The Formation of a Secondary Shock Wave Behind a Shock Wave Diffracting at a Convex Corner," *Shock Waves*, Vol. 7, No. 5, 1997, pp. 287–295. https://doi.org/10.1007/s001930050083

[41] Friedman, M. P., "A Simplified Analysis of Spherical and Cylindrical Blast Waves," *Journal of Fluid Mechanics*, Vol. 11, No. 1, 1961, pp. 1–15. https://doi.org/10.1017/S0022112061000810

[42] Hornung, H., "Regular and Mach Reflection of Shock Waves," *Annual Review of Fluid Mechanics*, Vol. 18, No. 1, 1986, pp. 33–58. https://doi.org/10.1146/annurev.fl.18.010186.000341

[43] Edgington-Mitchell, D., Honnery, D. R., and Soria, J., "The Underexpanded Jet Mach Disk and Its Associated Shear Layer," *Physics of Fluids*, Vol. 26, No. 9, 2014, p. 1578. https://doi.org/10.1063/1.4894741

[44] Ishii, R., Fujimoto, H., Hatta, N., and Umeda, Y., "Experimental and Numerical Analysis of Circular Pulse Jets," *Journal of Fluid Mechanics*, Vol. 392, Aug. 1999, pp. 129–153. https://doi.org/10.1017/S0022112099005303

[45] Franquet, E., Perrier, V., Gibout, S., and Bruel, P., "Free Underexpanded Jets in a Quiescent Medium: A Review," *Progress in Aerospace Sciences*, Vol. 77, Aug. 2015, pp. 25–53. https://doi.org/10.1016/j.paerosci.2015.06.006

[46] Kleine, H., Le, C. V., Takehara, K., and Etoh, T. G., "Development of Shock-Vortex Systems Emitted from an Open Shock Tube," *29th International Congress on High-Speed Imaging and Photonics Proc. ICHSIP-29*, 2010.

[47] Dora, C., Murugan, T., De, S., and Das, D., "Role of Slipstream Instability in Formation of Counter-Rotating Vortex Rings Ahead of a Compressible Vortex Ring," *Journal of Fluid Mechanics*, Vol. 753, Aug. 2014, pp. 29–48. https://doi.org/10.1017/jfm.2014.353

[48] Fernández, J. J. P., and Sesterhenn, J., "Compressible Starting Jet: Pinch-Off and Vortex Ring–Trailing Jet Interaction," *Journal of Fluid Mechanics*, Vol. 817, April 2017, pp. 560–589. https://doi.org/10.1017/jfm.2017.128

[49] Radulescu, M. I., and Law, C. K., "The Transient Start of Supersonic Jets," *Journal of Fluid Mechanics*, Vol. 578, May 2007, pp. 331–369. https://doi.org/10.1017/S0022112007004715

[50] Kleine, H., Le, C. V., Takehara, K., and Etoh, T. G., "Time-Resolved Visualization of Shock–Vortex Systems Emitted from an Open Shock Tube," *Journal of Visualization*, Vol. 13, No. 1, 2010, pp. 33–40. https://doi.org/10.1007/s12650-009-0009-2

[51] Hamzehloo, A., and Aleiferis, P., "Large Eddy Simulation of Highly Turbulent Under-Expanded Hydrogen and Methane Jets for Gaseous-Fuelled Internal Combustion Engines," *International Journal of Hydrogen Energy*, Vol. 39, No. 36, 2014, pp. 21275–21296. https://doi.org/10.1016/j.ijhydene.2014.10.016

[52] Nadolski, M., Rezay Haghdoost, M., Gray, J. A. T., Edgington-Mitchell, D., Oberleithner, K., and Klein, R., "Validation of Under-Resolved Numerical Simulations of the PDC Exhaust Flow Based on High Speed Schlieren," *Active Flow and Combustion Control 2018*, Notes on Numerical Fluid Mechanics and Multidisciplinary Design, Vol. 141, edited by R. King, Springer International Publishing, Cham, Switzerland, 2019, pp. 237–253. https://doi.org/10.1007/978-3-319-98177-2_15

C. Lee
Associate Editor

4.3 Publication III

Shock Waves (2022) 32:195–211
https://doi.org/10.1007/s00193-021-01062-2

ORIGINAL ARTICLE

Numerical and experimental evaluation of shock dividers

M. Rezay Haghdoost[1] · B. S. Thethy[2] · M. Nadolski[3] · B. Seo[1] · C. O. Paschereit[4] · R. Klein[3] · D. Edgington-Mitchell[2] · K. Oberleithner[1]

Received: 30 March 2020 / Revised: 14 October 2021 / Accepted: 10 November 2021 / Published online: 17 January 2022

Abstract
Mitigation of pressure pulsations in the exhaust of a pulse detonation combustor is crucial for operation with a downstream turbine. For this purpose, a device termed the shock divider is designed and investigated. The intention of the divider is to split the leading shock wave into two weaker waves that propagate along separated ducts with different cross sections, allowing the shock waves to travel with different velocities along different paths. The separated shock waves redistribute the energy of the incident shock wave. The shock dynamics inside the divider are investigated using numerical simulations. A second-order dimensional split finite volume MUSCL-scheme is used to solve the compressible Euler equations. Furthermore, low-cost simulations are performed using geometrical shock dynamics to predict the shock wave propagation inside the divider. The numerical simulations are compared to high-speed schlieren images and time-resolved total pressure recording. For the latter, a high-frequency pressure probe is placed at the divider outlet, which is shown to resolve the transient total pressure during the shock passage. Moreover, the separation of the shock waves is investigated and found to grow as the divider duct width ratio increases. The numerical and experimental results allow for a better understanding of the dynamic evolution of the flow inside the divider and inform its capability to reduce the pressure pulsations at the exhaust of the pulse detonation combustor.

Keywords Supersonic flow · Shock divider · Bifurcated ducts · Channels · Cut-cell method · GSD · Total pressure

1 Introduction

The pulse detonation engine (PDE) has been the focus of propulsion research efforts in the last few decades, due to its potential to drastically increase the efficiency when compared to conventional gas turbines [1–3]. In a hybrid-PDE configuration, an annular array of pulse detonation combustors (PDCs) replaces conventional isobaric combustion chambers. One of the main challenges for implementing a hybrid PDE is to maintain reliable and efficient operation of the downstream turbine. Poor coupling of the PDC with the turbine could eliminate any potential gain in cycle efficiency provided from pressure gain combustion. The inherent cyclic operation of a PDC results in highly transient pressure and temperature fields at the PDC exhaust, which are highly undesirable for conventional turbines.

Efficient attenuation of the leading shock wave in the PDC exhaust flow is essential for turbine work extraction. Numerous studies of PDC–turbine applications confirm the occurrence of strong reflected shock waves at the turbine inlet resulting in significant losses [4–8]. Therefore, it is desirable to attenuate the strong leading shock wave transmitted from the detonation wave before it enters the turbine.

There are a number of studies on devices influencing the PDE exhaust flow. While most of the studies focus on the impact of different nozzles and ejectors on the performance of a single PDE engine [9–14], limited research has focused on the mitigation of the leading shock pressure in the PDE exhaust flow [15], despite its relevance for the integration of the PDC with a downstream turbine. One approach is to divide the leading shock wave in multiple

Communicated by K. Kontis.

M. Rezay Haghdoost
rezayhaghdoost@tu-berlin.de

[1] Laboratory for Flow Instabilities and Dynamics, Institute of Fluid Dynamics and Technical Acoustics, Technische Universitët Berlin, Berlin, Germany

[2] Laboratory for Turbulence Research in Aerospace and Combustion, Department of Mechanical and Aerospace Engineering, Monash University, Melbourne, Australia

[3] Department of Mathematics and Computer Science, Institute of Mathematics, Freie Universität Berlin, Berlin, Germany

[4] Chair of Fluid Dynamics, Institute of Fluid Dynamics and Technical Acoustics, Technische Universität Berlin, Berlin, Germany

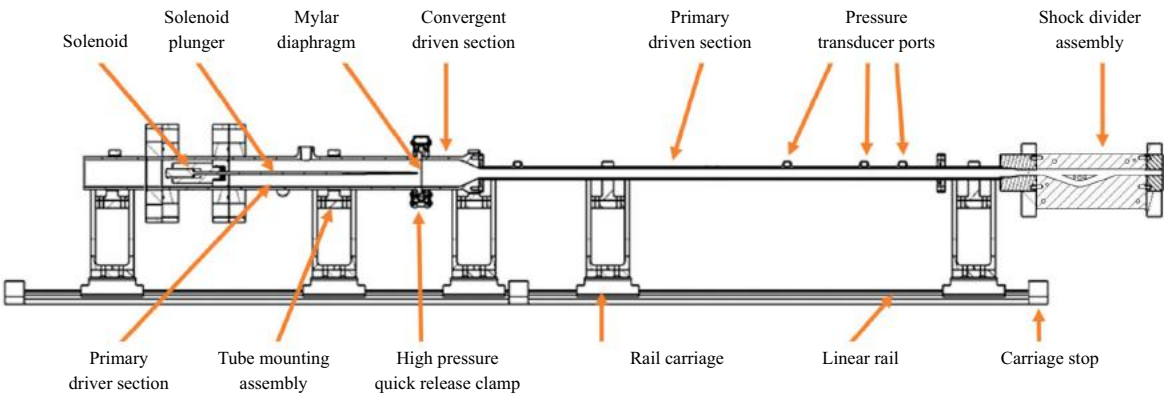

Fig. 1 Schematic diagram of the shock tube experimental facility with the shock divider assembly attached

weaker shock waves. In this manner, the energy produced in a single PDE cycle will be redistributed temporally. The temporal redistribution of the pressure across one PDE cycle results inherently in lower pressure fluctuations in a multi-cycle operation mode. Hence, a more suitable turbine-inlet flow can be obtained by dividing the leading shock wave into weaker shock waves.

A shock divider (thereafter simply termed *divider*) is proposed here as a method to spread the leading shock energy. This divider consists of a bifurcating section and a recombination section. In the bifurcating section, the incident strong shock wave is split and guided through two different ducts. The separated shock waves travel with different velocities along two pathways with different cross sections. The two shock waves are then transmitted into a single duct, after leaving the device. The key requirement for a divider design is a large temporal separation of the shocks at a minimum addition of losses.

Numerous studies on the propagation of shock waves through ducts with area changes were conducted in the last decades [16–19]. It was shown that the shock wave Mach number and the area ratio significantly impact the flow evolution. Moreover, the shock wave propagation in branched ducts was subject of various studies [20–23]. It was shown that losses due to reflection and diffraction of the shock wave can result in significant shock attenuation. However, to the best of the authors' knowledge, there is only very limited research on the recombination of separated shock waves.

For an efficient divider design, it is crucial to understand the determining fundamental flow dynamical mechanisms. Therefore, the aim of the current study is to provide a better understanding of the flow physics inside a generic divider. We employ numerical simulations and experimental methods to study the flow inside a divider with an incident shock Mach number of $M_s = 1.61$. For this purpose, the divider is mounted at the exit of an open-end shock tube, where high-speed schlieren images along with total pressure measurements are conducted. We use a second-order dimensional split finite volume MUSCL-scheme to solve the compressible Euler equations. Furthermore, the propagation of the leading shock waves inside the divider is modelled by using a simplified model called geometrical shock dynamics (GSD) [18]. We first validate our numerical results based on schlieren images and pressure recordings. Different divider geometries are then evaluated numerically to gain a better understanding of their impact on the flow evolution.

2 Methodology

2.1 Shock tube facility

Experiments are undertaken using an open-end shock tube facility. The facility, manufactured from stainless steel, consists of a 35.1-mm-diameter driver section and a 12.5-mm-diameter driven section. A diagram of the facility is shown in Fig. 1. The driver and driven sections are separated by a diaphragm made of polyester film with a 0.1-mm thickness. The operating gas for the driver section is a mixture of atmospheric air and helium, while the operating gas for the driven section is atmospheric air. Bursting of the diaphragm occurs through actuation of a linear solenoid and plunger. The driver section is 250 mm long with the solenoid located in a 90-mm section, unsealed from the primary driver section. The driven section is 675 mm long and contains a 25-mm conical converging section beginning 50 mm from the diaphragm. The driver and driven sections are held together under pressure using a high-pressure quick release clamp. Further details on the facility are given in [14].

Gauge pressure is measured in the driver section using a Gems Series 3100 Pressure Transducer to give the diaphragm pressure ratio. The signals from the pressure transducer are captured on a 16-bit National Instruments DAQ. The trigger

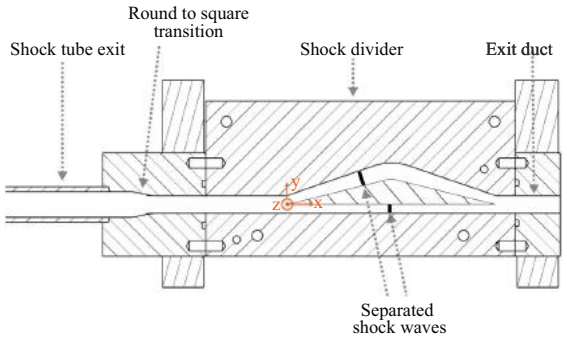

Fig. 2 Schematic diagram of the shock divider assembly

signal for the Ledex linear solenoid is provided as an output from the DAQ.

2.2 Shock divider

To separate a strong shock wave in multiple weaker shock waves, the assembly shown in Fig. 2 is utilised. This assembly is termed the shock divider. The shock divider connects to the end of the shock tube facility, as shown in Fig. 1. A shock wave is generated by the shock tube, which then travels into the shock divider assembly. The shock first travels through the round-to-square transition section (Fig. 2). There, the cross section of the geometry is transformed from a circular cross section to a square cross section using a seventh-order spline, as proposed by Wilson [24]. After the transition, the cross section of the geometry remains square throughout the divider assembly. The origin of the Cartesian coordinate system is the inlet of the divider centre body (Fig. 2).

After the shock wave passes through the round-to-square transition section, it enters the central divider assembly. The divider assembly, indicated in Fig. 2, separates the initial incident shock wave into two shock waves. Each shock is allowed to travel along different paths with different duct width and path length. The central divider assembly consists of two flat transparent perspex sides surrounded by a central machined aluminium section. The perspex walls allow for optical access to the internal flow within the divider. The separated shock waves then enter the same exit pathway before being diffracted out of the open end of the divider.

Three different shock dividers are investigated in the current study, as shown in Fig. 3. The investigated shock dividers consist of two branches: the upper branch and the lower branch. The lower branch in all dividers is a simple constant-width straight duct, whereas the upper branch is characterised by a curvature.

The leading edge of the divider centre body is located at the divider inlet prior to the separation of the divider branches (Fig. 3a). Therefore, the shock wave does not

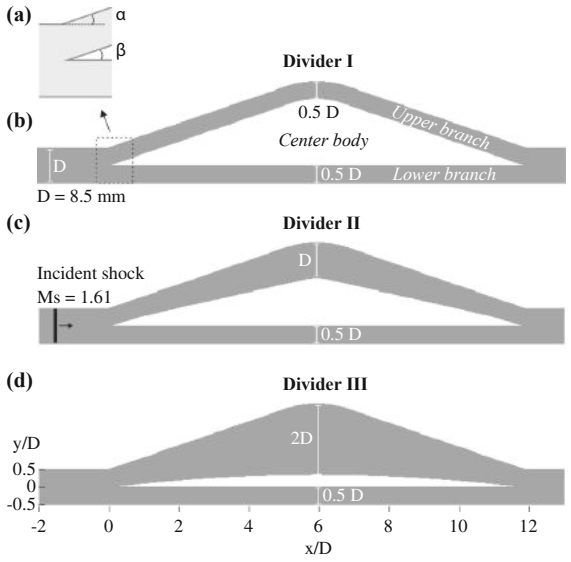

Fig. 3 Divider assemblies. Dimensions are normalised by the divider square side length D

diffract before it enters the divider. Consequently, the shock waves transmitted to the divider branches are expected to have nearly the same Mach number at the divider inlet. To induce different arrival times of the shock waves at the divider outlet, the path of the upper branch is longer than that of the lower branch. While the duct width of the lower and upper branches is equal in divider I (Fig. 3b), this is not the case for dividers II and III (Fig. 3c, d). In a parametric study, the width of the upper branch is increased from 0.5 to 2 D from dividers I–II (Fig. 3). The upper branches are modified simply by changing the centre body of the divider. Hence, the angle $\alpha = 19$ shown in Fig. 3a remains unchanged for all dividers, whereas β decreases from dividers I–III. The angle β is 19, 13, and 7 for dividers I, II, and III, respectively. Accordingly, the transmitted shock wave into the upper channel of divider III faces a distinctive increase in cross section, a smaller increase in divider II, and no change in cross section in dividers I. The length of the channel centreline is 5, 4, and 2% longer than the lower branch for dividers I–III, respectively. The Mach number of the incident shock wave at the divider inlet is $M_s = 1.61$ for all investigated configurations in the current study.

2.3 Schlieren setup

To complement the numerical results, schlieren measurements of the shock divider flow are taken using a Toepler Z-Type schlieren system [25], as shown in Fig. 4. The 8" schlieren mirrors have a focal length of 1219 mm. Images

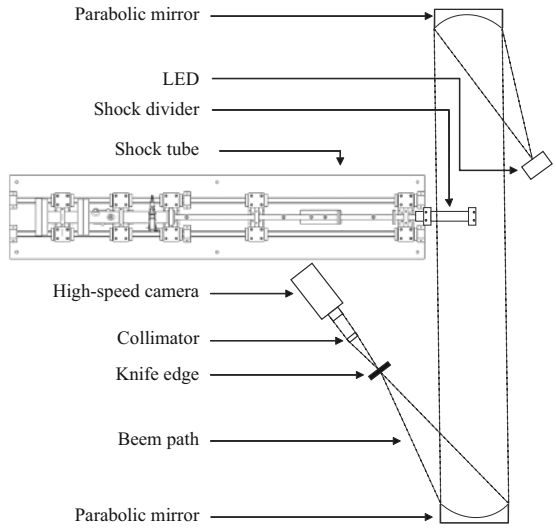

Fig. 4 Schematic diagram of the shock tube experimental facility with attached shock divider assembly

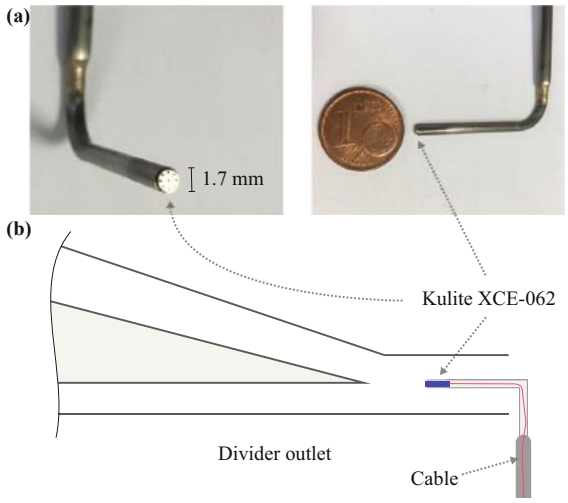

Fig. 5 **a** Photographs of the total pressure probe and **b** the measurement position inside the divider

are acquired using a Photron FASTCAM SA-Z 2100K up to a frame rate of 210 kHz. This provides ultra-high-speed images of the motion of the shock wave within the divider. The flow motion is illuminated using a pulsed LED light source with an exposure time of 1 μs [26]. The signal from PCB pressure transducer located 50 mm from the divider inlet is used as a trigger for the camera. A precise timing control is provided by a Beaglebone Black processor, developed by Fedrizzi and Soria [27].

2.4 High-frequency total pressure probe

Time resolved measurement of total pressure behind transient shock waves is very challenging [28–30]. In this work, an in-house-made high-frequency total pressure probe is used to measure the total pressure at the exit of the divider. Figure 5a shows two photographs of the probe. The probe design is based on the probe used previously by Paxson and Dougherty [31] to measure the total pressure behind a pulsejet. To allow for high-frequency pressure measurements, the transducer is placed directly at the head of the probe (Fig. 5). A Kulite XCE-062 miniature transducer is mounted in a L-shaped tube, allowing the sensor to be placed within the divider (Fig. 5b). A Kulite KSC-2 signal conditioner is used to amplify the measured signal. The relatively high resonance frequency of the sensor allows for a nearly non-oscillating signal behind the shock wave [29,32]. The probe is mounted at $x/D = 12.5$ inside the divider. Simultaneous schlieren measurements of the probe head are used to ensure the absence of a bow shock in front of the sensor.

2.5 Numerical methods

2.5.1 Geometrical shock dynamics (GSD)

Geometrical shock dynamics (GSD) is a simplified approach to predict shock wave propagation. It was first introduced by Whitham [33]. An illustration of the approach is presented in Fig. 6. The method is based on the decomposition of the shock front into elementary parts propagating independently along ray tubes. A ray tube is treated as a duct of cross-sectional area A with rigid walls. The approach is based on the assumption that the motion of the shock only depends on the variation of the local ray tube. Hence, the motion of the shock wave is determined without calculating the flow field downstream of the shock wave.

The motion of the shock wave is determined by a relation between the cross-sectional area A and the local Mach number M, using the A–M relation:

$$\frac{A_i(t)}{A_i(0)} = \frac{f(M_i(t))}{f(M_i(0))}, \tag{1}$$

where the subscript i denotes the index of each segment and A and M are their area and shock Mach number, respectively. The function $f(M)$ is given as

$$f(M) = \exp(-f_e(M)), \tag{2}$$

$$f_e(M) = \int_{M_{\min}}^{M} \frac{M\lambda(M)}{M^2-1} dM, \tag{3}$$

$$\lambda(M) = \left(1 + \frac{2}{\gamma+1}\frac{1-\mu^2}{\mu}\right)\left(1 + 2\mu + \frac{1}{M^2}\right), \tag{4}$$

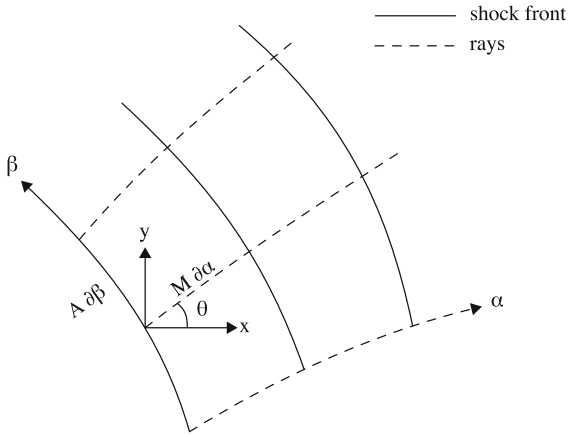

Fig. 6 Rectangular (x, y) and curvilinear (α, β) coordinate systems. Shock front given by $\alpha = \text{const}$ and rays given by $\beta = \text{const}$

$$\mu^2 = \frac{(\gamma - 1)M^2 + 2}{2\gamma M^2 - (\gamma - 1)}, \tag{5}$$

where γ is the specific heat ratio.

Numerous methods are used for numerical implementation of GSD [34–38]. The implementation used in the current study is based on the front tracking method introduced by Henshaw et al. [34]. A short overview of the applied numerical implementation is given in the following. Detailed information regarding the numerical scheme can be found in [34].

The discretised elements of the shock wave propagate along rays normal to the shock front $\mathbf{n_i}$, with a local speed depending on the local Mach number M_i (Fig. 6). As shown by Henshaw et al. [34], the transformation from the curvilinear coordinate system to the rectangular system along a ray leads to

$$\frac{\partial x(\beta, t)}{\partial \alpha} = M(\beta, t)\cos\theta, \tag{6}$$

$$\frac{\partial y(\beta, t)}{\partial \alpha} = M(\beta, t)\sin\theta, \tag{7}$$

$$\frac{\mathrm{d}}{\mathrm{d}t}\mathbf{x}_i(t) = a_0 M_i(t)\mathbf{n}_i(t), \quad i = 1, \ldots, N. \tag{8}$$

Equation (8) is the vector form of (6)–(7), while α is eliminated in favour of time t using $\alpha = a_0 t$, where a_0 is the speed of sound upstream of the shock. This results in a nonlinear system of ordinary differential equations, which is closed by (2)–(5).

An explicit second-order two-step leap-frog scheme is used for the numerical integration, while the time step Δt is adapted in every step to maintain the CFL condition:

$$\mathbf{x_i}(t + \Delta t) = \mathbf{x_i}(t - \Delta t) + 2\Delta t a_0 M_i(t)\mathbf{n_i}(t). \tag{9}$$

$$A_i(t) = \frac{1}{2}\begin{cases} s_{i+1}(t) - s_i(t), & \text{if } i = 1; \\ s_{i+1}(t) - s_{i-1}(t), & \text{if } i = 2, \ldots, N-1; \\ s_i(t) - s_{i-1}(t), & \text{if } i = N, \end{cases} \tag{10}$$

where the arclength $s(t)$ represents the geometry of the shock and is given by

$$s_i(t) = \begin{cases} 0, & \text{if } i = 1; \\ s_{i-1}(t) + |x_i(t) - x_{i-1}(t)|, & \text{if } i = 2, \ldots, N. \end{cases} \tag{11}$$

The Mach number in (9) is determined by using (1). As given in (10), the cross-sectional area $A_i(t)$ is determined by a one-sided scheme at the endpoints and a centred scheme about the point $x_i(t)$.

2.5.2 Numerical simulation scheme (CFD)

Numerical simulation of the flow inside the shock divider is conducted based on the compressible Euler equations. The equations are given in their two-dimensional conservative form as

$$\frac{\partial}{\partial t}\begin{pmatrix}\rho \\ \rho u \\ \rho v \\ \rho E\end{pmatrix} + \frac{\partial}{\partial x}\begin{pmatrix}\rho u \\ \rho u^2 + p \\ \rho v u \\ u(\rho E + p)\end{pmatrix} + \frac{\partial}{\partial y}\begin{pmatrix}\rho u \\ \rho u v \\ \rho v^2 + p \\ v(\rho E + p)\end{pmatrix} = 0, \tag{12}$$

where ρ is the density, $\mathbf{u} = (u, v)$ the particle velocity, $E = e + \|\mathbf{u}\|^2/2$ the total energy, e the internal energy, and p the pressure. Equations (12) are closed by the caloric perfect gas approximation $p = \rho(\gamma - 1)e$, where the adiabatic index $\gamma = C_p/C_v = 1.4$ is assumed to be constant. To solve these equations, a fully conservative second-order dimensional split finite volume MUSCL-scheme is used [39,40]. To prevent artificial oscillations in the numerical solution, the slopes of the reconstruction step are limited with the van-Leer limiter. The solution is discretised on a structured grid. A level set is used to embed the boundary of the divider into the structured grid and results into irregular cut cells, which need special treatment. A conservative cut-cell method is used to ensure stability for arbitrarily small cells such that no mass flows through the boundary [41,42].

In the simulations, the shock tube and the divider are initially filled with air at atmospheric pressure and room temperature. An initial Riemann problem is set up at the exit of the shock tube. Using the Rankine–Hugoniot conditions, the left state of the Riemann problem is set to be the post-shock state of a shock with a Mach number of $M_s = 1.61$. Transmissive boundary conditions are set at the upstream and downstream domain boundaries.

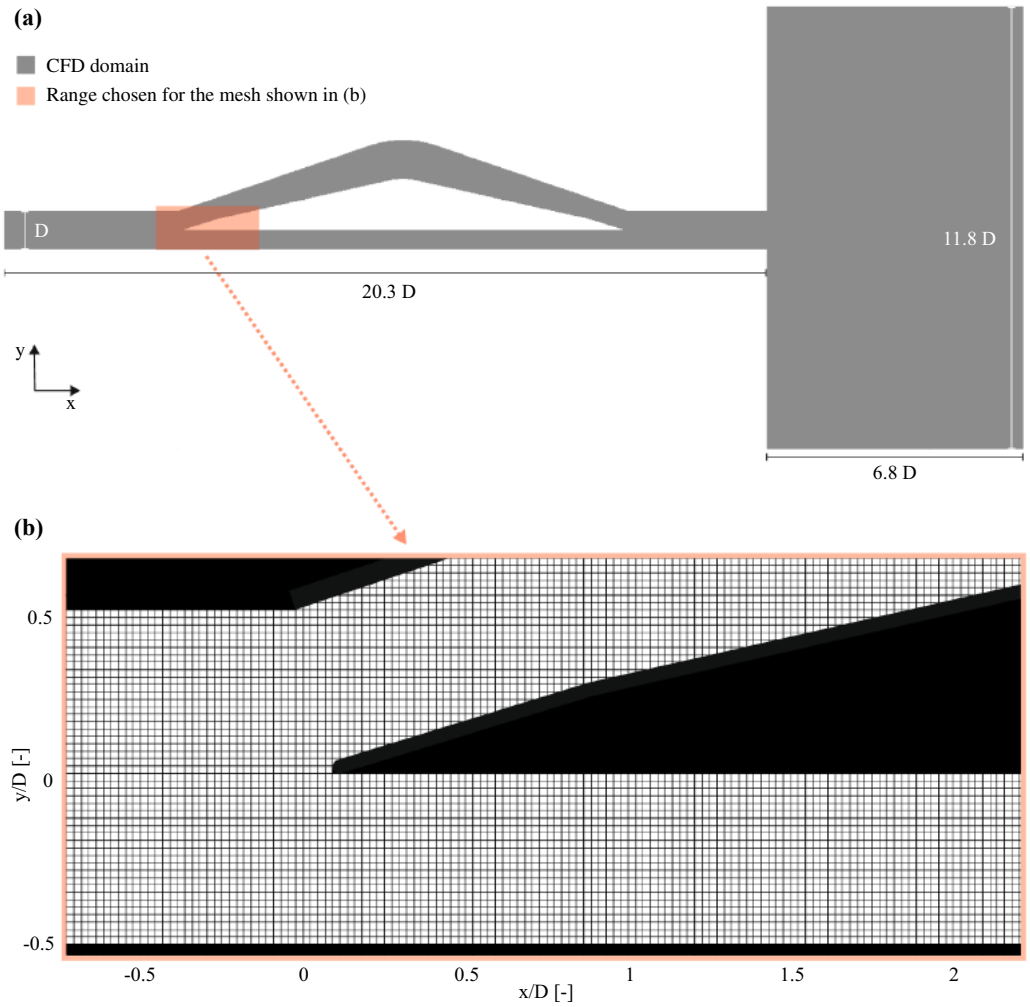

Fig. 7 **a** CFD domain and **b** grid with 46 cells in y-direction discretising the inlet channel of divider II ($N_D = 46$)

The measurement domain used for the CFD simulations is shown exemplary for divider II in Fig 7a. Figure 7b illustrates the Cartesian structured grid using 46 cells in y-direction to discretise the divider channel width ($N_D = 46$). While $N_D = 46$ is used for all simulations conducted in this work, the total number of cells increases slightly from dividers I to III. The total number of cells for the entire domain shown in Fig 7a is 198,603, 204,846, and 216,297 for dividers I–III, respectively.

Five simulations using a Cartesian structured grid with different resolutions from $N_D = 11$–184 are conducted to investigate the grid dependency. For the grid dependency study, divider III is used, which represents presumably the most critical configuration, as it results in the strongest diffraction of the shock wave in its upper branch. Figure 8a illustrates the shock wave inside the upper branch of divider III for the time when the shock wave reaches the centre of the divider's centre body; lower end of the blue line in Fig. 8a is at $x/D = 6$. A pink box in Fig. 8a represents the range chosen for the data shown in Fig. 8b. The pressure shown in Fig. 8b represents the pressure from $x/D = 2$ to 6.4 and $y/D = 0.4$ for different grid resolutions at $t = 0.156$ ms. Downstream of the shock wave $2 < x/D < 6$, the pressure profiles differ only slightly, except for $N_D = 11$. The pressure in the vicinity of the shock wave is presented in Fig. 8c. The results show that regardless of grid resolution the shock wave is captured approximately across four to six cells. Hence, the pressure rise across the shock wave is captured more distinctively for finer grid resolution. However, even the coarsest grid using only 11 cells to discretise the divider's channel width ($N_D = 11$) resolves the position of the shock wave remarkably well when compared to the finer

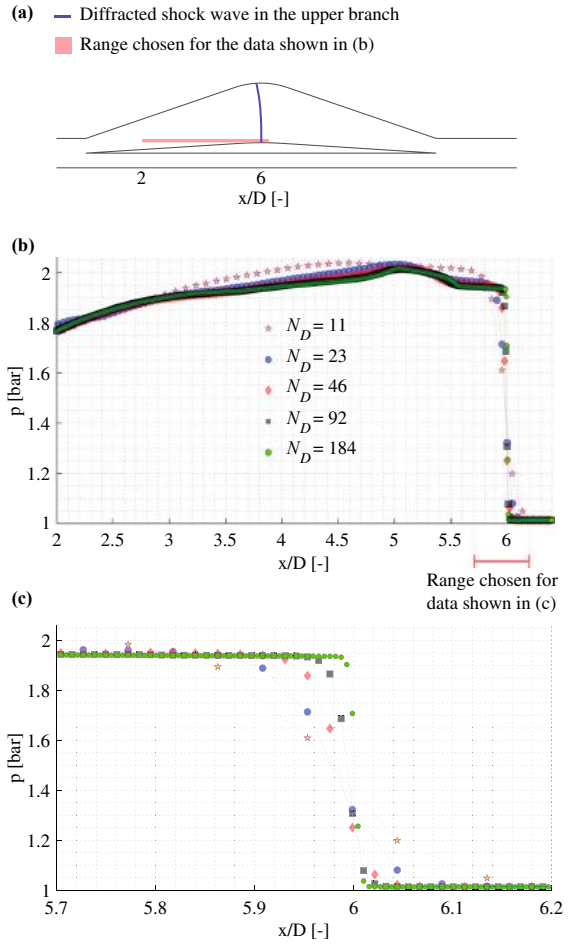

Fig. 8 **a** Schematic illustration of the incident shock wave inside the upper channel of divider III. **b** Pressure in the cell next to the centre body in the vicinity and far downstream of the incident shock at $t = 0.156$ ms. **c** Zoomed view of the data shown in **b**

grids (Fig. 8b, c). While the pressure downstream of the shock wave is about 5% larger for $N_D = 11$ compared to the others, the results of $N_D = 23$–184 do not differ significantly regarding both the position and the pressure downstream of the shock.

3 Results and discussion

We start with the validation of the numerical schemes by comparison with the experimental results. The validated numerical results are then used to analyse the flow evolution inside the shock dividers. Finally, we evaluate the impact of the divider width ratio on the separation of the shock waves.

3.1 Validation of numerical schemes

Figure 9 presents a series of experimental and numerical snapshots spanning the early evolution of the flow inside divider I. Experimental (EXP) schlieren images are compared with CFD schlieren images and GSD results. Figure 9a shows the incident shock wave just before it enters the shock divider. The time given above the images is given relative to the moment the incident shock wave passes the divider inlet at $x/D = 0$.

As seen in Fig. 9b, at $t = 0.008$ ms, the incident shock wave is divided in two separated shock waves, which propagate into the upper and lower branches of the divider. The figure shows that the position and shape of the separated incident shock waves in both branches of the divider are very well captured by both numerical schemes. As mentioned in Sect. 2.5.1, the GSD approach considers only the evolution of the incident shock waves. Therefore, the post-shock structures in the flow are not captured in the GSD results. However, the CFD results show an excellent agreement with the experimental schlieren images in terms of separated shock waves as well as flow structures upstream of the incident shock waves. This agreement is well demonstrated in Fig. 9b–d. These flow structures will be discussed in more detail in Sect. 3.2. The qualitative comparison of the results based on Fig. 9 shows an excellent agreement between the numerical and experimental results.

As mentioned before, GSD neglects any influence of the post-shock flow on the propagation of the leading shock. Therefore, the good agreement between GSD and experiment leads to the conclusion that the post-flow does not significantly affect the shock propagation inside the divider. Furthermore, no viscosity is considered in the CFD approach, yet the agreement between CFD and experiment is very good. Consequently, the impact of turbulence on the flow inside the divider must be marginal.

To compare the results in a quantitative manner, the position of the separated shock wave in the lower and upper branches is captured at the outer wall of the divider: at the upper wall of the upper branch and at the lower wall of the lower branch. Figure 10 presents the corresponding x–t diagram of the transient shock waves based on the CFD, GSD, and experimental data. The comparison demonstrates a very good agreement between the CFD and GSD results regarding the evolution of the leading shock wave in both divider branches. However, both numerical schemes slightly overestimate the shock propagation velocity compared to the experiment. The spatial displacements between the shock waves in the upper and lower branches ξ differ slightly between the numerical and experimental data, as shown in Fig. 10. The quantity ξ at the divider exit is in the CFD case 4% and in the GSD case 20% smaller compared to the experiment (Fig. 10).

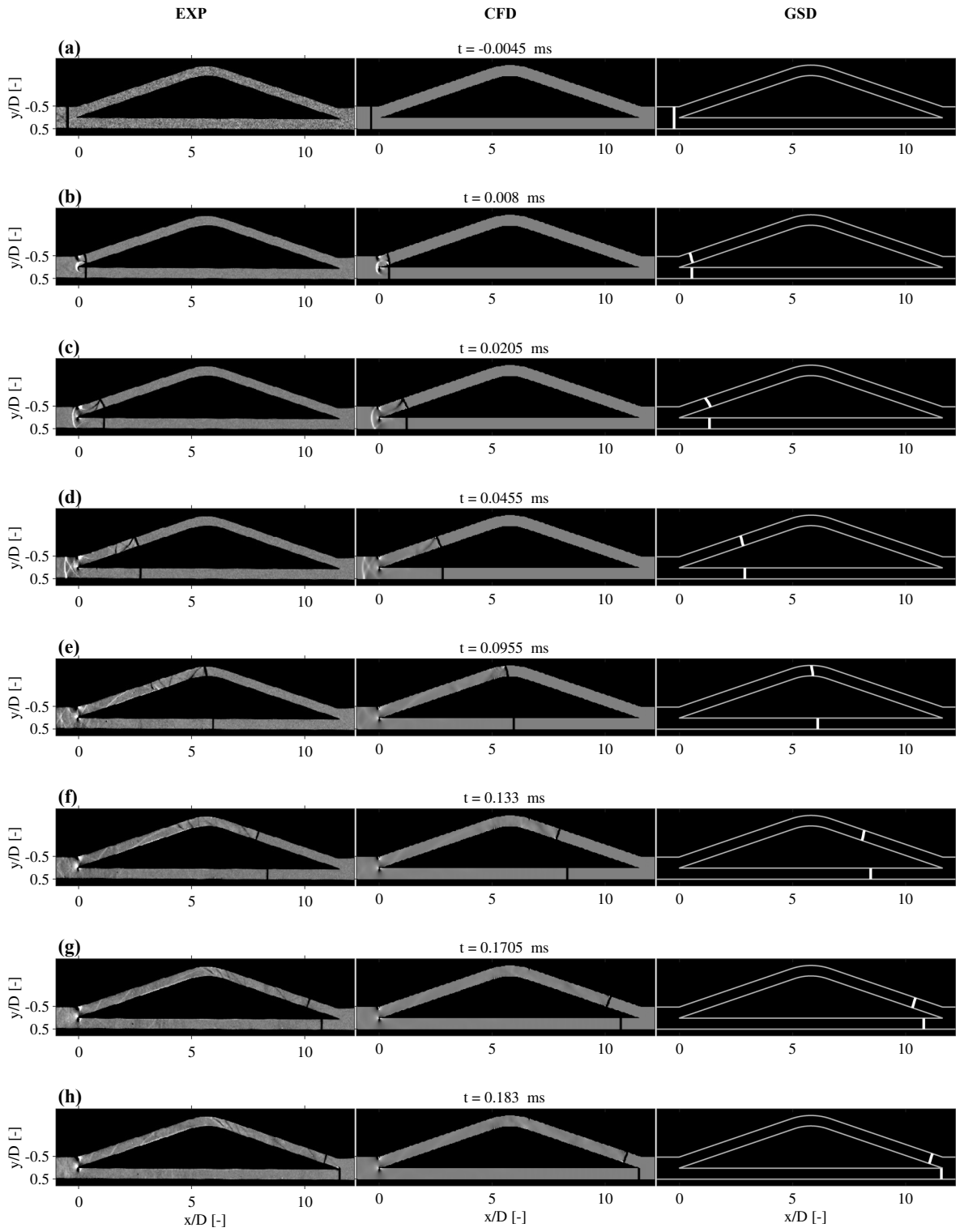

Fig. 9 Experimental schlieren (left row), CFD schlieren (mid row), GSD results (right row) showing the flow evolution inside the divider I

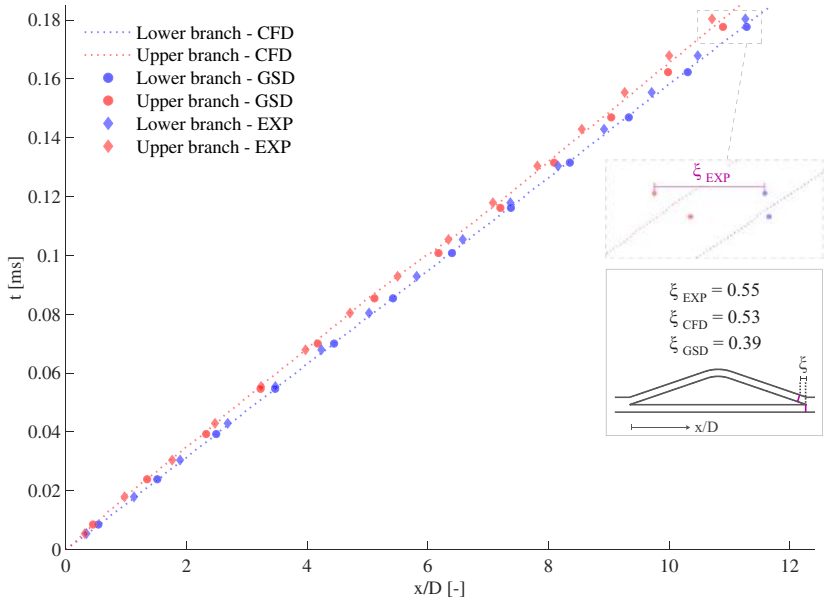

Fig. 10 X–t diagram of the leading shock at the upper and lower branches of the divider based on experiment, CFD and GSD simulations for divider I

The numerical approaches slightly overestimate the shock strength as they do not account for all mechanisms, leading to entropy generation. The discrepancy between the experimental and numerical results is larger in the upper divider branch compared to the lower branch. This is to be expected, as multiple mechanisms in the upper branch lead to entropy generation, whereas in the lower branch the shock wave simply propagates through a constant cross-sectional straight duct. The entropy generation mechanisms will be discussed to some extent in the next section. The comparison between the numerical and experimental data shows the capability of both GSD and CFD approaches to resolve the propagation of the incident shock waves in the divider branches. However, unsurprisingly the CFD results replicate the experiments more accurately compared to the GSD.

3.2 Divider flow evolution

The CFD results are used to analyse the flow evolution inside the shock divider. Figure 11 presents four snapshots of contour plot pairs showing the pressure and Mach number distributions inside divider II. In the Mach number plots, the subsonic and supersonic regions of the divider flow are colour-coded with blue and red colours, respectively.

Once the shock wave reaches the divider inlet at $x/D = 0$, a number of different events take place. The planar incident shock separates in two different shock waves. One propagates along the lower branch and the other along the upper branch. As shown in Fig. 11a, the part in the lower branch is transmitted as a planar shock wave, whereas the separated shock in the upper branch is slightly curved. Here, the upper part of the shock wave diffracts at the convex corner of the divider at $x/D = 0$. Furthermore, a small part of the incident shock wave reflects at the leading edge of the centre body and propagates upstream (Fig. 11a-i). This reflected shock wave is linked at the triple point with the Mach stem close to the wall, and the diffracted shock (Fig. 11a-iv). This triple point configuration is known as a single Mach reflection [43]. As shown in the Mach number contour plots, the flow inside the entire divider is subsonic at this stage. This is to be expected as the shock strength of $M_s = 1.61$ planar shock results in subsonic post-shock flow conditions based on 1D gas dynamic equations.

The flow inside the divider accelerates due to various mechanisms. The diffraction of the shock wave at the convex corner of the upper branch ($x/D = 0$) results in an upstream propagating expansion wave (Fig. 11a-i). Hence, the flow velocity increases, resulting in supersonic flow at the convex corner of the divider inlet. This supersonic region and a steady, but growing, Prandtl–Meyer (PM) expansion wave are highlighted in the close-up view, shown in Fig. 11b-iii. A quasi-steady normal shock adjusts the pressure mismatch between the expanded flow through the PM expansion wave and the compressed flow by the transient shock in the upper branch (Fig. 11b-iii). Furthermore, an additional PM expansion wave in the upper branch at $x/D = 1$ can be observed in Fig. 11b-iv. This is initiated by a barely visible convex corner in the divider centre body at $x/D = 1$ (Fig. 11b-ii). The duct width in the upper branch of the divider is constant from $x/D = 0$ to 1, while for $x/D > 1$, the duct width increases linearly up to the centre of the divider at $x/D = 6$, resulting in a convex corner at $x/D = 1$ (Fig. 11b). The convex corner

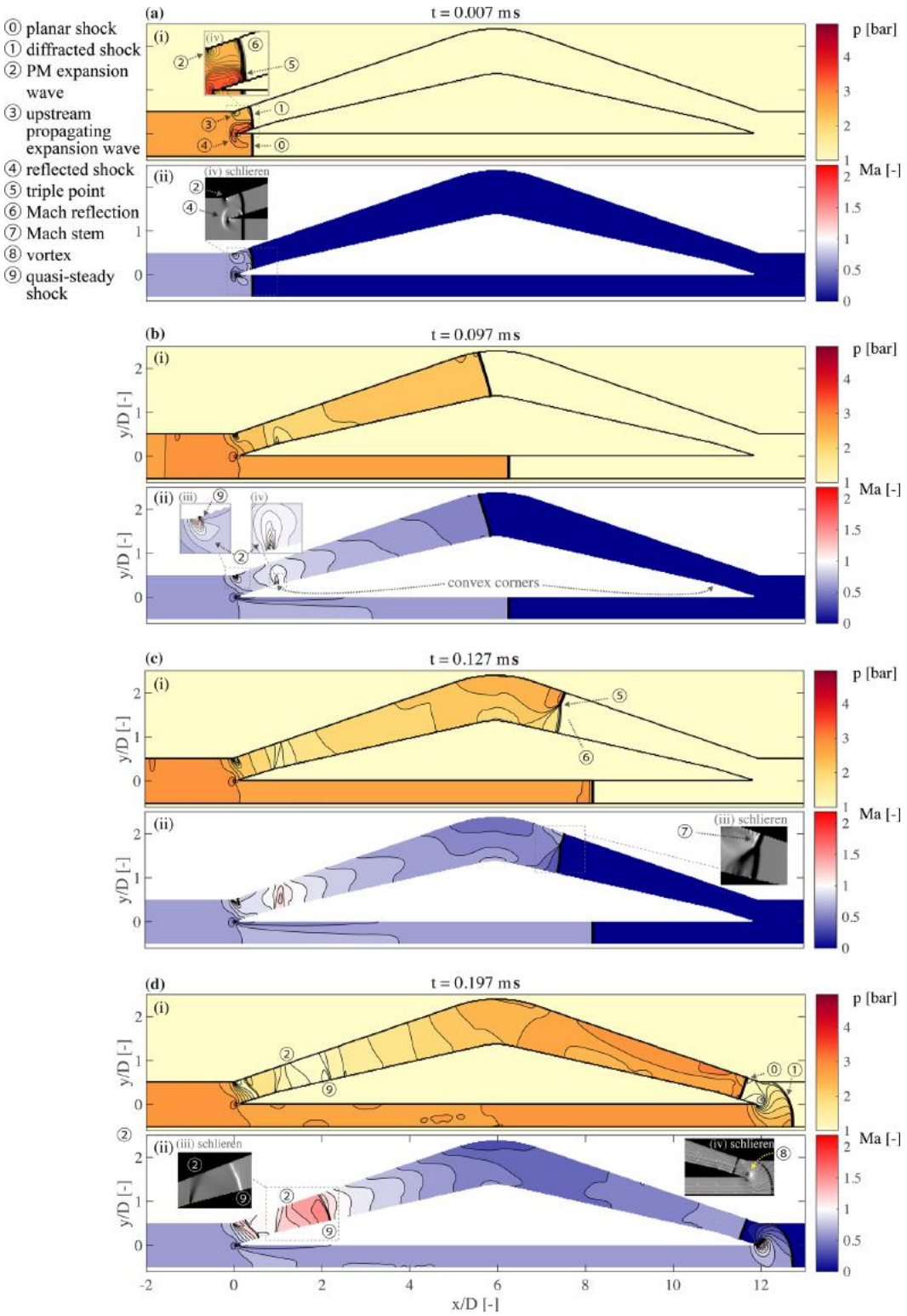

Fig. 11 Time series of pressure and Mach number contours showing the evolution of the flow inside the divider II

leads to further acceleration of the supersonic flow through a steady PM expansion wave (Fig. 11b-iv).

The flow inside the upper and lower branches differs considerably from one another. Within the diverging section of the upper branch, the leading shock wave is a single shock with a nearly planar shape. However, the shock structure changes significantly as the planar shock reaches the turning point of the divider at $x/D = 6$. As the shock wave transmits to the concave section, a relatively strong Mach reflection occurs at the divider outer wall, resulting in a non-planar shock wave (Fig. 11c-i). The triple point of the Mach reflection reflects several times from both the inner and outer walls of the duct as the shock wave propagates through the divider (not shown here). Consequently, the pressure distribution in the converging section of the upper branch ($x/D = 6$ to 11) is highly non-uniform (Fig. 11d-i). Furthermore, the flow Mach number decreases from the convex corner at $x/D = 1$ up to the leading shock wave at $x/D \approx 5.5$, as shown in Fig. 11b-ii. This is mainly caused by the diverging shape of the upper duct, which decelerates the transient shock wave. On the contrary, the shock wave becomes gradually stronger as it propagates along the converging section of the upper branch. Hence, the flow Mach number in the converging section ($x/D = 6$ to 11) increases along the narrowing duct (Fig. 11d-ii).

In contrast to the upper branch, the flow evolution inside the straight lower branch is inherently simple. The transient shock wave maintains its planar shape up to the trailing edge of the centre body at $x/D = 12$ (Fig. 11a–d). The shock velocity barely changes in the constant cross-sectional duct. Hence, the shock wave propagates at almost the same speed as the undivided incident shock wave ($M_s = 1.61$). Therefore, the pressure and Mach number distributions are almost uniform upstream of the transient shock in the lower branch of the divider (Fig. 11a–c).

While the lack of noticeable shock attenuation in the lower branch is expected for the numerical results due to neglection of viscous effects, the nearly constant shock velocity in the experiments may be surprising. Hence, the expected shock attenuation throughout the lower branch is estimated based on the literature on shock attenuation inside shock tubes. Non-ideal effects resulting in attenuation of the incident shock wave of shock tubes are of significant interest in particular for chemical kinetic studies [44,45]. These non-ideal effects mainly depend on the boundary layer, experimental conditions, and the shock tube geometry, particularly the inner diameter of the tube [46–48]. To estimate the shock attenuation for the divider, the recently determined empirical relations given in [47] are used. Nativel [47] measured the shock attenuation across a range of pressures and incident shock Mach numbers for four different shock tube facilities. The driven section diameters of the shock tubes varied from 5 to 16 cm. For each diameter, an empirical relation was given based on a least-squares method to obtain a linear fit. Accordingly, the empirical relations for different shock tube diameters given in [47] are extrapolated to the divider's lower branch channel width. The resulting shock attenuation for the lower branch is

$$\text{attenuation } (\%/m) = 0.73 + 4.12\,(p_1^{-0.14}\sqrt{M_s}),$$

where p_1 is the shock upstream pressure. For the considered configuration in this study, the shock attenuation is 7.9%/m. Taking into account the relatively short length of the divider, the shock wave is estimated to attenuate by only 0.8% throughout the divider's lower branch.

The upper and lower separated shock waves reach the divider outlet at different times, as shown in Fig. 11d. The shock wave in the upper branch reaches the divider outlet at a later time due to a number of reasons. The path length of the upper branch is higher than that of the lower branch. Furthermore, the upper shock wave propagates at a lower average velocity. This is mainly due to two different mechanisms. Firstly, the divergent section of the divider weakens the shock wave due to diffraction. Secondly, the reflection of the shock wave from the divider walls, in particular at the turning point of the divider, weakens the shock wave. However, the shock wave in the lower branch propagates at a nearly constant velocity along the shortest path from the divider inlet to the outlet through a straight duct. Therefore, the shock wave from the lower branch reaches the divider exit first.

When the shock wave in the lower branch reaches the end of the centre body, it encounters an increase in duct width from $D/2$ to D. The area expansion results in diffraction of the shock wave (Fig. 11d). As shown in Fig. 11d-iv, a recirculation region occurs at the corner of the centre body ($x/D = 12$). The resulting vortex separates from the corner at a later time and propagates further downstream while interacting with the following shock wave from the upper branch (Fig. 13d). These results show the dynamic evolution of the wave patterns inside the divider and the capability of the divider to separate shock waves into multiple, weaker, consecutive shock waves.

3.3 Impact of divider width ratio on shock separation

The impact of the divider width ratio on the separation of the shock waves is investigated in this section. The divider width ratio is defined as the ratio of the upper branch maximum channel width to the lower branch. The width ratios of the investigated dividers are 1, 2, and 4 for dividers I, II, and III, respectively.

An x–t diagram, based on the CFD simulations, is presented in Fig. 12a. The results show a nearly identical shock

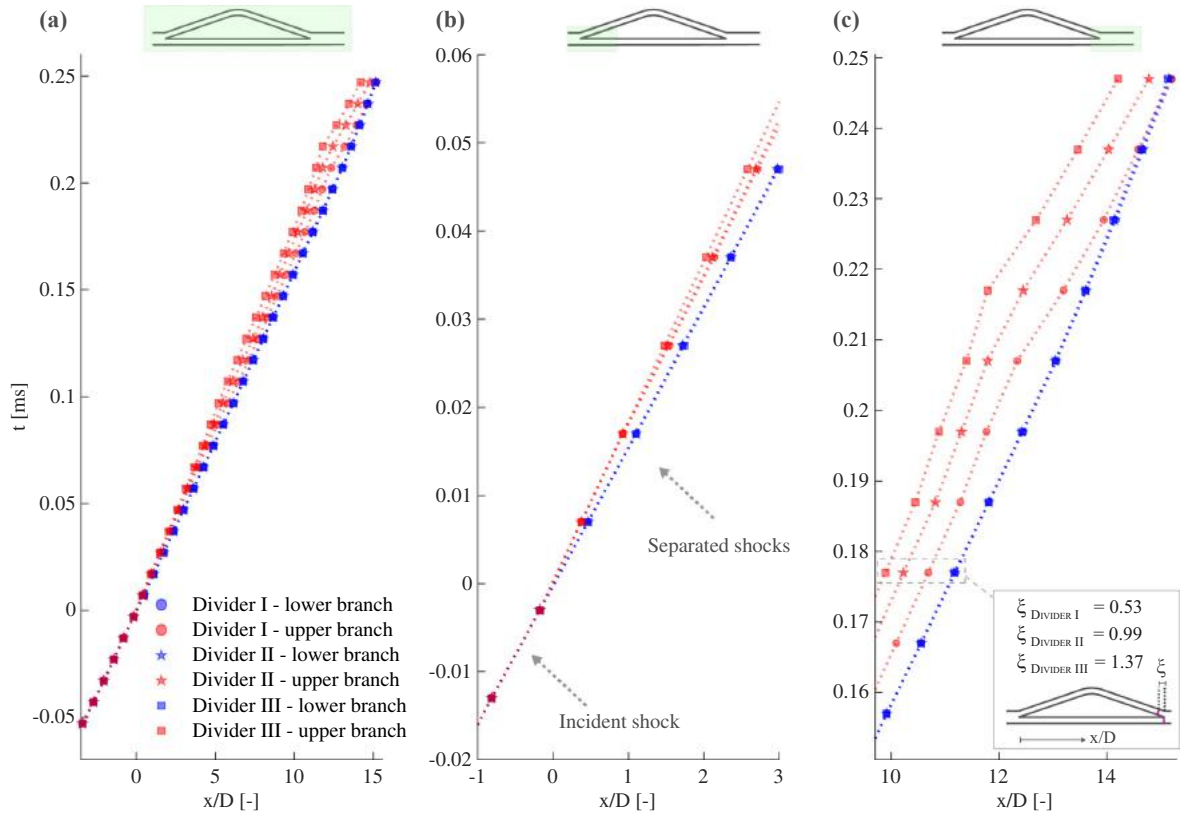

Fig. 12 *X–t* diagram of both divider branches based on CFD simulations for divider I–III showing the shock propagation in the **a** entire divider and in its **b** inlet and **c** outlet sections

velocity in the lower branch for all three dividers, as all *x–t* lines for the lower branches lie on top of each other. As presented in a close-up view in Fig. 12b, the separated shock wave in the lower branch propagates with nearly the same velocity as the initial incident shock wave upstream of the divider. However, the velocity of the shock in the upper branches varies between the dividers. As shown in Fig. 12c, the shock velocity decreases as the width ratio increases. Hence, the shock separation distance ξ at divider outlet increases with a larger width ratio, as indicated in Fig. 12c. This is to be expected, as a larger width ratio results in further deceleration of the shock velocity due to diffraction.

3.4 Recombination of the separated shocks

A straight exit duct is attached to the outlet of the dividers to investigate the further evolution of the separated shock waves and their interaction with each other (Fig. 13). As shown in Fig. 12c, for all dividers, the velocity of the shock wave from the upper branch increases continuously after the shock wave is transmitted to the exit duct. The flow inside the exit duct is mainly driven by two consecutive shock waves propagating in the same direction. The leading shock increases the speed of sound and sets the flow into motion as it propagates through the air, initially at rest. Therefore, the subsequent shock wave velocity increases gradually. Given a long enough exit duct, two shock waves travelling in the same direction must collide [49].

Figure 13 shows numerical schlieren images of the three dividers and their exit ducts. The images in Fig. 13a–c show the very moment the shock wave from the upper branch reaches the trailing edge of the divider centre body. The shock waves from the lower branch are already diffracting into the exit ducts. The images in Fig. 13a–c clearly show that a larger width ratio results in a larger separation of the shock waves at the divider outlet. The separation distance ξ between the shock waves at this stage for divider III is 2.6 times larger than divider I. The shock wave from the lower branch propagates in two different directions after it is diffracted around the trailing edge of the divider centre part. A part of the shock wave is transmitted to the exit duct. This part of the shock propagates as a strong Mach reflection in downstream direction, whereas the remaining part of the shock propagates back into the upper branch.

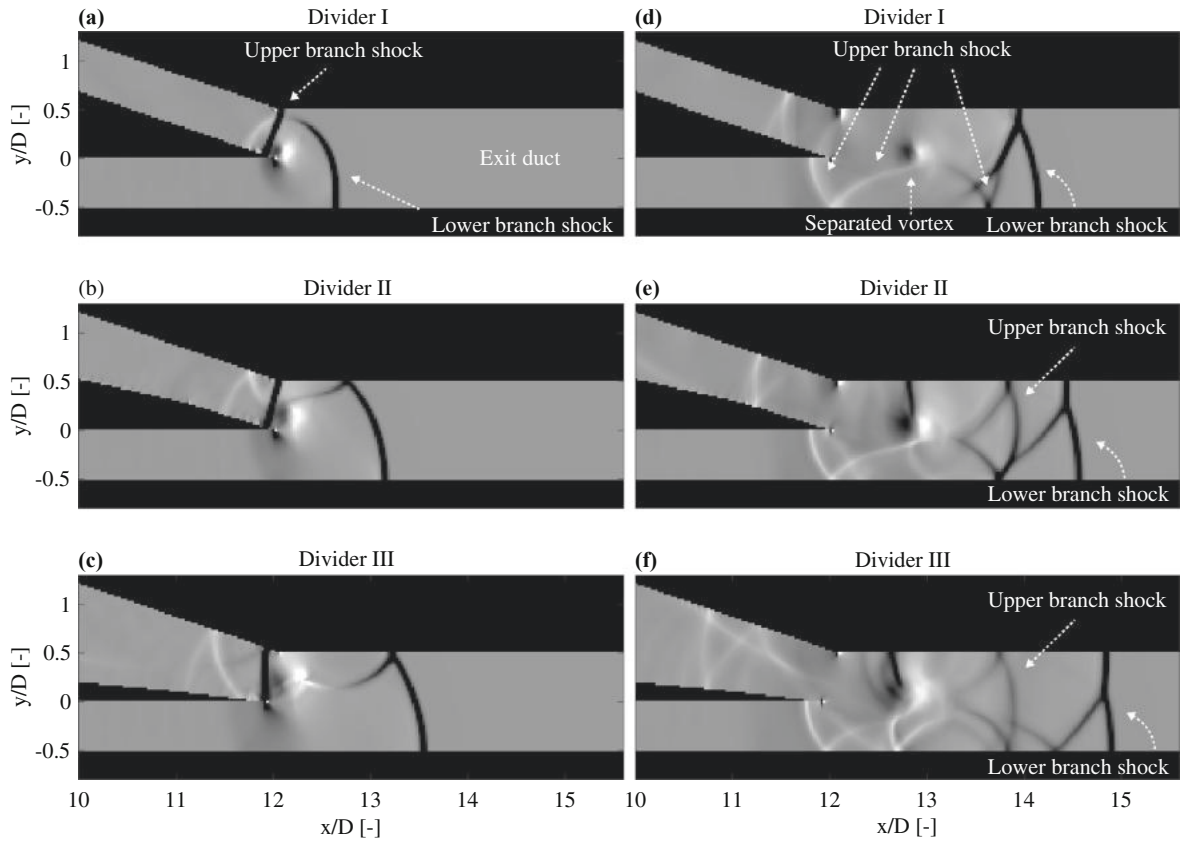

Fig. 13 Numerical schlieren images showing the interaction of the separated shock wave after exiting the divider for dividers I–III at two different times

The schlieren images in Fig. 13d–f show the flow evolution for a short time later for all three dividers. As shown in Fig. 13d for divider I, the shock wave from the upper branch has diffracted around the corner. A part of this shock propagates back into the lower branch. Another part of this shock wave is reflected from the lower wall of the exit duct. The remaining part of the shock wave propagates downstream along the exit duct. In Fig. 13d, the part which is moving downstream is behind the leading shock wave from the lower branch. In contrast, in the case of divider II the rearward shock wave in the exit duct is separated from the preceding shock (Fig. 13e). In Fig. 13f, the shock waves in the exit duct of divider III are separated by a larger distance. In addition, the schlieren images show that only a part of the lower and upper branch shock waves is transmitted to the exit duct, while the rest propagates back towards the divider inlet. Furthermore, the separation of the shock waves is larger and lasts longer for larger divider width ratio.

3.5 Temporal redistribution of the incident shock wave energy

The temporal redistribution of the energy of a single shock wave is further examined by analysing the total pressure. Figure 14 presents the total pressure in the exit duct for all dividers based on the CFD simulations. For the sake of comparability, the time is set to zero when the first shock wave reaches the sensor position. As shown in Fig. 13, the diffracted shock from the lower branch reaches the exit duct and therefore the pressure sensor, first. In addition to the pressure obtained from CFD simulations, the experimentally measured pressure for divider II is shown in Fig. 14. The signal is filtered with a 50-Hz–150-kHz band-pass filter to remove noise. The delay of nearly 9 µs between the shock arrival and the plateau pressure corresponds to the rise time of the sensor [32,50]. The measured plateau pressure after the passage of the first shock wave is 8% less than the CFD predicted pressure. The numerically overestimated pressure complies with our observations in Sect. 3.1 that the numer-

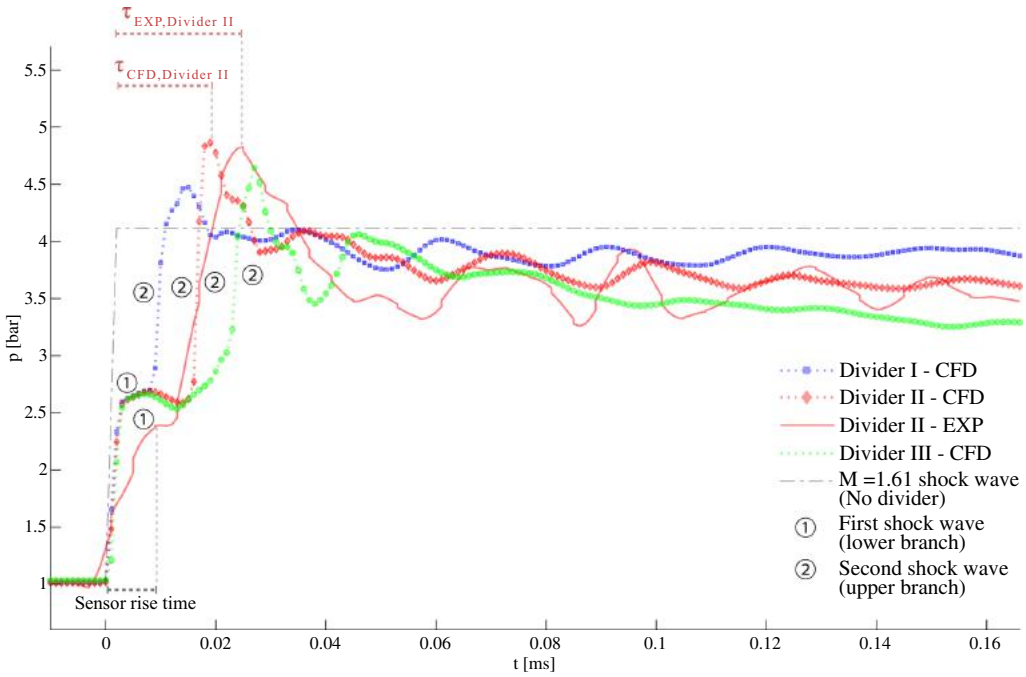

Fig. 14 Total pressure at the divider outlet at $x/D = 12.5$ showing two separated shock waves

ical shock strengths are slightly overestimated compared to the experiments. Furthermore, there is very good agreement between CFD and experiments for the second shock wave and the proceeding oscillations. The oscillations of the pressure are mainly caused by multiple reflections of the shock wave from the upper and lower walls of the exit duct. The oscillations converged towards a plateau pressure of nearly 3.7 bar for divider II. These results support the ability of the high-frequency total pressure probe to measure the transient total pressure.

In Fig. 14, the total pressure behind a $M_s = 1.61$ shock wave is given as a reference based on normal shock expression. It allows for estimation of the entropy generation produced by the divider. The plateau total pressure behind the secondary shock is 5, 12, and 20% smaller than the reference configuration, without a divider, for dividers I to III. Hence, the pressure loss increases with increasing separation of the shock waves. These results show that any attempt to reduce impulsive loading on the turbines through the use of shock divider will come at the cost of total pressure loss.

As shown in Fig. 14, the time τ is taken as a measure for the temporal redistribution of the shock energy. The time τ is the interval between the moment when the pressure first increases and the moment at which the maximum pressure is reached (Fig. 14). For the configuration without a divider $\tau = 0$, as the maximum pressure occurs directly behind the incident shock wave. However, $\tau > 0$ when the divider separates the shock waves and increases with larger divider width ratios. The time τ based on the CFD simulations is 15, 19, and 27 µs for the dividers I, II, and III, respectively. A good agreement for τ between CFD and experiment is evident, as τ_{EXP} = 25 µs and τ_{CFD} = 19 µs for divider II (Fig. 14). The discrepancy between these quantities is mainly attributed to the sensor rise time. The temporal evolution of the total pressure at the divider exit demonstrates the ability of the divider to redistribute the energy of a shock wave. Furthermore, the comparison between the dividers in Fig. 14 shows that the temporal redistribution of the energy can be further increased through the divider width ratio, but at the expense of total pressure.

4 Conclusion

The redistribution of transient incident shocks into multiple shock waves is investigated by utilising a device termed a shock divider. The shock divider consists of two pathways with different path lengths and channel widths. A transient shock wave is generated using an open-end shock tube. The divider is connected to the end of the shock tube. As the shock wave enters the divider, it separates into two primary shock waves propagating through the two divider branches. The path length of the upper branch is higher than that of the lower branch, allowing the separated shock waves to exit

the divider one after each other. The separated shock waves transmit to a single duct at the downstream end of the divider.

Numerical and experimental methods are used to evaluate the flow evolution inside the divider for an initial shock wave with a Mach number of $M_s = 1.61$. A second-order dimensional split finite volume MUSCL-scheme (CFD) is used to solve the compressible Euler equations for a 2D Riemann problem. Furthermore, low-cost geometrical shock dynamics (GSD) simulations are used to estimate its eligibility to predict the wave dynamics inside the divider. High-speed schlieren images of the divider flow are used to validate the numerical approaches. In addition, a high-frequency pressure probe is used to measure the transient total pressure at the divider exit.

The comparison between the CFD results with experimental schlieren and total pressure measurements shows very good agreement. Moreover, the GSD approach predicts the propagation of the leading shock waves inside the divider with high accuracy. The CFD approach is shown to be more accurate while requiring relatively low computational resources. However, the numerical approaches slightly overpredict the shock velocity in the upper divider branch, as they do not account for the boundary layer growth due to the lack of viscosity. The computational time for the simulation of the divider flow is in the order of 5 minutes for the GSD and 10 minutes for the CFD using a 2.9-GHz i7 work station. We conclude that both schemes are appropriate for efficient design studies due to the very low computational cost.

Supersonic regions, quasi-steady shock waves, and Prandtl–Meyer expansion waves occur inside the divider, even though the initial flow behind a $M_s = 1.61$ planar shock is subsonic. The flow transitions from subsonic to supersonic as the shock wave diffracts at the convex corner of the divider inlet. Induced by the shock diffraction, an upstream-propagating expansion wave increases the flow velocity. Furthermore, the planar incident shock wave separates into a planar shock and a slightly curved shock in the lower and upper branches, respectively. While the shock wave in the lower branch propagates at a nearly constant velocity, the leading shock in the upper branch is exposed to various loss mechanisms. A relatively strong Mach reflection occurs at the turning point of the upper branch. Its triple point reflects a number of times from the inner walls of the divider before it transmits to the exit duct downstream of the divider. Furthermore, the gradual diffraction of the incident shock within the diverging section decelerates the shock wave further. Therefore, the shock wave from the upper branch reaches the divider exit after the lower branch.

The impact of the divider channel width ratio on the separation of the divided shock waves is studied. For this purpose, three different divider width ratios of 1, 2, and 4 are investigated. The time interval between the arrival time of the two shock waves at the divider exit increases with increasing width ratio. This is mainly caused by the diffraction of the shock wave, as further diverging of the upper channel results in further deceleration of the shock wave. Therefore, the leading shock wave from the upper channel exits the tube at a later time. Consequently, the separation of the shock waves downstream of the divider lasts longer with increasing divider width ratio.

Total pressure is measured at the exit of the divider using a high-frequency pressure probe. The comparison with the numerical results shows the capability of the probe for measurement of highly transient flow. Furthermore, the temporal redistribution of the initial shock wave energy is investigated by analysing the temporal evolution of the total pressure. It is shown that the temporal redistribution of energy increases with increasing divider width ratio, but at the expense of total pressure.

The divider may be an approach for mitigating the load on the turbine in future PDC–turbine applications. The results of the current study show promise towards the ability of the divider to redistribute the energy of a shock wave. However, future studies are needed to minimise the entropy generation induced by the divider.

Acknowledgements The authors gratefully acknowledge the support of the Deutsche Forschungsgemeinschaft (DFG) as a part of collaborative research centre SFB 1029 "Substantial efficiency increase in gas turbines through direct use of coupled unsteady combustion and flow dynamics" in Project C01. The authors also acknowledge financial support from the Australian Research Council through discovery project DP190102220. This research is supported by an Australian Government Research Training Program (RTP) Scholarship and by a German Academic Exchange Service (DAAD) Fellowship. This work was supported by the HPC-Service of ZEDAT (Freie Universität Berlin) by providing computing resources and storage capacity.

Funding Open Access funding enabled and organized by Projekt DEAL.

Declarations

Conflict of interest The authors declare that they have no conflict of interest.

References

1. Pandey, K., Debnath, P.: Review on recent advances in pulse detonation engines. J. Combust. (2016). https://doi.org/10.1155/2016/4193034
2. Stathopoulos, P., Vinkeloe, J., Paschereit, C.O.: Thermodynamic evaluation of constant volume combustion for gas turbine power cycles. Proceedings of the ASME Turbo Expo GT2016-57813 (2015). https://doi.org/10.1115/GT2016-57813
3. Rezay Haghdoost, M., Edgington-Mitchell, D.M., Paschereit, C.O., Oberleithner, K.: Investigation of the exhaust flow of a pulse detonation combustor at different operating conditions based on high-speed schlieren and PIV. AIAA Scitech Forum 2009, AIAA Paper 2019-1512 (2019). https://doi.org/10.2514/6.2019-1512
4. Dean, A.J., Rasheed, A., Tangirala, V., Pinard, P.F.: Operation and noise transmission of an axial turbine driven by a pulse detonation combustor. Proceedings of the ASME Turbo Expo GT2005-69141 (2005). https://doi.org/10.1115/GT2005-69141
5. Rasheed, A., Tangirala, V., Dean, A., Vandervort, C.L., Haubert, C.: Interactions of a pulsed detonation engine with a 2d blade cascade. 42nd AIAA Aerospace Sciences Meeting and Exhibit, AIAA Paper 2004-1207 (2004). https://doi.org/10.2514/6.2004-1207
6. VanZante, D., Envia, E., Turner, M.G.: The attenuation of a detonation wave by an aircraft engine axial turbine stage. NASA/TM-2007-214972 (2007)
7. St. George, A., Gutmark, E.: Trends in pulsating turbine performance: pulse-detonation driven axial flow turbine. 50th AIAA Aerospace Sciences Meeting including the New Horizons Forum and Aerospace Exposition, AIAA Paper 2012-769 (2012). https://doi.org/10.2514/6.2012-769
8. Xisto, C., Petit, O., Grönstedt, T., Rolt, A., Lundbladh, A., Paniagua, G.: The efficiency of a pulsed detonation combustor-axial turbine integration. Aerosp. Sci. Technol. **82**, 80 (2018). https://doi.org/10.1016/j.ast.2018.08.038
9. Kailasanath, K.: A review of research on pulse detonation engine nozzles. 37th Joint Propulsion Conference and Exhibit 2001-3932 (2001). https://doi.org/10.2514/6.2001-3932
10. Kaemming, T., Dyer, R.: The thermodynamic and fluid dynamic functions of a pulsed detonation engine Nozzle. 40th AIAA/ASME/SAE/ASEE Joint Propulsion Conference and Exhibit 2004-3916 (2004). https://doi.org/10.2514/6.2004-3916
11. Tangirala, V., Dean, A.: Performance estimations of a pulse detonation engine with exit nozzle. 42nd AIAA/ASME/SAE/ASEE Joint Propulsion Conference and Exhibit, AIAA Paper 2006-4792 (2006). https://doi.org/10.2514/6.2006-4792
12. Yungster, S.: Analysis of nozzle and ejector effects on pulse detonation engine performance. 41st Aerospace Sciences Meeting and Exhibit, AIAA Paper 2003-1316 (2003). https://doi.org/10.2514/6.2003-1316
13. Opalski, A.B., Paxson, D.E. , Wernet, M.P.: Detonation driven ejector exhaust flow characterization using planar DPIV. 41st AIAA/ASME/SAE/ASEE Joint Propulsion Conference, AIAA paper 2005-4379 (2005). https://doi.org/10.2514/6.2005-4379
14. Thethy, B., Rezay Haghdoost, M., Oberleithner, K., Honnery, D., Edgington-Mitchell, D.M.: Influence of Nozzle geometry on detonation-driven and shock-driven transient supersonic jet flow. Proceedings of the 24th International Society for Air Breathing Engines Conference (2019)
15. Janka, A.M.: Methods of Diffusing Pulse Detonation Combustion. PhD Thesis, Virginia Tech (2014)
16. Chester, W.: The propagation of shock waves in a channel of non-uniform width. Q. J. Mech. Appl. Math. **6**(4), 440 (1953). https://doi.org/10.1093/qjmam/6.4.440
17. Chisnell, R.: The normal motion of a shock wave through a non-uniform one-dimensional medium. Proc. R. Soc. Lond. A **232**(1190), 350 (1955). https://doi.org/10.1098/rspa.1955.0223
18. Whitham, G.: On the propagation of shock waves through regions of non-uniform area or flow. J. Fluid Mech. **4**(4), 337 (1958). https://doi.org/10.1017/S0022112058000495
19. Igra, O., Elperin, T., Falcovitz, J., Zmiri, B.: Shock wave interaction with area changes in ducts. Shock Waves **3**(3), 233 (1994). https://doi.org/10.1007/BF01414717
20. Marty, A., Daniel, E., Massoni, J., Biamino, L., Houas, L., Leriche, D., Jourdan, G.: Experimental and numerical investigations of shock wave propagation through a bifurcation. Shock Waves **29**(2), 285 (2019). https://doi.org/10.1007/s00193-017-0797-6
21. Igra, O., Wang, L., Falcovitz, J., Heilig, W.: Shock wave propagation in a branched duct. Shock Waves **8**(6), 375 (1998). https://doi.org/10.1007/s001930050130
22. Maggs, R.: The propagation of shock waves in a complex tunnel system. J. S. Afr. Inst. Min. Metall. **91**(4), 137 (1991)
23. Biamino, L., Jourdan, G., Igra, O., Mariani, C., Tosello, R., Leriche, D., Houas, L.: Experimental investigation of shock wave propagation in a 90 branched duct. Shock Waves **24**(3), 307 (2014). https://doi.org/10.1007/s00193-013-0481-4
24. Wilson, J.F.: Smooth mixed geometry profiles of nozzles and transition ducts. J. Mech. Des. **127**(6), 1211 (2005). https://doi.org/10.1115/1.1913704
25. Settles, G.S.: Schlieren and Shadowgraph Techniques: Visualizing Phenomena in Transparent Media, Springer (2012). https://doi.org/10.1007/978-3-642-56640-0
26. Willert, C.E., Mitchell, D.M., Soria, J.: An assessment of high-power light-emitting diodes for high frame rate Schlieren imaging. Exp. Fluids **53**(2), 413 (2012). https://doi.org/10.1007/s00348-012-1297-1
27. Fedrizzi, M., Soria, J.: Application of a single-board computer as a low-cost pulse generator. Meas. Sci. Technol. **26**(9), 095302 (2015). https://doi.org/10.1088/0957-0233/26/9/095302
28. Bach, E., Thethy, B.S., Edgington-Mitchell, D.M., Rezay Haghdoost, M., Oberleithner, K, Paschereit, C.O., Stathopoulos, P., Bohon, M.: Uncertainty quantification of Kiel probes for RDC applications. AIAA Scitech 2021 Forum (2021). https://doi.org/10.2514/6.2021-0293
29. Rezay Haghdoost, M., Thethy, B.S., Edgington-Mitchell, D., Habicht, F., Vinkeloe, J., Djordjevic, N., Paschereit, C.O., Oberleithner, K.: Mitigation of pressure fluctuations from an array of pulse detonation combustors. J. Eng. Gas Turbines Power (2020). https://doi.org/10.1115/1.4049857
30. Rezay Haghdoost, M., Edgington-Mitchell, D., Nadolski, M., Klein, R., Oberleithner, K.: Dynamic evolution of a transient supersonic trailing jet induced by a strong incident shock wave. Phys. Rev. Fluids **5**(7), 073401 (2020)
31. Paxson, D., Dougherty, K.: Ejector enhanced pulsejet based pressure gain combustors: an old idea with a new twist. 41st AIAA/ASME/SAE/ASEE Joint Propulsion Conference and Exhibit, AIAA Paper 2005-4216 (2005). https://doi.org/10.2514/6.2005-4216
32. Hurst, A.M., Olsen, T.R., Goodman, S., VanDeWeert, J., Shang, T.: An experimental frequency response characterization of MEMS piezoresistive pressure transducers. ASME Turbo Expo 2014: Turbine Technical Conference and Exposition GT2014-27159 (2014). https://doi.org/10.1115/GT2014-27159
33. Whitham, G.: A new approach to problems of shock dynamics, part I: two-dimensional problems. J. Fluid Mech. **2**(2), 145 (1957). https://doi.org/10.1017/S002211205700004X
34. Henshaw, W., Smyth, N., Schwendeman, D.: Numerical shock propagation using geometrical shock dynamics. J. Fluid Mech. **171**, 519 (1986). https://doi.org/10.1017/S0022112086001568

35. Bryson, A., Gross, R.: Diffraction of strong shocks by cones, cylinders, and spheres. J. Fluid Mech. **10**(1), 1 (1961). https://doi.org/10.1017/S0022112061000019
36. Noumir, Y., Le Guilcher, A., Lardjane, N., Monneau, R., Sarrazin, A.: A fast-marching like algorithm for geometrical shock dynamics. J. Comput. Phys. **284**, 206 (2015). https://doi.org/10.1016/j.jcp.2014.12.019
37. Qiu, S., Liu, K., Eliasson, V.: Parallel implementation of geometrical shock dynamics for two dimensional converging shock waves. Comput. Phys. Commun. **207**, 186 (2016). https://doi.org/10.1016/j.cpc.2016.06.003
38. Best, J.: A generalisation of the theory of geometrical shock dynamics. Shock Waves **1**(4), 251 (1991). https://doi.org/10.1007/BF01418882
39. Leer, B.V.: On the relation between the upwind-differencing schemes of Godunov, Engquist-Osher and Roe. Upwind and High-Resolution Schemes (1997)
40. Toro, E.F.: Riemann Solvers and Numerical Methods for Fluid Dynamics, Springer, Berlin (2009). https://doi.org/10.1007/b79761
41. Klein, R., Bates, K.R., Nikiforakis, N.: Well-balanced compressible cut-cell simulation of atmospheric flow. Philos. Trans. R. Soc. A Math. Phys. Eng. Sci. **367**(1907), 4559 (2009). https://doi.org/10.1098/rsta.2009.0174
42. Gokhale, N., Nikiforakis, N., Klein, R.: A dimensionally split Cartesian cut cell method for hyperbolic conservation laws. J. Comput. Phys. **364**, 186 (2018). https://doi.org/10.1016/j.jcp.2018.03.005
43. Ben-Dor, G., Igra, O., Elperin, T.: Handbook of Shock Waves, Cambridge University Press (2001). https://doi.org/10.1017/S0022112002217693
44. Petersen, E.L., Hanson, R.K.: Nonideal effects behind reflected shock waves in a high-pressure shock tube. Shock Waves **10**(6), 405 (2001). https://doi.org/10.1007/PL00004051
45. Zander, L., Vinkeloe, J., Djordjevic, N.: Ignition delay and chemical-kinetic modeling of undiluted mixtures in a high-pressure shock tube: nonideal effects and comparative uncertainty analysis. Int. J. Chem. Kinet. **53**(5), 611 (2021). https://doi.org/10.1002/kin.21469
46. Chaos, M., Dryer, F.L.: Chemical-kinetic modeling of ignition delay: considerations in interpreting shock tube data. Int. J. Chem. Kinet. **42**(3), 143 (2010). https://doi.org/10.1002/kin.20471
47. Nativel, D., Cooper, S.P., Lipkowicz, T., Fikri, M., Petersen, E.L., Schulz, C.: Impact of shock-tube facility-dependent effects on incident-and reflected-shock conditions over a wide range of pressures and Mach numbers. Combust. Flame **217**, 200 (2020). https://doi.org/10.1016/j.combustflame.2020.03.023
48. Hargis, J.W., Petersen, E.L.: Shock-tube boundary-layer effects on reflected-shock conditions with and without Co2. AIAA J. **55**(3), 902 (2017). https://doi.org/10.2514/1.J055253
49. Bull, G.: The interaction of two similarly facing shock waves. J. Aeronaut. Sci. **21**(3), 210 (1954). https://doi.org/10.2514/8.2968
50. Stankevič, V., Šimkevičius, Č: Use of a shock tube in investigations of silicon micromachined piezoresistive pressure sensors. Sens. Actuators A **86**(1–2), 58 (2000). https://doi.org/10.1016/s0924-4247(00)00432-5

4.4 Publication IV

Mitigation of Pressure Fluctuations from an Array of Pulse Detonation Combustors

Mohammad Rezay Haghdoost
Laboratory for Flow Instabilities and Dynamics
Technische Universität Berlin, Germany
Email: rezayhaghdoost@tu-berlin.de

Bhavraj S. Thethy
Laboratory for Turbulence Research in Aerospace and Combustion
Monash University, Australia

Daniel Edgington-Mitchell
Laboratory for Turbulence Research in Aerospace and Combustion
Monash University, Australia

Fabian E. Habicht
Chair of Fluid Dynamics
Technische Universität Berlin, Germany

Johann Vinkeloe
Chair of Combustion Kinetics
Technische Universität Berlin, Germany

Neda Djordjevic
Chair of Combustion Kinetics
Technische Universität Berlin, Germany

Christian O. Paschereit
Chair of Fluid Dynamics
Technische Universität Berlin, Germany

Kilian Oberleithner
Laboratory for Flow Instabilities and Dynamics
Technische Universität Berlin, Germany

An annular plenum is integrated downstream of six pulse detonation combustors arranged in a can-annular configuration. The primary purpose of the plenum is the mitigation of pressure and velocity fluctuations, which is crucial for operation with a downstream turbine. The flow inside the plenum is investigated by means of flush-mounted pressure transducers arranged in the axial and circumferential directions. The test rig is operated in different firing patterns at 16.7 Hz per tube. Two firing patterns are studied to characterize the shock dynamics inside the plenum. The obtained data allows for a better understanding of shock interaction and attenuation inside the plenum, as well as the quantification of pressure fluctuations at the plenum outlet. Furthermore, a comparison is made between piezoresistive and piezoelectric pressure transducers, showing the capability of piezoresistive transducers for dynamic pressure measurements. The performance of the piezoresistive transducers allows for time-resolved measurement of both static and total pressure at the exit of the plenum. Moreover, the plenum results in a significant attenuation of the leading shock wave while redistributing its energy both spatially and temporally.

1 Introduction

The pulse detonation engine (PDE) has been a focal point of propulsion research in recent decades, due to its potential to drastically increase efficiency as compared to conventional gas turbines containing isobaric combustion chambers [1]. In a hybrid-PDE configuration, these combustors are replaced by an annular array of pulse detonation combustors (PDCs) [2]. To maximise the potential gain in efficiency, the coupling between the PDCs and the turbine in the hybrid-PDE must account for the highly transient pressure and temperature fields, which are undesirable for conventional turbines [3–5].

At the heart of the problem is the transient flow, which begins with the emission of a high-amplitude shock wave from each PDC [6]. Recent work has demonstrated that high-amplitude inlet pressure fluctuations are responsible for a large portion of the losses in a pulsating-flow driven turbine [7]. Attempts to mitigate the pressure fluctuations have included geometrical changes at the PDC exit, including the introduction of nozzles [8–10] or shock dividers [11–13], while others have proposed modifying the turbine blades to account for the supersonic PDC flow [14, 15]. An alternative approach involves the use of a high-pressure transition

plenum situated between the PDC exit and turbine inlet [16]. The authors observed a significant damping effect as a result of the area change experienced by the detonation waves. In another study, Rasheed et al. [17] found a significant decrease in the peak pressure experienced by an axial turbine located downstream of a transition plenum in a multi-tube PDC. Accordingly, the inclusion of a plenum chamber between the PDC outlet and the turbine may be an effective method of mitigating pressure fluctuations. However, care must be given in the design of such a plenum as any additional device will result in an increase in weight and length of the PDE engine.

Key to the assessment of pressure-fluctuation mitigation is the ability to accurately measure the pressure within the plenum. Pressure measurements by Rasheed et al. [16, 17] were only undertaken at the inlet and outlet of the plenum, with no evaluation of the pressure history through the plenum. These measurements provided evidence of wave interactions occurring within the plenum, which were found to affect the optimal performance of the PDCs. A deeper understanding of the shock interactions within a plenum is needed to facilitate the mitigation of pressure fluctuations from PDCs.

Accurate measurement of both total and static pressure is of great interest in pressure-gain combustion (PGC) devices. Typically, pressure measurements are undertaken using piezoelectric transducers [17], which are known to be susceptible to thermal effects such as thermal shock [18]. In spite of this, their very short response times make them suitable for dynamic measurements of static pressure, such as the passage of a shock wave in a PDC [6, 10, 17, 19, 20]. However, the accurate measurement of the impulsive pressure remains a challenging task due to the finite bandwidth of the measurement devices and their susceptibility to potential interference sources.

The need to measure the pressure-gain is crucial in the development of PGC devices. Measurement of the pressure-gain in rotating detonation engines was undertaken in recent works, which have related pressure-gain to the total pressure [21, 22]. Total pressure measurements in PGC devices have also been conducted via recessed transducers using pitot and Kiel probes [23, 24]. However, no validated time-accurate measurements of total pressure have ever been reported for a PDC to the best of the authors' knowledge. Accurate determination of the transient total pressure is fundamental to the evaluation of the performance of a PDC and indeed, all other PGC devices.

Various types of dynamic pressure generator devices are used to assess the dynamic performance of pressure transducers. These devices can be categorized into two different classes: periodic and aperiodic devices. The most common periodic device is a sinusoidal pressure generator. However, the periodic devices are usually limited in the usable range of frequency [25]. Using a speaker-driven pressure generator, Hurst et al. [26] conducted dynamic calibration of pressure transducers in a range of 1-50 kHz. One of the most widely used aperiodic devices is a shock tube [27–30]. A pressure transducer mounted at the end-wall of the shock tube senses the reflected shock wave at the end-wall, which results in a sufficiently small rise time to excite all of the transducers natural frequencies [25]. While the shock tube method is suitable for determination of transducer responses in the high-frequency range, it is less effective in the low-frequency range (0 - 20 kHz), in particular where the transducer response is flat [26]. Nonetheless, shock tubes have frequently been used in recent decades for assessing the accuracy and dynamic characteristics of pressure transducers [27–34].

This paper presents an experimental investigation of the shock propagation inside a plenum, downstream of an array of six can-annular PDCs. The pressure inside the plenum is measured and compared for two firing patterns: sequential firing of all six tubes and single ignition of one tube. The shock dynamics inside the plenum are evaluated using a number of flush-mounted piezoresistive and piezoelectric pressure transducers. The accuracy and dynamic response of the transducers are examined in a preliminary study using a shock tube. A comparison is made between the transducers, exploring their limitations and capabilities. These transducers are then used to investigate the mitigation of the peak pressure from an array of PDCs through a plenum. Finally, the measured pressure distribution along the exit of the plenum circumferences provides insight into the inlet conditions for a downstream turbine.

2 Methodology

2.1 Multi-Tube PDC Test Rig

A multi-tube PDC facility is used in the current study, with a cross-section of the test rig shown in Fig. 1. The multi-tube PDC consists of six PDCs arranged in a can-annular configuration on a 260 mm pitch-circle diameter. Each PDC tube consists of a deflagration-to-detonation transition (DDT) section and a detonation tube, each with an inner diameter of 30 mm. The DDT section contains five orifices, each with a blockage ratio of 43%, intended to accelerate the flame propagation velocity and enhance DDT [35]. An annular ring plenum, with an outer annular diameter of 392 mm, an annular ring size of 130 mm, and an overall length of 500 mm, is mounted at the exit of the PDCs. Each PDC outlet is connected to the plenum inlet through a divergent nozzle with an exit diameter of 45 mm and a nozzle length of 60 mm.

The PDC tubes are fed by a continuous airflow via a plenum that is connected to the upstream end of the DDT section through six choked nozzles. The nozzles each have a cross-sectional area of 4.65 mm^2. Three high-speed solenoid valves (Bosch NGI2) are used for each PDC for the injection of hydrogen. The mass flow rate of hydrogen is controlled with a high-speed pressure regulator (Swagelok RD8). A fixed supply pressure is set for the duration of the injection period.

The progression of the combustion front is tracked along a detonation tube using three in-house fabricated ionization probes, each located 300 mm apart (Fig. 1). Similarly, the shock front progression is tracked using three PCB pressure transducers, located 300 mm apart along the length of the

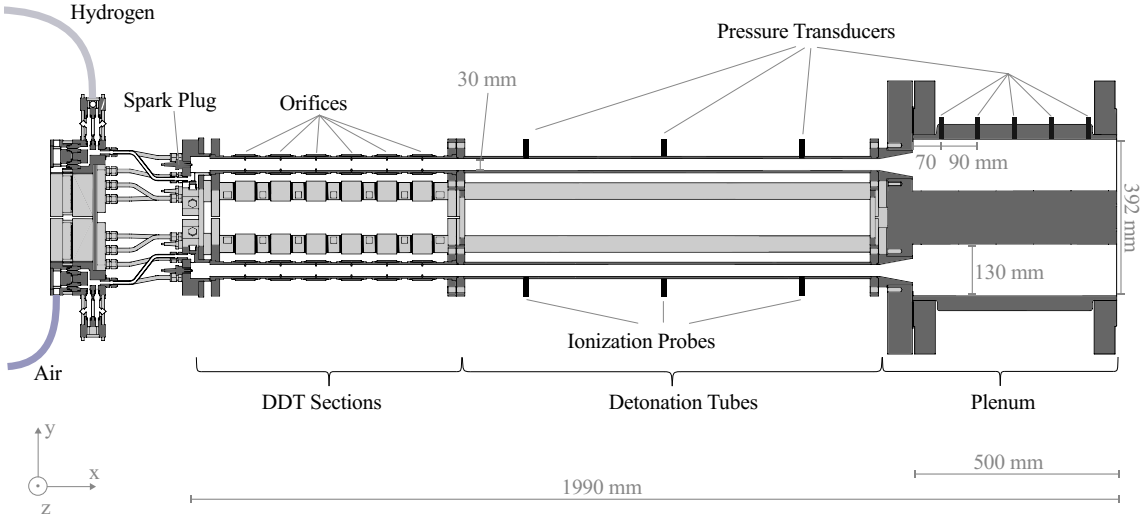

Fig. 1: Can-annular multi-tube PDC test rig with an annular plenum.

detonation tube. The ionization and pressure probe data are used to determine the equivalence ratio and the fill-fraction, which is the percentage of the tube filled with a reactive mixture. The detonation velocity is determined based on the time-of-flight method; the velocity is calculated by measuring the time taken by the wave to travel the distance between the transducers. The experimentally determined detonation velocity, based on the time-of-flight method, is compared with the Chapman-Jouguet (CJ) detonation velocity computed with the NASA CEA code [36]. It was shown that the set supply air and hydrogen pressure result in a stoichiometric mixture. The data from ionisation sensors, pressure transducers and schlieren images of the detonation tube exhaust shows a fill-fraction in the range of 0.76 to 1.1 for the hydrogen injection time of 30 ms.

The shock dynamics inside the plenum are captured using different pressure transducers flush-mounted to the plenum wall. As shown in Fig. 2, a pressure transducer is mounted inside the plenum, 70 mm downstream of the end of each nozzle. Furthermore, there is an additional array of six transducers located 70 mm upstream of the plenum outlet. With the exception of tube 5, the pressure transducers downstream of each tube are PCB piezoelectric transducers of type 112A05 or 113B03. PCB 422E53 charge converters and PCB 482C15 amplifiers are used to provide a voltage signal for the DAQ system. Data is acquired using four PCI-7334 National Instrument cards at 1 MHz resulting in a Nyquist frequency of 500 kHz.

Downstream of tube 5, three additional ports are located along the plenum body, with an axial spacing of 90 mm between each transducer (Fig. 1). This gives a total of five ports inside the plenum, located directly downstream of tube 5, allowing for the evaluation of wave dynamics in the axial direction. These ports are equipped with five piezoresistive Kulite DTL transducers (KP51 to KP55 in Fig. 2). In-house fabricated amplifiers, with a ± 3 dB flat frequency up to 2.8 MHz, are used for amplification of the DTL transducers. Furthermore, a high-frequency total pressure probe is mounted 10 mm upstream of the plenum exit, close to the plenum wall as shown in Fig. 2. This probe consists of a Kulite XCE-062 piezoresistive transducer externally mounted in an L-shaped tube (KP56 in Fig. 2). The transducer is mounted at the head of the probe allowing for transient measurement of the highly unsteady total pressure. Amplification of the measured signal is provided using a

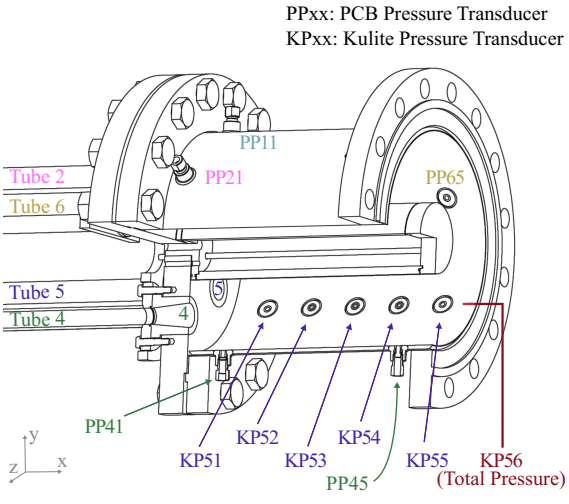

Fig. 2: Annular plenum and transducer labeling.

Kulite KSC-2 signal conditioner. Further information about the probe can be found in [12, 13, 37].

The air flows continuously with a total mass flow rate of 0.2 kg/s, resulting in a bulk velocity of 40 m/s inside the detonation tubes. The maximum deviation in the flow rate is 0.7%, controlled by a closed-loop circuit consisting of a Coriolis mass flow meter (Endress+Hauser Promass 80A) and an electronic proportional valve (Bürkert 2712). In each cycle, hydrogen is injected for 30 ms while ignition, via automotive spark plugs, takes place 4 ms after the hydrogen valves are closed.

Two firing patterns are considered in the current study: a sequential firing of all six tubes and single ignition of one tube. The main parameters of both firing patterns are given in table 1. As illustrated in Fig. 3, in case of the sequential firing pattern, the tubes fire in a clockwise direction with an ignition delay of 10 ms between each tube. The corresponding firing tube order is given in table 1. In the single tube firing pattern, only tube 5 is filled with the combustible mixture while all other PDCs are fed with pure air. The PDC cycle duration is set to 60 ms for each tube and a total of 20 cycles are captured for both firing patterns. As each tube is operated with the same frequency of $f_{\text{tube}} = 16.7$ Hz, the effective firing frequency f_{eff} differ for both firing patterns as given in Table 1. The effective firing frequency f_{eff} is defined as [17]:

$$f_{\text{eff}} = \frac{m f_{\text{tube}}}{n},$$

where m is the total number of PDCs and n is the number of tubes firing simultaneously.

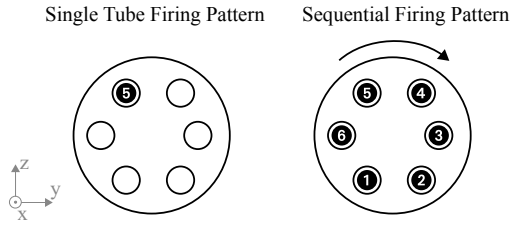

Fig. 3: Illustration of the firing patterns.

	Single tube firing pattern	Sequential firing pattern
Number of detonating tubes	1	6
Firing tube order in a cycle (Tube Nr.)	5	1-6-5-4-3-2-1
f_{tube} (Hz)	16.7	16.7
f_{eff} (Hz)	16.7	100
Cycle duration (ms)	60	60
Time between two subsequent detonation events (ms)	60	10

Table 1: Firing pattern properties.

2.2 Shock Tube Facility

A high-pressure shock tube facility is used to investigate the characteristics of the pressure transducers. Both the accuracy and dynamic response of the pressure transducers are investigated by measuring transducer responses to a well-defined and well-formed shock wave. The shock tube has an inner diameter of D = 95 mm and a total inner length of 12.7 D. A 1 mm thick pre-scored aluminum diaphragm divides the driven and driver sections. The latter is filled slowly with helium until the pressure difference between the two sections exceeds the burst pressure of the diaphragm. Prior to filling of the driver gas, the driven section is evacuated and filled with synthetic air (20.5% O2 and 79.5% N2) up to a pressure of 1 bar. A Baratron 121A manometer with a full-scale range of 6.6 bar and three resistance thermometers (Pt100) measure the pre-shock conditions.

Post-shock conditions behind the incident and the reflected shock wave depend on the initial conditions as well as the shock wave velocity. The shock wave velocity is determined based on signals from pressure transducers. For this purpose, three piezoelectric pressure transducers (PCB 113B03) are axially distributed along the last 1.5 m of the driven section with a distance to end-wall of 15.5, 6 and 2.9 D. A spectrum M2i4912-exp card provides a data acquisition rate of 10 MHz with a resolution of 16 bit. The propagation velocity of the shock wave is determined using the time of flight method. Post-shock conditions such as p_2 and p_5 are calculated by solving the one-dimensional conservation equations of mass, momentum, and energy, including temperature-dependent gas properties. A detailed description of the experimental facility and data processing can be found in Djordjevic et al. [38] and Vinkeloe et al. [39].

Figure 4(a) presents a detailed view of the shock tube end-wall section. The shock tube is equipped with multiple ports at its side-wall and end-wall. Two side-wall transducer ports are located 2.9 D away from the end-wall. The flush-mounted transducers will sense a change in pressure as the shock wave passes. The rise time of the pressure step depends on shock wave velocity as well as the transverse length of the transducer diaphragm in the direction of shock wave propagation. As the side-wall ports imitate the manner in which the transducers are mounted in the PDC plenum (shock wave passing over the transducers), they are well-suited for assessment of the transducers response to the passage of a shock wave. However, the side-wall ports are not best-suited for the transducer dynamic response characterization as small rise time is desired for determination of the ringing frequencies. In contrast to the side-wall, the reflected shock wave at the end-wall of the shock tube is characterized by a much shorter rise time and a higher pressure amplitude. The rise time of the reflected shock, which is in the range

of nanoseconds, is sufficiently short to excite all the ringing frequencies associated with a flush-mounted transducer [25]. Hence, the four ports at the shock tube end-wall are used for the determination of the transducers dynamic response.

In the sectional view of the shock tube end-wall presented in Fig. 4(b) the detailed layout is given for the transducers mounting. The transducers are screwed in a connector, allowing for a flush mount installation. The connector is sealed with a Bridgman seal using three different sealing materials, which are pressed by a fitting against the connector head (Fig. 4(b)), allowing for sealing up to 400 bar. As the transducer mounting is critical to its dynamic performance [30], the exact same layout is used for the plenum ports, while maintaining the torques for all the transducers and the fittings throughout of all shock tube and PDC plenum measurements to ensure the applicability of the shock tube results to the plenum measurements.

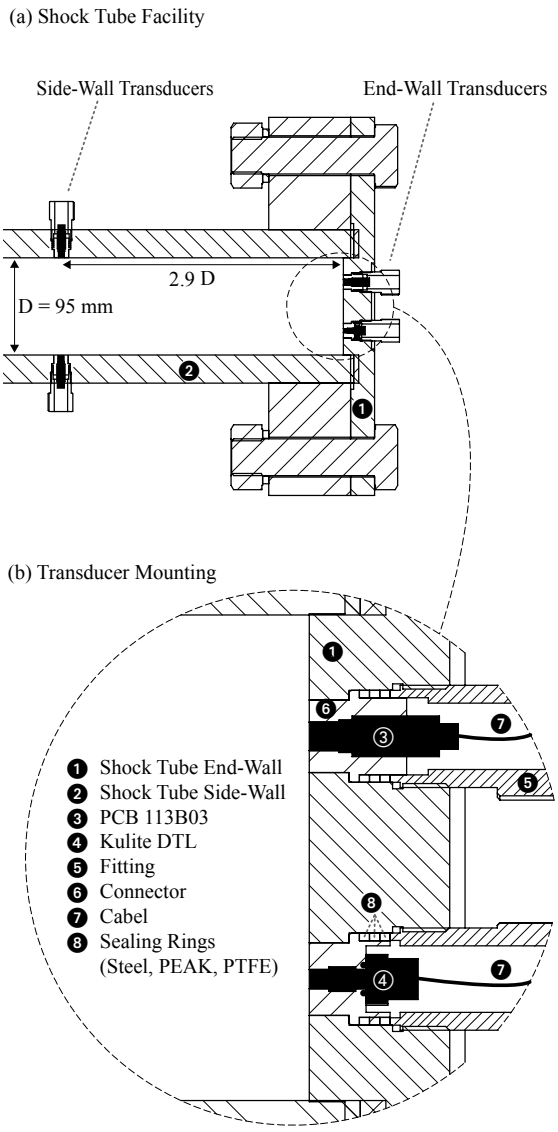

Fig. 4: (a) End-section of the shock tube facility illustrating the transducer ports at its side-wall and end-wall. (b) Detailed illustration of the transducer mounting.

3 Results and Discussion

3.1 Assessment of Transducer Accuracy and Dynamic Response

Using the pressure records from the shock tube transducers, evaluation is undertaken for both the transducer accuracy as well as dynamic response. Commonly, an under-damped second-order system is used to describe the response of piezoresistive and piezoelectric transducers [25–27, 40]. Figure 5 illustrates the response of an under-damped second-order system to a step function. The time signal represents the typical response of a pressure transducer to a shock wave. Some of the general properties of the signal are labeled in Fig 5, which have specific applications for the dynamic response characterization. The time required to rise from 10% of its final pressure to 90% of its final pressure is known as the transducer rise time. The overshoot represents the amount of pressure beyond the final pressure. The frequency of the oscillations in the transducer response to a step-change is called ringing frequency. These quantities are determined from the pressure records of the transducers.

Typical shock tube pressure records are shown in Fig. 6 for a PCB 113B03, a Kulite DTL and a Kulite XCE transducer, mounted at the shock tube end-wall. In addition, a Kulite DTL transducer is mounted at the side-wall of the shock tube. The strength of the incident shock wave Mach number is Ms = 1.97. The time is set to zero for the arrival of the incident shock wave at the end-wall. At t = -0.4 ms, the incident shock wave passes the side-wall ports, resulting in an increase of the pressure from p_1 to p_2 in the corresponding Kulite DTL pressure record (blue line in Fig. 6). After an overshoot of 0.3 in bar, the signal converges to a plateau which is about 4 % higher than the theoretical p_2. Once the incident shock wave reflects from the shock tube end-wall at t = 0, a pressure rise occurs from p_1 to p_5 at the shock tube end-wall. The pressure record of the PCB transducer shows a distinctive high-frequency oscillation right after the arrival of the shock wave ($0 < t < 0.2$ ms). The amplitude of this oscillation decreases significantly with time. The pressure then increases approximately linearly up to t = 3.75 ms. The rate of the pressure rise is 2% per millisecond, which was also observed by Pang et al. [41] behind the reflected shock waves in their shock tube facility. The relatively small increase in pressure is attributed to non-ideal effects such as boundary layer growth and incident-shock attenuation inside the shock tube [41–43]. The pressure decrease from t = 3.75 ms indicate the arrival of the reflected expansion waves at the shock tube end-wall. A similar evolution of the signal can be observed for the Kulite XCE. However, the rise time of the XCE is about three times larger than the PCB transducer, which is noticeable in the enlarged view on the top illustra-

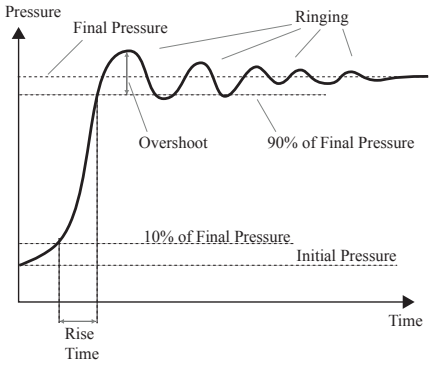

Fig. 5: Sketch of pressure transducer response to a pressure step, as a function of time.

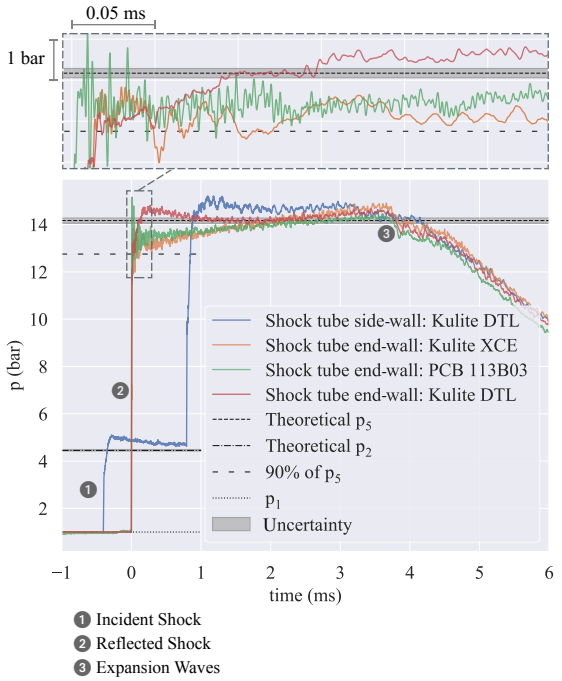

Fig. 6: Transducer responses at the end-wall and side-wall of the shock tube.

tion of Fig. 6. Moreover, the response of the DTL transducer clearly differs from the XCE and PCB transducers. The DTL signal shows also a rapid increase beginning at t = 0, but a larger rise time compared to the XCE and PCB transducers. However, before the signal reaches its maximum value at t = 0.25 ms the slope of the pressure record decreases noticeably. The DTL pressure record exhibits an overshoot of nearly 0.5 bar before it converges to its plateau value. The plateau pressure is within the uncertainty range for the theoretically determined p_5. Similar to the XCE and PCB pressure records, the signal of the DTL transducer shows a temporally linear increase, beginning approximately at t = 2 ms, which terminates with the arrival of the expansion waves at t = 3.75 ms.

All transducers at the shock tube end-wall will be exposed to the same pressure if the shock wave has a uniform plane shape. To assess the uniformity of the shock wave, four PCB transducers are mounted at the shock tube end-wall. The distortion of the shock is evaluated by measuring the arrival time of the shock wave based on the signal of the four PCB transducers. A maximum time delay of 0.2 μs between the four PCB transducers was measured, which corresponds to 0.1 mm distortion of the shock wave. The relatively small distortion of the shock indicates a well-formed plane shock wave. Hence, it is assumed that the pressure behind the reflected shock remains constant over the shock tube end-wall cross-section for all shock tube measurements. Although all transducers at the shock tube end-wall shown in Fig. 6 resolve the dynamic pressure behind the reflected shock, their pressure records differ to some extent. As the transducers are exposed to the same pressure, their different responses must be due to their dissimilar dynamic characteristics.

To shed more light on the dynamic response and accuracy of the transducers, various quantities are determined from a series of measurement runs. A total of five measurement runs for the Kulite DTL and PCB 113B03 and three runs for the Kulite XCE are used to determine transducer characteristics. The different incident shock Mach numbers among the measurement runs result in pressure rise behind the reflected shock from $p_5 = 12.8$ to 15 bar. The results of these measurements are given in Fig. 7 as mean and standard deviation for different quantities. We first discuss the accuracy of the transducers and proceed further with the characterization of their dynamic response.

The accuracy of the transducers is evaluated based on the difference between the measured and theoretically determined pressure behind the reflected shock, p_5. The experimentally determined p_5 is specified in a conservative manner; it is not simply the plateau value but it is determined as the mean pressure in the interval beginning from the 90 % of p_5 up to the arrival of the expansion waves. Figure 7(a) shows p_{error} for the different transducers, which specifies the percentage deviation between the measured and theoretical value. All the transducers resolve the pressure behind the reflected shock with an error of less than 2 % while the PCB transducers exhibit the smallest error with 0.85 %.

Different quantities are commonly used for the characterization of the transducers dynamic response. One indicator is the rise time of the transducer to a step-change in pressure. The mean and standard deviation of the rise time is given in Fig. 7(b) for each transducer. The piezoelectric PCB transducer exhibits the shortest rise time, which is about 3 and 6 times smaller than the peizoresistive Kulite XCE and DTL transducers, respectively. The dynamic performance of the PCB transducer is not only superior in terms of the shortest rise time but also regarding the ringing frequencies. The first dominant ringing frequency as a response to the re-

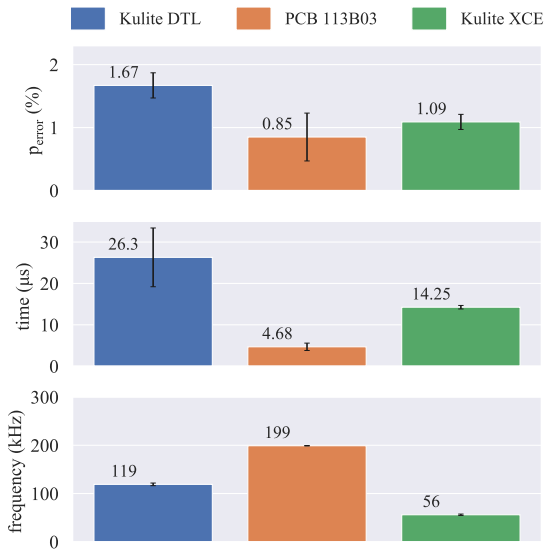

Fig. 7: Transducer accuracy and dynamic response to the reflected shock at the end-wall of the shock tube. Mean and standard deviations are given for (a) transducer error (measured vs. theoretical p_5), (b) transducer rise time and (c) first dominant ringing frequency.

flected shock is given for the three traducers in Fig. 7(c). The PCB transducer shows a dominant ringing at 199 kHz. However, the ringing frequencies of DTL and XCE transducers are considerably lower at 119 and 56 kHz, respectively. The ringing frequency of the XCE transducer is in the same range of the resonant frequency for similar microelectromechanical systems (MEMS) transducers [40].

Although the Kulite transducers are flush-mounted at the shock tube wall, their sensing elements are usually recessed and protected with a screen. The lower ringing frequency of the Kulite transducers may correspond to the Helmholtz frequency of the cavity or the natural frequency of the sensing element. Moreover, an attempt to determine a transfer function for the transducers based on the shock tube data was not successful as the shock tube measurement method inherently suffers at lower frequencies resulting in inconsistencies [26, 44]. Therefore, the natural frequency and the commonly used ± 3 dB frequency of the transducers are not given based on the limited shock tube data. Measurements with a periodic pressure function generator may provide a suitable complementary data set in lower frequencies for identification of an accurate transfer function [25, 26]. However, the dominant ringing frequencies obtained from the shock tube study indicate the limit of the different transducers. Hence, these frequencies are used to specify the cutoff frequencies for low-pass filters applied to the measured data in the PDC plenum application. Furthermore, based on the shock tube results, it can be concluded that all investigated transducers are able to resolve the dynamic pressure behind a reflected shock wave. However, in the low-noise environment of the shock tube facility, the piezoelectric PCB transducers show better performance in terms of accuracy and dynamic response compared to the piezoresistive Kulite transducer.

3.2 Noise Sources and Digital Filter Setting

In addition to the characterization of the dynamic response of the measurement systems, an assessment of potential interference sources is carried out to obtain an accurate measurement of the highly transient pressure inside the PDC plenum. For this purpose, the spectra of the measured pressure in the PDC plenum are considered. Fig. 8 shows the power spectral density (PSD) of the pressure signals for two different cases. In the first case, all the DAQ inputs are terminated with 70 Ω resistors to evaluate the noise level of the DAQ system. The sequential firing pattern is used to evaluate the response of the entire measurement system for the PDC plenum application. As shown in Fig. 8, the DAQ noise appears to be sufficiently small to not bias the actual measurement signal. For the sequential firing pattern, the Kulite transducers (KPxx) show no significant peaks in Fig. 8. However, there are several peaks for different PCB transducers at relatively low frequencies such as 3, 38, 46, and 67 kHz. These frequencies are far below the first dominant frequency obtained from the shock tube measurements as discussed in section 3.1. Hence, the origin of these peaks may indicate a problem with the transducers or interference from noise sources in the test facility. As discussed in section 3.1, different PCB transducers were tested in the shock tube, yet no transducer exhibited the distinctive low-frequency fluctuations seen in Fig. 8. Thus, the ringing of the PCB transducers in the current study is assumed not to be the result of damaged transducers. Instead, the ringing might be due to the susceptibility of these transducers to electromagnetic interference or magnetic fields (e.g. generated by the solenoid valves used for hydrogen injection).

To obtain an accurate pressure signal at the PDC plenum wall, it is desirable to minimize the high-frequency ringing caused by the measurement system. For this purpose, all the pressure signals used to evaluate the pressure evolution inside the PDC plenum are filtered with a Butterworth fourth-order low-pass zero-phase filter. The first dominant ringing frequency obtained from the shock tube study is used to determine the cut-off frequency for the DTL and XCE transducers, as no dominant peaks at lower frequencies are found in the PDC plenum measurements. Hence, cut-off frequencies of 45 and 100 kHz are chosen for the XCE and DTL transducers, respectively. However, a much lower cut-off frequency is chosen for the PCB transducers, compared to their first ringing frequency of 119 kHz in the shock tube study (Fig. 7(c)). This is to suppress the noise-related osculations at lower frequencies in the PDC plenum test rig. Thus, the PCB pressure records are low-pass filtered at a cut-off frequency of 35 kHz, which is a trade-off between the suppression of noise sources and the dynamic representation of the highly transient signal. In addition, a band-stop filter in the range of 1.7 to 5 kHz is used for a limited number of trans-

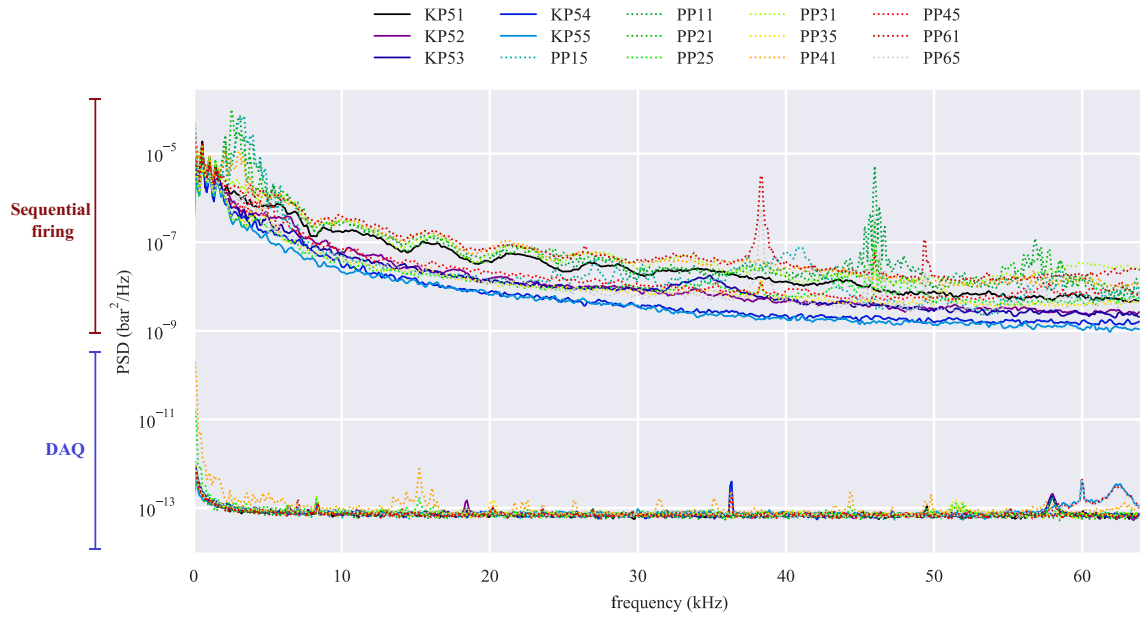

Fig. 8: Power spectral density (PSD) of all plenum pressure transducers and the DAQ system.

ducers, which show high amplitudes in the PSD plot in the corresponding frequency interval (Fig. 8). Furthermore, the signal of the PCB transducers is filtered with a 55 Hz high pass filter to minimize thermal drift.

To evaluate the impact of the digital filter, the original and filtered pressure records for the passage of a shock wave are shown for different cases in Fig. 9. The time is set to zero when the shock wave reaches the transducer. Figure 9(a) presents the original and filtered pressure record of the DTL transducer mounted at the shock tube end-wall. The filtered signal differs only slightly from the original one, indicating the negligible impact of the low-pass filter. Figure 9(b) shows the pressure record of a DTL transducer at the plenum wall after the passage of two shock waves. A relatively strong shock wave passes at t = 0 while a second weaker shock wave passes the transducer at t $\approx$ 0.2 ms. The impact of the filter is relatively marginal, as it only removes some high-frequency oscillations above 100 kHz. On the contrary, the impact of the low-pass filter on the PCB signal is significant. As shown in Fig. 9(c) the ringing due to the excitation of the natural frequencies is suppressed significantly. However, the small cut-off frequency of the low-pass filter inherently alters the signal in an undesirable manner, as a widening or smoothing of the sharp transient pressure at t = 0 is demonstrated. The low-pass filter also results in ripples around larger signal changes, which is distinctive in the interval -0.25 $<$ t $<$ 0.25 ms in Fig. 9(c).

Figure 9(d) shows a typical PCB pressure record in the PDC plenum as a response to the passage of a shock wave. The comparison between the PCB transducer signal in the shock tube with the one in the PDC plenum (Fig. 9(c) vs. (d)) demonstrates that the signal in the plenum shows significantly stronger oscillations than in the shock tube. The excitation of the natural frequencies is assumed to be significantly stronger compared to the plenum due to the mounting of the transducers. The transducer in the shock tube is mounted at the shock tube end-wall resulting in much stronger excitation of natural frequencies, due to the short rise time of the input signal when compared to the side-wall mounting in the plenum measurements. Hence, the comparison of the signals in Fig. 9(c) and (d) supports the hypothesis that the strong ringing in the plenum signal is not caused by the excitation of the natural frequencies but by the susceptibility of the transducers to noise.

The recorded PCB signal at the plenum wall shown in Fig. 9(d) is the counterpart to the DTL signal presented in Fig. 9(b). The comparison of these signals shows that the distinctive ringing of the PCB signal at relatively low frequencies (Fig. 9(d)) is superimposed onto the actual pressure at the plenum wall. The ringing can be suppressed by using an appropriate low-pass filter. Although the filtered PCB signal agrees relatively well with its counterpart DTL signal (Fig. 9(b)), the PCB filtered signal suffers from additional ripples, as well as from substantial smoothing of the transient pressure. Therefore, the Kulite DTL transducers are considered to be better suited for the measurement of the highly transient pressure pulses inside the plenum.

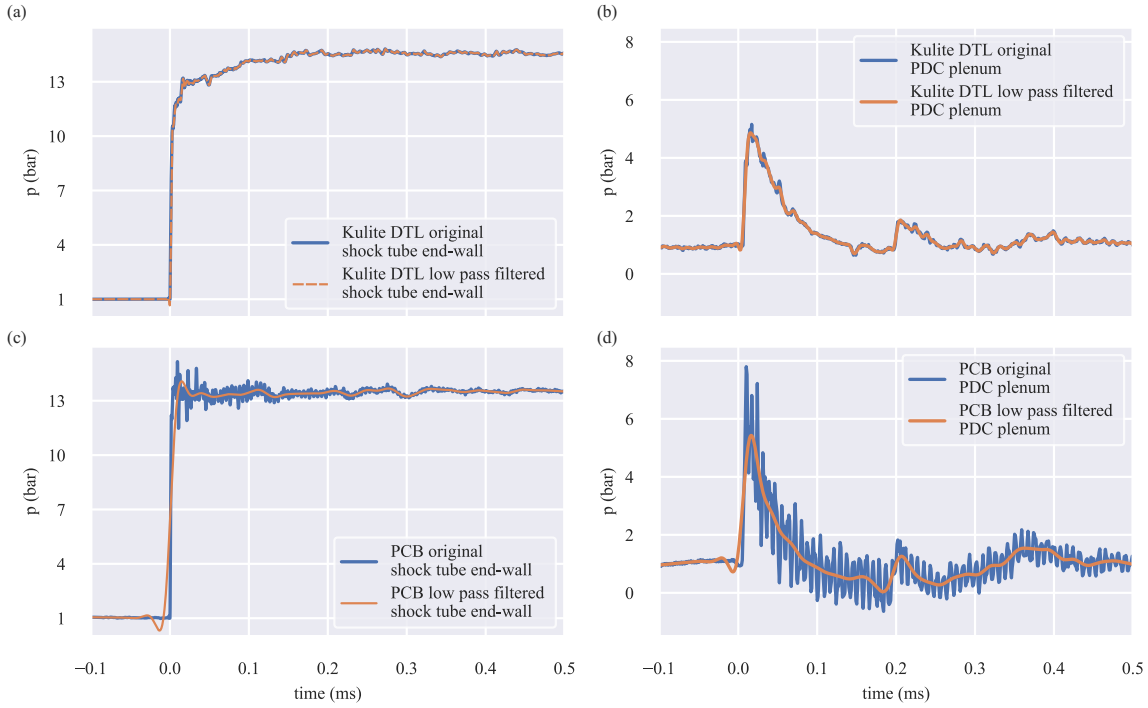

Fig. 9: Impact of the digital low-pass filter on the measured pressure at the (a) shock tube end-wall for Kulite DTL, (b) shock tube end-wall for PCB, (c) PDC plenum for Kulite DTL and (d) PDC plenum for PCB transducers.

3.3 Assessment of Transducer Response & Plenum Inlet Pressure

Using the pressure records from the transducers in the plenum, evaluation is undertaken of both different measurement techniques and shock dynamics inside the plenum. The evolution of the pressure at the plenum inlet, for the sequential firing pattern, is shown in Fig. 10. Pressure readings are ensemble-averaged using the last 19 of the total 20 cycles undertaken in the test. The first cycle is neglected in the remainder of the paper to account for a possibly non-uniform flow inside the plenum as a result of a precursor cycle. Non-dimensional time τ, as a percentage of the total cycle duration, is given in the axis above. This is provided for all subsequent figures.

Assuming a fill-fraction of unity, the detonation waves in each tube transmit as shock waves before they enter the plenum. The shock waves first diffract through the divergent nozzle and again at the plenum entry, due to the increasing cross-sectional area. As the shock waves pass their corresponding pressure transducers (e.g. PP11 for tube one, PP21 for tube two, etc.), a sudden increase in pressure is registered by the transducer. The six pressure pulses shown in Fig. 10 represent the passage of the shock waves for each of the six detonation tubes. Although the same setup is used for all six detonation tubes, the ensemble-averaged peak pressure varies between the tubes from 4.5 to 5.2 bar. The standard deviation for the peak pressure over all 114 considered detonation events occurring in the sequential firing pattern is 10%. However, the standard deviation for the peak pressure of the transducers corresponding to the firing of one specific tube (e.g. PP11 for tube one, PP21 for tube two, etc.) is relatively small; the largest variations occurs in tube one, where PP11 exhibits a standard deviation of 6%. Hence, the variation of the peak pressure is attributed, to some extent, to the stochastic nature of combustion, as well as small differences in the experimental setup across the detonation tubes. Between different tubes there may be small variations in air mass flow rate, H2-supply pressures, spark plug response times and solenoid valve response times.

As mentioned in section 2, transducer KP51 is a piezoresistive Kulite DTL while all the other transducers (PPxx) shown in Fig. 10 are fast-response piezoelectric PCB dynamic pressure transducers. Fig. 10 shows that not only is the Kulite transducer able to resolve the passing shock wave, despite its limited dynamic response, but it also measures a peak pressure in the same range as the other transducers. Hence, the Kulite DTLs are used for further evaluation of the wave dynamics inside the plenum.

The single tube firing pattern is used to investigate both the signal response of the different pressure transducers and the wave dynamics inside the plenum. To this end, only tube 5 is filled with combustible mixture. Fig. 11 presents the pressure measured at the inlet of the plenum for six different azimuthal positions, which correspond to the positions of

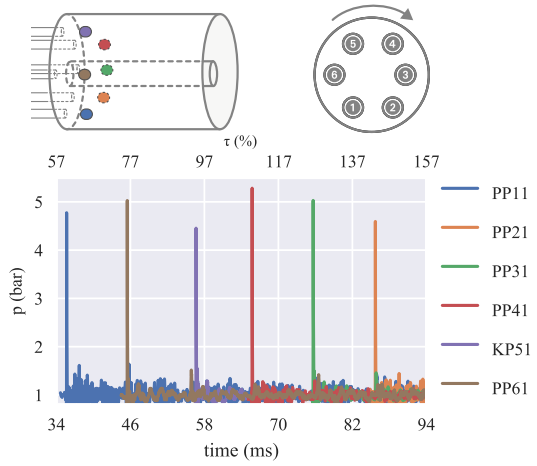

Fig. 10: Ensemble-averaged pressure recorded at the inlet of the plenum for the sequential firing pattern.

the detonation tube axes. As noticeable in Fig 11, the signals from the PCBs show significantly less high-frequency fluctuations when compared to the Kulite signal (PPxx vs. KP51). This is due to the different cut-off frequencies of the digital low-pass filters that were applied to the signal of the PCB and Kulite transducers as discussed in section 3.2.

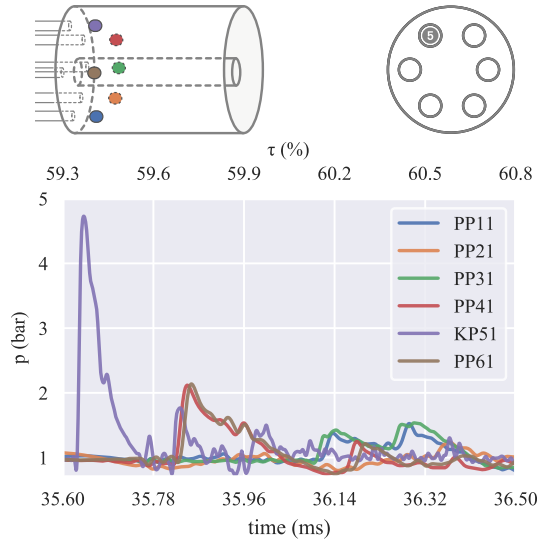

Fig. 11: Pressure recorded at the inlet of the plenum for the first cycle of the single tube firing pattern.

The transducer KP51 is the first transducer to record a pressure increase, as the incident shock wave emanating from tube 5 reaches the KP51 transducer first, at t = 35.62 ms. After approximately 0.2 ms, a secondary peak in the pressure record occurs. This is likely due to the reflection of the diffracted incident wave from the plenum center body. At nearly the same moment, t = 35.82 ms, the shock wave reaches the transducers of its neighboring tubes, PP41 and PP61. The pressure evolution of PP41 and PP61 is very similar, which is expected since the transducers are equidistant from the exit of tube 5. The incident shock continues to propagate further in the circumferential direction and reaches the transducers PP31 and PP11. While the shock initially produced a peak pressure of 4.9 bar at the inlet (KP51), it greatly weakens as it expands inside the plenum. Hence, the pressure peaks decrease at the neighboring tubes (tube 4 and 6) to 2.2 bar and continue to decrease to 1.5 bar at tubes 1 and 3 (PP11 and PP31). These pressure peaks indicate the strength of the waves which could propagate back upstream the neighboring PDCs.

The signal from the transducers in the detonation tube 5 is used to evaluate the strength of the upstream propagating shock wave for the sequential firing pattern. The strongest upstream propagating shock wave occurs in tube 5 after the firing of its neighboring tubes 4 and 6. The shock wave results in a pressure increase of 0.3 bar, which agrees very well with the shock strength calculated by the time-of-flight method. The upstream propagating shock wave is relatively weak, with a shock Mach number of Ms = 1.1. Considering the weak shock wave and the large time delay of 10 ms between the shots in the sequential firing pattern, the impact of the interaction of neighboring tubes is assumed to be minimal. However, the upstream propagating wave may gain in importance for different firing patterns, in particular when the time delay between the firing of neighboring tubes decreases.

3.4 Pressure Pulse Mitigation Downstream of a Firing Tube

Transient pressure inside the plenum is measured with the Kulite DTL transducers, thereby determining the attenuation of the transient shock waves. The transducers are mounted in the axial port array along the plenum wall, downstream of tube 5. Fig. 12(a) shows the static pressure measured by these transducers (KP51 to KP55) as well as the total pressure at the plenum exit (KP56) for the first cycle of the single tube firing pattern. Furthermore, the measured static and total pressure are validated based on the time-of-flight method and one-dimensional gas dynamic laws.

To obtain the static and total pressure, one-dimensional gas dynamic laws for a transient shock wave moving into a stagnant calorically perfect gas are considered [45]. Figure 13 schematically illustrates a moving shock wave in the laboratory reference frame, propagating inside the plenum. The Mach number of the moving shock wave M_s is calculated by measuring the shock velocity and gas temperature. For this purpose, the shock velocity $\hat{u_s}$ between the two transducers is determined using the time-of-flight method; the shock wave velocity is calculated by measuring the time

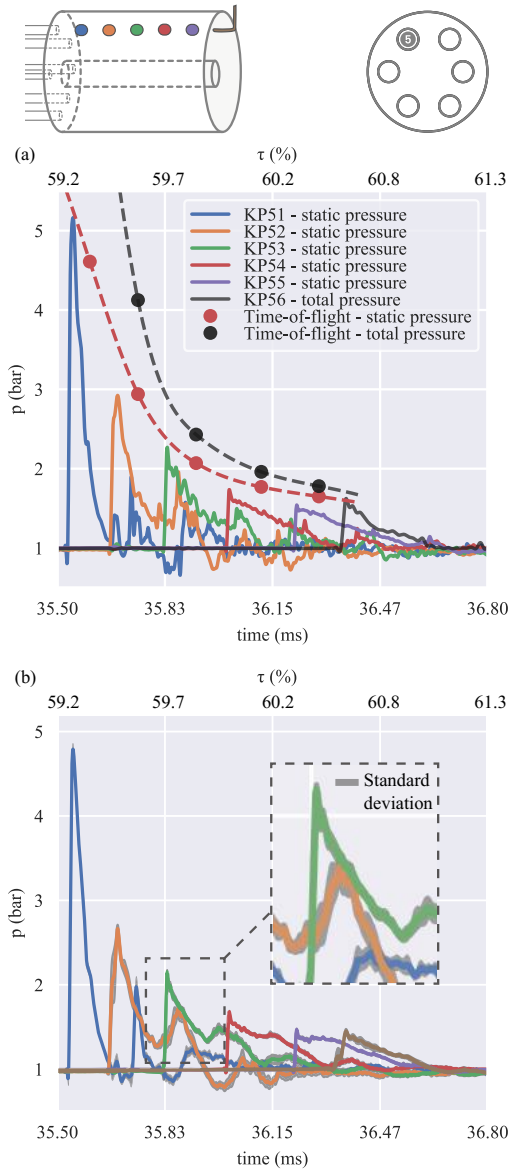

Fig. 12: Pressure record along the plenum in the axial direction, for the single tube firing (a) first cycle (b) ensemble-averaged and standard deviation.

Δt taken by the wave to travel the distance Δx between the transducers: $\hat{u_s} = \frac{\Delta x}{\Delta t}$. The shock wave propagating inside the plenum is moving into the air which is not stagnant ($u_{\text{plenum}} > 0$ in Figure 13). Hence, the shock wave velocity u_s in the reference frame of the wave is determined by accounting for the air velocity in the plenum prior to the arrival of the shock: $u_s = \hat{u_s} - u_{\text{plenum}}$. As the very first cycle of the multi-cycle measurement is considered here, the air velocity inside the plenum u_{plenum} is simply determined based on the set air mass flow rate assuming a steady flow. The speed of sound a_1 upstream of the shock wave is determined from the gas temperature assuming an ideal gas: $a_1 = \sqrt{\gamma \frac{RT_1}{M}}$, where γ, R, T and M denote the specific heat ratio, the universal gas constant, temperature and molar mass of air respectively.

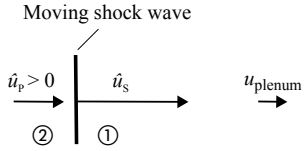

Fig. 13: Schematic illustration of a normal shock wave propagating inside the plenum.

For the first cycle of the multi-cycle measurement the gas temperature inside the plenum prior to arrival of the incident shock is simply taken as the measured air temperature from the laboratory compressed air supply line. Using the shock Mach number $M_s = \frac{u_s}{a_1}$ the static pressure downstream of the leading shock wave can be determined from [45]:

$$\frac{p_2}{p_1} = 1 + \frac{2\gamma}{\gamma+1}(M_s^2 - 1). \tag{1}$$

A shock wave propagating into a stagnant gas induces a bulk motion behind the wave, with velocity u_p in the laboratory reference frame (Fig. 13). The velocity u_p behind the shock wave can be determined by combining the Hugoniot equation with the continuity equation for a normal shock [45] as:

$$u_p = \frac{a_1}{\gamma}\left(\frac{p_2}{p_1} - 1\right)\left[\frac{\frac{2\gamma}{\gamma+1}}{\frac{p_2}{p_1} + \frac{\gamma-1}{\gamma+1}}\right]^{\frac{1}{2}}. \tag{2}$$

By using the Mach number of the induced motion relative to the laboratory, the total pressure $p_{t,2}$ behind the shock wave can be determined by using the isentropic equation for pressure

$$p_{t,2} = p_2\left(1 + \frac{\gamma-1}{2}\left(\frac{u_p}{a_2}\right)^2\right)^{\frac{\gamma}{\gamma-1}}. \tag{3}$$

Both the static and total pressure, which are predicted based on the time-of-flight method and equations 1 and 3, are given in Fig. 12(a). The curves in this figure represent the cubic spline fit for the peak static and total pressure behind the decaying shock wave. There is good agreement between the peaks of the static pressure records and the theoretically determined static pressure. The averaged discrepancy between the measured pressure and the one based on the time-of-flight

method is 7 %. The good agreement demonstrates the ability of the Kulite DTL transducers to resolve the peak pressure behind the shock wave traveling through the plenum. Furthermore, the total pressure is measured near the exit of the plenum using a Kulite XCE transducer. The measured total peak pressure also demonstrates a good agreement with the predicted total pressure. The discrepancy between the measured and calculated total pressure is 4 %. This is the first reported time-accurate measurement of the total pressure at the outlet of a PDC-plenum test rig. Further work is required to determine how the total pressure measurements change across the plenum exit and how they relate to the multi-tube cycle. However, the agreement between both the total and static predictions and the measured data provides confidence in the measurement techniques and the obtained data.

The pressure record for each of the 19 cycles is ensemble-averaged using the peak pressure of the pulse. The ensemble-average and standard deviation of the signals are shown in Fig. 12(b). Given the small cycle-to-cycle variation indicated by the standard deviation, the averaged signal can be used to evaluate the mitigation of the pressure pulsations inside the plenum. Assuming a fill-fraction of one, the CJ detonation wave transmits as a shock wave before its entrance to the plenum. The shock wave at the first transducer (KP51) at the inlet of the plenum results in a pressure increase up to nearly 5 bar. This corresponds to an attenuation of nearly 70% compared to the pressure peak behind the CJ detonation wave in the PDC. The CJ pressure is determined using the NASA CEA code [36]. The measured pressure peak corresponds to a shock wave with a Mach number of 2; this shock wave further weakens as it propagates inside the plenum. The peak pressure measured near the plenum outlet (KP55) is 1.5 bar, which corresponds to further attenuation of the CJ pressure by 90% of its original value. The attenuation of the leading shock wave is not only attributed to the expansion of the shock wave inside the plenum, but also to the trailing Taylor wave, which weakens the leading shock wave [46]. Finally, the total pressure data at the plenum exit shows the temporal evolution of the total pressure at the exit of the plenum close to its outer wall. The peak pressure at this location is approximately 2 bar, corresponding to a shock wave with a Mach number of 1.24 exiting the plenum.

The small standard deviation and the good agreement between the measured pressure peaks and those predicted via the time-of-flight method shows the suitability of the transducers for measuring the static and total pressure inside the plenum. Furthermore, the small standard deviation demonstrates the high repeatability of the measurements.

The signal of the transducer at the plenum inlet shows a secondary peak. Based on the shock propagation velocity and the corresponding distance, this peak is attributed to the reflection of the incident shock wave from the plenum center body. The increase of pressure from the reflected shock wave is also notable in the signal of the pressure transducers KP52 to KP53. However, the pressure record of KP55 shows no additional pressure increase after the pressure rise from the passing incident shock wave. Hence, The strength of the reflected shock decreases as it propagates toward the exit.

The pressure at the inlet of the plenum shows some intervals where pressure falls below atmospheric pressure. The sub-atmospheric pressure is attributed to the vortex ring occurring behind the transmitted shock wave, after its entrance to the plenum [37]. Despite some intervals of sub-atmospheric pressure at the inlet (KP51 and KP52), the static pressure in the downstream half of the plenum (KP54 and KP55) remains above atmospheric pressure. This could be caused by the distortion of the vortex ring as it propagates inside a confined area [47], while it interacts with the plenum wall and its center body. Moreover, the recorded pressure at the inlet (KP51) of the plenum shows a relatively high peak and remains over atmospheric pressure for about 1.3 ms. On the contrary, at the outlet of the plenum, the peak pressure is relatively low and the pressure remains above atmospheric pressure for about 3 times longer. These results show that by using the plenum, the pressure pulse from the CJ detonation is significantly (90%) mitigated, while its energy is redistributed temporally. The significant mitigation of the peak pressure and subsequent reduction of the strongest pressure fluctuations at the inlet of a downstream turbine are of great significance for hybrid-PDE applications [7].

Although the attenuation of the peak pressure with respect to the CJ pressure is expected to increase the turbine performance [7], it is not the primary quantity that determines the turbine efficiency. The definition of turbine efficiency under pulsating inflow conditions is still the subject of research, with various proposals using different averaging techniques [7, 15, 48–51]. However, it is well accepted that turbine performance may be significantly affected by a number of different turbine inlet flow parameters including the flow Mach number, the Mach number of the incident shock, the level of fluctuations with respect to their averaged value as well as the max-min amplitude variation in flow quantities. The latter is of great importance for flow separation in both stator and rotor blades, particularly due to variation in the incident angle, which can result in significant losses [15, 48]. A quantity of great importance is the Mach number of the leading shock wave entering the turbine. A strong incident shock wave may result in significant reflections resulting in transient shock waves propagating both upstream and downstream toward the stator and rotor vanes. These shock reflections can contribute to a considerable amount of performance losses [15]. Another quantity of interest for turbine performance is the the level of fluctuations of flow quantities e.g. pressure with respect to their averaged value. However, due to the limited available data in the current study, neither mass-averaging nor a work-averaging of pressure can be conducted. Thus, the quantity used in this paper to evaluate the plenum outflow is the attenuation of peak pressure with respect to peak pressure in the detonation tube (CJ pressure), which is directly related to the strength of the leading shock.

Similarities and differences between the two firing patterns are examined based on the signal of transducers downstream of the tube 5, via the pressure recordings of transducers KP51 to KP56 shown in Fig. 14. Figure 14 (a) and (b) show a detailed view of the pressure records for the time

interval beginning shortly before the arrival of the incident shock wave originating from tube 5 for the single tube and sequential firing patterns, respectively. For both firing patterns, the incident shock wave enters the plenum approximately 1.5 ms after the ignition (t = 34 ms) and reaches the transducer at the outlet of plenum (KP56) about 1 ms later. Despite some variations, the overall pressure evolution in terms of amplitude and temporal evolution is similar for both firing patterns. Therefore, it can be assumed that the time delay of 10 ms between the firing of each tube is too large for significant cycle-to-cycle interactions to impact the evolution of the transmitted shock wave along the plenum axial axis.

The two different firing patterns are further investigated by considering the pressure record for an entire cycle. Figure 14(c-d) show the pressure records for the very same transducers as for Fig. 14(a-b), again for both single tube and sequential firing patterns, respectively. As discussed before, the detonation in tube 5 results in passage of the incident shock through the plenum in the interval of 35.5 to 36.5 ms for both firing patterns (Fig. 14(a-b)). Besides these peaks, there are some pressure oscillations and peaks in the remainder of the cycle for both firing patterns (Figure 14(c-d)). For the single tube firing (Figure 14(c)), a distinctive oscillation is evident, which decreases in amplitude with time. Moreover, for the sequential firing patterns, there are multiple peaks with an amplitude in the range of 1.6 to 2.3 bar occurring in an interval of 10 ms (Fig. 14(d)). These peaks correspond to the passage of the incident shock waves transmitted from the detonation waves of the remaining five tubes. As discussed earlier, the incident shock waves expand in both axial and radial direction once they enter the plenum. Therefore, they arrive at the transducers downstream of the tube 5, one after each other, in intervals of nearly 10 ms, which corresponds to the time delay for the ignition between the six tubes. Moreover, similar to the single tube firing pattern (Fig. 14(c)), additional oscillations in the pressure records are notable for the sequential firing pattern (Fig. 14(d)). Spectral analysis of the transducer signals shows that the pressure oscillate at distinct frequencies. Besides the effective firing frequency and its harmonics, the signal shows high energy oscillations at other frequencies. The power spectral density of the pressure signals show peaks at 580 Hz for sequential firing pattern, and at 470 Hz for the single tube firing pattern. These frequencies may represent the different acoustic modes of the plenum being excited by the two firing patterns. The excitation of acoustic modes by varying the firing pattern is of significant interest to find an optimized firing pattern with the objective of pressure fluctuation minimization at the plenum outlet [52], which will be addressed in future work.

To account for the temporal pressure variation during an entire cycle, a time integral of the ensemble-averaged pressure ξ over the entire cycle is evaluated as

$$\xi = \int_{\tau=0}^{\tau=100} \hat{p}\, d\tau,$$

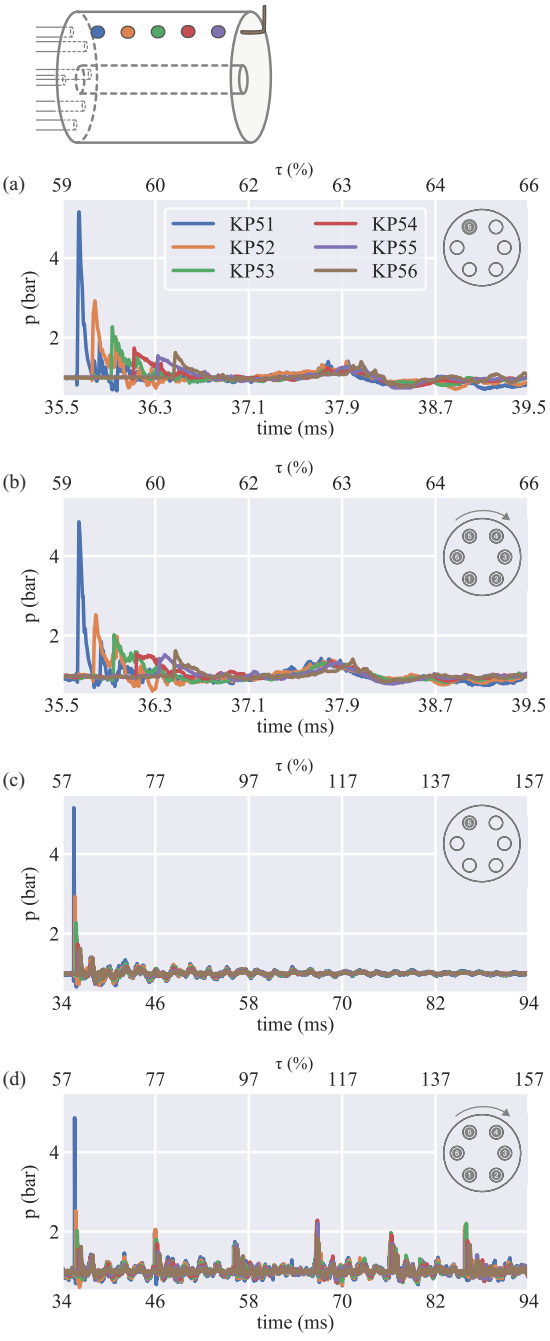

Fig. 14: Pressure record in the axial direction for both single tube firing and sequential firing patterns. (a) Single tube firing - detailed view. (b) sequential firing - detailed view. (c) single tube firing - one cycle. (d) sequential firing - one cycle.

where $\hat{p} = p - p_{\text{atm}}$ denotes the gauge pressure, and p_{atm} the atmospheric pressure. Figure 15 shows ξ for both single tube and sequential firing pattern. In the single tube firing pattern, a small consecutive increase of ξ from KP51 to KP55 is evident despite the decreasing peak pressure from the plenum inlet to its outlet (Fig. 12). Decreasing the peak pressure while maintaining the energy provided by the pressure-gain combustion is the primary objective of the plenum. However, to assess the latter from pressure measurements, the total pressure over the entire cross-section at both the inlet and outlet of the plenum would be necessary, which is not available. Nevertheless, the comparison of ξ for total (KP56) and static pressure can give some insight into the plenum flow evolution. The given values of ξ in Fig. 15 show that for the single tube firing pattern the time integral of total and static pressure are in the same range. Furthermore, the pressure record of KP55 and KP56 are very similar over the entire cycle, resulting in a correlation coefficient of 0.75 for the pressure signals. Therefore, it can be concluded that the static pressure represents a significant portion of the total pressure for the single tube firing pattern, suggesting the fluid kinetic energy exiting the plenum is relatively small.

The interpretation of the results of Fig. 15 for the sequential firing pattern is more difficult, as there is not only one incident shock wave propagating from plenum inlet to its outlet, but there are multiple shock waves presumably reflecting and interacting with each other. However, the ξ value for the transducer at the plenum inlet (KP51) is smaller compared the other transducers. Also, KP51 shows the maximum deviation regarding ξ between the two firing patterns. Hence, the small value for ξ at the inlet of the plenum for the sequential firing pattern is assumed to be caused not by the firing tube but the remaining tubes. The low pressure at the inlet for the sequential firing is attributed to the trailing vortex ring in the exhaust of the neighbouring detonation tubes resulting in lower pressure in the vicinity of the tube exit [37]. Moreover, the ξ value for the total pressure at the plenum outlet (KP56) is 6% larger compared to the single tube firing pattern, indicating the contribution of the 5 other tubes in total pressure at the plenum outlet downstream of tube 5.

3.5 Circumferential Pressure Distribution at the Plenum Outlet

The flow evolution over the entire cross-section of the plenum outlet is of interest, as it sets the inlet conditions for a downstream turbine. Hence, the spatial distribution of pressure over time at the plenum outlet is significant for the assessment of a firing pattern. For this purpose, the records of static pressure transducers distributed circumferentially at the outlet of the plenum are considered.

Figure 16(a) shows the ensemble-averaged pressure records of all six transducers, located just upstream of the plenum outlet, for the entire cycle for the single tube firing pattern. The shock waves reach the plenum outlet at about $\tau = 60\%$, followed by oscillations about the atmospheric pressure. However, the amplitude of these oscillations quickly settles down to near the atmospheric pressure. After only a further 10 % of the entire cycle, the peak pressure of the oscillations is less than 10 % of the maximum oscillation measured (2.4 bar). The temporal evolution of the pressure shows that the flow at the plenum outlet is affected distinctively only for a short time as a result of the firing of one detonation tube.

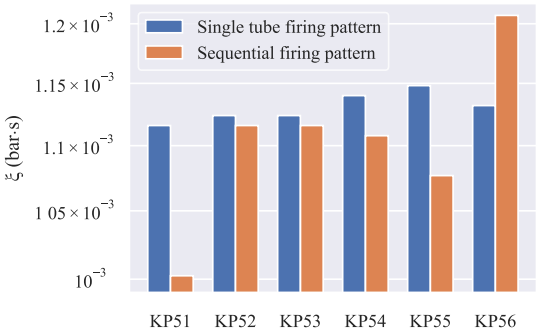

Fig. 15: Time integral of the ensemble-averaged pressure over the entire cycle.

A detailed view of the pressure records for the single tube firing pattern at the plenum outlet is shown in Fig. 16(b) representing the primary response of the transducers to the passage of the incident shock wave. As discussed in section 3.3, the shock wave from the detonation tube diffracts after its entrance to the plenum. It reflects from plenum walls and its center body. As shown in Fig. 16(b), the incident shock wave originating from tube 5 reaches the transducer KP55 first, which is directly downstream of tube 5, mounted at the plenum outlet (Fig. 2). The pressure record of PP45 and PP65 shows the simultaneous arrival of the incident shock wave at t = 36.3 ms. The evolution of the pressure at the plenum outlet (Figure 16(b)) shows some similarities to the plenum inlet (Fig. 11). The incident shock wave reaches the transducer downstream of the tube first (KP55). Then it arrives at the transducers of the neighboring tubes (PP45 and PP65), before it reaches the transducers of the two tubes further away (PP15 and PP35). However, the peak pressure of the pressure records at the plenum outlet differs significantly from the one at the plenum inlet (Fig. 11). As discussed in section 3.3, the peak pressure at the plenum inlet decreases continuously from tube 5 to the neighboring tubes as the shock wave diffracts in the circumferential direction. On the contrary, at the plenum outlet, the peak pressure of KP55 (1.55 bar) is the smallest compared to the remaining transducers, while the peak pressure of its neighboring tubes (PP45 and PP65) and their neighboring tubes (PP15 and PP35) are all in the same range (1.7 to 1.8 bar). However, the maximum peak pressure at the plenum outlet occurs at the opposite tube transducer (PP25). The peak pressure of PP25 is 2.4 bar, which is 1.6 times larger than KP55. The underlying mechanism leading to the pressure evolution at the plenum outlet cannot be determined based

on the available pressure records. However, the signal of the transducer PP25 shows a precursor pressure wave resulting in pre-compression, before the arrival of the stronger shock wave at t = 36.8 ms, which leads to its peak pressure of 2.4 at t = 36.84 ms. One possible explanation for such a pressure evolution is that the first pressure wave reaching the transducer is the part of the incident shock wave, which moves along the shortest path to the transducer. The continuous expanding incident shock wave weakens, resulting in a pressure increase of only 0.5 bar at PP25. The second stronger wave may be the part of the incident shock wave which propagates first in a different direction (e.g. circumferential direction) before it moves toward the plenum outlet. The absolute pressure behind this shock wave would be relatively high as it propagates within pre-compressed gas. Nevertheless, these results indicate the complex flow field of the plenum consisting of multiple shock wave reflections and interactions. However, the pressure records show clearly that a transmitted shock wave from a detonation tube will result in shock waves reaching the end of the plenum along its entire circumference, with maximum pressure occurring on the opposite side of the firing tube. These results show that by using a plenum, the peak pressure at the plenum outlet is reduced by 85 % compared to the peak pressure (CJ pressure) in the detonation tube.

Before discussing the plenum outlet pressure for the sequential firing pattern, we use the example of the band-stop filter to emphasize the impact of the applied digital filter on the biased pressure data. Figure 16(c) is the counterpart to Fig. 16(b) with the only difference that in Fig. 16(c) the band-stop filter is turned off for PP15 and PP45. As discussed before, the pressure record of the transducers, which have the same distance to the outlet of tube 5, are assumed to be equal for reasons of symmetry (Fig. 2). This concerns the transducer pairs PP15 - PP35 as well as PP45 - PP65. In contrast to PP15 and PP45, the spectral analysis shows no high peaks in the low-frequency range (frequency $<$ 5 kHz) for PP35 and PP65 (Fig. 8). Hence, the pressure record of these transducers is assumed to be unbiased in the low-frequency range and is therefore not processed with a band-stop filter. Thus, the impact of the applied filter can be emphasized by comparing the signal of the transducer pairs PP15 - PP35 and PP45 - PP65.

The comparison of the filtered and unfiltered PP45 signal in Fig. 16(b) and (c) shows that the band-stop filter results presumably in the correction of the peak pressure, as the peak pressure of PP45 and PP65 agree if the filter is applied. However, it leads to significant ripples before and after the peak pressure ($36.18 < t < 36.28$ and $36.4 < t < 36.5$). In case of PP15 the band-stop filter is absolutely crucial, as its signal suffers from high amplitude fluctuations in low-frequency ranges, which is evident in the frequency domain (Fig. 8) and in the time domain (Fig. 16(c)). These fluctuations are suppressed significantly by the applied filter, although the signal still suffers from some noise (Fig. 16(b), as it does not fully comply with the pressure record of its corresponding transducer pair PP35. Moreover, the signal of all transducers shown in Figs. 16(b) and(c) show a very small standard deviation, which indicates the high repeatability of the measurements. However, the comparison between the filtered and unfiltered pressure records shows a small standard deviation is not a sufficient measure for the accuracy of the signal, if the transducer is biased. Hence, these results underline the significance of appropriate filter in the post-processing of noisy pressure records to prevent misrepresentation of the measurand.

Figure 17 presents the ensemble-averaged and standard deviation pressure at the plenum outlet for the sequential firing pattern. As mentioned in section 2, the tube firing order in the sequential firing pattern is 6, 5, 4, 3, 2, and 1, where each tube fires 20 times in an interval of 60 ms resulting in a time delay of 10 ms between each shot. Figure. 17(a) shows a sequence of 1 ms as the incident shock waves originating from tube 1 reaches the transducers at the plenum outlet. Figures 17(b) to (f) show the corresponding sequences for the incident shock waves originating from tube 6 to 2, respectively. We first discuss the features which all the curves shown in Fig 17 have in common before emphasizing the differences. Similar to the single tube firing sequence, the first transducer being passed by a shock wave is the one downstream of the firing tube (e.g. PP15 in Fig. 17(a)). Also, the last transducer exposed to the incident shock wave is the one on the opposite tube (e.g. PP45 in Fig. 17(a)). This transducer is also the one with the maximum peak pressure. However, there are some differences compared to the single tube firing pattern. With the exception of the transducer corresponding to the firing tube (e.g. PP15 in Fig. 17(a)), the peak pressures of the remaining five transducers are on average 15 % smaller compared to the single tube firing pattern. Furthermore, the timing for the occurrence of the incident shock waves at the various transducers is different, when compared to the single tube firing case. In fact, the timing for the occurrence of the shock waves varies from tube to tube in the sequential firing pattern (Fig. 17(a) to (f)). This is attributed to the small variations in the experimental setup across the detonation tubes (i.e. H2-supply pressure, spark plug response time, valve response time, etc.) Contrary to the single tube case, there are no pairs of similar pressure records through entire pressure records of six tubes (Fig. 17(a) to (f)), but the incident shock waves reach the transducers one after another. Hence, the flow evolution inside the plenum is not symmetric for the sequential firing pattern. The differences with the single tube case can be attributed to the inhomogeneous flow inside the plenum, prior to the arrival of the incident shock wave, which results in asymmetrical evolution of the pressure. In contrast to the evolution of pressure in the axial plenum direction (Fig. 12), the pressure evolution in the circumferential direction is noticeably affected by the prior shot. Hence, it can be assumed that further reduction of delay time between the shots would result in more significant interaction of the consecutive shots and hence the flow inside the plenum. This is again of significant interest for future work regarding the determination of optimal firing sequences, which rely on the interaction of successive firings within a cycle inside the plenum [52].

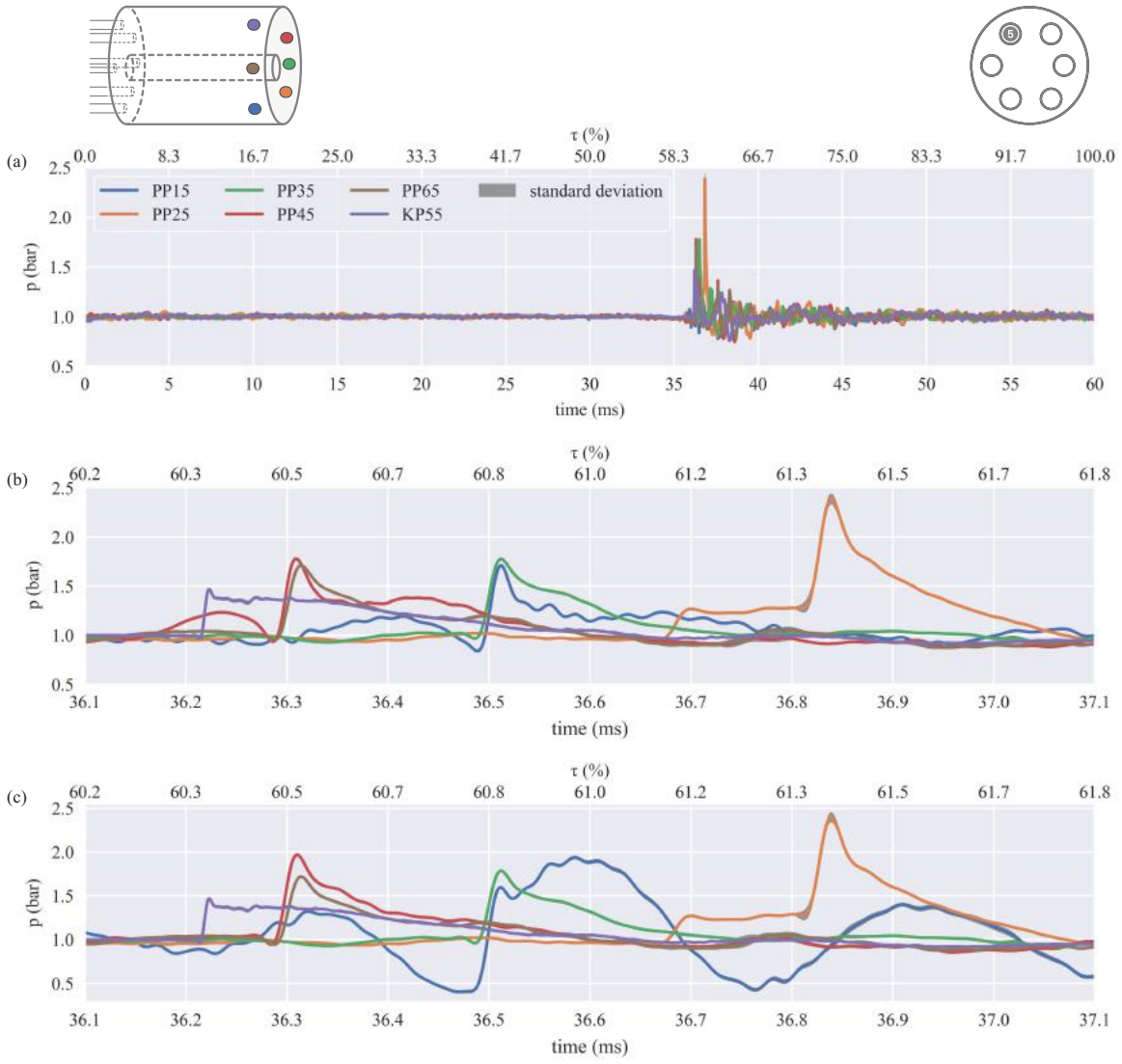

Fig. 16: Ensemble-average and standard deviation of pressure record at the plenum outlet for the single tube firing pattern. (a) Entire cycle. (b) Detailed view. (c) Detail view without band-stop filter.

4 Conclusion

The pressure evolution inside an annular ring plenum downstream of an array of six PDCs arranged in a can-annular configuration is investigated. The main purpose of the plenum is the mitigation of pressure fluctuation from the pulsating flow exhausting from each PDC, which is crucial for operation with a downstream turbine. Two firing patterns, a single tube and a sequential firing pattern in a multi-cycle operation mode are investigated based on pressure measurements. Each tube operates at 16.7 Hz with a total of 20 cycles.

The accuracy, as well as the dynamic response of both PCB and Kulite pressure transducers, is investigated in a preliminary study using a shock tube. The transducers are flush-mounted to the end-wall of the shock tube, allowing the assessment of their response to well-defined and well-formed shock waves. All transducers prove to be capable of resolving the dynamic pressure behind the shock waves. The piezoelectric PCB transducers show better performance regarding both accuracy and dynamic response compared to the Kulite transducers in the low noise environment of the shock tube facility.

The pressure in the PDC plenum test rig is measured using the same PCB and Kulite transducers flush-mounted

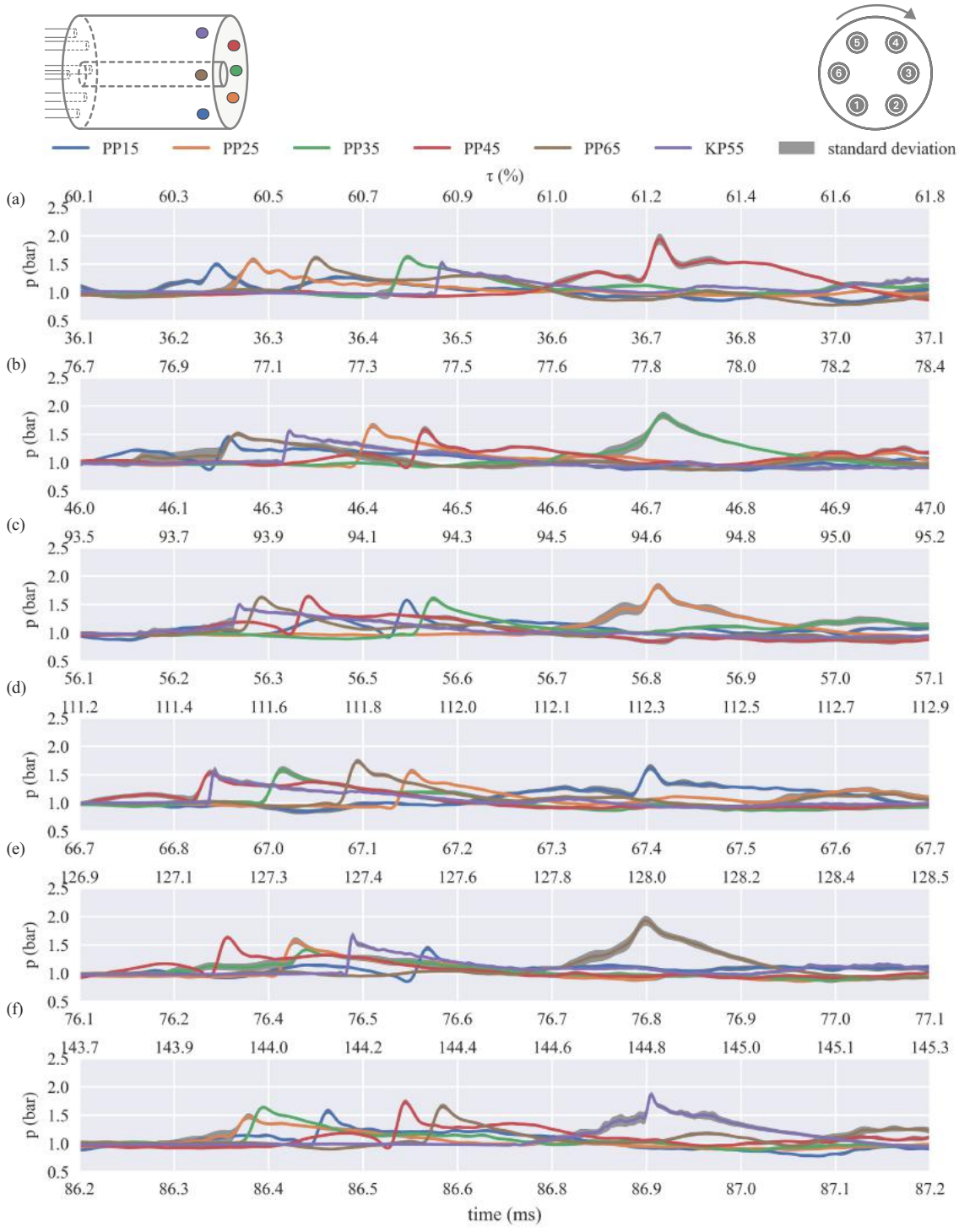

Fig. 17: Ensemble-average and standard deviation of pressure record at the plenum outlet for the sequential firing pattern showing the time sequence for passage of shock waves originating from tube (a) 1, (b) 6, (c) 5, (d) 4, (e) 3, (f) 2.

to the plenum inner wall. However, the signals from most of the PCB transducers suffer from substantial fluctuations at frequencies far below their resonant frequencies. This is attributed to their susceptibility to interfering sources such as electromagnetic interference. In contrast, the Kulite transducers are considerably less affected by external noise sources. The Kulite transducers are able to resolve the sudden pressure rise behind the leading shock wave inside the plenum with a remarkably small standard deviation despite their inferior dynamic response, compared to the PCB transducers. Furthermore, the measured peak pressure of the leading shock wave using the Kulite transducers is validated using the time-of-flight method. Both the static and the high-frequency total pressure probe show a very good agreement with the theoretically determined quantities. Furthermore, in an attempt to suppress the noise, a spectral analysis of the PCB transducer signals in both shock tube and PDC plenum is conducted to define an appropriate digital filter for each individual transducer. The comparison of unfiltered and filtered biased signals with the signal of the unbiased transducers demonstrates the necessity of filter application to obtain an accurate representation of the actual pressure.

The signal of the pressure transducers is used to assess the flow evolution inside the plenum. With a fill-fraction of approximately one, the detonation wave transmits as a shock wave at the intersection of the combustible mixture with the air buffer before entering the plenum. The wave diffracts first through the nozzle before its entrance to the plenum. Once the leading shock wave enters the plenum it diffracts further and it expands in both axial and radial directions as it propagates through the plenum. The pressure data at the plenum inlet shows that although the strength of the leading shock wave decreases as it propagates, a pressure rise of more than one bar occurs at the neighboring detonation tubes. This provides insight into the strength of the waves which propagate back upstream through neighboring PDCs. However, the interaction of the neighboring tubes for the studied firing patterns is marginal as the backward propagating shock wave for the studied firing patterns is relatively weak with a shock Mach number of 1.1. Moreover, the measured total and static pressure at the plenum outlet for the single tube firing pattern indicate that the fluid kinetic energy of the plenum exhaust is relatively small, while the main portion of the total pressure is contributed by the static pressure.

The flow evolution inside the plenum shows some similarities for the two different firing patterns. For both firing patterns significant changes in pressure at the plenum outlet occur only for a short time relative to the cycle duration due to the firing of a detonation tube. The circumferential distribution of pressure at the plenum outlet differs significantly from the one at the plenum inlet. The peak pressure at the plenum inlet decreases in the circumferential direction as the incident shock wave expands toward the neighboring tubes. On the contrary, at the plenum outlet, the peak pressure of the transducers downstream of the neighboring tubes is higher compared to the firing tubes. The maximum pressure at the plenum outlet occurs at the opposite side of the firing tube. However, there are also some dissimilarities between the two firing patterns. While the pressure evolution for the single tube firing pattern is indicative of symmetrical flow evolution inside the plenum, the plenum flow for the sequential firing pattern is asymmetric. Hence, it can be assumed that there is an interaction of the consecutive firings inside the plenum, which can be presumably increased by reduction of the time delay between the tube firings. This is of significant interest for future work regarding the determination of optimal firing sequences that rely on the interaction of successive firings within a cycle inside the plenum.

The peak pressure at the plenum exit is of major interest for a downstream turbine, as it determines the maximum fluctuations in a multi-cycle operation mode. The pressure evolution inside the plenum is used to assess the impact of the plenum on the mitigation of the pressure pulses. The peak pressure of nearly 5 bar, measured at the plenum inlet for both firing patterns, corresponds to an attenuation of nearly 70% compared to the initial CJ-pressure inside the detonation tube. The pressure behind the leading shock wave inside the plenum continuously decreases along its axial direction from 5 bar at the inlet to 1.5 bar at the outlet. This corresponds to a total attenuation of the CJ pressure by 90%. As the flow evolution over the entire cross-section of the plenum outlet is of interest for a downstream turbine, the pressure records distributed circumferentially at the plenum outlet are considered. The averaged peak pressure over all shots at the plenum outlet is 1.8 bar for the sequential firing pattern which is about 30 % smaller than the 2.4 bar observed for the single tube firing pattern. These peak pressures correspond to a total attenuation of the CJ pressure by 85 % for the single tube and 89 % for the sequential tube firing pattern. Thus, the plenum results in a significant attenuation of the leading shock wave and redistributes the energy both spatially and temporally. This is highly encouraging for integrating the multi-tube PDC-plenum with a downstream turbine. The excellent performance of the piezoresistive pressure transducer demonstrated in this work allows for a more accurate measurement of both the static and total pressure inside and at the exit of the plenum. In particular, the measurement of total pressure allows for evaluation of the net pressure gain, which will be addressed in future work.

Acknowledgements

The authors gratefully acknowledge the support of the Deutsche Forschungsgemeinschaft (DFG) as part of the collaborative research centre SFB 1029 "Substaintial efficiency increase in gas turbines through direct use of coupled unsteady combustion and flow dynamics" in Projects A01, A08 and C01. The authors also acknowledge financial support from the Australian Research Council through discovery project DP190102220. This research is supported by an Australian Government Research Training Program (RTP) Scholarship and by a German Academic Exchange Service (DAAD) Fellowship.

References

[1] Heiser, W. H., and Pratt, D. T., 2002. "Thermodynamic cycle analysis of pulse detonation engines". *Journal of Propulsion and Power,* **18**(1), pp. 68–76.

[2] Rasheed, A., Furman, A. H., and Dean, A. J., 2011. "Experimental investigations of the performance of a multitube pulse detonation turbine system". *Journal of Propulsion and Power,* **27**(3), pp. 586–596.

[3] Rasheed, A., Furman, A., and Dean, A. J., 2005. "Experimental investigations of an axial turbine driven by a multi-tube pulsed detonation combustor system". *AIAA Paper,* **4209**, p. 2005.

[4] Glaser, A., Caldwell, N., and Gutmark, E., 2006. "Performance measurements of a pulse detonation combustor array integrated with an axial flow turbine". In 44th AIAA aerospace sciences meeting and exhibit, p. 1232.

[5] Paxson, D. E., and Kaemming, T., 2014. "Influence of unsteadiness on the analysis of pressure gain combustion devices". *Journal of Propulsion and Power,* **30**(2), pp. 377–383.

[6] Rezay Haghdoost, M., Edgington-Mitchell, D. M., Paschereit, C. O., and Oberleithner, K., 2020. "High-speed schlieren and particle image velocimetry of the exhaust flow of a pulse detonation combustor". *AIAA Journal,* **58**(8), pp. 3527–3543.

[7] Fernelius, M. H., and Gorrell, S. E., 2020. "Mapping efficiency of a pulsing flow driven turbine". *Journal of Fluids Engineering*.

[8] Eidelman, S., and Yang, X., 1998. "Analysis of the pulse detonation engine efficiency". In 34th AIAA/ASME/SAE/ASEE Joint Propulsion Conference and Exhibit, p. 3877.

[9] Allgood, D., Gutmark, E., Hoke, J., Bradley, R., and Schauer, F., 2006. "Performance measurements of multicycle pulse-detonation-engine exhaust nozzles". *Journal of Propulsion and Power,* **22**(1), pp. 70–779.

[10] Thethy, B., Rezay Haghdoost, M., Oberleithner, K., Honnery, D., and Edgington-Mitchell, D. M., 2019. "Influence of nozzle geometry on detonation-driven and shock-driven transient supersonic jet flow". In 24th International Society for Air Breathing Engines Conference, pp. 1–22.

[11] Janka, A. M., 2014. "Methods of diffusing pulse detonation combustion". Master's thesis, Virginia Tech.

[12] Rezay Haghdoost, M., Thethy, B. S., Nadolski, M., Klein, R., Honnery, D., Edgington-Mitchell, D. M., Seo, B., Paschereit, C. O., and Oberleithner, K., 2020. "Evaluation of shock dividers using numerical and experimental methods". In AIAA Scitech 2020 Forum, p. 0926.

[13] Thethy, B. S., Rezay Haghdoost, M., Paschereit, C. O., Honnery, D., Edgington-Mitchell, D. M., and Oberleithner, K., 2020. "Redistribution of transient shock waves using shock dividers". In AIAA Scitech 2020 Forum, p. 0925.

[14] Paniagua, G., Iorio, M., Vinha, N., and Sousa, J., 2014. "Design and analysis of pioneering high supersonic axial turbines". *International Journal of Mechanical Sciences,* **89**, pp. 65–77.

[15] Xisto, C., Petit, O., Grönstedt, T., Rolt, A., Lundbladh, A., and Paniagua, G., 2018. "The efficiency of a pulsed detonation combustor–axial turbine integration". *Aerospace Science and Technology,* **82**, pp. 80–91.

[16] Rasheed, A., Furman, A., and Dean, A., 2006. "Wave attenuation and interactions in a pulsed detonation combustor-turbine hybrid system". In 44th AIAA aerospace sciences meeting and exhibit, p. 1235.

[17] Rasheed, A., Furman, A. H., and Dean, A. J., 2009. "Pressure measurements and attenuation in a hybrid multitube pulse detonation turbine system". *Journal of Propulsion and Power,* **25**(1), pp. 148–161.

[18] Carter, S., Ned, A., Chivers, J., and Bemis, A., 2016. "Selecting piezoresistive vs. piezoelectric pressure transducers". *Kulite Semiconductor Products, Inc*.

[19] Habicht, F. E., Yücel, F. C., Gray, J. A., and Paschereit, C. O., 2020. "Detonation initiation by shock focusing at elevated pressure conditions in a pulse detonation combustor". *International Journal of Spray and Combustion Dynamics,* **12**, p. 1756827720921718.

[20] Thethy, B., Kaebe, B., Honnery, D., Edgington-Mitchell, D., and Kleine, H., 2020. "Influence of pressure transducer protrusion depth on pressure measurements of shock waves in shock tubes". *Review of Scientific Instruments*.

[21] Kaemming, T. A., and Paxson, D. E., 2018. "Determining the pressure gain of pressure gain combustion". In 2018 Joint Propulsion Conference, p. 4567.

[22] Fievisohn, R. T., Hoke, J., and Holley, A. T., 2020. "Equivalent available pressure measurements on a laboratory rde". In AIAA Scitech 2020 Forum, p. 2285.

[23] Bach, E., Bohon, M. D., Paschereit, C. O., and Stathopoulos, P., 2019. "Impact of outlet restriction on rdc performance and stagnation pressure rise". In AIAA Scitech 2019 Forum, p. 0476.

[24] Paxson, D., and Dougherty, K., 2005. "Ejector enhanced pulsejet based pressure gain combustors: an old idea with a new twist". In 41st AIAA/ASME/SAE/ASEE Joint Propulsion Conference & Exhibit, p. 4216.

[25] of Mechanical Engineers, A. S., 1972. "A guide for the dynamic calibration of pressure transducers". ASME.

[26] , 2014. An Experimental Frequency Response Characterization of MEMS Piezoresistive Pressure Transducers, Vol. Volume 6: Ceramics; Controls, Diagnostics and Instrumentation; Education; Manufacturing Materials and Metallurgy of *Turbo Expo: Power for Land, Sea, and Air*. V006T06A031.

[27] Stankevic, V., and Simkevicius, C., 2000. "Use of a shock tube in investigations of silicon micromachined piezoresistive pressure sensors". *Sensors and Actuators A: Physical,* **86**(1), pp. 58 – 65.

[28] Persico, G., Gaetani, P., and Guardone, A., 2005. "Dynamic calibration of fast-response probes in low-pressure shock tubes". *Measurement Science and Technology,* **16**(9), p. 1751.

[29] Bivolaru, D., and Papadopoulos, G., 2019. "Plasma driven shock tube for dynamic characterization of sensors". In Fluids Engineering Division Summer Meeting, Vol. 59070, American Society of Mechanical Engineers, p. V004T04A005.

[30] Downes, S., Knott, A., and Robinson, I., 2014. "Towards a shock tube method for the dynamic calibration of pressure sensors". *Philosophical Transactions of the Royal Society A: Mathematical, Physical and Engineering Sciences,* **372**(2023), p. 20130299.

[31] Esward, T., Matthews, C., Downes, S., Knott, A., Eichstädt, S., and Elster, C., 2012. "Uncertainty evaluation for traceable dynamic measurement of mechanical quantities: a case study in dynamic pressure calibration". In *Advanced Mathematical And Computational Tools In Metrology And Testing IX*. World Scientific, pp. 143–150.

[32] Damion, J., 1994. "Means of dynamic calibration for pressure transducers". *Metrologia,* **30**(6), p. 743.

[33] Hjelmgren, J., 2002. *Dynamic measurement of pressure.-A literature survey*.

[34] Li, Q., Wang, Z., Wang, Z., and Yan, H., 2015. "Novel method for estimating the dynamic characteristics of pressure sensor in shock tube calibration test". *Review of Scientific Instruments,* **86**(6), p. 065002.

[35] Gray, J. A., Paschereit, C. O., and Moeck, J. P., 2015. "An experimental study of different obstacle types for flame acceleration and ddt". In *Active Flow and Combustion Control 2014*. Springer, pp. 265–279.

[36] McBride, B. J., 1996. *Computer program for calculation of complex chemical equilibrium compositions and applications*, Vol. 2. NASA Lewis Research Center.

[37] Rezay Haghdoost, M., Edgington-Mitchell, D., Nadolski, M., Klein, R., and Oberleithner, K., 2020. "Dynamic evolution of a transient supersonic trailing jet induced by a strong incident shock wave". *Phys. Rev. Fluids,* **5**, Jul, p. 073401.

[38] Djordjevic, N., Rekus, M., Vinkeloe, J., and Zander, L., 2019. "Shock tube and kinetic study on the effects of co2 on dimethyl ether autoignition at high pressures". *Energy & Fuels,* **33**(10), pp. 10197–10208.

[39] Vinkeloe, J., Zander, L., Szeponik, M., and Djordjevic, N., 2020. "Tailoring the temperature sensitivity of ignition delay times in hot spots using fuel blends of dimethyl ether, methane, and hydrogen". *Energy & Fuels,* **34**(2), pp. 2246–2259.

[40] , 2015. Real-Time, Advanced Electrical Filtering for Pressure Transducer Frequency Response Correction, Vol. Volume 6: Ceramics; Controls, Diagnostics and Instrumentation; Education; Manufacturing Materials and Metallurgy; Honors and Awards of *Turbo Expo: Power for Land, Sea, and Air*. V006T05A015.

[41] Pang, G., Davidson, D., and Hanson, R., 2009. "Experimental study and modeling of shock tube ignition delay times for hydrogen–oxygen–argon mixtures at low temperatures". *Proceedings of the combustion institute,* **32**(1), pp. 181–188.

[42] Petersen, E. L., and Hanson, R. K., 2001. "Nonideal effects behind reflected shock waves in a high-pressure shock tube". *Shock Waves,* **10**(6), pp. 405–420.

[43] Grogan, K., and Ihme, M., 2020. "Stanshock: a gas-dynamic model for shock tube simulations with non-ideal effects and chemical kinetics". *Shock Waves*, pp. 1–14.

[44] Mersinligil, M., Brouckaert, J.-F., Courtiade, N., and Ottavy, X., 2012. "A high temperature high bandwidth fast response total pressure probe for measurements in a multistage axial compressor". *Journal of engineering for gas turbines and power,* **134**(6).

[45] Anderson Jr, J. D., 2010. *Fundamentals of aerodynamics*. Tata McGraw-Hill Education.

[46] Taylor, G. I., 1950. "The dynamics of the combustion products behind plane and spherical detonation fronts in explosives". *Proceedings of the Royal Society of London. Series A. Mathematical and Physical Sciences,* **200**(1061), pp. 235–247.

[47] Allgood, D., Gutmark, E., Rasheed, A., and Dean, A. J., 2005. "Experimental investigation of a pulse detonation engine with a two-dimensional ejector". *AIAA journal,* **43**(2), pp. 390–398.

[48] George, A. S., Driscoll, R., Gutmark, E., and Munday, D., 2014. "Experimental comparison of axial turbine performance under steady and pulsating flows". *Journal of Turbomachinery,* **136**(11).

[49] Suresh, A., Hofer, D. C., and Tangirala, V. E., 2011. "Turbine efficiency for unsteady, periodic flows". *Journal of Turbomachinery,* **134**(3), pp. 1–6.

[50] Liu, Z., Braun, J., and Paniagua, G., 2020. "Thermal power plant upgrade via a rotating detonation combustor and retrofitted turbine with optimized endwalls". *International Journal of Mechanical Sciences,* **188**, p. 105918.

[51] Cumpsty, N. A., and Horlock, J. H., 2006. "Averaging nonuniform flow for a purpose". *Journal of Turbomachinery,* **128**(1), pp. 120–129.

[52] Wolff, S. D., and King, R., 2019. "Optimal control for firing synchronization in an annular pulsed detonation combustor mockup by mixed-integer programming". In AIAA Scitech 2019 Forum, p. 1742.

Chapter 5

Discussion

In this chapter, the main results of the publications presented in the previous chapter are reviewed. As the main objectives of this work are twofold, the findings are summarized in two categories. First, the transient exhaust of the PDC is discussed. This is followed by an overview of the investigations with the objective of modifying the PDC exhaust. Finally, a discussion regarding the limitations and shortcomings is provided. The chapter closes with some incentives for follow-up studies.

5.1 Exhaust of the Pulse Detonation Combustor

This section reviews the collective findings on the exhaust of the PDC. As discussed in chapter 1, the characterization of the PDC exhaust flow dynamics is of interest for both PDC-nozzle and PDC-turbine engines.

Fill Fraction

The PDC exhaust is investigated for different fill fractions. The fill fraction represents one of the primary operation control parameters for both PDC-nozzle and PDC-turbine engines. Enhancing the specific impulse in a PDC-nozzle engine can be achieved by decreasing the fill fraction [62, 114]. In a fully filled or overfilled PDC, wherein the fill fraction ≥ 1, the wave leaving the combustor is a detonation wave. It transmits to a strong shock wave only after it enters the atmosphere. Thus, a significant amount of energy leaves the engine with the detonation wave, without producing thrust. By reducing the fill fraction, a weaker shock wave leaves the engine. Therefore, the amount of unused energy decreases, which can result in a larger specific impulse for the PDC-nozzle engine.

The fill fraction is also of interest in the application of PDC-turbine engines. Depending on the turbine design, a smaller fill fraction can lead to a higher turbine efficiency as the strength of the incident shock entering the turbine decreases with lower fill fractions. Furthermore, the fill fraction is one of the primary control parameters for partial loading of the engine, as less chemical energy is converted into thrust or work for a smaller fill fraction. Accordingly, the impact of fill fraction on the PDC exhaust is investigated.

5.1.1 Initial Phase of the Exhaust

The schlieren technique (chapter 3.3) is used as one of the primary techniques to investigate the PDC exhaust. The high-resolution, high-speed schlieren images allow for a

detailed study of the initial jet evolution. It is observed that with increasing fill fraction, the combustion products leave the PDC earlier, and thereby overlay the exhaust flow structures in the schlieren images. Hence, a relatively small fill fraction is used for a detailed investigation of the initial phase of the exhaust process. The term *initial phase* refers to the the time interval between the exit of the incident shock wave and the vortex ring pinch-off, which represents the separation of the vortex ring from the trailing jet.

PDC Exhaust vs. Shock Tube Exhaust

Reviewing the literature on the flow evolution of a transient compressible starting jet, which is commonly investigated through the exhaust of an open-end shock tube, revealed a very large similarity between the initial phase of the exhaust of a classical non-reactive shock tube and the exhaust of a small fill fraction PDC [1]. This is not surprising as in both cases the initial phase of the exhaust flow is determined by a shock wave diffracting out of a tube. However, the PDC and the shock tube exhaust differ, even if the incident shock Mach number at the tube exit is kept equal. Roughly speaking, the differences between the PDC and the shock tube exhaust are mainly due to the different "histories" of the leading shock. The thermodynamic quantities behind the incident shock, up to the contact surface, are constant in an ideal one-dimensional shock tube as the shock wave propagates with a constant velocity toward the tube exit [2]. Therefore, the incident shock Mach number remains constant until the shock wave leaves the shock tube. In contrast, the Mach number of the incident shock wave decreases continuously while it propagates toward the tube exit in a partially filled PDC, as shown in the publication in chapter 4.2. This is mainly due to the Taylor wave overreaching the incident shock wave, as discussed in chapter 2.2.2. Therefore, the flow quantities such as pressure, temperature, and velocity directly behind the shock wave decrease as the shock wave propagates toward the PDC exit. Hence, even for the same shock Mach number leaving the tube, the time-dependent flow quantities such as pressure, density, and velocity at the tube exit deviate for the PDC and the ideal shock tube. While these quantities coincide right after the exit of an equally strong shock wave, the discrepancies increase with time. Nevertheless, at least the *initial* phase of the partially filled PDC exhaust is shown to remain highly comparable with the shock tube exhaust. This is favorable for the PDC exhaust characterization, as the shock tube exhaust has been the subject of extensive research in the past.

Characterization of the Exhaust Initial Phase

The high-resolution, high-speed schlieren images of the partially filled PDC allow for a detailed characterization of the PDC exhaust. As discussed before, the flow features occurring in the initial phase of the PDC exhaust are similar to those of a shock tube. Several features of the exhaust flow were reported in the literature for the shock tube

[1] The initial phase of the PDC exhaust is also similar to the flow evolution following a leakage from a pressurized vessle [115].

[2] It should be noted that a decaying pressure wave, similar to the pressure profile behind a transmitted shock in a partial filled PDC, emerges behind a blast wave inside a so called *explosive driven* shock tube. However, for the discussion here, conventional shock tubes are considered, which consist of a driver and driven section, separated by a diaphragm. The *ideal* shock tube refers to such a tube for inviscid flow.

exhaust. A brief overview of the initial phase of the starting jet and its primary features is given below, before reviewing the findings on the PDC exhaust conducted in the scope of this thesis. The first stage of the PDC exhaust is the shock diffraction that occurs at the nozzle lip immediately after the exit of the incident shock wave. The incident shock is considered as a normal straight shock while it propagates along the tube. However, the diffraction at the tube exit initiates the transition of the straight incident shock from the inside to a curved shock wave outside of the tube. The ongoing shock diffraction results in a continuous weakening of the incident shock as the curved shock transfers the same amount of energy to a larger volume of gas.

Perhaps the most essential characteristic of a jet is whether it is subsonic or supersonic. Depending on the incident shock wave strength, the post-shock flow in the laboratory reference frame can be either subsonic or supersonic. If the post-shock flow is supersonic, the exhaust jet remains supersonic, at least during the initial phase of the exhaust. However, a subsonic post-shock flow can occur for sufficiently small fill fractions, which is the case for the smallest fill fraction considered in publications 4.1 and 4.2. As discussed in chapter 2.2.2, when the post-shock flow is subsonic, a reflected expansion wave propagates back toward the head-end of the tube subsequent to the exit of the leading shock. The expansion wave accelerates the flow further, which initially is set to motion by the incident shock or the detonation wave. Due to the flow acceleration by the reflected expansion wave, the flow at the tube exit becomes sonic (choked). The initial subsonic flow inside the tube may even become locally supersonic upstream of the nozzle exit in the presence of a divergent nozzle. Thus, the PDC exhaust becomes supersonic shortly after the incident shock exits the tube, even for a considerably smaller fill fraction, producing an initial subsonic post-shock flow.

The supersonic exhaust flow expands through a pseudo-steady **P**randtl-**M**eyer (PM) expansion fan, which is centered at the nozzle lip. A pressure mismatch occurs between the pressure at the tail of the PM expansion fan and the evaluated pressure behind the incident shock wave. The pressure mismatch is a result of the overexpansion of the flow, which occurs initially at the outer region of the jet, but moves toward the jet center as time elapses. Consequently, a secondary shock wave adjusts the pressure mismatch at the outer region of the jet. Following the pressure mismatch, the secondary shock wave elongates toward the jet centerline to form a single shock wave. The schlieren images demonstrate that this is the origin of the well-known Mach disk of the underexpanded jet.

In contrast to the exhaust of an ideal shock tube, no quasi-steady state jet is observed during the initial phase of the PDC exhaust. A large enough initial pressure ratio in a shock tube results in a strong shock wave, producing a supersonic post-shock flow. The supersonic flow prevents the penetration of the reflected expansion wave back into the tube [116]. Hence, the flow at the shock tube exit relaxes from the conditions behind the shock wave to sonic conditions once the tail of the expansion fan arrives at the tube exit. As the arrival of the expansion fan takes a relatively long time, the steady pressure at the tube exit results in a quasi-steady jet including a quasi-steady Mach disk [117]. However, this is not the case for the PDC exhaust. The schlieren images show that shortly after its emergence, the Mach disk decreases in size while moving back toward the PDC exit. This particular evolution of the Mach disk is observed regardless of fill fraction and PDC nozzle

shape, including straight, convergent, divergent and convergent-divergent nozzles. The shrinking Mach disk in the PDC exhaust is attributed to the decreasing nozzle pressure as a result of the trailing Taylor wave. Accordingly, while a quasi-steady state jet can emerge already during the initial phase of the shock tube exhaust, the initial phase of the PDC exhaust is highly unsteady.

The Mach disk is part of a triple shock configuration consisting of the barrel shock, Mach disk, and the reflected shock. The latter is initially located within a vortex ring, which occurs as the jet shear layer at the trailing edge rolls up. The vortex ring contains two further distinct shock waves, the vortex-induced shock and the vortex-ring-embedded shock (VRES). In addition to the main vortex ring, there are several small counter-rotating vortex rings (CRVRs) originating from the triple point, generated by Kelvin-Helmholtz instability of the shear layer along the slipstream. The schlieren images show clear evidence of the pairing process of the CRVRs, resulting in a spatially growing slipstream.

Besides the eddy pairing, the schlieren images show an additional feature: a shocklet originating from the intersection of the reflected shock and the VRES, leading to a second triple point. As pointed out in chapter 4.1, this feature does not exist in steady-state underexpanded jets, yet has received little attention in past research on transient supersonic jets. Hence, the origin and evolution of the secondary triple point and the corresponding shocklet is investigated experimentally and numerically. Furthermore, a model is developed to propose a mechanism for the formation of the triple point. The output of the model, combined with the results of the numerical simulations, suggests that the triple point formation is due to a different mechanism than the classical Mach reflection, responsible for the first triple point. The formation of the triple point is attributed to the transient motion of the reflected shock. As the reflected shock is initially located inside the vortex ring, the convection of the vortex ring results in tilting of the part of the reflected shock next to the core. Eventually, a kink appears in the reflected shock, which separates the reflected shock from the VRES. While the subsequent motion of the VRES is predominantly in the translational direction, the reflected shock rotates toward the jet core. The rotational motion of the reflected shock results in a pronounced pressure gradient downstream of the reflected shock, lowering the pressure just below the kink. Conversely, the combination of the vertical VRES moving mainly in the axial direction and predominantly axial flow upstream of the VRES results in large pressure ratios downstream of the VRES. Thus, the pressure downstream of the VRES, particularly near the kink is relatively high. Consequently, an abrupt pressure rise along the kink occurs. Eventually, the kink becomes a triple point while the abrupt pressure rise leads to the formation of a new shock wave, the shocklet.

The described mechanism for the dynamic evolution of the transient jet is observed in different numerical and experimental studies for transient underexpanded jets. In addition, the second triple point and the shocklet can be observed in highly underexpanded jet studies reported in the literature, e.g., originating from shock tubes [118–120]. Hence, the findings related to the jet evolution, including the above-discussed mechanism for the second triple point, are not only restricted to PDC exhaust but are applicable for highly underexpanded compressible starting jets in general.

To examine the impact of the fill fraction on the PDC exhaust, the transient jet is further

investigated for other fill fractions. The fill fraction is increased gradually from very small fill fractions, up to overfilled configurations. Very similar flow features are observed in the PDC exhaust among all configurations, as documented in the publication provided in chapter 4.2. It is found that by increasing the fill fraction, the strength and size of the flow features during the initial exhaust phase grow; however, the jet undergoes the same dynamic evolution, in terms of flow topology and features. Moreover, the fill fraction has a strong impact on the full cycle of the PDC exhaust, which will be discussed in the next section.

5.1.2 Full Cycle of the Exhaust

Increasing the fill fraction leads to the combustion products leaving the tube earlier. Thus, the high density gradient combustion products overlay the flow features in the schlieren images for high fill fractions. To investigate the full cycle of the exhaust flow, high-speed PIV measurements are conducted, which are not restricted to limitations by the high density gradients. To the author's knowledge, this is the first time high-speed PIV is used to resolve the full PDC cycle. It is found that the PDC exhaust consists of several pronounced exhaust and suction phases. These multiple phases are attributed to the compression and expansion waves reflecting from the closed head and open end of the combustor.

A larger fill fraction is found to only affect the first exhaust phase by increasing the local axial velocity and global volume flux of the first exhaust phase. Interestingly, the subsequent suction and exhaust phases are found to be very similar in terms of timing, velocity, and volume flux. As the exhaust velocity decreases significantly for the subsequent exhaust phases, one may conclude that only the first exhaust phase is of interest for thrust or work generation. However, the schlieren images reveal that a considerable amount of energy, in the form of high-temperature combustion products, leaves the combustor in the third exhaust phase. Hence, the combination of the PIV and schlieren results reveal that although the first exhaust phase contains a considerable amount of total energy, due to the elevated pressure and high kinetic energy, the subsequent exhaust phases are still relevant to work production, due to the exhaust of high-temperature combustion products.

Nozzles Impact on the Exhaust

While different approaches can be used for altering the PDC exhaust, the objectives for enhancing the PDC exhaust strongly depend on the specific application of the combustor. For example, in PDC-nozzle engines, a single high momentum exhaust phase may be favorable for thrust generation, however this is not necessarily the case for PDC-turbine engines. Thus, possible approaches or parameters that allow for modification of the combustor exhaust are of interest. As already discussed in chapter 1, various nozzle geometries have been investigated extensively for PDC-nozzle engines in the past. It is well known that the wave dynamics inside the PDC can be modified by using a nozzle at the tube exit. However, the impact of the nozzle on the full cycle of the PDC exhaust has received little attention so far. Accordingly, an effort is made to determine the impact of

different nozzles on the PDC exhaust. Please note that this study is not documented in the publications provided in chapter 4. The investigated nozzles are a straight, convergent, divergent, and convergent-divergent nozzle, with diameter ratios of 1:1, 1:0.5, 1:1.5 and 1:0.5:1.5, respectively. The length to diameter ratio of all investigated nozzles is 2. Based on the schlieren images, it is found that the exhaust and suction phases can be substantially modified by using different nozzle shapes. The exhaust phases contain between zero and two suction phases, depending on the nozzle shape, fill fraction, and equivalence ratio of the mixture. While the convergent-divergent nozzle exhibits no suction phases over a wide range of equivalence ratios and fill fractions, two suction phases are observed consistently for the straight and divergent nozzle, regardless of fill fraction and equivalence ratio. On the contrary, the convergent nozzle exhibits either none or a relatively short suction phase, depending on fill fraction and equivalence ratio. These differences in the exhaust flow are attributed to the high dependency of the combustor wave dynamics on the nozzle shape. For instance, the nozzle shape strongly affects the first reflected wave (reflection of the detonation wave or incident shock wave) from the nozzle. The reflection of the leading wave from the straight or divergent nozzle is an expansion wave, while it is a compression wave for a convergent and convergent-divergent nozzle. Hence, subsequent to the exit of the leading wave, the pressure at the tube's open-end either increases or decreases depending on the nozzle shape, having a significant impact on the PDC exhaust. These results identify the nozzle geometry, in combination with the fill fraction and equivalence ratio, as a control parameter for altering the strength and the amount of exhaust and suction phases for a single detonation event in a PDC.

Applications of the Exhaust Characterization

The provided PDC exhaust characterization can be used for different purposes. For example, in a numerical study conducted by Xisto et al. [38], a conventional turbine stage was attached to the PDC exit. The purging phase of the PDC cycle was found to deliver thermodynamic states close to the turbine design conditions, resulting in relatively low losses during the purge sequence. However, a substantial variation in the rotor incident angle occurs when high-temperature combustion products pass through the turbine stage. The resulting mismatch of the rotor incident angle was attributed to a considerable amount of turbine efficiency penalization [38]. As discussed before, the exhaust of the PDC can be modified by different parameters. Accordingly, by matching these parameters, one may allow for high-temperature exhaust products passing the turbine stage with smaller fluctuations in flow parameters, thereby resulting in higher turbine efficiency. Depending on the turbine design, another possible source of substantial losses in PDC-turbine engines is a result of the high kinetic energy PDC exhaust entering the turbine. The excessive mass flow rate can lead to strong blockage of the turbine stage [121, 122], and large incident angles in the rotor [38], resulting in flow separation and substantial losses. As shown in chapter 4.2 by reducing the fill fraction, the volume flux can be more than halved, which has the potential for mitigating the aforementioned loss mechanisms by reducing the excessive flow rate. Despite modifying the PDC exhaust to utilize conventional turbines in PDE hybrid engines, another possible approach is developing new turbine concepts [123, 124] that allow turbines to operate with varying

inlet conditions at efficiencies comparable to the turbines of conventional gas turbines. The development of such concepts requires detailed knowledge of the PDC exhaust process. Hence, the gained insight on the PDC exhaust in this thesis may contribute to developing concepts allowing for efficient expansion of the PDC exhaust.

5.2 Damping of the Exhaust Transient Characteristic

For efficient PDC-turbine engines, a critical, if not the most critical element, is the ability to efficiently expand the highly transient exhaust flow through a turbine. The reduction of the level of fluctuations exhibited by the PDC exhaust is crucial for an efficient PDC-turbine engine since conventional turbines are mainly designed for steady inflow conditions. As described before, a conventional turbine attached directly to PDCs results in high entropy generation, particularly during the early phase of the exhaust flow, which begins after the passage of the incident shock wave [38]. In a multi-cycle operation mode, the peak pressure occurring in a cycle is a measure for the maximum fluctuation level. Hence, reducing the peak pressure in a PDC exhaust cycle is considered as a means to increase the turbine efficiency. Accordingly, it was found recently that high-amplitude inlet pressure fluctuations are responsible for a large portion of losses in a pulsating-flow driven turbine [47]. As the peak pressure in a cycle directly depends on the strength of the incident shock wave, reducing the shock strength is supposed to increase the efficiency of a PDC driven turbine. Besides which, a weaker incident shock entering the turbine results in a lower post-shock mass flow rate. Reducing the excessive mass flow rate can prevent a potential blockage of the turbine vanes, which may occur in the initial exhaust phase. Thus, a reduction of the incident shock wave strength can avert the intense blockage losses that are mainly caused by large flow separations at the turbine vanes [121, 122]. Furthermore, the incident shock wave reflects from the turbine vanes, causing considerable pressure loss[125]. The intensity of the reflected shock and its associated losses are sensitive to the incident shock strength. Hence, despite the minimization of the overall turbine inflow fluctuations, an efficient reduction of the incident shock wave strength is considered as a promising approach to enhance the PDC-turbine engine efficiency.

Two different approaches for modification of the PDC exhaust, with the aim of turbine efficiency enhancement, are investigated in the scope of this thesis. The first approach aims to mitigate the strength of transient shock waves (e.g., incident shock) before entering the turbine. The underlying concept relies on the redistribution of transient shock waves by dividing them into multiple waves. For this purpose, a device termed *divider* (shock divider) is designed, which divides a strong shock wave into multiple weaker waves. The incident shock wave normally represents the strongest shock wave in a PDC cycle and accordingly, the main purpose of the divider is an efficient mitigation of the incident shock prior to its entry to the turbine. As the strength of the incident shock wave increases with fill fraction, efficient mitigation of the incident shock for high fill fraction PDCs can be essential for performance purposes. Efficient mitigation of a strong shock wave by redistributing the largest part of the shock wave energy represents the primary objective of the divider. The second approach aims to not only mitigate the incident shock, but also to decrease the overall unsteadiness of the PDC exhaust. This approach relies on

the addition of a plenum between the PDC and the turbine. The plenum is supposed to mitigate the fluctuation level of the PDC exhaust by merely providing a relatively large volume in which the incident shock mitigates due to expansion, and the subsequent exhaust flow smoothes out due to mixing. In the following section, the divider approach is first reviewed before proceeding further with the plenum.

5.2.1 Divider

Within the scope of this thesis, a generic divider design is proposed to evaluate the suitability of this approach for efficient attenuation of the leading shock. The investigated dividers consist of two branches with a bifurcating and recombination section. A transient shock wave is generated using an open-end shock tube. After the shock wave enters the divider, it is separated into two parts and guided into two branches. While the lower branch is a straight channel with a constant cross-section, the upper branch consists of a converging and diverging section. The two sections are compound in a way so that the exit of the upper branch ends in the lower branch exit. The merging of the two branches results in a divider with a single output, as illustrated in the publication presented in chapter 4.3. .

The experimental investigations are supplemented by two numerical approaches: **g**eometrical **s**hock **d**iffraction (GSD) and CFD. The applied CFD approach is an advanced compressible Euler solver utilizing a novel cut-cell method, whereas GSD is a simplified approach to predict shock propagation. While the latter is developed in the scope of this thesis, the CFD solver is developed by Nadolski et al. [126]. The results of both numerical approaches show a very good agreement with the experimentally obtained schlieren and pressure. Although the numerical approaches do not account for viscosity, both only slightly overpredict the shock propagation velocity. Hence, the viscosity is found to have only a minor impact on the shock propagation inside the divider.

The comprehension of the fundamental flow dynamical mechanism of the divider is crucial for efficient design purposes. Accordingly, the flow features inside the divider are investigated based on the experimentally validated CFD results. As intended, the shock wave originating from the lower straight channel is shown to exit the divider before the one from the upper channel. The two shock waves leaving the divider one after the other result in a temporal redistribution of the initial single shock wave energy, and thereby provide the proof of concept for the divider. The underlying mechanisms for the shock wave propagation, as well as the post-shock flow evolution in the different branches, are determined and discussed in detail in the publication presented in chapter 4.3.

The low-cost numerical approaches are shown to be highly suitable for divider design studies. Hence, the impact of the channel width ratio, as one of the primary design parameters, is investigated numerically by varying the ratio from one to four. It is found that the width ratio considerably affects the flow evolution inside the divider. While the entire post-shock flow remains subsonic in the divider with the width ratio of one, a distinctive supersonic region, including several steady oblique shock waves, occurs in the upper branch of the divider with the highest width ratio. More importantly, all investigated dividers show their ability to separate a single shock wave into two subsequent shock waves exiting the divider. It is found that the channel width ratio

correlates with the time interval between the arrival of the shock wave at the divider exit. The shock waves separate further with increasing width ratio, resulting in a redistribution of energy in a more extended time period. While a large separation of the shock waves may well be desirable for a downstream turbine, it comes at an additional expense of total pressure. Hence, the divider width ratio can be used as a control parameter to modify the turbine inlet flow toward its design condition, but care must be given for the additional entropy generation.

The analysis of the shock propagation at the divider exit reveals the importance of the divider position with respect to the turbine. For a divider with a single exit channel, the separated shock waves exit the divider one after another from the very same channel. However, two shock waves propagating successively in the same direction in a channel interact with each other; the leading shock wave increases the speed of sound and the flow velocity in the post-shock region. Consequently, the subsequent shock wave propagation velocity increases. Thus, the second shock wave eventually coalesces with the leading shock wave in a long exit channel. However, any coalescing of the separated shock waves should be prevented, as it would otherwise eliminate the purpose of the divider. Accordingly, the time interval between the entrance of the shock wave to the turbine, and thus the temporal redistribution of the shock wave energy, can be increased by minimizing the divider exit channel length as well as the distance between the divider exit and the turbine inlet.

The exhaust of the divider can be further modified by various design parameters such as length and cross-section of the divider branches. Besides this, a single shock wave can be divided into multiple shock waves by increasing the total number of branches. Furthermore, the shape of the divider branches can be modified. However, the shape of the branches is considered to affect the divider induced total pressure loss considerably. The turning section of the divider branches induces pressure loss due to shock reflection from the wall, as discussed in chapter 4.3. Thus, minimizing the total bend of the branches is considered as a promising approach to reduce the reflection-caused pressure losses. Accordingly, a divider with multiple exit channels without any recombination section can minimize the total bend. Such a divider can be implemented in a PDC-turbine engine, e.g., by positioning the exit channels directly upstream of multiple turbine vanes. Multiple divider exits lead not only to a temporal but also a spatial redistribution of the incident shock wave energy. Hence, such a divider is considered to provide a smoother inlet flow for the turbine, thereby increasing the turbine efficiency.

5.2.2 Plenum

Although the divider has the potential for substantial mitigation of the incident shock strength and the subsequent kinetic energy of the jet, the level of fluctuation may still be too large, if the divider is the only device connecting the PDC to the turbine. Hence, another approach is investigated in the scope of this thesis with the objective of enhancing the turbine inflow conditions. For this purpose, a generic plenum is placed downstream of an array of six PDCs. The purpose of the plenum is not only to mitigate the incident shock and the shock induced trailing jet during the initial exhaust phase, but it also serves to reduce the unsteadiness of the PDC exhaust throughout the entire cycle. Simple firing

patterns, including a single tube and sequential tube firing patterns, are used to determine the plenum impact on the PDC exhaust. The flow inside the plenum is investigated based on static and total pressure measurements. Although the available data is limited as the measurements are conducted only at the plenum wall, it allows for further information on the plenum flow evolution. Accordingly, an attempt is made to reconstruct the flow evolution inside the plenum by combining the measured pressure data with the findings regarding the PDC exhaust, as discussed in chapter 5.1.

The relatively large volume provided by the plenum is shown to mitigate the pressure fluctuation level considerably. The attenuation of the fluctuations is attributed to different mechanisms. First, the pressure pulse intensity attenuates considerably as the incident shock wave diffracts immediately after it enters the plenum. The diffraction lasts until the incident shock is spread over the entire plenum cross-section with subsequent reflections from the plenum wall and center body. The large diffraction of the shock wave results in significant mitigation of the leading shock, since the shock wave transfers the same amount of energy to a considerably larger gas volume. Hence, the pressure behind the incident shock wave decreases considerably already at the plenum inlet due to shock diffraction. Furthermore, the pressure behind the leading shock decreases further as the sock wave propagates toward the plenum exit; the leading shock wave mitigates further as it propagates toward the plenum outlet. The mitigation of the leading shock along the plenum length is attributed mainly to the trailing Taylor wave as well as wall reflections, and to some extent to viscous effects.

A comparison between the total and static pressure at the plenum outlet is conducted to determine the fluid kinetic energy leaving the plenum. It is found that the main contribution to the total pressure is the static pressure, which indicates the ability of the plenum to mitigate the kinetic energy of the high impulsive jet emanating from the PDC. Pressure data at the inlet and outlet of the plenum enable the quantification of the impact of the plenum on the mitigation of the PDC exhaust's kinetic energy. However, as time-resolved static and total pressure at the plenum inlet are not available, a direct comparison of measured data between the plenum inlet and outlet is not feasible. Hence, CEA [127] computations are used to estimate the static-to-total pressure ratio at the plenum inlet based on the CJ condition. As the CJ condition only represents the condition directly behind the detonation wave, it is a strong simplification of the temporal pressure evolution of the plenum inlet. Nevertheless, the static pressure for a CJ detonation at the operating condition accounts for 70% of the total pressure, while the measured time-integrated pressure shows that this ratio increases to more than 90% at the plenum outlet.

The increase of static-to-total pressure ratio across the plenum is attributed mainly to two different mechanisms: the conversion of dynamic to static pressure and the dissipation of kinetic energy. The conversion of dynamic to static pressure is attributed to the PDC exhaust jet spreading over a relatively large cross-section in the plenum. Also, the weakening of the leading shock across the plenum contributes to some extent to the increased static-to-toal pressure ratio, as this ratio increases with the decreasing shock strength according to the 1D gasdynamic relations (equations 1-3 in chapter 4.4). The dissipation of the exhaust kinetic energy is mainly attributed to the shock waves of the underexpanded jet, viscous effects, mixing of the PDC exhaust with the gas inside the

plenum as well as flow separation and recirculation zones. The essential question, what portion of the exhaust kinetic energy is dissipated and what portion is converted into static pressure, cannot be answered based on available data. However, the generic plenum design leaves much room for further optimization to minimize the dissipation of kinetic energy. Perhaps the simplest improvement for the current plenum design is a geometric modification of the plenum inlet to allow for a smooth transition instead of sudden expansion. A smooth transition mitigates shock reflection and flow separation while reducing the recirculation zone at the plenum inlet, and thereby reducing the dissipation of kinetic energy. Efficient mitigation of the PDC exhaust kinetic energy is of great importance for integrating a multi-tube PDC with a downstream turbine as any reduction of the peak mass flow rate entering the turbine can reduce the flow separation and blockage of the turbine vanes [38, 121]; thus increasing the overall efficiency of the engine.

The peak pressure at the plenum outlet is of significant interest, as it determines the level of maximum fluctuation that a downstream turbine would be exposed to. Contrary to the plenum inlet, the peak pressure at the plenum outlet does not occur downstream of the firing tube, as one may expect. It is found that for both investigated firing patterns, the peak pressure at the plenum outlet occurs at the opposite side of the firing tube. This is attributed to reflections of the incident shock from the plenum wall and the center body. To quantify the attenuation of the peak pressure caused by the plenum, the plenums outlet peak pressure is compared to the CJ pressure, representing the PDC peak pressure. With respect to the CJ pressure, the peak pressure at the plenum outlet is mitigated by 85% for the single tube and 89% for the sequential tube firing pattern. Thus, these results demonstrate the ability of the plenum to considerably attenuate the incident shock wave while redistributing the energy, both spatially and temporally.

Although the plenum leads to considerable mitigation of the peak pressure, the pulsating character of the PDC exhaust remains pronounced at the plenum outlet. For both firing patterns, significant changes in pressure at the plenum outlet occur only for a short time relative to the cycle duration (short duty cycle). Thus, the pulsating plenum exhaust emphases the necessity of further measures to improve the turbine inlet flow. The level of fluctuation may well be further mitigated, if a combination of various approaches is used. For instance, by combining the plenum with dividers, the fluctuations may well be further suppressed. Another approach may be the optimization of the operating conditions, including firing frequency and firing pattern. The obtained data indicate an interaction of the consecutive firings inside the plenum, which provides the basis for optimizing the firing pattern with the objective of fluctuation minimization.

While the mitigation of the fluctuation level is crucial for the turbine, it is not the only measure to be considered. Despite the fact that any additional device, such as a plenum or divider, increases the length and weight of the engine, they also come at the cost of entropy generation. Hence, there is a trade-off between the losses induced by additional devices and the exergy loss due to the fluctuating turbine inflow conditions. Nevertheless, considering the substantial pressure gain of PDCs compared to conventional combustors, and the fact that the performance of conventional turbines is sensitive to transient inflow conditions, a not too small margin for entropy generation is available for devices such as plenum or dividers [128]. Further studies are needed to optimize this trade space.

5.3 Concluding Remarks & Future Work

The present work investigated the exhaust flow field of a pulse detonation combustor. The main flow features of the exhaust flow were extracted. Using different optical measurement techniques, time-resolved data were obtained for characterizing the fundamental problem of the compressible starting jet. By combining experimentally and numerically obtained data of a highly underexpanded starting jet, a model was developed to identify the underlying mechanism leading to the formation of the second triple point of the starting jet. Furthermore, the flow field properties of the PDC exhaust during a full cycle were identified, including the impact of the fill fraction. With the objective of enhancing the turbine inflow conditions, two concepts (shock divider and plenum) were developed. The ability of both approaches for damping the PDC exhaust transient characteristic was demonstrated. The excessive energy of an incident shock wave is successfully redistributed by using a shock divider. The impact of design parameters on the divider flow evolution, as well as design improvement suggestions, were discussed. Moreover, an assessment of the accuracy and dynamic response of pressure transducers was conducted. The transducers were then used to measure the pressure evolution in a plenum, downstream of an array of PDCs. The capability of the plenum for enhancing the exhaust flow for a downstream turbine was demonstrated.

Although the proposed approaches for modifying the PDC exhaust, as well as a few corresponding parameters, are studied, the conducted investigations barely exceed the level of proof of concept. Hence, there are a variety of incentives left for follow-up studies. Parametric studies and optimization of the divider geometry are essential to optimize the trade space for the divider induced entropy generation and the efficiency gain of the turbine. Furthermore, a simple generic plenum design is used in this study, leaving much room for future optimizations. Moreover, the applied methods can be extended for future studies. Although the progress made within the scope of this thesis regarding the application of different measurement techniques allow for high-quality time-resolved data, further combinations with numerical approaches may well be beneficial for various reasons. Generally, numerical simulations are capable of capturing much more parameters than experimentally feasible in such a harsh environment. The numerical approaches can further be essential for optimization purposes in future design studies. As the numerical approaches used in the current thesis were validated using experimental data, they can be used for the validation of other measurement techniques.

As for PDC-turbine engines, different open questions remain for future work to answer concerning an efficient combination of the combustor with a turbine. Although some insights on the impact of nozzle geometry on the full cycle of the PDC were given in this thesis, further comprehensive studies are needed to evaluate their impact on the gas dynamic features, engine operability, and the overall efficiency of the PDC-turbine engine. Moreover, the impact of the PDC geometry, including its diameter and length, on the combustor exhaust needs to be considered for future studies. The operability of smaller PDCs, with high success rates at operation frequencies in excess of 1.9 kHz, has been demonstrated recently [129]. Utilizing a large number of small PDCs at low fill fraction may reduce the pulsating character of the plenum exhaust, while providing enough mass

flow at operating frequencies of kHz rates to drive a downstream turbine without having to rely on a secondary air flow.

Another open question is the interaction of a turbine with an upstream plenum, as reflections of the waves may considerably impact the plenum flow evolution. Furthermore, it is worth noting that the conclusions made in this thesis based on plenum measurements are limited, as the pressure was only measured at the plenum wall. The wall pressure is not necessarily representative of the entire cross-section. The reflection of the compression and expansion waves from the plenum wall, center body, and its outlet presumably result in a non-uniform flow. Hence, data from the entire cross-section would be necessary for a comprehensive evaluation of the plenum. The applied high-frequency total pressure probe may well be a simple and suitable diagnostic technique for such follow-up studies. Those measurements could also address the very important question regarding the total pressure loss caused by an additional device, such as a plenum or divider. Also other measurement techniques can contribute to a comprehensive assessment of the proposed approaches. For example, measuring the gas temperature based on TDLAS can provide time-resolved turbine inlet gas temperature, which is significant for the turbine thermal efficiency.

To increase the overall efficiency of PDC-turbine engines, a combination of different approaches may be indispensable. A device between the PDCs and the turbine could consist of a plenum with ejectors at its inlet for injecting secondary air for cooling and mixing, thereby mitigating the overall unsteadiness. Additional shock dividers could further mitigate the pressure fluctuations and peak loads on the downstream turbine. The combination of such a device with an optimized firing pattern may well result in a significant efficiency gain compared to conventional gas turbines. The findings of this thesis may provide a basis for future studies necessary to design an efficient PDE.

Bibliography

[1] DEUTSCHES KLIMA-KONSORTIUM. URL: https://www.deutsches-klima-konsortium.de/en/klima-debatten.html (visited on 10/13/2020).

[2] B. LOONEY. *BP statistical review of world energy 2020*. 2020.

[3] INTERNATIONAL ENERGY AGENCY. "CO2 Emissions from Fuel Combustion 2019" (2019).

[4] P. MORIARTY & D. HONNERY. "Can renewable energy power the future?" *Energy policy* 93 (2016), pp. 3–7.

[5] C. DE CASTRO, M. MEDIAVILLA, L. J. MIGUEL, & F. FRECHOSO. "Global solar electric potential: A review of their technical and sustainable limits". *Renewable and Sustainable Energy Reviews* 28 (2013), pp. 824–835.

[6] INTERNATIONAL ENERGY AGENCY 2019. "World Energy Outlook" (2019).

[7] V. DUSCHA, J. WACHSMUTH, J. ECKSTEIN, & B.PFLUGER. *GHG Neutral EU2050 - a scenario of an EU with net-zero greenhouse gas emissions and its implications*. Tech. rep. German Environment Agency, 2019.

[8] ROLLS ROYCE. *Zero carbon by 2050*. URL: https://www.rolls-royce.com/media/press-releases/2020/05-06-2020-rr-puts-net-zero-carbon-by-2050-at-the-heart-of-future-innovation-and-growth.aspx (visited on 10/13/2020).

[9] EUROPEAN TURBINE NETWORK. *ETN position on the public consultation "A EU hydrogen strategy"*. Tech. rep. 2020.

[10] J. I. HILEMAN, D. S. ORTIZ, J. T. BARTIS, H. M. WONG, P. E. DONOHOO, M. A. WEISS, & I. A. WAITZ. *Near-term feasibility of alternative jet fuels*. Tech. rep. Rand Corporation, 2009.

[11] R. O. PRICE. "Liquid hydrogen-an alternative aviation fuel". *Aerospace Engineering;(USA)* 11 (1991).

[12] S. C. GÜLEN. "Beyond Brayton cycle: It is time to change the paradigm". *Journal of Engineering for Gas Turbines and Power* 140.11 (2018), pp. 1–10. DOI: 10.1115/1.4039828.

[13] W. H. HEISER & D. T. PRATT. "Thermodynamic cycle analysis of pulse detonation engines". *Journal of Propulsion and Power* 18.1 (2002), pp. 68–76.

[14] S. M. JONES & D. E. PAXSON. "Potential benefits to commercial propulsion systems from pressure gain combustion". In: *49th AIAA/ASME/SAE/ASEE Joint Propulsion-Conference*. 2013, p. 3623.

[15] D. E. PAXSON & T. KAEMMING. "Influence of unsteadiness on the analysis of pressure gain combustion devices". *Journal of Propulsion and Power* 30.2 (2014), pp. 377–383. DOI: 10.2514/1.B34913.

[16] M. R. NALIM. "Thermodynamic limits of work and pressure gain in combustion and evaporation processes". *Journal of Propulsion and Power* 18.6 (2002), pp. 1176–1182.

[17] J. KENTŽFIELD. "Thermodynamics of airbreathing pulse-detonation engines". *Journal of Propulsion and Power* 18.6 (2002), pp. 1170–1175.

[18] J. GRAY, J VINKELOE, J MOECK, C. PASCHEREIT, P STATHOPOULOS, P BERNDT, & R KLEIN. "Thermodynamic evaluation of pulse detonation combustion for gas turbine power cycles". In: *Turbo Expo: Power for Land, Sea, and Air*. Vol. 49767. American Society of Mechanical Engineers. 2016, V04BT04A044.

[19] D. E. PAXSON & T. A. KAEMMING. "Foundational performance analyses of pressure gain combustion thermodynamic benefits for gas turbines". *50th AIAA Aerospace Sciences Meeting Including the New Horizons Forum and Aerospace Exposition* January (2012), pp. 1–13. DOI: 10.2514/6.2012-770.

[20] Z. C. OWENS & R. K. HANSON. "Single-cycle unsteady nozzle phenomena in pulse detonation engines". *Journal of Propulsion and Power* 23.2 (2007), pp. 325–337. DOI: 10.2514/1.22415.

[21] E. A. BARBOUR & R. K. HANSON. "Analytic model for single-cycle detonation tube with diverging nozzles". *Journal of Propulsion and Power* 25.1 (2009), pp. 162–172. DOI: 10.2514/1.35420.

[22] J. T. PEACE. "Gasdynamic Phenomena and Propulsive Performance of Pulse Detonation Engines". PhD thesis. 2019.

[23] K KAILASANATH. "A review of research on pulse detonation engine nozzles". In: *37th Joint Propulsion Conference and Exhibit*. 2001, p. 3932.

[24] J. KENTŽFIELD. "Fundamentals of idealized airbreathing pulse-detonation engines". *Journal of Propulsion and Power* 18.1 (2002), pp. 77–83.

[25] D. ALLGOOD, E. GUTMARK, J. HOKE, R. BRADLEY, & F. SCHAUER. "Performance studies of pulse detonation engine ejectors". *Journal of Propulsion and Power* 24.6 (2008), pp. 1317–1323.

[26] D. ALLGOOD, E. GUTMARK, A. RASHEED, & A. J. DEAN. "Experimental investigation of a pulse detonation engine with a two-dimensional ejector". *AIAA journal* 43.2 (2005), pp. 390–398.

[27] A. OPALSKI, D. PAXSON, & M. WERNET. "Detonation driven ejector exhaust flow characterization using planar DPIV". In: *41st AIAA/ASME/SAE/ASEE Joint Propulsion Conference & Exhibit*. 2005, p. 4379.

[28] N. ENDUT, J. MORLEY, & P.-L. TIEN. "The changing transmission mechanism of US monetary policy". *Empirical Economics* 54.3 (2018), pp. 959–987.

[29] R. J. SANTORO & S. PAL. "Thrust Augmentation Measurements Using a Pulse Detonation Engine Ejector" (2003).

[30] A. GLASER, N. CALDWELL, & E. GUTMARK. "Experimental investigation into the acoustic performance of a pulse detonation engine with ejector". In: *43rd AIAA aerospace sciences meeting and exhibit*. 2005, p. 1345.

[31] R. SHEHADEH, S. SARETTO, S.-Y. LEE, & R. SANTORO. "Thrust augmentation measurements for a pulse detonation engine driven ejector". In: *40th AIAA/ASME/SAE/ASEE Joint Propulsion Conference and Exhibit*. 2004, p. 3398.

[32] J. WILSON. "Effect of pulse length and ejector radius on unsteady ejector performance". *Journal of Propulsion and Power* 23.2 (2007), pp. 345–352.

[33] D PALFREYMAN & R. MARTINEZ-BOTAS. "The pulsating flow field in a mixed flow turbocharger turbine: An experimental and computational study". *J. Turbomach.* 127.1 (2005), pp. 144–155.

[34] M. PADZILLAH, S RAJOO, & R. MARTINEZ-BOTAS. "Influence of speed and frequency towards the automotive turbocharger turbine performance under pulsating flow conditions". *Energy conversion and management* 80 (2014), pp. 416–428.

[35] A. COSTALL, R. F. MARTINEZ-BOTAS, & D. PALFREYMAN. "Detailed study of pulsating flow performance in a mixed flow turbocharger turbine". In: *Turbo Expo: Power for Land, Sea, and Air*. Vol. 47306. 2005, pp. 1415–1433.

[36] F. HELLSTRÖM. "Numerical computations of the unsteady flow in turbochargers". PhD thesis. KTH, 2010.

[37] L. CHEN, W. ZHUGE, Y. ZHANG, Y. LI, & S. ZHANG. "Investigation of flow structure in a turbocharger turbine under pulsating flow conditions". *SAE International Journal of Fuels and Lubricants* 1.1 (2009), pp. 1167–1174.

[38] C. XISTO, O. PETIT, T. GRÖNSTEDT, A. ROLT, A. LUNDBLADH, & G. PANIAGUA. "The efficiency of a pulsed detonation combustor–axial turbine integration". *Aerospace Science and Technology* 82-83 (2018), pp. 80–91. DOI: 10.1016/j.ast.2018.08.038. URL: https://doi.org/10.1016/j.ast.2018.08.038.

[39] M. H. FERNELIUS. "Experimental and computational analysis of an axial turbine driven by pulsing flow" (2017).

[40] A. J. DEAN, V. TANGIRALA, A. RASHEED, & P. F. PINARD. "Operation and noise transmission of an axial turbine driven by a pulse detonation combustor". *Proceedings of the ASME Turbo Expo* 6 PART B (2005), pp. 1275–1284. DOI: 10.1115/GT2005-69141.

[41] A. SURESH, D. C. HOFER, & V. E. TANGIRALA. "Turbine efficiency for unsteady, periodic flows". *Journal of Turbomachinery* 134.3 (2011), pp. 1–6. DOI: 10.1115/1.4003246.

[42] A. GLASER, N. CALDWELL, & E. GUTMARK. "Performance of an axial flow turbine driven by multiple pulse detonation combustors". In: *45th AIAA Aerospace Sciences Meeting and Exhibit*. 2007, p. 1244.

[43] A. S. GEORGE, R DRISCOLL, E GUTMARK, & D MUNDAY. "Experimental comparison of axial turbine performance under steady and pulsating flows". *Journal of Turbomachinery* 136.11 (2014).

[44] V. ANAND, A. ST. GEORGE, E. KNIGHT, & E. GUTMARK. "Investigation of pulse detonation combustors — Axial turbine system". *Aerospace Science and Technology* 93 (2019), p. 105350. DOI: 10.1016/j.ast.2019.105350. URL: https://doi.org/10.1016/j.ast.2019.105350.

[45] A. RASHEED, A. H. FURMAN, & A. J. DEAN. "Pressure measurements and attenuation in a hybrid multitube pulse detonation turbine system". *Journal of Propulsion and Power* 25.1 (2009), pp. 148–161. DOI: 10.2514/1.31893.

[46] A. RASHEED, A. H. FURMAN, & A. J. DEAN. "Experimental investigations of the performance of a multitube pulse detonation turbine system". *Journal of Propulsion and Power* 27.3 (2011), pp. 586–596. DOI: 10.2514/1.B34013.

[47] M. H. FERNELIUS & S. E. GORRELL. "Mapping Efficiency of a Pulsing Flow-Driven Turbine". *Journal of Fluids Engineering* 142.6 (2020), pp. 1–8. DOI: 10.1115/1.4045993.

[48] W. FICKETT & W. C. DAVIS. *Detonation: theory and experiment*. Courier Corporation, 2000.

[49] E. WINTENBERGER & J. E. SHEPHERD. "Stagnation Hugoniot analysis for steady combustion waves in propulsion systems". *Journal of propulsion and power* 22.4 (2006), pp. 835–844.

[50] J. VON NEUMANN. *Theory of detonation waves*. U.S. Government Document. A progress report to the National Defense Research Committee Div. B, OSRD-549, April 1, 1942. May 1942, p. 34.

[51] D. L. CHAPMAN. "VI. On the rate of explosion in gases". *The London, Edinburgh, and Dublin Philosophical Magazine and Journal of Science* 47.284 (1899), pp. 90–104.

[52] Y. ZEL'DOVICH. "On the Theory of the Propagation of Detonation in Gaseous Systems". *Zh. Eksp. Teoret. Fiz.* 10 (1940), pp. 542–568.

[53] W. DÖRING. "On detonation processes in gases". *Ann. Phys* 43.421-436 (1943), p. 9.

[54] J. H. LEE. *The detonation phenomenon*. 2008.

[55] J. LEE & M. RADULESCU. "On the hydrodynamic thickness of cellular detonations". *Combustion, Explosion and Shock Waves* 41.6 (2005), pp. 745–765.

[56] J. H. LEE. "Dynamic parameters of gaseous detonations". *Annual review of fluid mechanics* 16.1 (1984), pp. 311–336.

[57] A. OPPENHEIM & R. SOLOUKHIN. "Experiments in gasdynamics of explosions". *Annual Review of Fluid Mechanics* 5.1 (1973), pp. 31–58.

[58] P. BERNDT. "Mathematical modeling of the shockless explosion combustion". PhD thesis. 2016.

[59] T. ENDO, J. KASAHARA, A. MATSUO, K. INABA, S. SATO, & T. FUJIWARA. "Pressure history at the thrust wall of a simplified pulse detonation engine". *AIAA journal* 42.9 (2004), pp. 1921–1930.

[60] K KAILASANATH. "Recent developments in the research on pulse detonation engines". *AIAA journal* 41.2 (2003), pp. 145–159.

[61] C. LI & K KAILASANATH. "Partial fuel filling in pulse detonation engines". *Journal of Propulsion and Power* 19.5 (2003), pp. 908–916.

[62] S. SATO, A. MATSUO, T. ENDO, & J. KASAHARA. "Numerical studies on specific impulse of partially filled pulse detonation rocket engines". *Journal of Propulsion and Power* 22.1 (2006), pp. 64–70.

[63] G. RUDINGER. "Improved wave diagram procedure for shock reflection from an open end of a duct". *Journal of Applied Physics* 26.11 (1955), pp. 1339–1341.

[64] J. PEACE & F. LU. "Detonation-to-shock wave transmission at a contact discontinuity". *Shock Waves* 28.5 (2018), pp. 981–992.

[65] V. BIRMAN. "Thermal effects on measurements of dynamic processes in composite structures using piezoelectric sensors". *Smart materials and structures* 5.4 (1996), p. 379.

[66] J. A. T. GRAY. *Reduction in the run-up distance for the deflagration-to-detonation transition and applications to pulse detonation combustion*. Technische Universitaet Berlin (Germany), 2018.

[67] A. A. BARLIAN, W.-T. PARK, J. R. MALLON, A. J. RASTEGAR, & B. L. PRUITT. "Semiconductor piezoresistance for microsystems". *Proceedings of the IEEE* 97.3 (2009), pp. 513–552.

[68] S. CARTER, A. NED, J. CHIVERS, & A. BEMIS. "Selecting piezoresistive vs. piezoelectric pressure transducers". *Kulite Semiconductor Products, Inc* (2016).

[69] C. A. STEVENS, M. L. FOTIA, J. L. HOKE, & F. R. SCHAUER. "Comparison of transient response of pressure measurement techniques with application to detonation waves". In: *53rd AIAA Aerospace Sciences Meeting*. Innovative Scientific Solutions Inc. Dayton United States. Jan. 2015.

[70] R. M. GEJJI, I. V. WALTERS, S. BEARD, A. LEMCHERFI, S. V. SARDESHMUKH, S. D. HEISTER, & C. D. SLABAUGH. "Transducer Installation Effects on Pressure Measurements in PGC Devices". In: *2018 AIAA Aerospace Sciences Meeting*. Reston, Virginia: American Institute of Aeronautics and Astronautics, Jan. 2018, pp. 1–12.

[71] D. E. PAXSON & K. DOUGHERTY. "Ejector enhanced pulsejet based pressure gain combustors: An old idea with a new twist". *41st AIAA/ASME/SAE/ASEE Joint Propulsion ...* (2005).

[72] J. E. ROGERS, Y.-K. YOON, M. SHEPLAK, & J. W. JUDY. "A passive wireless microelectromechanical pressure sensor for harsh environments". *Journal of Microelectromechanical Systems* 27.1 (2017), pp. 73–85.

[73] G. S. SETTLES. *Schlieren and shadowgraph techniques: visualizing phenomena in transparent media*. Springer Science & Business Media, 2012.

[74] M. J. HARGATHER & G. S. SETTLES. "A comparison of three quantitative schlieren techniques". *Optics and Lasers in Engineering* 50.1 (2012), pp. 8–17.

[75] G. ELSINGA, B. VAN OUDHEUSDEN, F SCARANO, & D. WATT. "Assessment and application of quantitative schlieren methods: Calibrated color schlieren and background oriented schlieren". *Experiments in Fluids* 36.2 (2004), pp. 309–325.

[76] A. GLASER, N. CALDWELL, & E. GUTMARK. "Performance Measurements of a Pulse Detonation Combustor Array Integrated with an Axial Flow Turbine". In: *44th AIAA Aerospace Sciences Meeting and Exhibit*. Reston, Virigina: American Institute of Aeronautics and Astronautics, 2006.

[77] Z. C. OWENS. *Flowfield Characterization and Model Development in Detonation Tubes*. ProQuest, 2008.

[78] D. ALLGOOD, E. GUTMARK, T MEYER, & J. L. HOKE. "Computational and experimental studies of pulse detonation engines". *... Sciences Meeting and ...* 17.4 (2003), p. 5.

[79] A. GLASER, D. ALLGOOD, & E. GUTMARK. "Experimental investigation into the off-design performance of a pulse detonation engine". *42nd AIAA Aerospace Science ...* (2004).

[80] Y NAGURA, J KASAHARA, & A. MATSUO. "Multi-frame visualization for detonation wave diffraction". *Shock waves* 26.5 (2016), pp. 645–656.

[81] RACINE. "Experimental Analysis of a Hybrid Pulse Detonation Combustor / Gas Turbine Engine" (Jan. 2008), pp. 1–12.

[82] E. SCHULTZ. "Detonation diffraction through an abrupt area expansion". PhD thesis. Citeseer, 2000.

[83] A KAWASAKI & J KASAHARA. "A novel characteristic length of detonation relevant to supercritical diffraction". *Shock Waves* 30.1 (2020), pp. 1–12.

[84] C. E. WILLERT, D. M. MITCHELL, & J. SORIA. "An assessment of high-power light-emitting diodes for high frame rate schlieren imaging". *Experiments in fluids* 53.2 (2012), pp. 413–421.

[85] J OJEDA-CASTANEDA & D MALACARA. *Optical shop testing*. 1978.

[86] M. RAFFEL, C. E. WILLERT, F. SCARANO, C. J. KÄHLER, S. T. WERELEY, & J. KOMPENHANS. *Particle image velocimetry: a practical guide*. Springer, 2018.

[87] D. MITCHELL, D. HONNERY, & J. SORIA. "Particle relaxation and its influence on the particle image velocimetry cross-correlation function". *Experiments in fluids* 51.4 (2011), pp. 933–947.

[88] M. R. HAGHDOOST, J. FÖRSTER, D. EDGINGTON-MITCHELL, & K. OBERLEITHNER. "Experimental Investigation of Solid Tracer Particle Response Across a Mach Disk by PIV and Schlieren". In: *Proceedings of the 19th International Symposium on Application of Laser and Imaging Techniques to Fluid Mechanics, Lisbon, PT*. 2018.

[89] E. GUILLOU, M. GANCEDO, E. GUTMARK, & A. MOHAMED. "PIV investigation of the flow induced by a passive surge control method in a radial compressor". *Experiments in fluids* 53.3 (2012), pp. 619–635.

[90] S. KLINE & F. MCCLINTOCK. "Describing uncertainty in single sample experiments". *Mech. Engineering* 75 (1953), pp. 3–8.

[91] J. WESTERWEEL. "Theoretical analysis of the measurement precision in particle image velocimetry". *Experiments in Fluids* 29.1 (2000), S003–S012.

[92] M. RAFFEL. "Background-oriented schlieren (BOS) techniques". *Experiments in Fluids* 56.3 (2015), p. 60.

[93] K. ROUSER, P. KING, F. SCHAUER, R. SONDERGAARD, L. GOSS, & J. HOKE. "Time-accurate flow field and rotor speed measurements of a pulsed detonation driven

turbine". In: *49th AIAA Aerospace Sciences Meeting including the New Horizons Forum and Aerospace Exposition*. 2011, p. 577.

[94] T MIZUKAKI, K WAKABAYASHI, T MATSUMURA, & K NAKAYAMA. "Background-oriented schlieren with natural background for quantitative visualization of open-air explosions". *Shock Waves* 24.1 (2014), pp. 69–78.

[95] O. SOMMERSEL, D BJERKETVEDT, S. CHRISTENSEN, O KREST, & K VAAGSAETHER. "Application of background oriented schlieren for quantitative measurements of shock waves from explosions". *Shock Waves* 18.4 (2008), pp. 291–297.

[96] T. MIZUKAKI, B. F. BATHEL, S. E. BORG, P. M. DANEHY, S. M. MURMAN, T. MATSUMURA, K. WAKABAYASHI, & Y. NAKAYAMA. "Background-oriented Schlieren for large-scale and high-speed aerodynamic phenomena". In: *53rd AIAA Aerospace Sciences Meeting*. 2015, p. 1692.

[97] M. HARGATHER. "Background-oriented schlieren diagnostics for large-scale explosive testing". *Shock Waves* 23.5 (2013), pp. 529–536.

[98] K. O. WINTER & M. J. HARGATHER. "Three-dimensional shock wave reconstruction using multiple high-speed digital cameras and background-oriented schlieren imaging". *Experiments in Fluids* 60.6 (2019), p. 93.

[99] Y. XIONG, T. KAUFMANN, & N. NOIRAY. "Towards robust BOS measurements for axisymmetric flows". *Experiments in Fluids* 61.8 (2020), pp. 1–12.

[100] N. P. VAN HINSBERG & T. RÖSGEN. "Density measurements using near-field background-oriented schlieren". *Experiments in fluids* 55.4 (2014), p. 1720.

[101] L. VENKATAKRISHNAN. "Density measurements in an axisymmetric underexpanded jet by background-oriented schlieren technique". *AIAA journal* 43.7 (2005), pp. 1574–1579.

[102] A. W. CASWELL, S. ROY, X. AN, S. T. SANDERS, F. R. SCHAUER, & J. R. GORD. "Measurements of multiple gas parameters in a pulsed-detonation combustor using time-division-multiplexed Fourier-domain mode-locked lasers". *Applied optics* 52.12 (2013), pp. 2893–2904.

[103] C. A. FUGGER, K. Y. CHO, J. HOKE, M. GOMEZ GOMEZ, T. R. MEYER, S. A. SCHUMAKER, & A. W. CASWELL. "Detonation Dynamics Visualization From Megahertz Imaging". In: *AIAA Scitech 2020 Forum*. 2020, p. 0441.

[104] C. L. JOURNELL, R. M. GEJJI, I. V. WALTERS, A. I. LEMCHERFI, C. D. SLABAUGH, & J. B. STOUT. "High-Speed Diagnostics in a Natural Gas–Air Rotating Detonation Engine". *Journal of Propulsion and Power* (2020), pp. 1–10.

[105] D. DEPPERSCHMIDT, R. MILLER, J. TOBIAS, M. UDDI, A. K. AGRAWAL, & J. B. STOUT. "Time-Resolved PIV diagnostics to measure flow field exiting methane-fueled rotating detonation combustor". In: *AIAA Scitech 2019 Forum*. 2019, p. 1514.

[106] I. B. DUNN, J. SOSA, M. SALVADORI, K. A. AHMED, & S. MENON. "Flowfield Velocity Measurements of a Rotating Detonation Engine". In: *AIAA Scitech 2020 Forum*. 2020, p. 1176.

[107] J. TOBIAS, R. MILLER, & A. K. AGRAWAL. "Flow Measurements inside a Rotating Detonation Combustor". In: *AIAA Propulsion and Energy 2020 Forum*. 2020, p. 3869.

[108] V VILIMPOC, L. GOSS, & B SARKA. "Spatial temperature-profile measurements by the thin-filament-pyrometry technique". *Optics letters* 13.2 (1988), pp. 93–95.

[109] V VILIMPOC & L. GOSS. "SiC-based thin-filament pyrometry: theory and thermal properties". In: *Symposium (International) on Combustion*. Vol. 22. 1. Elsevier. 1989, pp. 1907–1914.

[110] J. D. MAUN, P. B. SUNDERLAND, & D. L. URBAN. "Thin-filament pyrometry with a digital still camera". *Applied optics* 46.4 (2007), pp. 483–488.

[111] C. S. GOLDENSTEIN, R. M. SPEARRIN, J. B. JEFFRIES, & R. K. HANSON. "Infrared laser-absorption sensing for combustion gases". *Progress in Energy and Combustion Science* 60 (2017), pp. 132–176.

[112] S. T. SANDERS, J. A. BALDWIN, T. P. JENKINS, D. S. BAER, & R. K. HANSON. "Diode-laser sensor for monitoring multiple combustion parameters in pulse detonation engines". *Proceedings of the Combustion Institute* 28.1 (2000), pp. 587–594.

[113] D. W. MATTISON, C. M. BROPHY, S. T. SANDERS, L. MA, K. M. HINCKLEY, J. B. JEFFRIES, & R. K. HANSON. "Pulse detonation engine characterization and control using tunable diode-laser sensors". *Journal of propulsion and power* 19.4 (2003), pp. 568–572.

[114] F. SCHAUER, J. STUTRUD, & R. BRADLEY. "Detonation initiation studies and performance results for pulsed detonation engine applications". In: *39th Aerospace Sciences Meeting and Exhibit*. 2001, p. 1129.

[115] X. TANG, M. ASAHARA, A. K. HAYASHI, & N. TSUBOI. "Numerical investigation of a high pressure hydrogen jet of 82 MPa with adaptive mesh refinement: The starting transient evolution and Mach disk stabilization". *International Journal of Hydrogen Energy* 42.10 (2017), pp. 7120 –7134. DOI: https://doi.org/10.1016/j.ijhydene.2017.01.016. URL: http://www.sciencedirect.com/science/article/pii/S0360319917300381.

[116] R HILLIER. "Computation of shock wave diffraction at a ninety degrees convex edge". *Shock waves* 1.2 (1991), pp. 89–98.

[117] A HASELBACHER, S BALACHANDAR, & S. KIEFFER. "Open-ended shock tube flows: Influence of pressure ratio and diaphragm position". *AIAA journal* 45.8 (2007), pp. 1917–1929.

[118] B. THETHY, M REZAY HAGHDOOST, K. OBERLEITHNER, D. HONNERY, & D. EDGINGTON-MITCHELL. "Influence of nozzle geometry on detonation-driven and shock-driven transient supersonic jet flow". In: *24th International Society for Air Breathing Engines Conference*. 2019, pp. 1–22.

[119] C. DORA, T MURUGAN, S DE, & D. DAS. "Role of slipstream instability in formation of counter-rotating vortex rings ahead of a compressible vortex ring". *Journal of fluid mechanics* 753 (2014), p. 29.

[120] R ISHII, H FUJIMOTO, N HATTA, & Y UMEDA. "Experimental and numerical analysis of circular pulse jets". *Journal of Fluid Mechanics* 392 (Aug. 1999), pp. 129–153.

[121] D. VANZANTE, E. ENVIA, & M. G. TURNER. "The attenuation of a detonation wave by an aircraft engine axial turbine stage" (2007).

[122] A. ST. GEORGE & E. GUTMARK. "Trends in pulsating turbine performance: Pulse-detonation driven axial flow turbine". In: *50th AIAA Aerospace Sciences Meeting including the New Horizons Forum and Aerospace Exposition*. 2012, p. 769.

[123] G PANIAGUA, M. IORIO, N VINHA, & J SOUSA. "Design and analysis of pioneering high supersonic axial turbines". *International Journal of Mechanical Sciences* 89 (2014), pp. 65–77.

[124] C. CUCIUMITA & C. O. PASCHEREIT. "Numerical Performance Assessment of a Turbine Blade Row Operating Under Pulsed Detonation Combustion Inlet Conditions". In: *Turbo Expo: Power for Land, Sea, and Air*. Vol. 58561. American Society of Mechanical Engineers. 2019, V02BT40A022.

[125] A. RASHEED, V. TANGIRALA, A. DEAN, C. L. VANDERVORT, & C. HAUBERT. "Interactions of a pulsed detonation engine with a 2d blade cascade". In: *42nd AIAA aerospace sciences meeting and exhibit*. 2004, p. 1207.

[126] M NADOLSKI, M. R. HAGHDOOST, J. GRAY, D EDGINGTON-MITCHELL, K OBERLEITHNER, & R KLEIN. "Validation of under-resolved numerical simulations of the PDC exhaust flow based on high speed schlieren". In: *Active flow and combustion control 2018*. Springer, 2019, pp. 237–253.

[127] B. J. MCBRIDE. *Computer program for calculation of complex chemical equilibrium compositions and applications*. Vol. 2. NASA Lewis Research Center, 1996.

[128] P. STATHOPOULOS. "An alternative architecture of the Humphrey cycle and the effect of fuel type on its efficiency". *Energy Science & Engineering* 8.10 (2020), pp. 3702–3716.

[129] K. MATSUOKA, H. TAKI, A. KAWASAKI, J. KASAHARA, H. WATANABE, A. MATSUO, & T. ENDO. "Semi-valveless pulse detonation cycle at a kilohertz-scale operating frequency". *Combustion and Flame* 205 (2019), pp. 434–440.

Associated Publications

The publications associated with the thesis are given in the list below.

1. M. Rezay Haghdoost, J. Förster, D. Edgington-Mitchell, K. Oberleithner. *Experimental Investigation of Solid Tracer Particle Response Across a Mach Disk by PIV and Schlieren.* Proceedings of the 19th International Symposium on Application of Laser and Imaging Techniques to Fluid Mechanics, Lisbon, 2018, pp. 1922-1940.

2. M. Nadolski, M. Rezay Haghdoost, J. A. T. Gray, D. Edgington-Mitchell, K. Oberleithner und R. Klein: *Validation of Under-Resolved Numerical Simulations of the PDC Exhaust Flow Based on High Speed Schlieren.* Active Flow and Combustion Control 2018. S. 237–253. Springer International Publishing, 2019. DOI: https://doi.org/10.1007/978-3-319-98177-2_15

3. M. Rezay Haghdoost, D. Edgington-Mitchell, C.O. Paschereit, K. Oberleithner. *Investigation of the Exhaust Flow of a Pulse Detonation Combustor at different Operating Conditions based on High-Speed Schlieren and PIV.* AIAA Scitech 2019 Forum. American Institute of Aeronautics and Astronautics, 2019. DOI: https://doi.org/10.2514/6.2019-1512

4. Thethy, B., M. Rezay Haghdoost, K. Oberleithner, D. Honnery und D. Edgington-Mitchell: *Influence of Nozzle Geometry on Detonation-Driven and Shock-Driven Transient Supersonic Jet Flow.* 24th ISABE conference. International Society for Air Breathing Engines. 2019.

5. M. Rezay Haghdoost, B. Thethy, S. Bonggyun, M. Nadolski , R. Klein, D. Honnery, D. Edgington-Mitchell, C.O. Paschereit und K. Oberleithner: *Evaluation of Shock Dividers using Numerical and Experimental Methods.* AIAA Scitech 2020 Forum. American Institute of Aeronautics and Astronautics, 2020. DOI: https://doi.org/10.2514/6.2020-0926

6. Thethy, B., M. Rezay Haghdoost, C.O. Paschereit., D. Honnery, D. Edgington-Mitchell und K. Oberleithner: *Redistribution of Transient Shock Waves Using Shock Dividers.* AIAA Scitech 2020 Forum. American Institute of Aeronautics and Astronautics, 2020. DOI: https://doi.org/10.2514/6.2020-0925

7. M. Rezay Haghdoost, D. Edgington-Mitchell, S. Bengoechea, B. Thethy, F. Rouholahnejad, F. Habicht, C.O. Paschereit, J. Reiss, K. Oberleithner. *Detonation Initiation and Exhaust of a Pulse Detonation Combustor.* 73th Annual Meeting of the APS Division of Fluid Dynamics - Gallery of Fluid Motion. American Physical Society. 2020. DOI: https://doi.org/10.1103/APS.DFD.2020.GFM.V0025